The University Of Sheffield.

University of Sheffield

Department of Chemistry

Novel DNA-binding ruthenium complexes with potential surface linkers for biosensor construction

Thomas Andrews

Supervisor: Prof. Jim Thomas

A thesis submitted for the degree of Doctor of Philosophy

August 2018

"For with much wisdom comes much sorrow; the more knowledge, the more grief."

Ecclesiastes 1:18

Abstract

This thesis discusses the design and attempted synthesis of a DNA binding ruthenium complex with a surface linking ligand. Initially this was attempted using the tris(pyrazolyl)methane (tpm) unit that has been previously used to create a linker for other metal centres. This route was unsuccessful leading to the creation of multiple novel ligands without realising the goal of the project.

The tpm unit was utilised to construct a ruthenium complex with a thiol tail which may be used to attach to nanoparticles or a surface. The compound is shown in figure 1. While this compound was studied for its UV-Visible and luminescent properties, sufficient quantities of the compound for further study were not obtained.
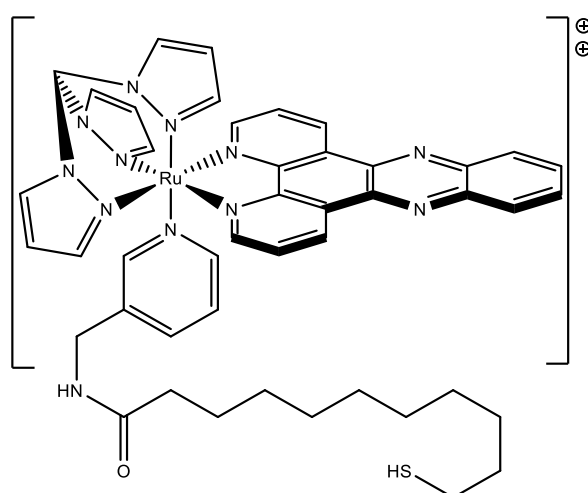
Figure 1 – Structure of [Ru(tpm)(dppz)(py-SH)]$^{2+}$ a novel potential DNA binding complex with a surface linker

Subsequently tris(pyridyl) ligands were investigated as a potential alternative. This led to the synthesis of a series of novel ruthenium complexes containing the tris(pyridyl)methylamine (tpyma) unit, not previously reported in use with ruthenium centres. The series included complexes not expected to bind to DNA, and to bind in different modes, to investigate the effect of the tpyma ligand on the DNA binding. These compounds are shown in figure 2.
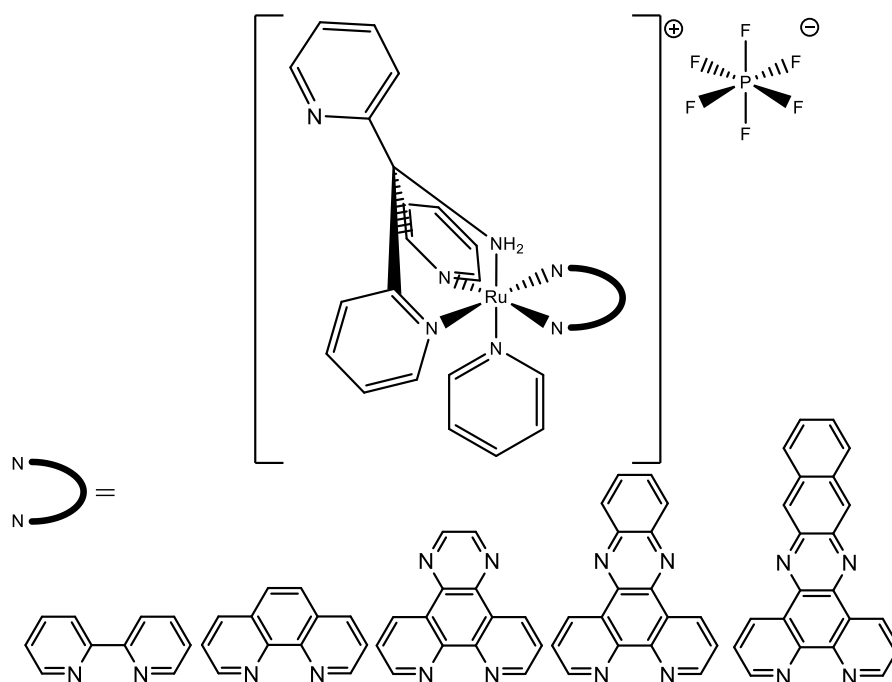
Figure 2 – Structures of [Ru(tpyma)(NN)(py)]$^{2+}$, novel ruthenium complexes containing the tpyma ligand

These complexes were found to bind to DNA in the expected mannar with association constants similar to those reported for analogues previously reported in literature. The photophysical, electrochemical and crystal structure studies are also reported. The crystal structures displayed an unexpected binding mode of the tpyma ligand making it unsuitable for the aim of the project. Subsequently attempts to synthetically alter the tpyma ligand to enable surface linkage are detailed.

Acknowledgements

I would like to thank my supervisor Prof. Jim Thomas for his help and guidance throughout the course of my studies. I would also like to thank my tutor, Prof. Graham Leggett and the other directors of the Molecular Scale Engineering DTC for their support and training through summer schools. I would also like to thank the EPSRC for funding the centre and making my PhD possible.

I would like to thank all the technical staff of the Department of Chemistry. In particular Rob Hanson for all the help with chromatography, Steve Atkin for technical support in the lab, Simon Thorpe for enabling the mass spec analysis and special thanks to Dr Craig Robertson for the extensive work on producing all the crystal structures presented in this thesis in a very short space of time. Also thanks to Dan for help with specialist glassware and Nick and Pete in the chemistry stores.

Thanks to all my fellow Thomas group members for your friendship and support through the length of my PhD, including Paul, Hiwa, Caroline, Mike, Stu, Sam, Sasha, Simon, Fliss, Kirsty and Charlotte. It would have not been the same without time shared with you all in the office and lab. Also thanks to my fellow members of the CDT, especially fellow E-floor friends PJ and Will.

During my PhD I was also fortunate to spend time in Italy with Prof. Colabufo and the Biofordrug team. Thanks to Ignazio, Mariangela, Alessandra, Tiziana, Julia and everyone in Bari for making it a very rewarding experience.

Outside chemistry I would like to thank all my friends who kept me sane, just about, through the ups and downs of studying. Thanks to all the members of UoSCC for shared time riding bikes and giving me a different obsession. Special thanks to Ross, without whom I would have given up long ago. Your support and encouragement was invaluable at some of the hardest and lowest points. Also thanks to Issac, Martin and Bart for keeping me going until the end.

Final thanks to my parents without whom I could not have completed this.

Declaration

Except where specific references have been made to other sources, the work within this thesis is the original work of the author. It has not been submitted, in whole or in part, for any other degree.

Thomas Andrews

August 2018

Abbreviations

A	adenine
AFM	Atomic force microscopy
bis-tppoe	1,5-bis(4-((2,2,2-tri(1H-pyrazol-1-yl)ethoxy)methyl)-1H-1,2,3-triazol-1-yl)pentane
bpm	2,2'-bipyrimidine
bpy	2,2-bipyridine
C	cytosine
COSY	NMR correlation spectroscopy
CT-DNA	Calf thymus DNA
CV	Cyclic voltammetry
cy	cyclohexane
DCC	N,N'-dicyclohexylcarbodiimide
DCM	dichloromethane
DIP	4,7-diphenyl-1,10-phenanthroline
DMF	dimethylformamide
dmso	dimethylsulfoxide
DNA	Deoxyribonucleic acid
dppn	benzo[i]dipyrido[3,2-a:2',3'-c]phenazine
dppz	dipyrido[3,2-a:2',3'-c]phenazine
dpq	1,10-phenanthroline-5,6-dione
dpqx	pyrazino[2,3-f][1,10]phenanthroline
dpyma	di(pyridin-2-yl)methanamine
E. Coli.	Escherichia coli
en	ethylenediamine

EtBr	ethidium bromide
G	guanine
H-bonds	Hydrogen bonds
HET	2-mercaptoethan-1-ol
HOBt	1-Hydroxybenzotriazole hydrate
HPLC	High-performance liquid chromatography
Hz	Hertz
LC-MS	Liquid chromatography - mass spectrometry
Me$_2$bpy	4,4′-dimethyl-2,2′-bipyridine
MLCT	Metal to ligand transfer
mRNA	Messenger RNA
NMR	Nuclear magnetic resonance
NPs	Nanoparticles
ORTEP	Oak Ridge Thermal Ellipsoid Plot
PDB	Protein data bank
phen	1,10-phenanthroline
phi	phenanthrene-9,10-diamine
ppm	parts per million
py	pyridine
py-SH	11-mercapto-N-(pyridin-2-ylmethyl)undecanamide
RNA	Ribonucleic acid
SAM	Self-assembled monolayer
sh	Shoulder
SPR	Surface plasmon resonance

T	thymine
terpy	2,2':6',2"-terpyridine
Tf	triflate
THF	tetrahydrofuran
tpamb	(4-((2,2,2-tri(1H-pyrazol-1-yl)ethoxy)methyl)phenyl)methanamine
tpazb	1,1',1"-(2-((4-(azidomethyl)benzyl)oxy)ethane-1,1,1-triyl)tris(1H-pyrazole)
tpbmb	1,1',1"-(2-((4-(bromomethyl)benzyl)oxy)ethane-1,1,1-triyl)tris(1H-pyrazole)
tpe	2,2,2-tri(1H-pyrazol-1-yl)ethan-1-ol
tpeib	2,2,2-tri(1H-pyrazol-1-yl)ethyl 4-iodobenzoate
tpm	tri(1H-pyrazol-1-yl)methane
tppoe	1,1',1"-(2-(prop-2-yn-1-yloxy)ethane-1,1,1-triyl)tris(1H-pyrazole)
tppoe-SH	3-(4-((2,2,2-tri(1H-pyrazol-1-yl)ethoxy)methyl)-1H-1,2,3-triazol-1-yl)propane-1-thiol
tpya	tris(pyridin-2-ylmethyl)amine
tpyaz	2,2',2"-(azidomethanetriyl)tripyridine
tpyc	tri(pyridin-2-yl)carbinol
tpyma	tri(pyridin-2-yl)methanamine
tpyma-SH	11-mercapto-N-(tri(pyridin-2-yl)methyl)undecanamide
tRNA	Transfer RNA
UV	Ultraviolet
XPS	X-ray photoelectron spectroscopy

Table of Contents

1.0 Introduction

1.1 Ruthenium

Ruthenium is a transition metal of the platinum group. As an element it displays a rich and diverse chemistry that has led to multiple uses and fields of research interest. Its discovery was first confirmed by the work of Russian chemist Karl Ernst Claus in 1844, when analysing the residues of platinum refining.[1] Claus named the new element after the latin name of his homeland, also honouring the name chosen in previous, unconfirmed reports of the element's discovery.[1] The element is found naturally alongside the other platinum metals (rhodium, palladium, iridium, osmium and platinum), and can be extracted using aqua regia and then exploiting the volatility of its tetroxide, which is separated by distillation.[2]

In its elemental form, ruthenium has been used as an alloying component alongside other platinum group metals as it can harden them. With platinum it has been used to form electrodes that are both cheaper and more chemically resistant to poisoning.[3] It is also an important heterogeneous catalyst, having been employed in the Fischer-Tropsch reaction which forms hydrocarbons from syngas. Ruthenium is two to three times more active than other metals used to catalyse this reaction.[4]

Arguably however, the greatest importance that ruthenium has in the research community is through the complexes it forms with other species. Early work in this area included the use of ruthenium red, a complex containing three aminated, oxygen bridged Ru centres, as a stain to image cellular structures.[5] Ruthenium complexes are also important homogeneous catalysts, with the Nobel Prize being awarded partly for work on the Grubbs catalyst in 2005. This ruthenium catalyst performs olefin metathesis, whereby the substituents of alkenes are redistributed, and has become a useful tool in organic synthesis.[6]

In more recent times complexes of ruthenium have been investigated for their anti-cancer properties, as less toxic alternatives to cis-platin.[7] One specific class of ruthenium complex that has generated a great deal of interest is that of polypyridyl-ruthenium complexes. In particular the complexes of 2,2-bipyridine (bpy) and 1,10-phenanthroline (phen) have been studied due to their stability and photophysical properties that could potentially be used to capture solar energy and play a role in

artificial photoshynthesis.[8,9] It is these polypyridyl complexes that are the subject of this project.

Ruthenium Red

1st Gen Grubbs catalyst
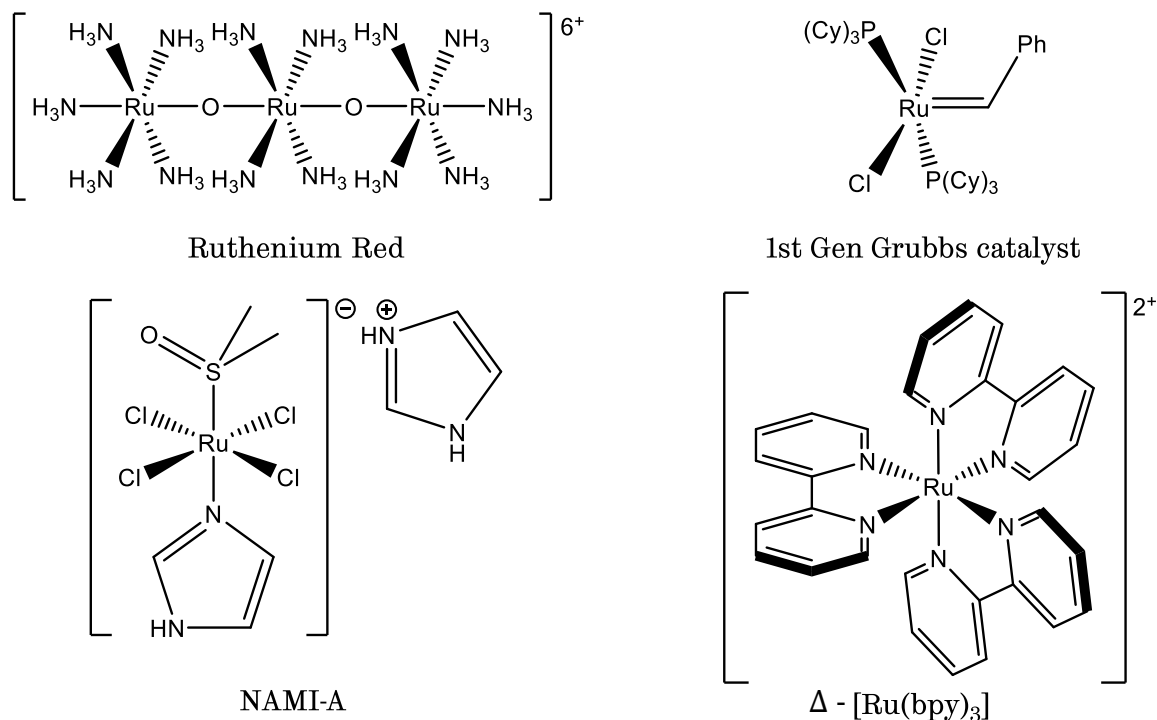
NAMI-A

Δ - [Ru(bpy)$_3$]

Figure 1.1 - Examples of ruthenium complexes important for staining (Ruthenium red), catalysis (Grubbs), chemotherapy (NAMI) and photochemistry ([Ru(bpy)$_3$])

1.2 Ru-polypyridyl complexes

[Ru(bpy)$_3$]$^{2+}$ was the first example of a transition metal complex that showed a charge transfer transition, resulting in a luminescent emission.[10] This effectively means that, in its excited state an electron moves from the ruthenium centre onto the bpy ligand. It is this charge separation that has led to the interest in polypyridyl complexes. As similar processes are key steps in natural photosynthesis, such complexes have become components in many artificial photosynthetic systems.[11] This class of complex also exhibits strong absorption in the visible region, and displays stable and long lived excited states whose photophysics can be tuned by altering the ligands coordinated to the metal.[12] These properties make them attractive prospects for a range of other applications.

One such application is as DNA probes. The first investigations of this kind were performed by Barton and co-workers, studying the interactions of [Ru(phen)$_3$]$^{2+}$ with

calf thymus DNA (CT-DNA).[13] The addition of DNA to the phen complex results in a decrease in absorbance and corresponding increase in luminescence, indicating that there is a binding interaction. The goal of this work was to find a probe that would be able to distinguish between different forms of DNA, owing to its chiral nature.[14] This was in response to the discovery of Z-DNA, which is a left handed helix, as opposed to the more common B-DNA, which is right handed.[15] This initial work has lead to a new field of research into the interactions of various Ru-polypyridyl complexes and DNA.
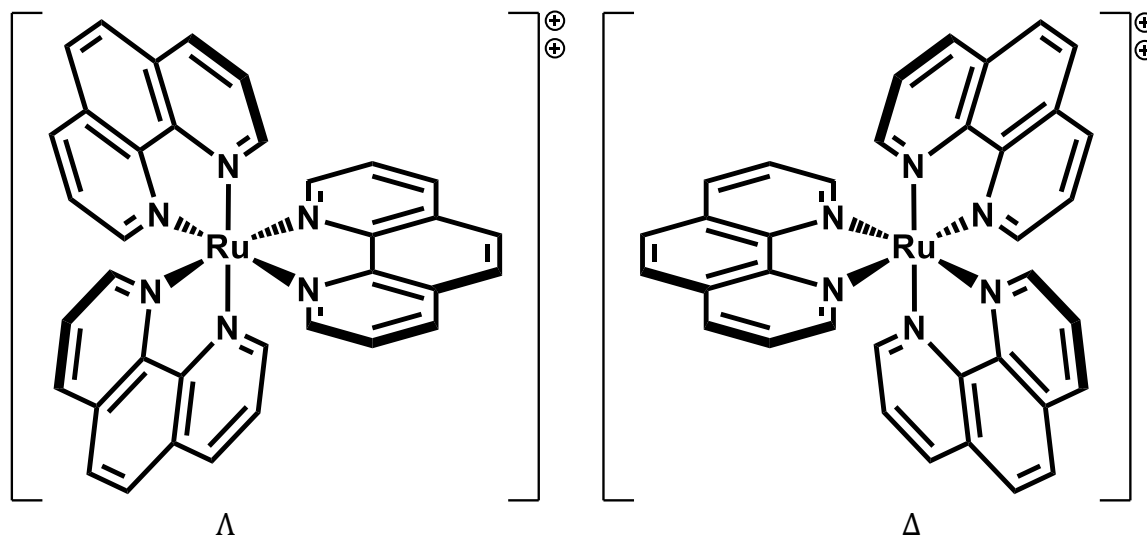
Figure 1.2 - The two enantiomers of $[Ru(phen)_3]^{2+}$

1.3 Deoxyribonucleic acid (DNA)

DNA is the fundamental information storage unit of life on earth. The code contained within its structure instructs the cell to create the structural proteins and enzymes that it requires to function. The process by which this information is thought to be translated into functional molecules is termed the "central dogma of molecular biology", illustrated by figure 1.3.[16] To synthesise proteins, the DNA helix is unwound and locally denaturedas the cellular machinery copies the required code, synthesising messenger RNA (mRNA) in a process called transcription. The mRNA then interacts with the protein synthesis apparatus and transfer RNA (tRNA) to produce a string of amino acids which folds to form the functional protein structure.[16]
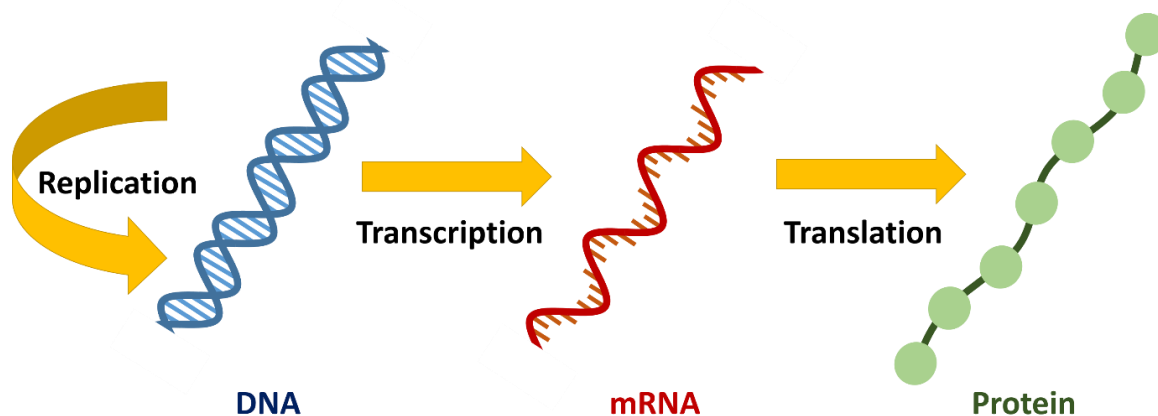
Figure 1.3 - The central dogma of molecular biology

As this process is vital to the construction of cells, and thus the growth of an organism, problems encountered in the process can lead to a range of diseases and disorders. If the DNA is damaged or mutated, important proteins may not be synthesised, leading to issues with cell function. This makes DNA a key focus of research, as gaining a greater understanding of the processes could lead to new treatments. Thus molecules that can act as probes by binding to DNA are of significant interest.

1.3.1 DNA structure

The structure of DNA is an exquisite example of self-assembly. The two strands of the molecule are held together by non-covalent hydrogen bonds. Individually each bond is weak, in chemical terms, but the additive nature of each bond gives a very strong cumulative force. This phenomenon is named Watson and Crick base pairing after the researchers who first devised the structure of DNA in 1958.[17] Based on X-ray evidence, their breakthrough came when they realized the structure was a double helix with two strands linked together. The bases are derivatives of the purines, adenine (A) and guanine (G) and the pyrimidines, thymine (T) and cytosine (C). The binding of these molecules in DNA is specific, so that only A will bind to T and likewise, G to C, as shown in figure 1.4. This gives rise to the complementarity of DNA strands in which one strand only binds to another that has the matching complimentary sequence. This has also led to non-biological applications, where DNA's structural properties are exploited to form scaffolds for a variety of nanostructures.[18]
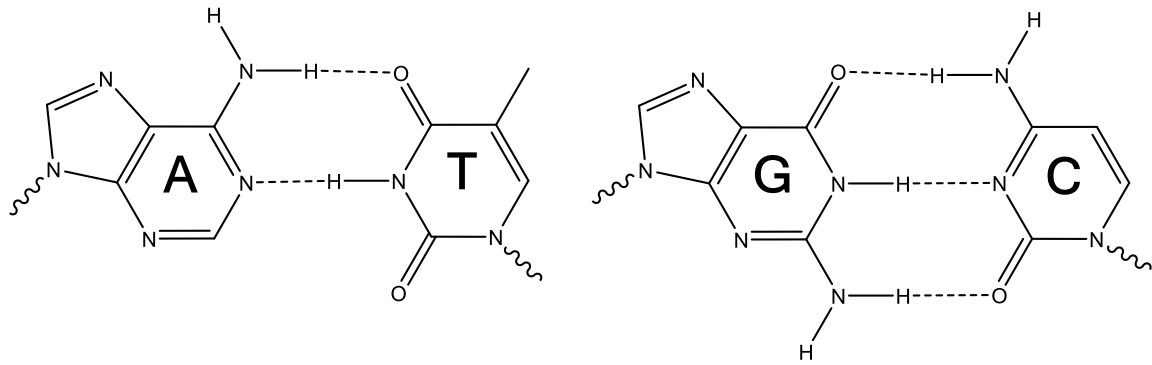
Figure 1.4 - Molecular structure of Watson-Crick base pairing, with adenosine (A) bound to thymine (T) and guanosine (G) bound to cytosine (C)

The base pairs form nucleotides when attached to a pentose sugar (deoxyribose) and a phosphate group. The phosphates form the backbone of the DNA *via* phosphodiester linkages, which polymerise to form a DNA strand.[16] The phosphodiester groups occupy the outer parts of the DNA structure and are negatively charged, making the overall structure hydrophilic. The base pairs are held in the interior of the DNA structure and engage in π-π stacking interactions, which enhance the stability of the helical structure.[19]
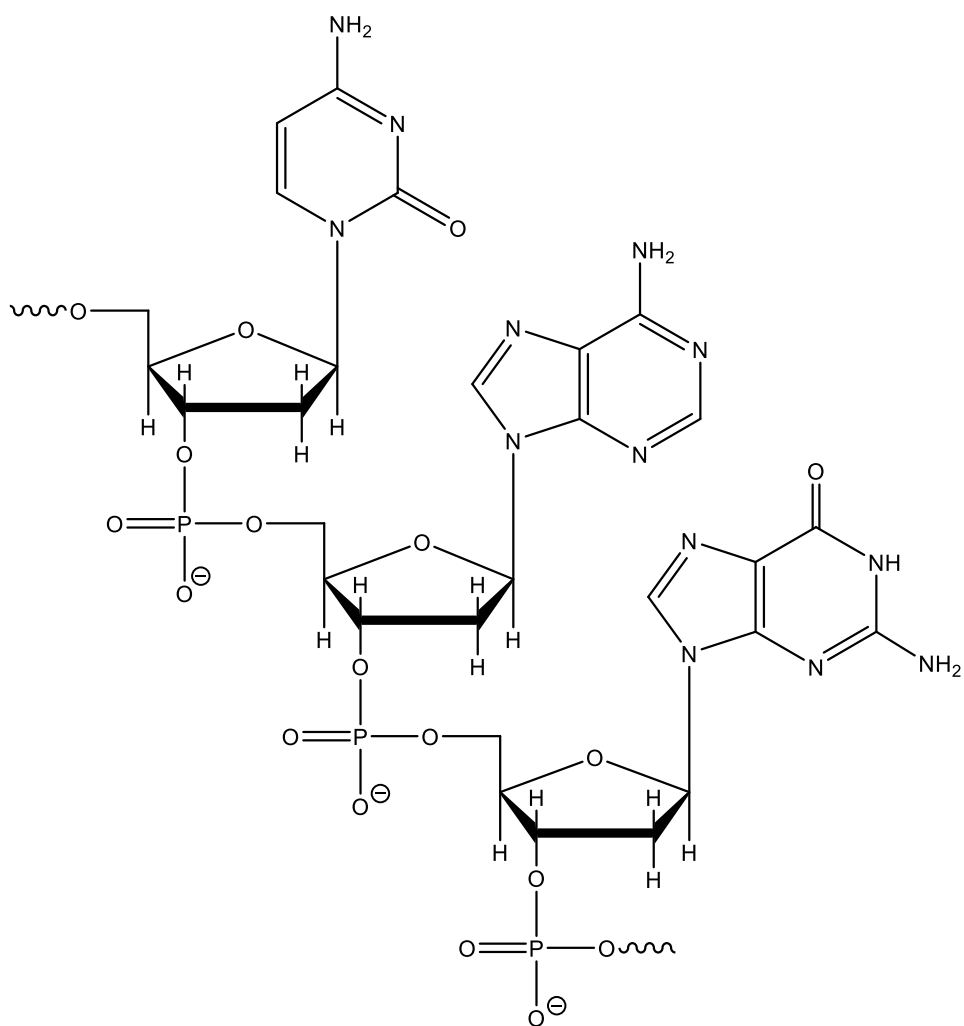
Figure 1.5 - An example of the molecular structure of one strand of DNA, including the sugar phosphate backbone

The combination of hydrogen bonding, π-π stacking and ionic charge arising from the molecular structure of DNA ultimately determines its 3D structure. In the most common form, as described by Watson and Crick, this results in B-DNA. In this case, two complimentary, anti-parallel strands bind to each other and wind into a helix, with one complete turn for every ten base pairs.[16] This leads to a surface structure of DNA with two grooves of 12 Å and 6 Å in width, known as the major and minor grooves respectively. These are shown in figure 1.6. These give differing binding sites to proteins and small molecules as they contain differing hydrogen bonding opportunities, alongside the different shape.
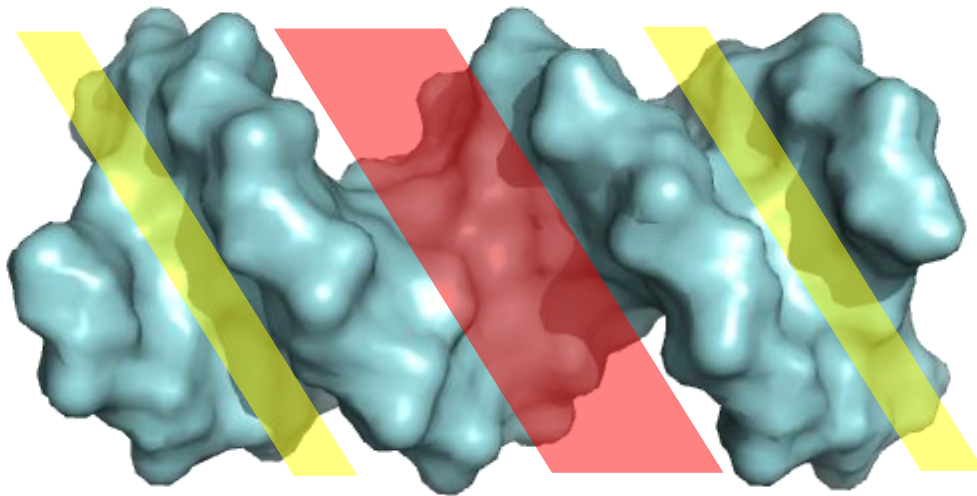
Figure 1.6 - Illustration of the major groove (red) and minor groove (yellow) of DNA, using the solution NMR structure of B-DNA (PDB: 1LAI)[20]

1.3.2 DNA Conformations

While B-DNA is the most common conformation of DNA, differences in humidity and salt concentration can lead to an array of different polymorphs,[21] with three major conformations being observed, A-, B- and Z-DNA.[22] Examples of these structures are shown in figure 1.7 with their corresponding structural parameters summarised in table 1.1. The A-form is the widest of the structures, with the base pairs rotated off axis and a more compact helical turn. The B-form is more compact, width wise, but has a taller helical turn and the base pairs sit in the axis of the helix. The Z-form is the most extreme, possessing a left handed helix with flipped base pairs, resulting in the narrowest and tallest helix with a dinucleotide repeat.[22]
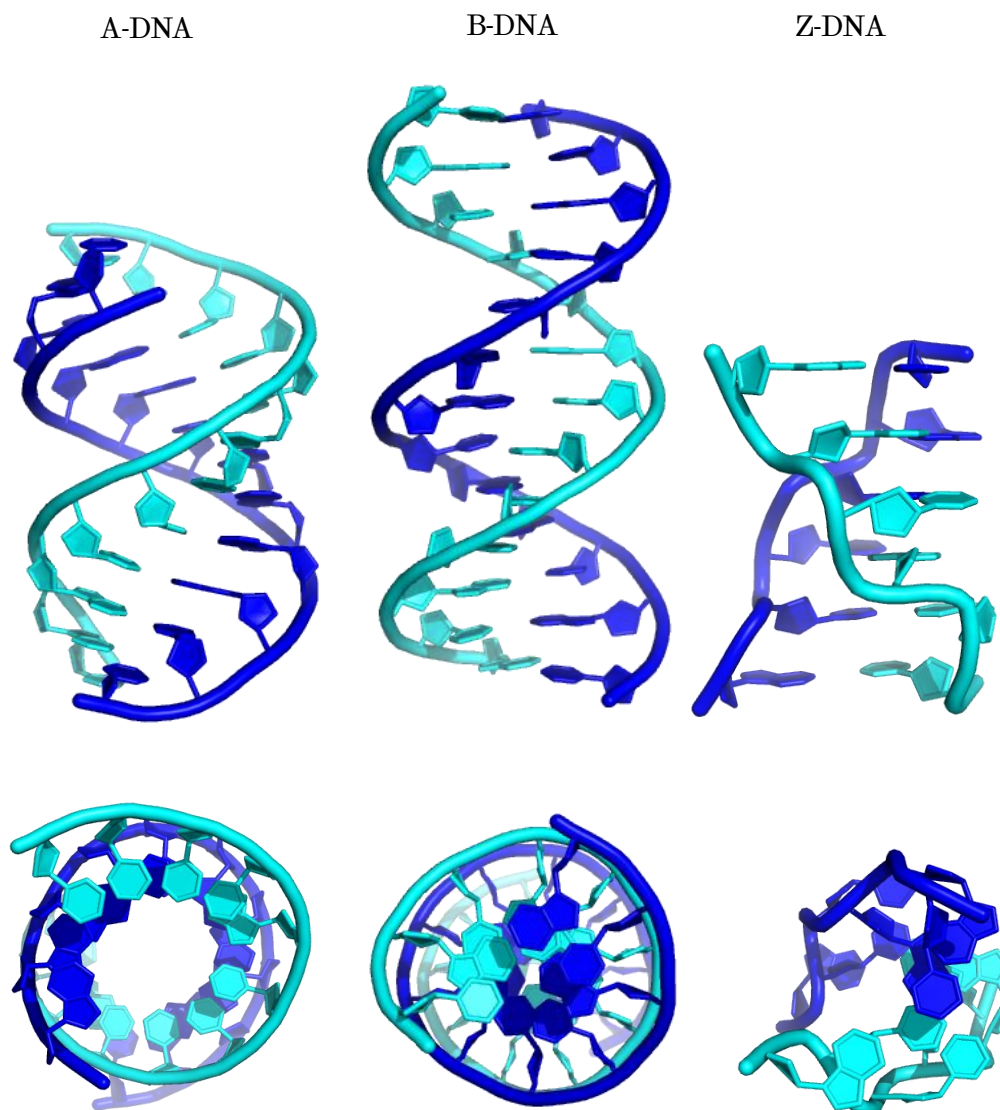
A-DNA   B-DNA   Z-DNA

Figure 1.7 - Side and top view of examples of the three main conformations of DNA, A-DNA (PDB :1ZJE)[23], B-DNA (PDB: 1LAI)[20] and Z-DNA (PDB: 400D)[24]

	A-DNA	B-DNA	Z-DNA
Helix Sense	Right	Right	Left
Residue per turn	11	10.5	11.6
Axial Rise	2.55 Å	3.4 Å	3.7 Å
Helix pitch	28 Å	36 Å	45 Å
Rotation per residue	32.7°	36°	-9°, -51°
Diameter of helix	23 Å	20 Å	18 Å
Major groove	Narrow, deep	Wide, deep	Flattened
Minor groove	Wide, Shallow	Narrow, deep	Narrow, deep

Table 1.1 Summary of structural parameters of DNA forms, taken from[22]

These different conformations are of interest as they may play specific roles in a biological environment. Thus molecules that can differentiate between them, and report on the different forms that are present in cellular environments, would be of interest in studying their roles. Alongside these fundamentally different helix forms, there are other non-canonical forms of DNA that are also thought to have specific biological roles. Some of these structures are summarised in figure 1.8.
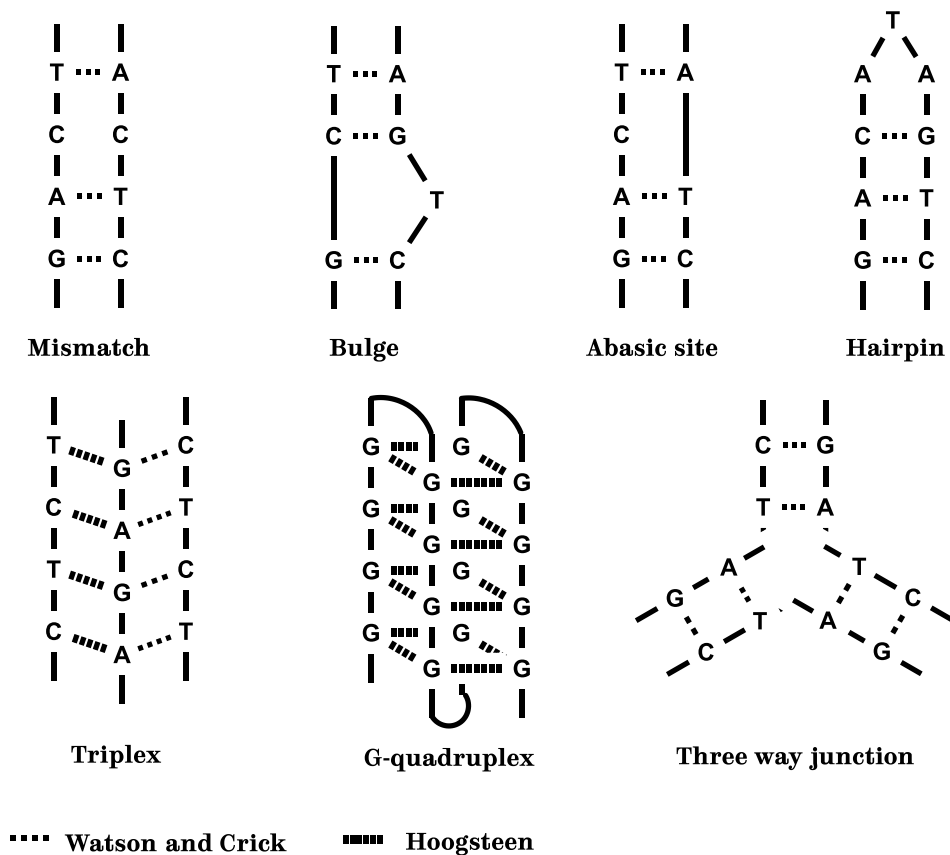
Figure 1.8 - Examples of non-canonical DNA structures, exhibiting both Watson and Crick and Hoogsteen binding.[25]

The duplex structures shown in figure 1.8, generally represent imperfections in the DNA and may be the result of errors in DNA replication. If they are not corrected by the cellular machinery they can lead to mutations and issues with genes and thus the function of the cell.[25] Bulges, for example, can be formed of one base , as shown, or multiple base that form a loop away from the DNA backbone. They are generally less stable than the Watson Crick duplex.[26] They can be a result of radiation or carcinogenic action on the DNA. This form of mutation have been linked to diseases such as hypercholesterolemia[27] and cancers.[26,28] It is also thought that the structures formed

by bulges could manifest as binding site indicators for proteins, Certain proteins have been found to bind preferentially to bulging DNA over standard DNA.[29] The hairpin form of DNA can also be as a result of errors in replication and has been linked to neurological diseases, such as fragile X disorder[30] and Huntingdon's disease.[31] With these structures being directly linked to disease, probes that indicate their presence would be invaluable for study of the diseases, and potentially diagnostics.

The G-quadruplex has also attracted a significant amount of research interest in recent times, first described in 1988[32] and then observed in cells for the first time in 2013.[33] It is formed from guanine rich sequences on DNA. It exhibits Hoogsteen binding, whereby the g-tetrads are held together by hydrogen bonds alternative to those seen for the Watson and Crick model. This structure is often formed when supported by a central metal ion. The structure is shown in figure 1.9.
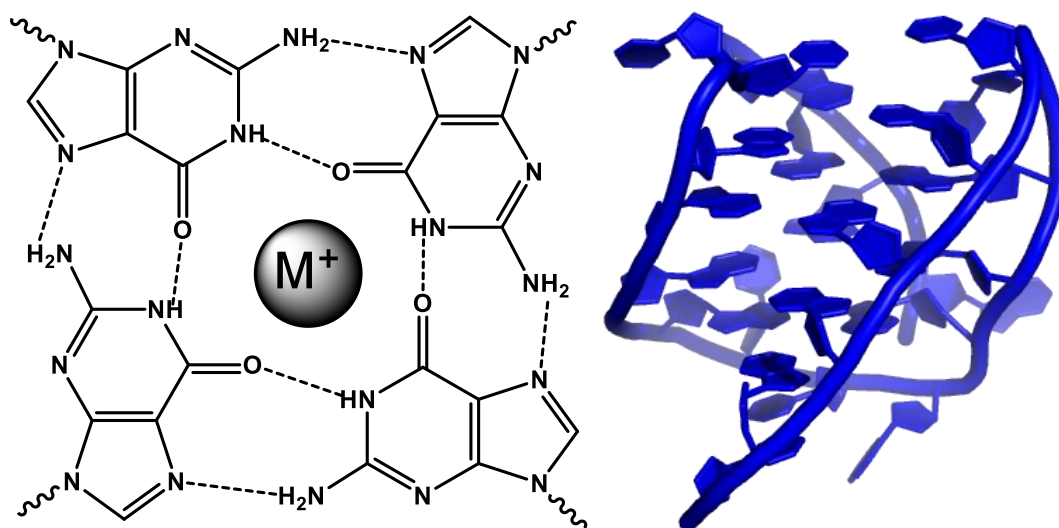
Figure 1.9 - Molecular structure of Hoogsteen H-bonding in G-quadruplex, alongside the NMR structure of an intramolecular quadruplex of human telomeric sequence DNA (PDB: 2KKA)[34]

The structure is more thermodynamically stable than the standard duplex of DNA, with a 20-30 °C higher melting temperature, which led to the hypothesis that it could be present under physiological conditions.[35] The structure has been shown to play an important role in cellular processes, with pyridostatin used to bind to it and stabilise the structure, resulting in DNA damage and cell cycle arrest.[36] Computational studies have shown there is potential for quadruplex formation at many points in the genome, and suggestions have been made that they may play a role in gene expression by

preventing access to the DNA.[37] Quadruplexes are also known to be prevalent in telomeres,[33] the sequences of DNA responsible for stabilisation of chromosomes, with some molecules inducing a damage response in these regions.[38] Telomeres have an important role in the proliferation of cancerous cells, as telomere length maintenance alongside upregulation of the enzyme responsible for telomere synthesis, telomerase, are observed in tumors.[39] This has led to the suggestion that binding probes for quadruplex in telomeres could lead to early cancer diagnostics.[40]

Alongside the G-quadruplex, another structure that has gained recent attention is the i-motif. It is also found in telomeres and is formed from cytosine rich sequences of DNA.[41] It relies on the protonation of one of the cytosine residues, to form three, intra-residue, H-bonds. These then intercalate with each other to form the motif. It has very recently been observed *in vivo* and could also be a useful target for future binding probes.[42]

1.3.3 Irreversible binding

Molecules can bind to DNA *via* covalent bonds, thus binding irreversibly. The most famous example is cis-platin, illustrated in figure 1.10, a square planar complex of platinum containing two chloride and two amine ligands in a cis formation. The action of the molecule was discovered serendipitously, when platinum electrodes reacted with the medium in which *E. coli* bacteria were being grown.[43] It was observed that the electrolysis products inhibited cell division. Subsequently, it was discovered that cis-platin binds to guanine residues kinking the DNA and inhibiting the cell cycle.[44] This led to use of cis-platin as an effective anti-cancer treatment, as it statistically targets the quickly dividing cells present in tumours. This was an early demonstration that DNA binding can have a profound effect on the cell cycle and led to intensified research into variants of cis-platin and molecules that can reversibly bind to DNA.
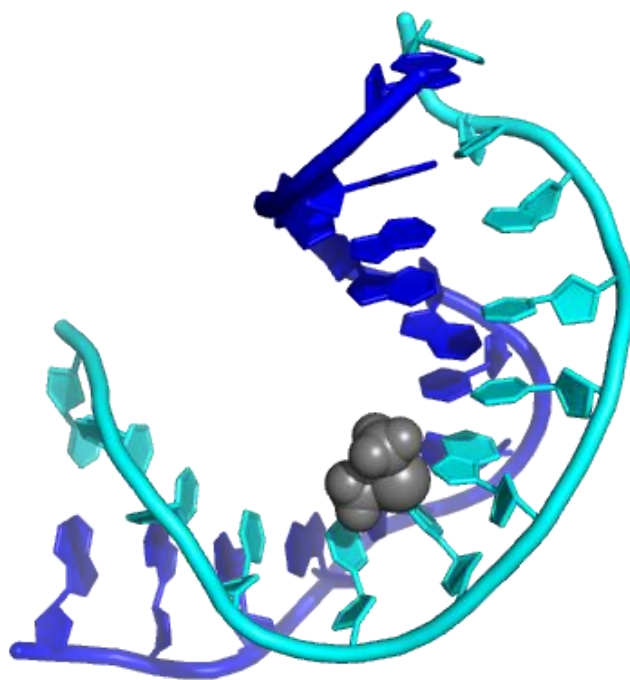
Figure 1.10 - NMR structure of cis-platin bound to DNA (PDB: 1A84)[45]

1.3.4 Reversible binding

Reversible binding is vital to the function of DNA, with proteins associating and dissociating in order to perform replication and translation. When considering small molecules reversibly binding to DNA, three key modes have been identified, electrostatic, groove binding and intercalation.[25] These modes rely on differing intermolecular forces that contribute to their binding. The modes are summarised in figure 1.11.
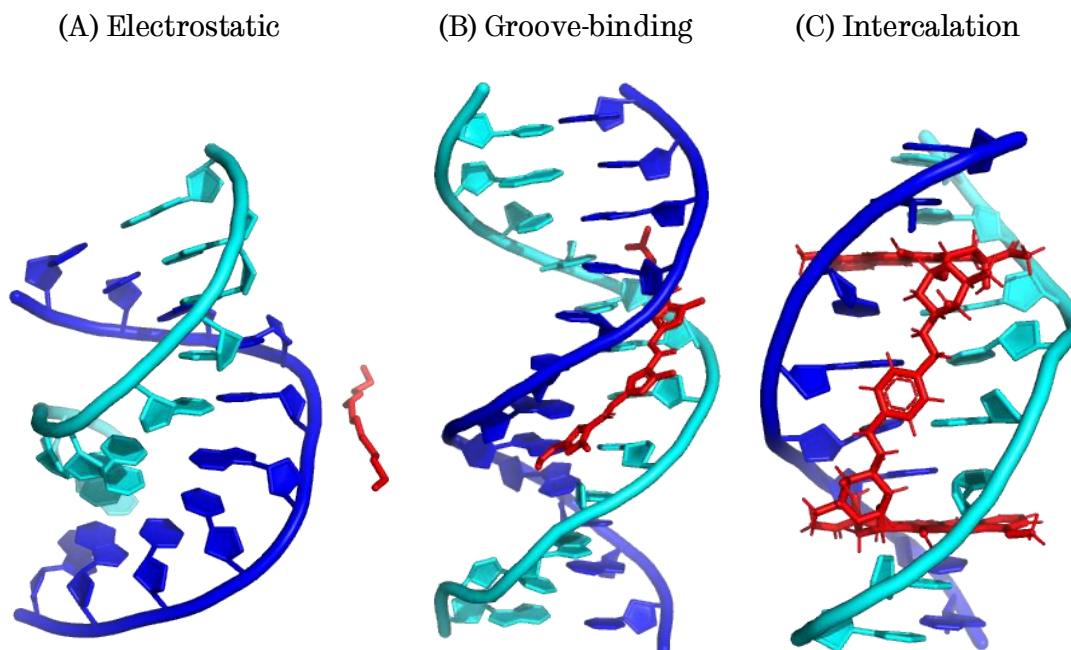
Figure 1.11 - Examples of the three key modes of DNA binding, (A) an x-ray structure of the electrostatic binding of spermine to a chimeric DNA/RNA hybrid (PDB: 100D)[46], (B) an x-ray structure of the groove binding of distamycin to a DNA dodecamer(PDB: 2DND)[47] and (C) a solution NMR structure of the intercalation of bis-daunomycin with DNA (PDB: 1AL9)[48]

1.3.5 Electrostatic binding

The simplest form of reversible binding is electrostatic. This arises from the structure of DNA, as the phosphate backbone results in a polyanionic nature, with negative charge running along the backbone. This makes the DNA strands hydrophilic, aiding their solubility, but can also result in interaction with cations. On the molecular level, electrostatic binding is the least intrusive to the DNA helix, yet it can have significant effects on structure and stability of the DNA. This includes simple metal ions, such as sodium or potassium, as in the case of the G-quadruplex discussed earlier, which is stabilised by binding these ions.[34] Alongside simple ions, charged molecules can also interact in this way. One example is the binding of spermine, as shown in figure 1.11. Spermine is a naturally occurring polyamine that can enhance the stability of DNA through binding, and is known to be in high concentration in proliferating cells.[49] It is thought to protect against thermal and irradiative damage and can affect the structure of DNA, for example stabilising the Z-form over the B-form.[50]

1.3.6 Groove binding

Groove binding describes an association within the grooves of the DNA double helix, as discussed in section 1.3.1. Generally the binding is more specific than purely electrostatic binding, with additional hydrogen bonding to the base pairs, solvophobic interaction and van der Waals forces all affecting the binding strength and location of the molecule.[51] The binding mode often leads to molecules becoming more closely associated with the DNA, compared with the electrostatic mode. However, groove binders do not tend to perturb the conformation of the DNA, as they fit snugly in its groove.[52] It has also been found that the interaction is largely driven by entropic contributions. The binding can be considered analogous to the lock and key model for the binding of enzymes and substrates.[52]

Owing to the strength of their interaction with DNA, many groove binders are effective drug molecules, able to disrupt cellular processes and can damage DNA. A natural example of this is Netropsin, which was isolated as an antibiotic agent in 1951.[53] It displays exclusive binding to B-DNA with no binding observed with single stranded, A-form or Z-form DNA.[54] It binds to DNA by sitting in the narrower, minor groove, displacing water molecules in the process. It is forced by sterics into the centre of the cavity. The binding also forces the molecule to distort and adopt a screw like form to match the shape of the DNA helix, while having little structural impact on the DNA helix itself. The molecular structure of netropsin, shown in figure 1.12, also contains multiple opportunities for hydrogen bonding. These bind to base sequences, preferring A-T over G-C, although this is due to the unfavourable binding sterics of the G-C pairing as much as any prefered interaction with A-T.[54]
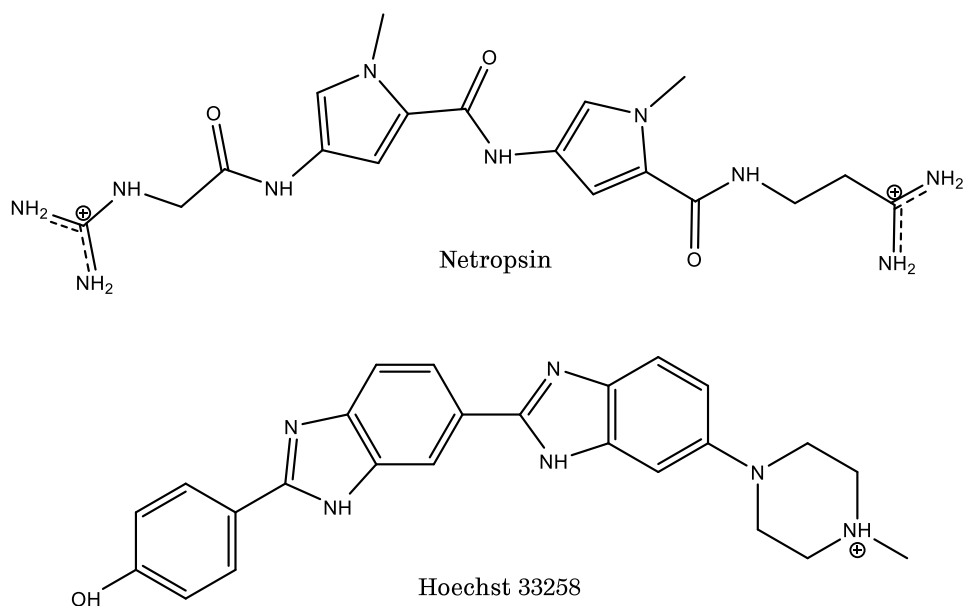
Figure 1.12 - The molecular structures of two examples of groove-binding molecules

Another important groove binder is the fluorescent dye, Hoechst 33258. It is a specific binder, binding in a similar fashion to netropsin, preferentially binding to A-T base pair sequences rather than G-C.[55] The dye is readily taken up into cells and binds strongly to nuclear DNA, which enhances its fluorescence in the process.[56] This enhancement makes it an ideal probe for DNA, as it is reporting on its environment. Similarly to netropsin it occupies the minor groove and deforms to fit within it, as confirmed by x-ray studies.[57] As with other groove binders, the effect on the structure of DNA is minimal leading to its use as a groove binding standard when studying the hydrodynamic properties of DNA solutions,[58] and is useful in comparison with intercalators, which are discussed in the following section.

1.3.7 Intercalation

Intercalation is the most intrusive form of reversible DNA binding. While hydrogen bonds and other interactions may be present to enhance binding, the primary interaction that drives intercalation is π-π stacking. It was first postulated by Lerman when considering the binding of acridine.[59] This was based on the observation that DNA became more viscous on the addition of the dye. It was suggested this was due to the dye molecule sliding between the base pairs in the DNA. This has the effect of pushing the base pairs apart and slightly unwinding the DNA, thus lengthening the DNA and increasing its hydrodynamic radius, and thus viscosity. The planar, polyaromatic nature of the acridine is the key feature that enables the stacking

interaction with the base pairs. Unlike the groove binding interaction, the primary drive for intercalation is enthalpic. It has been proposed that intercalation occurs in three steps, shown in figure 1.13.[52] Similar to other forms of binding, the consequent structural changes can lead to deleterious effects on the replication and transcription of DNA.
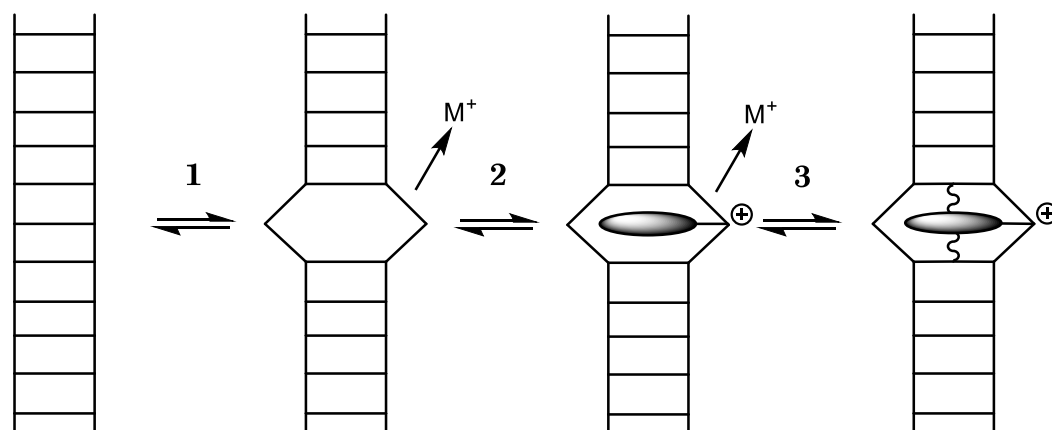
Figure 1.13 - Theoretical steps of intercalation, (**1**) Conformational change in DNA, including release of counterion, (**2**) Hydrophobic transfer of intercalator into DNA and (**3**) Anchoring by formation of molecular interactions.[52]

As with the groove binder, netropsin, intercalators can be isolated from bacteria as antibiotic agents. One such natural compound is daunomycin, extracted from the soil bacteria *Streptomyces peucetius* in the 1960s.[60] It was found to have antitumor properties,[61] and is used in the treatment of acute lukemia.[62] The molecular structure, shown in figure 1.14, illustrates the compact, polyaromatic and planer structure, in contrast to the longer, more flexible groove binders shown in figure 1.12. X-ray studies indicated that the intercalated unit is held in place by interactions between the substituents on the ring furthest right in figure 1.14, and the minor groove.[62] This allows the amino sugar to sit in the minor groove. As with the groove binders, daunomycin has shown some preferential binding, with preferred sites consisting of triplets 5'(X)GC or 5'(X)CG where (X) indicates either an A or T may be in that position.[63] Intercalators can have varying influence over the DNA, for example daunomycin unwinds the DNA helix by 11° while another agent, ethidium bromide, causes a 26° unwinding.[64]
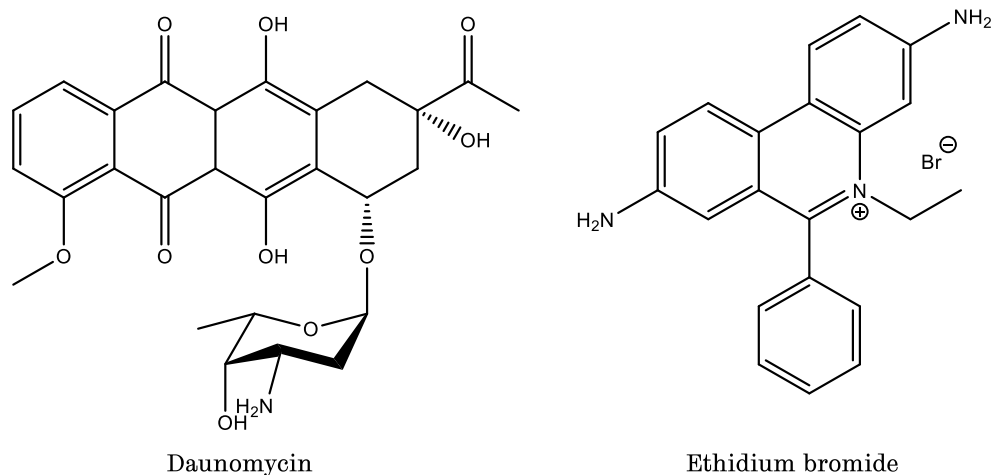
Figure 1.14 - The molecular structure of two examples of intercalators

The polyaromatic nature of these compounds can also result in luminescent properties. As with the groove binder Hoechst 33258, ethidium bromide (EtBr) is used as a stain of nucleic acids for this reason, showing strong luminescence when excited.[65] This allows for the visualisation of DNA in density gradients and cell chromosomes. The molecule shows strong binding to DNA but can be inhibited by high magnesium concentrations that restricts binding.[66] EtBr is a useful addition to agarose gel electrophoresis, which separates DNA fragments based on their mobility through the gel.[67] Although it helps to visualise the bands produced, it also changes the mobility of the DNA through the gel, inhibiting its progress due to the changes it induces in the DNA structure.[68] This can cause issues with the sizing of the DNA.

The application of EtBr that is of most interest to this study is its use in determining the binding modes of novel binding agents. As previously alluded to, it is used alongside Hoechst 33258, as a standard to which new molecules can be compared.[58] As a groove binder Hoechst 33258 does not increase the length of DNA, thus the viscosity does not increase as more of it binds. EtBr, as an intercalator increases the length of DNA and viscosity of its solution. When plotting the relative viscosity against the increase in concentration, a positive gradient is observed for intercalators, while no gradient is observed for groove binders. This is illustrated by the plot in figure 1.15. Adding the data obtained for novel agents allows for comparisons, to determine the mode of binding.
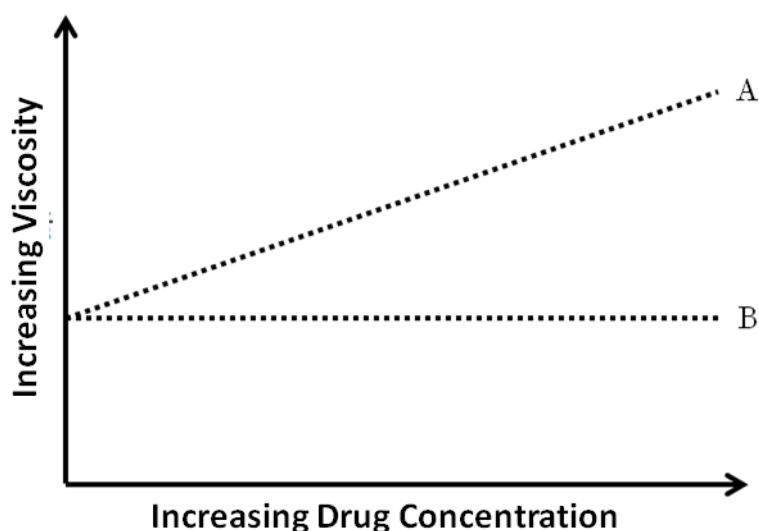
Figure 1.15 - An example of the plot to determine the binding mode of novel DNA binding agents (drug). (A) Represents the intercalation of EtBr while (B) represents the groove binding of Hoechst 33258

1.4 Metal complexes reversibly binding to DNA

Metal complexes can be designed to have multiple properties that make them suitable DNA binding agents. They are often charged, due to the redox chemistry of the central metal atom, and frequently exist as cationic salts with counter-ions. This enables electrostatic interaction with the anionic DNA. They can also be coupled with ligands that possess both hydrogen bonding potential and polyaromatic rings, which can enable π-π stacking interactions. The versatility of the design also allows for creation of multiple shapes that can complement DNA. These properties have lead to metal complexes exhibiting each of the binding modes described in section 1.3. This includes the electrostatic binding of [Ru(bpy)$_3$], groove binding from Ru(II) helicates and intercalation of complexes containing the dipyridophenazine (dppz) ligand.[25]

Although initial work on metals binding to DNA focussed on the complexes that bare metal ions would create on covalent binding to DNA,[69] early studies on pre-made metal complexes, centred on their biological activity, soon began to emerge. It was noted that complexes of iron and nickel are labile, and so biological activity may arise from an exchange of ligands. Complexes of ruthenium and osmium were preferred as their stability allowed for study of a known entity.[70] The first complexes reported to specifically bind DNA were platinum based, square planar complexes containing the terpy ligand.[71] An intercalative binding mode was suggested based on similarity

between the ligand and acridine that was reported by Lerman.[59] This was later confirmed by x-ray evidence.[72] Further work extended this study to look at the effect of changing the ligand, with a range of complexes studied, shown in figure 1.16. These showed a range of relatively weak association constants with CT-DNA, in the region of $\sim 10^{-4}$ M^{-1}, and an order of magnitude weaker than EtBr.[73] The strongest binding was observed for the phenanthroline (phen) based complex. It was this ligand that was employed for the first octahedral complexes shown to bind to DNA.

The advantage of octahedral centres, over the previous square planar examples, is the ability to exploit their chirality. This is in anticipation of the different enantiomers preferentially binding to either a left or right handed helix. This was first realised in 1976 when Norden and Tjerneld investigated the binding of Fe(bpy)$_3$ and DNA using linear dichroism.[74] It was discovered that the system showed the Pfieffer effect. Due to the lability of the complex, the chirality of the DNA induced the Δ-enantiomer of the complex to be formed. Building on this work, Barton and co-workers synthesised [Zn(phen)$_3$]$^{2+}$, which could be enantiomerically enriched on dialysis with right handed helix of CT-DNA.[75] In order to further study these interactions the metal centre was switched to ruthenium because of the stability of its complexes and the photophysical properties they display, eliminating the possibility of a Pfieffer effect.[13] In both cases an intercalative binding mode was initially proposed for the Barton complexes.
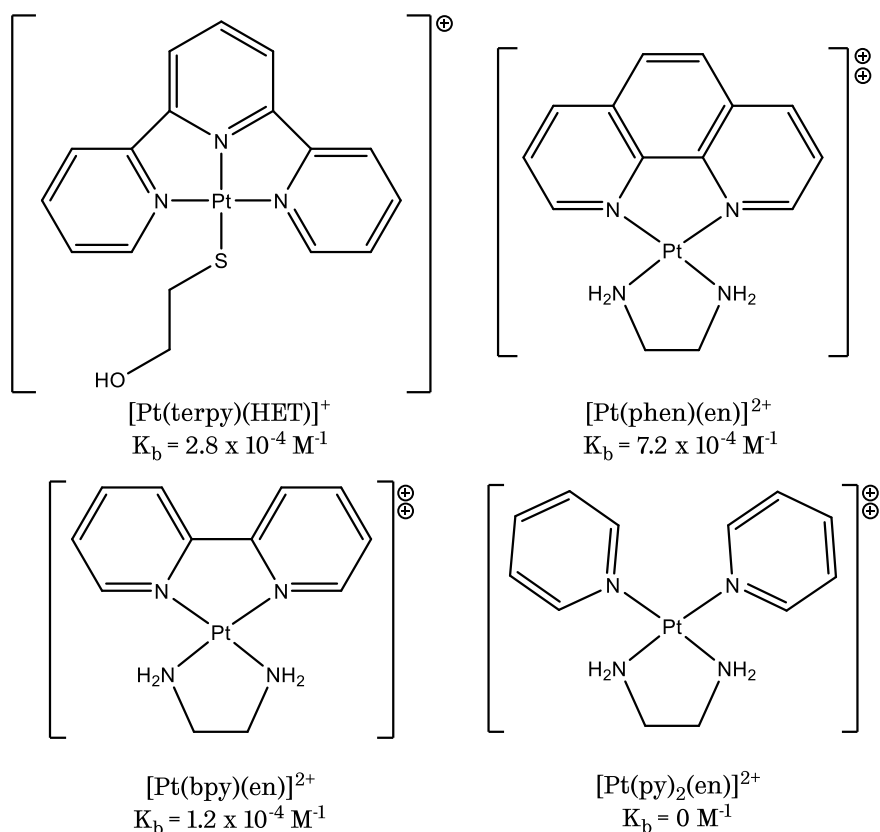
Figure 1.16 - Platinum complexes studied by Lippard and co-workers, showing binding constant estimated by ultracentrifuge technique.[73]

[Pt(terpy)(HET)]$^+$
K_b = 2.8 x 10^{-4} M^{-1}

[Pt(phen)(en)]$^{2+}$
K_b = 7.2 x 10^{-4} M^{-1}

[Pt(bpy)(en)]$^{2+}$
K_b = 1.2 x 10^{-4} M^{-1}

[Pt(py)$_2$(en)]$^{2+}$
K_b = 0 M^{-1}

1.4.1 Groove binding complexes

The binding mode of [Ru(phen)$_3$]$^{2+}$ was subsequently the subject of much study and debate in the literature. Having initially proposed the intercalative mode, Barton and co-workers extended their study to include [Ru(bpy)$_3$]$^{2+}$ and [Ru(DIP)$_3$]$^{2+}$ alongside [Ru(phen)$_3$]$^{2+}$, investigating the binding modes of each via photophysics.[76] At a similar time Kelly and co-workers were investigating [Ru(bpy)$_3$]$^{2+}$, [Ru(phen)$_3$]$^{2+}$ and [Ru(terpy)$_2$]$^{2+}$, studying photophysics alongside DNA unwinding experiments.[77] In both cases [Ru(bpy)$_3$]$^{2+}$ was found to have negligible binding. Barton suggested two binding modes for the two enantiomers of [Ru(phen)$_3$]$^{2+}$, it was suggested that one was intercalative and the other electrostatic. Kelly concurred that the binding of [Ru(phen)$_3$]$^{2+}$ was intercalative. Further work suggested that rather than purely electrostatic, the second binding mode Barton suggested was surface binding with the groove, in the case of the Λ-[Ru(phen)$_3$]$^{2+}$, while the Δ-[Ru(phen)$_3$]$^{2+}$ was only partially intercalated.[78] This was supported by evidence from NMR studies.[79,80]
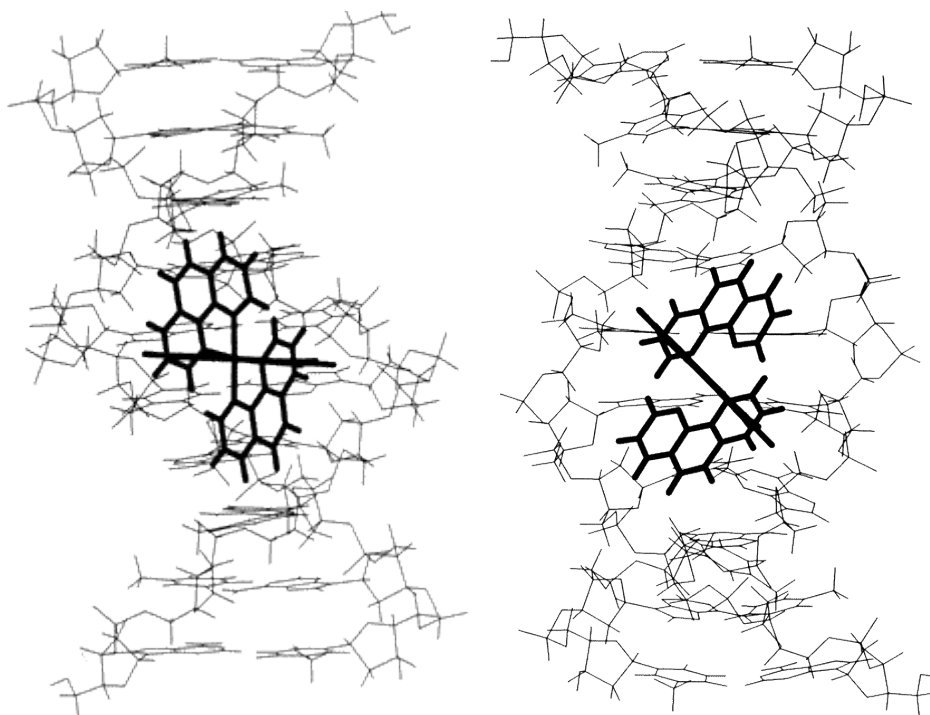
Figure 1.17 - Proposed models of the DNA binding of Λ-[Ru(phen)$_3$]$^{2+}$ (left), and Δ-[Ru(phen)$_3$]$^{2+}$ (right). Adapted from Coggan *et. al*.[81] Copyright (1999) American Chemical Society

This proposal was initially challenged by Hiort and co-workers, who used linear and circular dichromism studies to conclude that both the enantiomers of [Ru(phen)$_3$]$^{2+}$ are in fact bound in the groove of DNA.[82] The study also concluded that the two enantiomers have different binding modes, which potentially indicated that one binds to the minor and the other binds to the major groove. However, taken the evidence of this study in the whole, it was concluded that both bind to the major groove with Λ-[Ru(phen)$_3$]$^{2+}$ bound one phen ligand pointing into the helix and Δ-[Ru(phen)$_3$]$^{2+}$ having two. Further evidence for groove binding was provided by Chaires *et. al.* using the viscosity criteria previously discussed (section 1.3.7), indicating that [Ru(phen)$_3$]$^{2+}$ behaves in the same way as the known groove binder Hoechst 33258.[83] Combining linear and circular dichromism with computer modelling allowed Coggan and co-workers to suggest that [Ru(phen)$_3$]$^{2+}$ shows different binding modes in different circumstances.[81] Low concentrations resulted in partial insertion of Λ-[Ru(phen)$_3$]$^{2+}$ into the DNA, and facial groove binding of Δ-[Ru(phen)$_3$]$^{2+}$, as shown in figure 1.17. Higher concentrations resulted in a slotted mode.

While the binding of [Ru(phen)$_3$]$^{2+}$ is located in the DNA groove, it is markedly different to the organic groove binders discussed previously. It does not share many of the features seen with the likes of netropsin, lacking the long flexible structure that flexes to fit the groove. Contrastingly, the binding of [Ru(phen)$_3$]$^{2+}$ is analogous to an intercalator that is stuck in the groove, but is prevented from full insertion due to sterics.

Consequently, efforts have been made to create ruthenium complexes that are more structurally similar to conventional groove binders. One way to accomplish this goal is to create di-nuclear complexes, as exhibited by Keene and co-workers, who created ΔΔ-[{Ru(bpy)$_2$}(μ-bpm){Ru(Me$_2$bpy)$_2$}]$^{4+}$ (bpm = 2,2′-bipyrimidine, Me$_2$bpy = 4,4′-dimethyl-2,2′-bipyridine) which groove binds and targets DNA bulges.[84] The Thomas group have copied the azo-containing beneril, a known minor groove binder, to create a similar di-ruthenium complex that shows interesting colorimetric properties.[85] A supermolecular approach can also be utilised, with di-ruthenium helicates shown to bind DNA and coil it.[86] These examples are illustrated in figure 1.18.
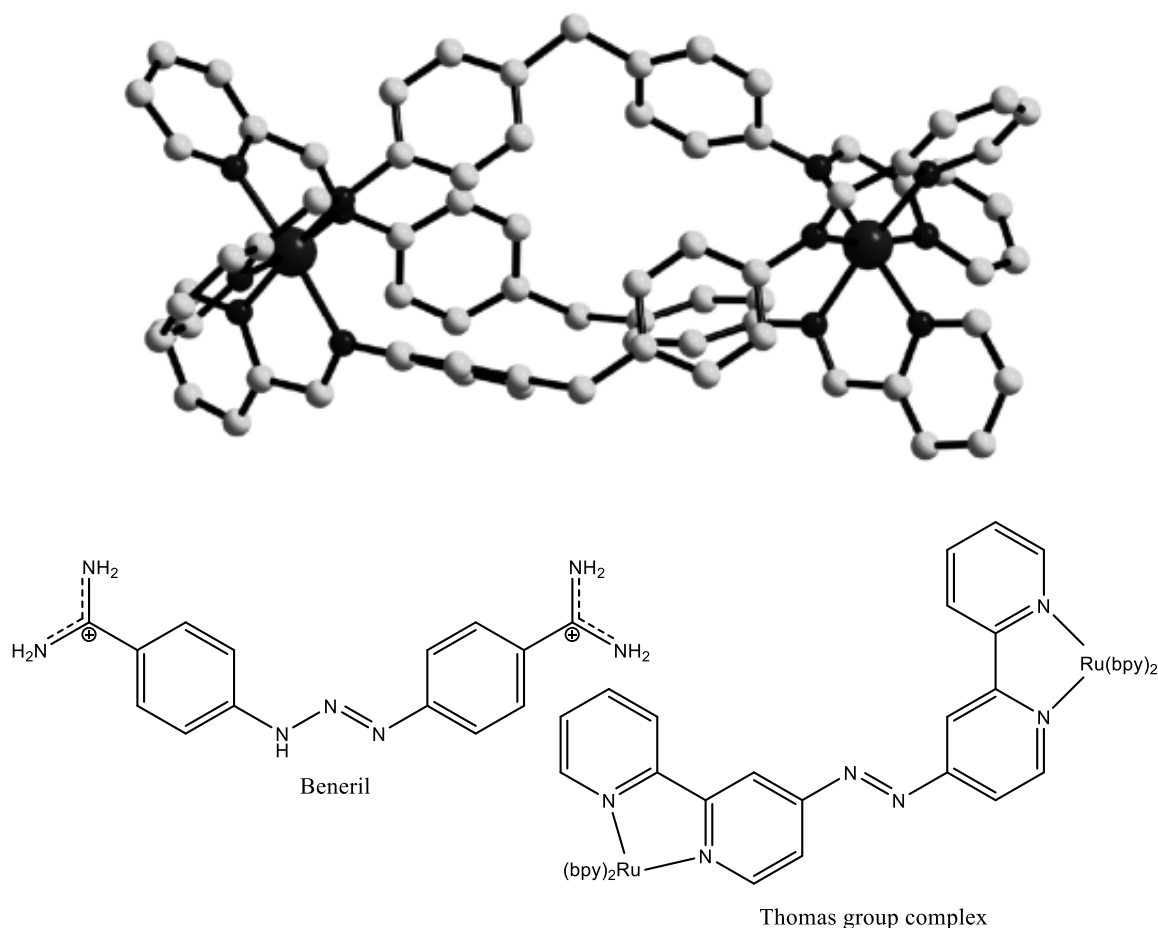
Figure 1.18 - Examples of metal complex groove binders, X-ray structure of Ru(II)-helicate adapted with permission from Hannon *et. al.*[86] (© John Wiley and Sons 2007)(top) and the beneril based complex of Thomas *et. al.*[85](bottom)

1.4.2 Metallointercalators

The complications in understanding the binding mode, alongside relatively weak DNA binding of [Ru(phen)$_3$] make it unsuitable as a DNA probe. Consequently attempts were made to increase the strength of binding and promote an intercalative binding mode.[87] This was achieved by extending the planar aromatic system away from the metal centre, so that it can stack with the DNA base pairs without steric hindrance. A wide array of ligands have been synthesised to achieve this goal. Two of the earlier examples were dipyridophenazine (dppz), where the phen ligand is extended by adding a quinoxaline unit, and phenanthrenequinone diamine (phi) which is effectively a reversal of the phen ligand so that more of the aromatic surface projects away from the complex.[88] In both cases this results in much stronger binding, as the aromatic rings are able to form the π-π stacking interactions with the base pairs, which is the driving

force of intercalative binding. As for the [Ru(phen)$_3$]$^{2+}$ there was some controversy over the binding mode of [Ru(dppz)(phen)$_2$]$^{2+}$ and whether it binds from the major or minor groove.[89] This was ultimately resolved by the production of crystal structures of the complex bound to DNA, as shown in figure 1.19.
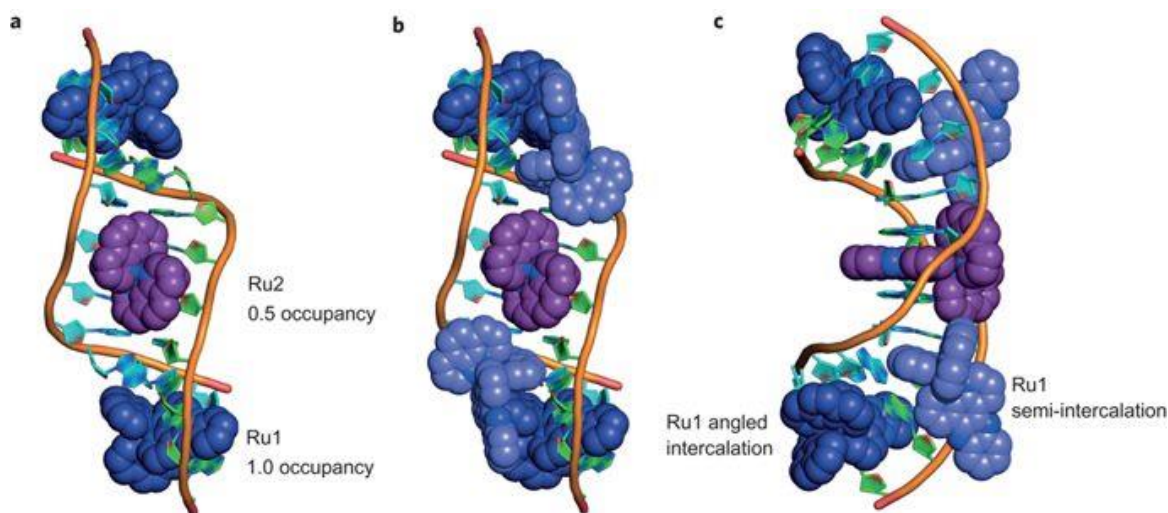
Figure 1.19 - Crystal structures showing (a) fully intercalated cations (b) fully and semi intercalated cations and (c) side view of (b). Adapted with permission from Cardin *et. al.*[90] (© Springer Nature 2012)

1.5 Ru-dppz complexes

The most studied metallointercalators are based around the Ru-dppz system. This has involved both combining the dppz ligand with various ancillary ligands in ruthenium complexes and altering the dppz ligand chemically. Both of these approaches have been shown to modulate the binding to DNA, often introducing selective binding. Such alterations have led to intercalators that are temperature sensitive.[91] The key reason that such interest has been given to dppz complexes is the existence of the light switch effect.

1.5.1 Light switch effect

The light switch effect was first described by Barton *et. al.* using a [Ru(dppz)(bpy)$_2$]$^{2+}$ complex.[92] When dissolved in an organic solvent the complex exhibits an emission that is ascribed to an MLCT (metal-ligand charge transfer) interaction. However, when dissolved in water the complex no longer shows the emission. This is attributed to hydrogen bonding of water molecule to the unbound nitrogens on the dppz ligand.

Ultimately this quenches the fluoresence *via* a non-radiative process. When the complex is intercalated within the DNA helix, the dppz ligand is held within an environment that acts like an organic solvent as the dppz nitrogen atoms are protected from the external water environment.[88] The term light switch refers to the point at which DNA is introduced to the complex as it acts to switch the light of the complex on, as demonstrated in figure 1.20. This is a key property and has lead to a wide range of applications including cellular imaging where the complex is taken up by a cell and localises where DNA is present due to binding. This then lights up these areas of the cell which can be imaged.
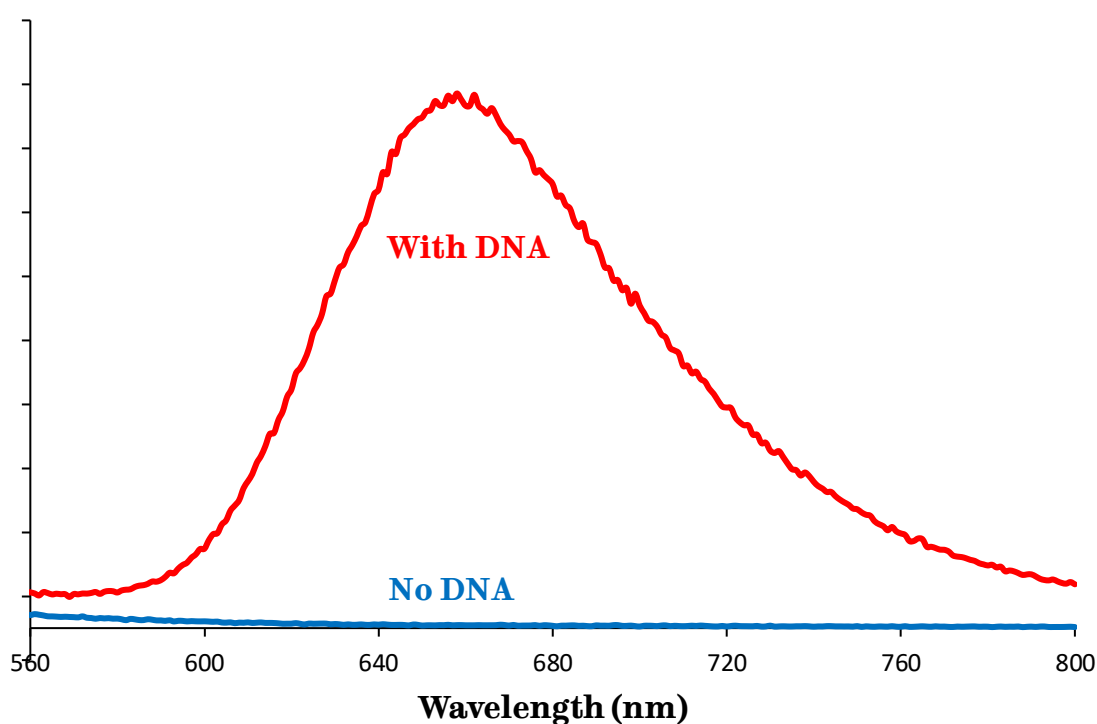
Figure 1.20 - General emission profile of a dppz based complex showing a significantly greater emission in the presence of DNA due to the light switch effect.

The mechanism by which this phenomenon occurs is a subject of much interest in the literature. Olson *et. al.* utilised transient absorption and emission techniques to propose a kinetic model for $[Ru(phen)_2(dppz)]^{2+}$ with two emitting MLCT states.[93] The model is shown in figure 1.21. Here the weak emission of the complex in an aqueous environment is explained by the internal conversion of the MLCT' state into an MLCT'' state that is destabilised by hydrogen bonding. The MLCT'' state is higher in energy in aprotic environments and as such is not accessible. This work was built on by Coates

et. al. who studied the mechanism using resonance raman probing.[94] They proposed a similar mechanism but discovered an additional "precursor state" which was solvent dependant but not thought to play a role in activating or deactivating the light switch. Temperature dependant studies on [Ru(bpy)$_2$(dppz)]$^{2+}$ by Brennaman *et al.* then concluded that, while there are two MLCT states, the dark state is always lowest in energy and the light switch results from dynamic equilibrium of the enthalpically favourable dark state and entropically favourable bright state.[95] Previous work suggested that the dark state only became lower in energy as a result of hydrogen bonding. The bright and dark states were subsequently directly observed by Kelly *et. al.* using ultrafast time resolved infrared.[96]
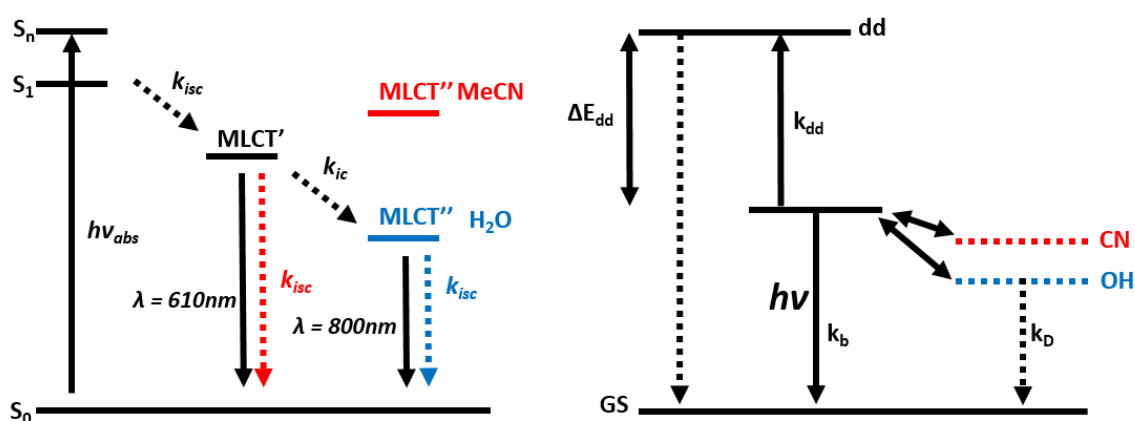
Figure 1.21 – Mechanisms proposed by Olson et. al.[93] (left) and Brennaman et. al.[95] (right) to describe the light switch effect.

1.5.2 Chemosensors

The light switch properties displayed by the Ru-dppz system have led to the development of multiple examples of chemosensors. These sensors do not only take advantage of the photoluminescence of the compound, with some example of sensors detecting changes in chemiluminesence, electochemiluminesence and photoelectrochemical signals.[89] The first attempt at a fluorimetric determination of DNA with [Ru(phen)$_2$(dppz)]$^{2+}$ was made by He *et. al.* who also tested their procedure in the presence of co-existing substances which did not affect the outcome.[97] Many of these sensors rely on the use of aptamers, using the DNA to detect other analytes, rather than detecting the DNA itself. One such example used a G-rich aptamer, which forms a quadruplex in the presence of K$^+$ ions.[98] The emission of [Ru(phen)$_2$(dppz)]$^{2+}$ when bound to the quadruplex is lower than the unfolded structure and so, as K$^+$ is

added, the emission decreases. This is not seen with other ions, thus allowing for the detection of K^+ ions. Another example uses an aptamer for ATP, whereby $[Ru(phen)_2(dppz)]^{2+}$ is bound to the aptamer and luminescent.[99] On binding of ATP the aptamer distorts, ejecting the complex which turns off the light switch, thus acting as a sensor for ATP.

Other sensors use irreversible binding to DNA to give a similar response. It is known that Hg^+ ions can bind to thymine residues within DNA. This property has been exploited to create sensors for Hg^+, which is a target due to its neurotoxicity. One example uses mismatched DNA strands, where the Hg^+ forms a pseudo base pair with two thymine residues, resulting in double stranded DNA.[100] This double stand accommodates the binding of $[Ru(phen)_2(dppz)]^{2+}$, resulting in the light switch being turned on with an increase in emission not seen with other ions. Kim and co-workers demonstrated the opposite approach, where the binding of Hg^+ to thymine rich DNA strands prevents the binding of $[Ru(phen)_2(dppz)]^{2+}$, turning off the light switch, as shown in Figure 1.22.[101]
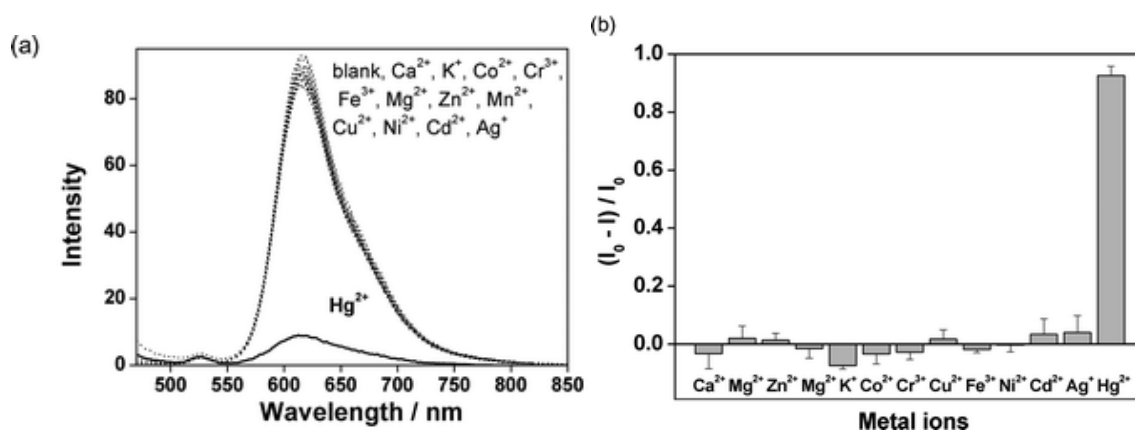
Figure 1.22 - (a) The turning off of the light switch effect by Hg^+ and (b) the selectivity of the sensor, compared with other ions. Adapted with permission from Kim *et. al.*[101]. (© Royal Society of Chemistry 2011)

Alongside these examples of the use of $[Ru(phen)_2(dppz)]^{2+}$, $[Ru(bpy)_2(dppz)]^{2+}$ has been employed in electrochemical sensing to detect Hg^+ when the DNA strand it attached to a surface.[102] In combination with SnO_2 electrodes, $[Ru(bpy)_2(dppz)]^{2+}$ has also been used in the detection of double stranded DNA,[103] DNA damage caused by H_2O_2[104] and DNA methylation damage.[105]

1.6 Surface Plasmon

The surface plasmon is a phenomenon whereby electromagnetic waves occur at the interface between a metal surface and other dielectric medium, such as water, where electrons are oscillating,[106] as illustrated in figure 1.23. First predicted by Ritchie in 1957,[107] the surface plasmon has become sufficiently important to seed its own field, known as plasmonics. One key application is surface plasmon resonance (SPR) that has been used for sensing of various analytes. This technique relies on the fact that the surface plasmon is very sensitive to changes close to the surface. When a metal film is used as the surface, light can be reflected off the reverse of the surface through a prism. Any binding events at the surface can be detected by a change in the angle of reflected light that has interacted with the plasmon.[108] SPR can be used for biosensing, with the adsorption of antibodies to a surface studied.[109] The surface plasmon has been found to enhance raman signals, and used for immunoassays, detecting low abundance biomarkers.[110]
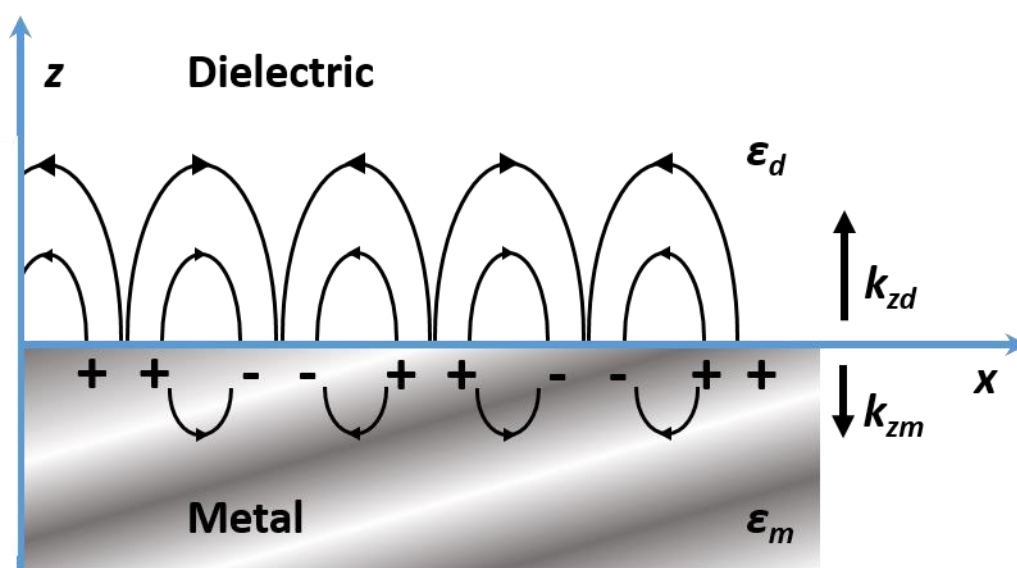
Figure 1.23 - Conceptual diagram of a surface plasmon, adapted from Yongqian[111]

The effect of the surface plasmon on optical properties is not observed visually for most metals as the surface constitutes a small part of the bulk material. However when the metal is formed into nanoparticles (NPs), the surface area is greatly increased and can result in coloured solutions dependant of the size of the NPs solvated. In close proximity the plasmons of these NPs can couple with one another, altering the colour of the solution. This effect was exploited by Mirkin *et. al.* when functionalising the NPs

with DNA. When the DNA was combined with a complimentary strand the NPs were held closely, resulting in a colour change.[112] The surface plasmon is also known to couple to the emission of fluorophores, enhancing their emission.[113]

1.6.1 Metal enhanced luminescence

Metal surfaces can quench any luminescence from molecules in close proximity by energy transfer from the lumophore to the surface.[114] Despite this, metal enhanced fluorescence has been demonstrated by constructing surfaces with silver metal islands.[115] This could be thought of as nanoparticles attached to the surface. This approach has been applied to biosensor applications such as immunoassays for myoglobin, where enhancement from silver islands allowed for the detection of sub 50 ng/ml detection.[116] There are multiple theories as to the physical processes that enable the enhancement. It could be conceived either that the resonance of the surface plasmon interacts with the fluorophore to enhance its emission, or the fluorophore transfers energy to the plasmon, which emits additional energy.[117] These are illustrated in Figure 1.24.
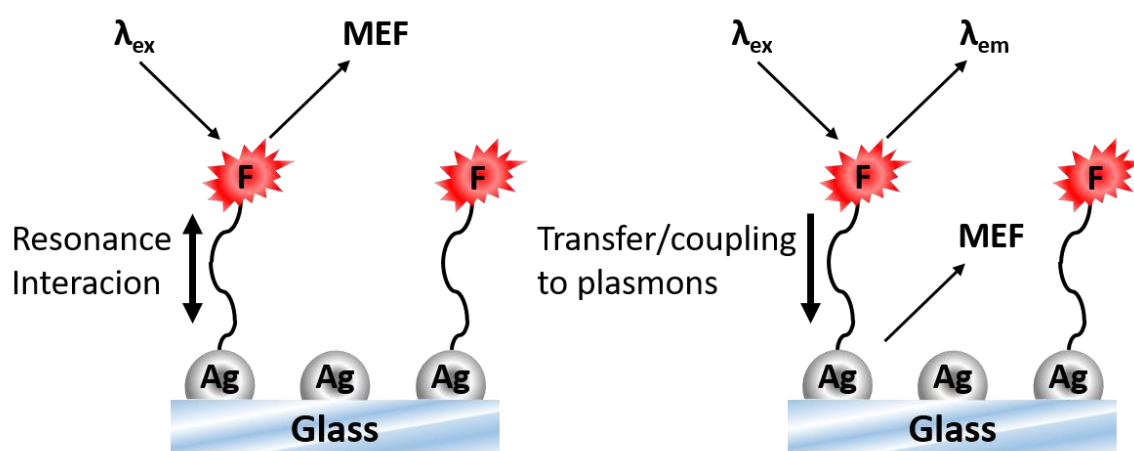
Figure 1.24 - Two potential mechanisms of metal enhanced fluorescence. Adapted from Geddes *et. al.*[117]

It has also been theorised that this mechanism should be able to enhance phosphoresce as well as fluorescence.[115] This has subsequently been demonstrated with a silver island surface and Rose Bengal.[117] This resulted in a fivefold increase in emission from the lumophore. While not using a surface there is a precedent for the enhancement of ruthenium complexes. It has been demonstrated that the surface plasmon of nanoparticles in solution can enhance their emission.[118] This phenomenon

has the potential to improve many biosensors, including biological assays, improving their sensitivity.

1.7 Project Aims

The aim of this project is to combine the technologies detailed previously, whereby a metallointercalator is attached to a surface, in order to enhance its emission and increase the sensitivity of a potential resulting biosensor device. As has been described, in solution, multiple examples exist of metallointercalators used as sensors on the basis of the light switch effect. These could be enhanced using a nanostructured surface to allow for the detection of lower concentrations of analyte. Taking the sensor out of solution allows for the easy regeneration and reuse of the sensor, creating a more useful device. It has also been discussed that ruthenium complexes can be synthetically altered to target specific structures of DNA. This could be utilised to create a biosensor that will detect DNA structures related to certain diseases, with a view to early diagnoses of conditions.

As $[Ru(phen)_2(dppz)]^{2+}$ is the most studied metallointercalator, and has already been proven for its sensor applications due to the light switch effect,[89] an adapted form of this complex will form the basis of the project. One problem with the use of the complex is the existence of the two enantiomers that have differing binding modes with DNA. It is therefore desired that an achiral complex will be synthesised through the use of a tridentate ligand, replacing the bidentate phen. This will simplify the understanding of the binding which will aid the construction of a robust biosensor.

There are multiple factors that could affect the performance of a biosensor constructed on this basis. Steric factors may hinder the reversible binding of DNA at a surface. Also the enhancement is known to be affected by the distance of the lumophore form the plasmon. For this reason the project aims to produce a ruthenium complex capable of click chemistry, such as the azide-alkyne cycloaddition. This approach allows for facile synthesis of a linker between the ruthenium complex and a self-assembled monolayer (SAM). It would enable the distance from the surface to be altered, simply by changing the SAM, without challenging synthetic changes to the ruthenium complex. The click chemistry approach is also versatile, such that a ruthenium complex with this functionality could be used for multiple other applications, such as attachment to

nanoparticles or addition of hydrogen bonding moieties for increased DNA binding affinity.

A more specific example of how this could be used is to improve the Hg$^+$ sensor discussed in section 1.5.2.[102] In this instance a sensor device was constructedwith the DNA strand attached to the surface. The sensor relies on the binding of Hg$^+$ to thymine residues which is difficult to remove from the sensor after use. This makes the sensor unsuitable as it cannot be regenerated easily, and as such cannot be calibrated to determine specific mercury concentrations. If the ruthenium complex were attached to the surface and the DNA reversibly bound, the thymine damaged DNA need only be washed away and replaced with a fresh sample of DNA in order the reuse the sensor.

The synthetic approach to achieve the desired DNA binding complex with a surface attachment is detailed in the following chapters.

1.8 References

1   M. E. Weeks, *J. Chem. Educ.*, 1932, **9**, 1017.

2   F. M. Hunt, L. B. and Lever, *Platin. Met. Rev.*, 1969, **13**, 126–138.

3   C. R. K. Rao and D. C. Trivedi, *Coord. Chem. Rev.*, 2005, **249**, 613–631.

4   P. M. Maitlis, H. C. Long, R. Quyoum, M. L. Turner and Z.-Q. Wang, *Chem. Commun.*, 1996, 1–8.

5   P. M. Colombo and N. Rascio, *J. Ultrastruct. Res.*, 1977, **60**, 135–139.

6   T. M. Trnka and R. H. Grubbs, *Acc. Chem. Res.*, 2001, **34**, 18–29.

7   E. S. Antonarakis and A. Emadi, *Cancer Chemother. Pharmacol.*, 2010, **66**, 1–9.

8   K. Kalyanasundaram, *Coord. Chem. Rev.*, 1982, **46**, 159–244.

9   A. Juris, V. Balzani, F. Barigelletti, S. Campagna, P. Belser and A. Von Zelewsky, *Coord. Chem. Rev.*, 1988, **84**, 85–277.

10   J. P. Paris and W. W. Brandt, *J. Am. Chem. Soc.*, 1959, **81**, 5001–5002.

11   T. J. Meyer, *Acc. Chem. Res.*, 1989, **22**, 163–170.

12   S. Serroni, S. Campagna, F. Puntoriero, C. Di Pietro, N. D. McClenaghan and F. Loiseau, *Chem. Soc. Rev.*, 2001, **30**, 367–375.

13   J. K. Barton, A. T. Danishefsky and J. M. Goldberg, *J. Am. Chem. Soc.*, 1984, **106**, 2172–2176.

14   J. K. Barton, *Science*, 1986, **233**, 727–734.

15   A. R. McDonald, Y. Guo, V. V. Vu, E. L. Bominaar, E. Münck and L. Que, *Chem. Sci.*, 2012, **3**, 1680.

16   B. Alberts, A. Johnson, J. Lewis, M. Raff, K. Roberts and P. Walter, *Molecular biology of the cell*, Garland Science, New York, 5th edn., 2008.

17   J. D. Watson and F. H. C. Crick, *Nature*, 1953, **171**, 737–738.

18   T. Maria, E. Ramon and F. Carmen, *ChemBioChem*, 2014, **15**, 1374–1390.

19   C. A. Hunter, *Philos. Trans. R. Soc. London. Ser. A Phys. Eng. Sci.*, 1993, **345**, 77 LP-85.

20   J. P. Weisenseel, G. R. Reddy, L. J. Marnett and M. P. Stone, *Chem.Res.Toxicol.*, 2002, **15**, 127–139.

21   A. G. W. Leslie, S. Arnott, R. Chandrasekaran and R. L. Ratliff, *J. Mol. Biol.*, 1980, **143**, 49–72.

22   P. Belmont, J. F. Constant and M. Demeunynck, *Chem. Soc. Rev.*, 2001, **30**, 70–81.

23   J. A. Dohm, M.-H. Hsu, J.-R. Hwu, R. C. C. Huang, E. N. Moudrianakis, E. E. Lattman and A. G. Gittis, *J. Mol. Biol.*, 2005, **349**, 731–744.

24   B. F. Eichman, G. P. Schroth, B. E. Basham and P. S. Ho, *Nucleic Acids Res.*, 1999, **27**, 543–550.

25   M. R. Gill and J. A. Thomas, *Chem. Soc. Rev.*, 2012, **41**, 3179.

26   F. R. Keene, J. A. Smith and J. G. Collins, *Coord. Chem. Rev.*, 2009, **253**, 2021–2035.

27   M. A. Austin, C. M. Hutter, R. L. Zimmern and S. E. Humphries, *Am. J. Epidemiol.*, 2004, **160**, 407–420.

28   J. Li, C. Yen, D. Liaw, K. Podsypanina, S. Bose, S. I. Wang, J. Puc, C. Miliaresis, L. Rodgers, R. McCombie, S. H. Bigner, B. C. Giovanella, M. Ittmann, B. Tycko, H. Hibshoosh, M. H. Wigler and R. Parsons, *Science,* 1997, **275**, 1943 LP-1947.

29   D. Payet and A. Travers, *J. Mol. Biol.*, 1997, **266**, 66–75.

30   J. R. Gatchel and H. Y. Zoghbi, *Nat. Rev. Genet.*, 2005, **6**, 743.

31   H. L. Paulson and K. H. Fischbeck, *Annu. Rev. Neurosci.*, 1996, **19**, 79–107.

32   D. Sen and W. Gilbert, *Nature*, 1988, **334**, 364.

33   G. Biffi, D. Tannahill, J. McCafferty and S. Balasubramanian, *Nat. Chem.*, 2013, **5**, 182.

34   Z. Zhang, J. Dai, E. Veliath, R. A. Jones and D. Yang, *Nucleic Acids Res.*, 2010, **38**, 1009–1021.

35   H. J. Lipps and D. Rhodes, *Trends Cell Biol.*, 2009, **19**, 414–422.

36   R. Rodriguez, K. M. Miller, J. V Forment, C. R. Bradshaw, M. Nikan, S. Britton, T. Oelschlaegel, B. Xhemalce, S. Balasubramanian and S. P. Jackson, *Nat. Chem. Biol.*, 2012, **8**, 301.

37   J. L. Huppert and S. Balasubramanian, *Nucleic Acids Res.*, 2005, **33**, 2908–2916.

38   R. Rodriguez, S. Müller, J. A. Yeoman, C. Trentesaux, J.-F. Riou and S. Balasubramanian, *J. Am. Chem. Soc.*, 2008, **130**, 15758–15759.

39   M. Engelhardt, P. Drullinsky, J. Guillem and M. A. Moore, *Clin. Cancer Res.*, 1997, **3**, 1931 LP-1941.

40   T.-L. Yang, L. Lin, P.-J. Lou, T.-C. Chang and T.-H. Young, *PLoS One*, 2014, **9**, e86143.

41   A. T. Phan, M. Guéron and J.-L. Leroy, *J. Mol. Biol.*, 2000, **299**, 123–144.

42   M. Zeraati, D. B. Langley, P. Schofield, A. L. Moye, R. Rouet, W. E. Hughes, T. M. Bryan, M. E. Dinger and D. Christ, *Nat. Chem.*, 2018, **10**, 631–637.

43   B. Rosenberg, L. Van Camp and T. Krigas, *Nature*, 1965, **205**, 698.

44   K. Cheung-Ong, G. Giaever and C. Nislow, *Chem. Biol.*, 2013, **20**, 648–659.

45   A. Gelasco and S. J. Lippard, *Biochemistry*, 1998, **37**, 9230–9239.

46   C. Ban, B. Ramakrishnan and M. Sundaralingam, *Nucleic Acids Res.*, 1994, **22**, 5466–5476.

47   M. Coll, C. A. Frederick, A. H. Wang and A. Rich, *Proc. Natl. Acad. Sci. U. S. A.*, 1987, **84**, 8385–8389.

48   H. Robinson, W. Priebe, J. B. Chaires and A. H.-J. Wang, *Biochemistry*, 1997, **36**, 8663–8670.

49   J. T. Thomas and A. V Bloomfield, *Biopolymers*, 1984, **23**, 1295–1306.

50   T. J. Thomas, U. B. Gunnia and T. Thomas, *J. Biol. Chem.*, 1991, **266**, 6137–6141.

51   J. B. Chaires, *Biopolymers*, 1997, **44**, 201–215.

52   J. B. Chaires, *Arch. Biochem. Biophys.*, 2006, **453**, 26–31.

53   A. C. Finlay, F. A. Hochstein, B. A. Sobin and F. X. Murphy, *J. Am. Chem. Soc.*, 1951, **73**, 341–343.

54   M. L. Kopka, C. Yoon, D. Goodsell, P. Pjura and R. E. Dickerson, *Proc. Natl. Acad. Sci.*, 1985, **82**, 1376 LP-1380.

55   K. D. Harshman and P. B. Dervan, *Nucleic Acids Res.*, 1985, **13**, 4825–4835.

56   B. P. Giovanni, B. Andrea, F. Francesca, P. Delia, T. M. Aghazadeh, P. M. Giovanna and R. Romeo, *Med. Res. Rev.*, 2004, **24**, 475–528.

57   M. Teng, N. Usman, C. A. Frederick and A. H.-J. Wang, *Nucleic Acids Res.*, 1988, **16**, 2671–2690.

58   D. Suh and J. B. Chaires, *Bioorganic Med. Chem.*, 1995, **3**, 723–728.

59   L. S. Lerman, *J. Mol. Biol.*, 1961, **3**, IN13-IN14.

60   F.-M. Arcamone, *Chem. – Eur. J.*, 2009, **15**, 7774–7791.

61   C. Tan, H. Tasaka, K.-P. Yu, M. L. Murphy and D. A. Karnofsky, *Cancer*, 1967, **20**, 333–353.

62   A. H. J. Wang, G. Ughetto, G. J. Quigley and A. Rich, *Biochemistry*, 1987, **26**, 1152–1163.

63   J. B. Chaires, J. E. Herrera and M. J. Waring, *Biochemistry*, 1990, **29**, 6145–6153.

64   S. Neidle, L. H. Pearl and J. V Skelly, *Biochem. J.*, 1987, **243**, 1–13.

65   D. J. Roser, *Soil Biol. Biochem.*, 1980, **12**, 329–336.

66   M. J. Waring, *J. Mol. Biol.*, 1965, **13**, 269–282.

67   P. Borst, *IUBMB Life*, 2008, **57**, 745–747.

68   J. Sigmon and L. Larcom, *Electrophoresis*, 1996, **17**, 1524–1527.

69   R. M. Izatt, J. J. Christensen and J. H. Rytting, *Chem. Rev.*, 1971, **71**, 439–481.

70   A. Shulman and F. P. Dwyer, in *Chelating agents and metal chelates*, eds. F. P. Dwyer and D. P. Mellor, Academic Press, New York, 1964, pp. 397–402.

71   K. W. Jennette, S. J. Lippard, G. A. Vassiliades and W. R. Bauer, *Proc. Natl. Acad. Sci.*, 1974, **71**, 3839–3843.

72   P. J. Bond, R. Langridge, K. W. Jennette and S. J. Lippard, *Proc. Natl. Acad. Sci.*, 1975, **72**, 4825–4829.

73   M. Howe-Grant and S. J. Lippard, *Biochemistry*, 1979, **18**, 5762–5769.

74   B. Nordén and F. Tjerneld, *FEBS Lett.*, 1976, **67**, 368–370.

75   J. K. Barton, J. J. Dannenberg and A. L. Raphael, *J. Am. Chem. Soc.*, 1982, **104**, 4967–4969.

76   C. V Kumar, J. K. Barton and N. J. Turro, *J. Am. Chem. Soc.*, 1985, **107**, 5518–5523.

77   A. B. Tossi, J. M. Kelly, C. OhUigin and D. J. McConnell, *Nucleic Acids Res.*, 1985, **13**, 6017–6034.

78   J. K. Barton, J. M. Goldberg, C. V Kumar and N. J. Turro, *J. Am. Chem. Soc.*, 1986, **108**, 2081–2088.

79   J. P. Rehmann and J. K. Barton, *Biochemistry*, 1990, **29**, 1701–1709.

80   J. P. Rehmann and J. K. Barton, *Biochemistry*, 1990, **29**, 1710–1717.

81   D. Z. M. Coggan, I. S. Haworth, P. J. Bates, A. Robinson and A. Rodger, *Inorg. Chem.*, 1999, **38**, 4486–4497.

82   C. Hiort, B. Norden and A. Rodger, *J. Am. Chem. Soc.*, 1990, **112**, 1971–1982.

83   S. Satyanarayana, J. C. Dabrowiak and J. B. Chaires, *Biochemistry*, 1992, **31**, 9319–9324.

84   B. T. Patterson, G. J. Collins, F. M. Foley and R. F. Keene, *J. Chem. Soc. Dalton Trans.*, 2002, 4343–4350.

85   V. Gonzalez, T. Wilson, I. Kurihara, A. Imai, J. A. Thomas and J. Otsuki, *Chem. Commun.*, 2008, 1868–1870.

86   G. I. Pascu, A. C. G. Hotze, C. Sanchez-Cano, B. M. Kariuki and M. J. Hannon, *Angew. Chemie Int. Ed.*, 2007, **46**, 4374–4378.

87   K. E. Erkkila, D. T. Odom and J. K. Barton, *Chem. Rev.*, 1999, **99**, 2777–2796.

88   B. M. Zeglis, V. C. Pierre and J. K. Barton, *Chem. Commun.*, 2007, 4565–4579.

89   G. Li, L. Sun, L. Ji and H. Chao, *Dalton Trans.*, 2016, **45**, 13261–13276.

90   H. Niyazi, J. P. Hall, K. O'Sullivan, G. Winter, T. Sorensen, J. M. Kelly and C. J. Cardin, *Nat. Chem.*, 2012, **4**, 621.

91   M. G. Walker, V. Gonzalez, E. Chekmeneva and J. A. Thomas, *Angew. Chemie Int. Ed.*, 2012, **124**, 12273–12276.

92   A. E. Friedman, J. K. Barton, J. C. Chambron, J. P. Sauvage, N. J. Turro and J. K. Barton, *J. Am. Chem. Soc.*, 1990, **112**, 4960–4962.

93   E. J. C. Olson, D. Hu, A. Hörmann, A. M. Jonkman, M. R. Arkin, E. D. A. Stemp, J. K. Barton and P. F. Barbara, *J. Am. Chem. Soc.*, 1997, **119**, 11458–11467.

94   C. G. Coates, J. Olofsson, M. Coletti, J. J. McGarvey, B. Önfelt, P. Lincoln, B. Norden, E. Tuite, P. Matousek and A. W. Parker, *J. Phys. Chem. B*, 2001, **105**, 12653–12664.

95   M. K. Brennaman, T. J. Meyer and J. M. Papanikolas, *J. Phys. Chem. A*, 2004, **108**, 9938–9944.

96   F. E. Poynton, J. P. Hall, P. M. Keane, C. Schwarz, I. V. Sazanovich, M. Towrie, T. Gunnlaugsson, C. J. Cardin, D. J. Cardin, S. J. Quinn, C. Long and J. M. Kelly, *Chem. Sci.*, 2016, **7**, 3075–3084.

97   L. Ling, G. Song, Z. He, H. Liu and Y. Zeng, 1999, **364**, 356–364.

98   M. S. Choi, M. Yoon, J.-O. Baeg and J. Kim, *Chem. Commun.*, 2009, 7419–7421.

99   J. Wang, Y. Jiang, C. Zhou and X. Fang, *Anal. Chem.*, 2005, **77**, 3542–3546.

100   X. Zhang, Y. Li, H. Su and S. Zhang, *Biosens. Bioelectron.*, 2010, **25**, 1338–1343.

101   B. N. Oh, S. Park, J. Ren, Y. J. Jang, S. K. Kim and J. Kim, *Dalton Trans.*, 2011, **40**, 6494–6499.

102   R.-F. Huang, H.-X. Liu, Q.-Q. Gai, G.-J. Liu and Z. Wei, *Biosens. Bioelectron.*, 2015, **71**, 194–199.

103   S. Liu, C. Li, J. Cheng and Y. Zhou, *Anal. Chem.*, 2006, **78**, 4722–4726.

104   Y. Liu, S. Jia and L.-H. Guo, *Sensors Actuators B Chem.*, 2012, **161**, 334–340.

105   Y. Wu, B. Zhang and L.-H. Guo, *Anal. Chem.*, 2013, **85**, 6908–6914.

106   E. Ozbay, *Science*, 2006, **311**, 189 LP-193.

107   R. H. Ritchie, *Phys. Rev.*, 1957, **106**, 874.

108   N. J. de Mol and M. J. E. Fischer, *Surface plasmon resonance: methods and protocols*, Humana Press, New York, 2010.

109   B. Liedberg, C. Nylander and I. Lunström, *Sensors and Actuators*, 1983, **4**, 299–304.

110   N. B. and A. F. and J. M. H. and Y. S. and B. Kim, *Nanotechnology*, 2017, **28**, 455101.

111   Y. Li, *Plasmonic optics: Theory and applications*, SPIE Press Bellingham, 2017.

112   C. A. Mirkin, R. L. Letsinger, R. C. Mucic and J. J. Storhoff, *Nature*, 1996, **382**, 607.

113   J. R. Lakowicz, *Anal. Biochem.*, 2001, **298**, 1–24.

114   A. Campion, A. R. Gallo, C. B. Harris, H. J. Robota and P. M. Whitmore, *Chem. Phys. Lett.*, 1980, **73**, 447–450.

115   C. D. Geddes and J. R. Lakowicz, *J. Fluoresc.*, 2002, **12**, 121–129.

116   K. Aslan, I. Gryczynski, J. Malicka, E. Matveeva, J. R. Lakowicz and C. D. Geddes, *Curr. Opin. Biotechnol.*, 2005, **16**, 55–62.

117   Y. Zhang, K. Aslan, S. N. Malyn and C. D. Geddes, *Chem. Phys. Lett.*, 2006, **427**, 432–437.

118   N. J. Rogers, S. Claire, R. M. Harris, S. Farabi, G. Zikeli, I. B. Styles, N. J. Hodges and Z. Pikramenou, *Chem. Commun.*, 2014, **50**, 617–619.

2.0 Synthesis of tris(pyrazolyl)methane (tpm) derived compounds

2.1 Introduction

This chapter describes the design and synthesis of novel tpm based ligands and complexes. This is to achieve the goal of a multi-functional complex that can both bind reversibly to DNA, and be tethered to a surface. The ligands in question are designed to bind both to a ruthenium metal centre and contain a moiety suitable for coupling to a surface.

Ruthenium polypyridyl complexes are known to interact with DNA in multiple ways. These include reversible binding due to interactions between the aromatic systems present in the complex and those present in the base pairs that form the backbone of DNA.[1] The extended aromatic system of the dppz binds through an intercalating interaction by inserting itself into the DNA structure, sliding between base pairs. On binding, a light switch effect is observed. In an aqueous environment the luminescent emission is quenched through interactions with the polar solvent, however when bound it is protected from the solvent and the complex becomes emissive.[2,3] This enables the ruthenium dppz complex to report on its environment, and has led applications as a sensor.[4]
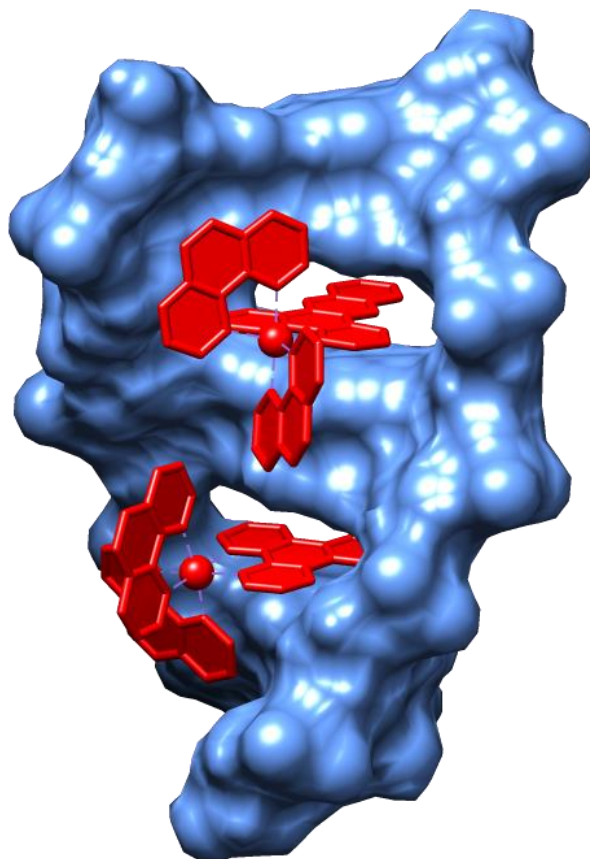
Figure 2.1 - X-ray structure of the Λ (top) and Δ (bottom) enantiomers of [Ru(phen)$_2$(dppz)] bound to DNA[5]

To construct reusable sensor devices from such complexes, it is useful to immobilise them on a surface. This allows for the re-generation of the sensor through a cleaning protocol, and is easier to handle and manipulate than a solution of the complex. This is commonly achieved using the strong thiol-gold bond. Another feature of gold surfaces is their surface plasmon. This describes the energy of oscillating electrons that flow across the surface of metallic materials. This energy can couple to the emission of luminescent compounds and enhance it.[6] This would enable a sensor device to be more sensitive, as smaller changes would be amplified. The nature of the plasmon can be tuned by altering the design of the surface, creating and altering the size of "islands" of metal on a non-metallic support.[7]

The design of ligands that could potentially take advantage of both the DNA light switch effect and metal enhanced luminescence is described in this chapter. Many of the synthesised ligands did not prove stable on reaction with ruthenium; however,

they may have interesting applications when used with other metal centres, such as crystal engineering.

2.2 Complex design

There are four key aspects to consider when designing a complex suitable for the desired application. The first of which, is what metal centre should be used and what geometry it will confer on the complex. Then consideration must be given to how the complex will interact with DNA. Also a linkage must be incorporated in the design to allow its attachment to a surface. Finally, any ancillary ligands must be selected to complete the complex, without interfering with the binding, or altering the photophysics of the complex in a way that disrupts the light switch effect.
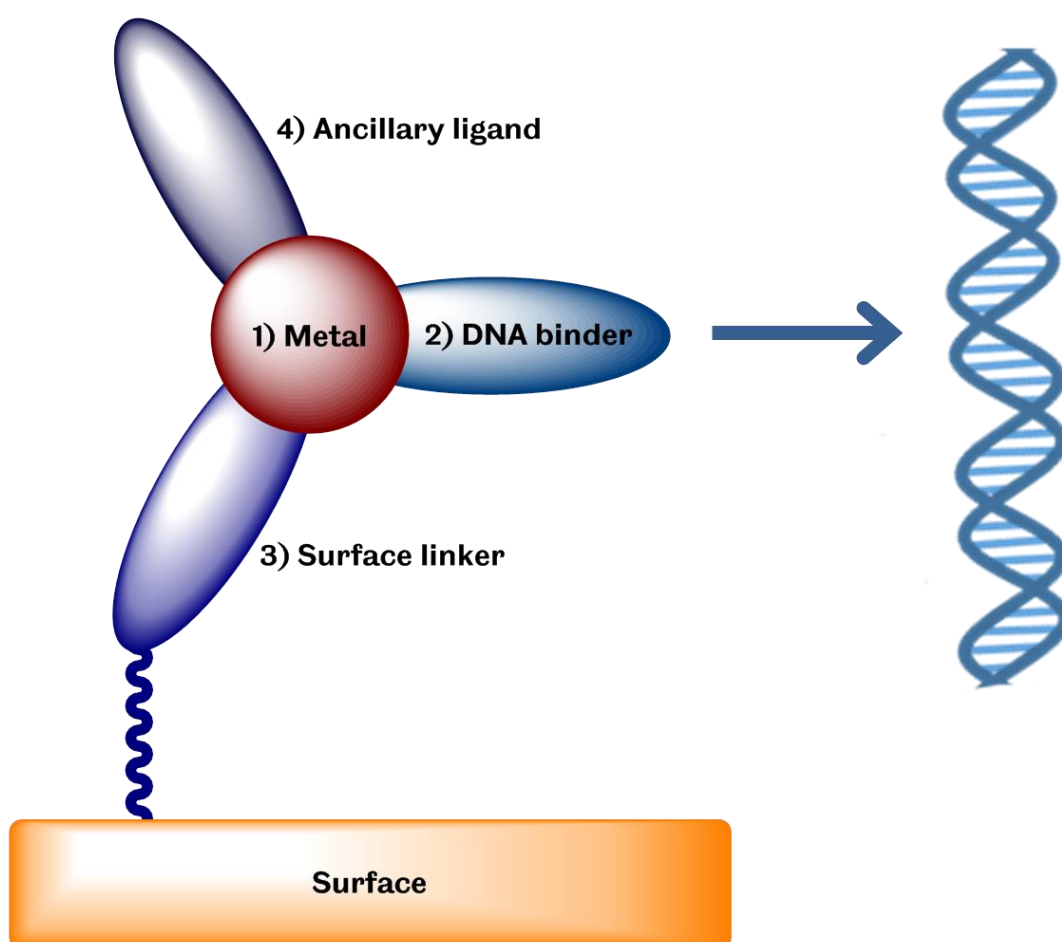
Figure 2.2 - Key design considerations for a DNA based biosensor

As already alluded to, the metal centre selected is ruthenium. This is due to extensive research that has shown ruthenium to be suitable as a luminescent probe for DNA, due to its stability and photophysical properties. Ruthenium polypyridyl complexes are relatively inert and stable over long periods,[8] so are less likely to degrade compared with other metal complexes. In addition, Ru complexes exhibit strong absorption, due to metal-ligand charge transfer (MLCT) and stable, relatively long lived excited states.[9] It is also possible to tune these photophysical properties by selecting different ancillary ligands.[10]

When coupled to the dppz unit, the ruthenium complex develops a capability for interaction with DNA through intercalation. While there are potential alternative ligands that possess binding capability, such as phenanthroline (phen), which can groove bind, and benzodipyridophenazine (dppn), which can also intercalate, dppz is preferred due to its light switch effect, previously discussed. This is the key property required for sensor applications.

Commonly Ru-dppz complexes are constructed using another bidentate ligand as the ancillary ligand. This is due to the straightforward two step synthesis, first combining the ancillary ligand with ruthenium trichloride, in the presence of LiCl to prevent the loss of all the chloride ligands, forming $[RuCl_2(NN)_2]$ (NN = ancillary ligand). Subsequently the remaining chloride ligands are removed and replaced by the dppz ligand. As an octahedral complex, with three tridentate ligands co-ordinated, this synthesis leads to two enantiomers. Since the first work in the field it has been suggested that this could lead to different interactions with DNA, since DNA itself is chiral.[11] Where dppz has been employed with phen or bpy ancillary ligands only slight differences in binding affinity have been observed,[12] however the Δ-enantiomer tends to show stronger luminescence.[13] To further complicate the situation the use of bulkier ancillary ligands, such as diphenylphenanthroline (DIP) could introduce steric clash and disrupt DNA binding.

It is possible to construct heteroleptic Ru(II) complexes with three different bidentate ligands,[15] however if a complex was designed on the basis, with the aim of use as a sensor, the resultant binding mechanics would exhibit too much complexity. Any result from such a device may be inconsistent depending on the relative amounts of each enantiomer, and the manner of their interaction with different DNA structures. In order to simplify binding studies attempts could be made to separate the

enantiomers, but this can be difficult and tends to lead to significant loss of compound; therefore this is often an unproductive approach. In addition, if the attachment consisted of a "tail" from a bidentate ancillary ligand, such as phen, the ligand would be asymmetric leading to two geometrical isomers of the complex, each with two enantiomers as shown in figure 2.3. This would make isolation of an individual isomer even more challenging.
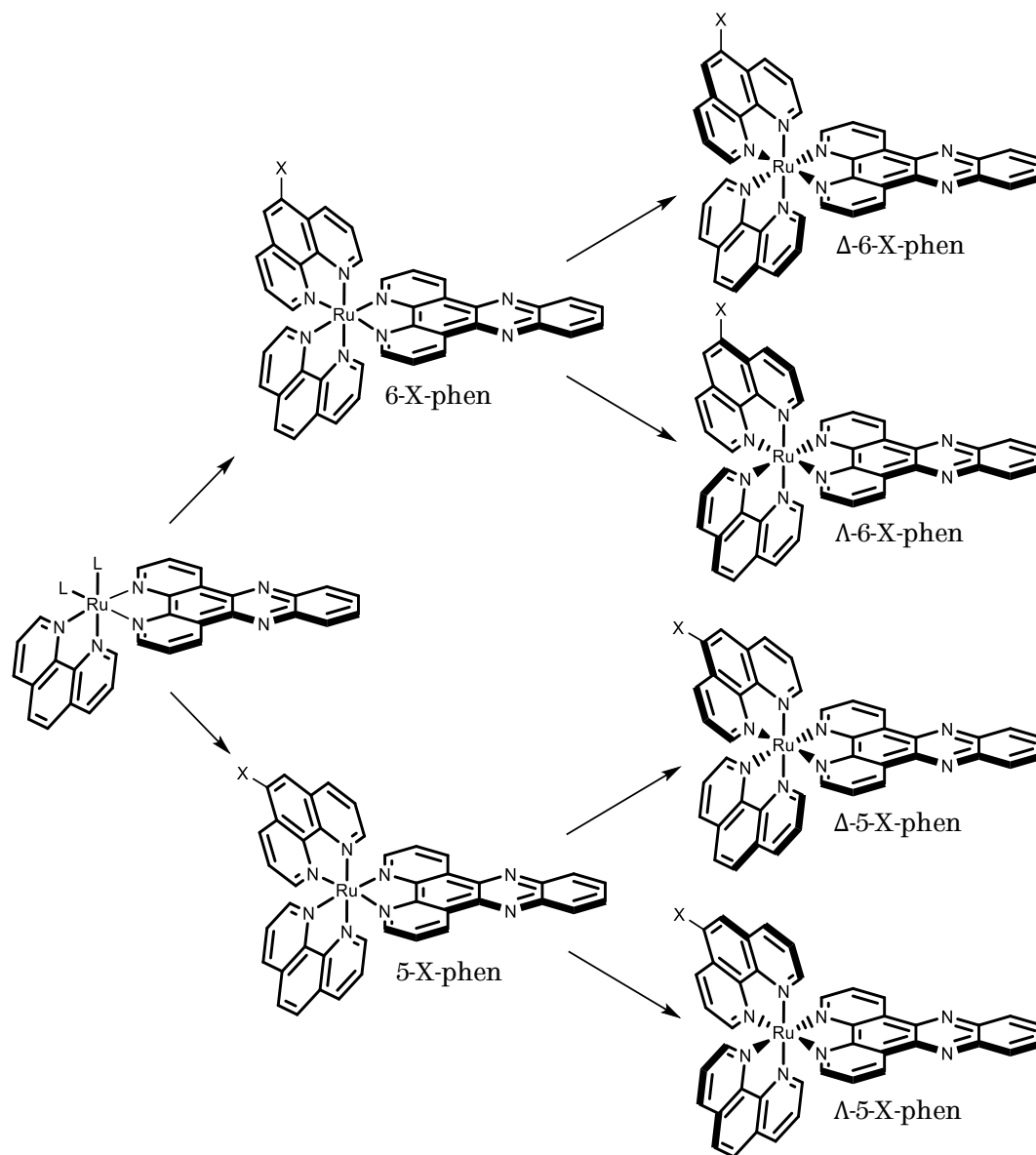
Figure 2.3 - Illustration of the possible isomers on adding a linker (X) to a bidentate ligand, such as phenanthroline

A solution to this chirality problem is to construct an achiral complex. This has been achieved by the Thomas group through employing the tridentate ligand, tris(pyrazolyl)methane (tpm).[16] The ligand consists of three pyrazole rings, covalently

attached to a methane group, leaving three free nitrogen atoms that can facially cap an octahedral metal centre. This confers a centre of symmetry upon the metal complex, thus eliminating chirality and resulting in a single isomer. Complexes combining the dppz ligand with tpm and a pyridine ancillary ligand showed binding properties comparable to that of $[Ru(phen)_2(dppz)]^{2+}$. The use of tpm with the dppz unit also leaves a single co-ordination site free that has been exploited to modulate the binding properties of the complex by introducing a substituent to the pyridine ring.[17]

Complexes of the form $[Ru(tpm)(dppz)(py)]^{2+}$ give two potential sites for a surface linker. The pyridine could be substituted, but - as alluded to above - this can affect the binding of DNA. The alternative is to add function to the tpm unit. This approach relies on the fact that the remaining proton on the methane unit is acidic, owing to the electron deficient nature of the pyrazole rings which inductively stabilise the anion that is formed on deprotonation. This approach was first demonstrated by Reger, *et. al.*[18], who extended the tpm ligand to include an alkyne group. This allowed for the use of tpm in crystal engineering, combining multiple units with aryl-halide units in cross-coupling reactions, forming semi-rigid linkers for multiple metal centres. The same approach was extended by Pfieffer, *et. al.*[19] who co-ordinated the tpm-alkyne ligand to molybdenum tricarbonyl, forming a CO release agent. This work realised the potential of the ligand, not just for cross-coupling, but also for azide-alkyne cycloaddition, otherwise described as click chemistry. This was employed to link the CO releasing moiety to a peptide, designed for targeted uptake by cancer cells.

Click chemistry is a versatile stratergy for linking molecules. It has been used in many applications from materials science to drug discovery.[20] Sharpless *et. al.* stated that click reactions are "modular, wide in scope, give very high yields, generate only inoffensive byproducts and are stereospecific" further advantages include "simple reaction conditions, readily available starting materials, the use of a solvent that is easily removed and simple product isolation".[21] While not the only example of click chemistry, the azide-alkyne cycloaddition is one of the most powerful, given the ease of synthesis of starting materials, tolerance of functional groups and mild reaction conditions.[20] This is especially true since the introduction of copper catalysis for the cycloaddition step.[22] Under thermal conditions the azide and alkyne will react, but can form two isomers. The use of copper confers a rate enhancement, and forces the product into forming a single isomer. This results in a fast and reliable linkage

mechanism, which has been applied to surface attachment using a wide array of surfaces, often through the use of an azide functional self assembled monolayer (SAM).[23]

It is therefore proposed that the design of the target complex for this project would consist of:

- A ruthenium metal centre, to take advantage of stable photophysics and octahedral geometry.
- A DNA binding moiety in the form of the bidentate dppz ligand, enabling sensor application through the light switch effect.
- A surface linking ligand, using a derivative of the tpm ligand containing an alkyne group, to be combined with an azide functional SAM.
- An ancillary pyridine ligand, used to enable the light switch effect while playing a passive role in the DNA binding properties of the complex.

This design and illustration of its application is shown in figure 2.4.
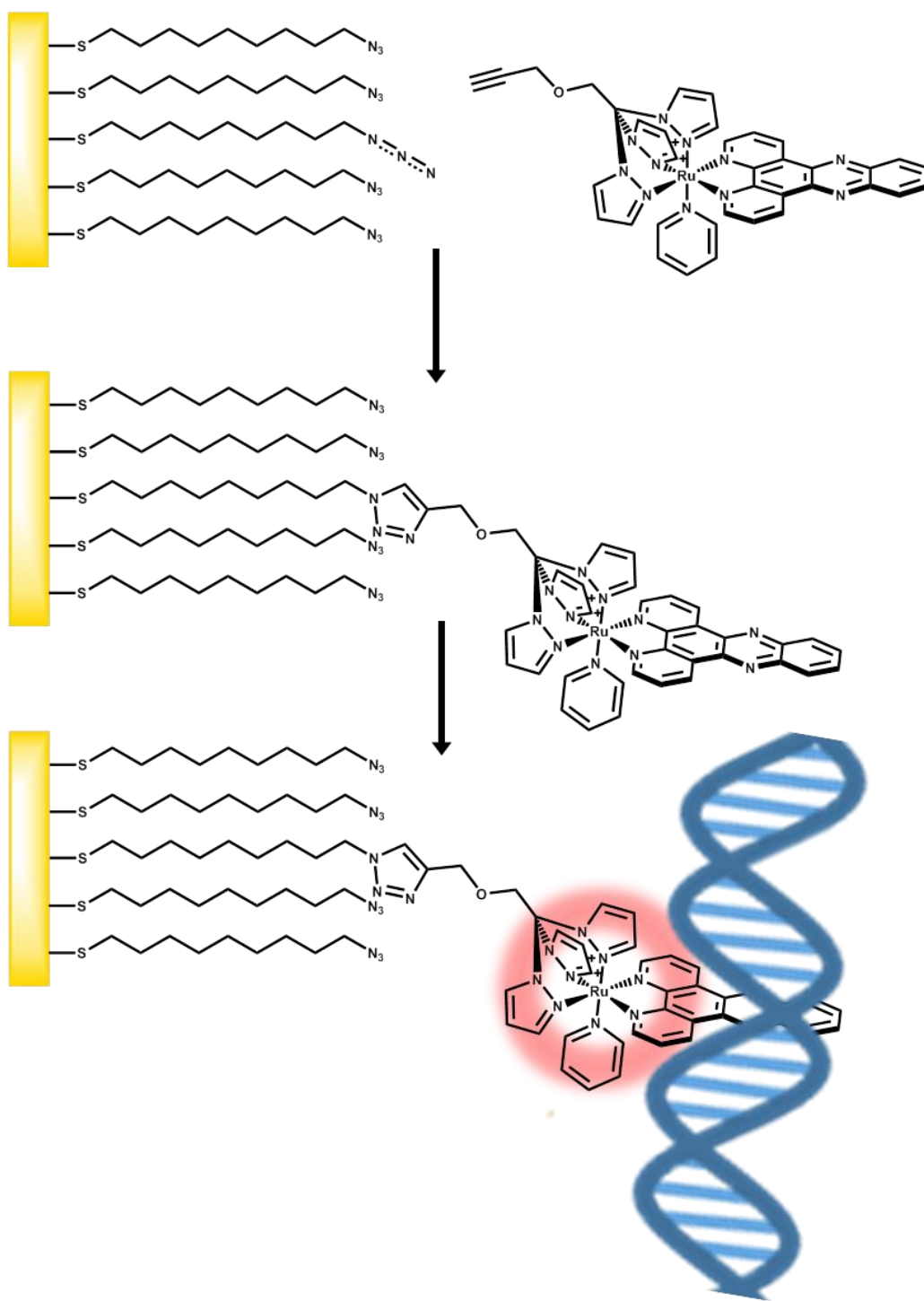
Figure 2.4 - Illustration of a the proposed surface bound, intercalating ruthenium complex

2.3 Ligand and complex synthesis

2.3.1 Synthesis of tpm

The synthesis of tpm is well established, most commonly achieved through the method of Reger, *et. al.*[24]. Pyrazole is deprotonated by a large excess of Na_2CO_3 in aqueous solution. This is mixed with chloroform, using tetra-n-butyl ammonium bromide as a phase transfer catalyst, allowing the pyrazole unit to displace the chlorine atoms of the chloroform molecule via nucleophilic substitution. The mixture is refluxed over multiple days to allow for full substitution. The resultant extract is recrystalised from water to give reliably pure off white crystals.
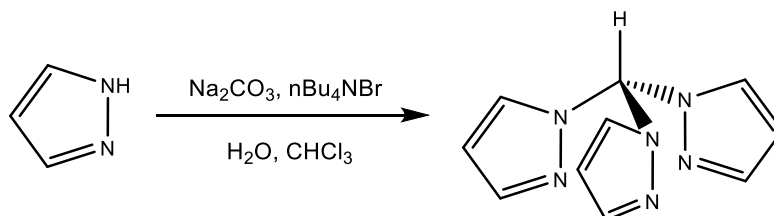
Figure 2.5 - Synthesis of tpm

2.3.2 Synthesis of [RuCl₃(tpm)]

The simple complex resulting from reaction of tpm and $RuCl_3.xH_2O$ was synthesised as an analogue to later attempts with derivative tpm ligands. Ruthenium chloride hydrate is refluxed with tpm in ethanol, yielding a brown precipitate which is isolated as the product. The product is insoluble in most solvents making NMR analysis difficult so characterisation is provided by mass spectrometry and the success of subsequent reaction.
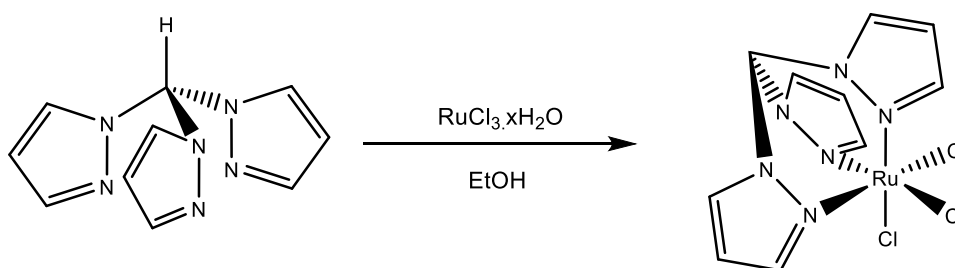
Figure 2.6 - Synthesis of [RuCl₃(tpm)]

2.3.3 Synthesis of phenanthroline dione (dpq)

Dpq is required as a starting material to form dppz, the intercalating part of the desired complex. It is formed by acidic oxidation, using potassium bromate in 60% sulphuric acid. After extraction, the product is purified by recrystallization from methanol and obtained as yellow crystals.
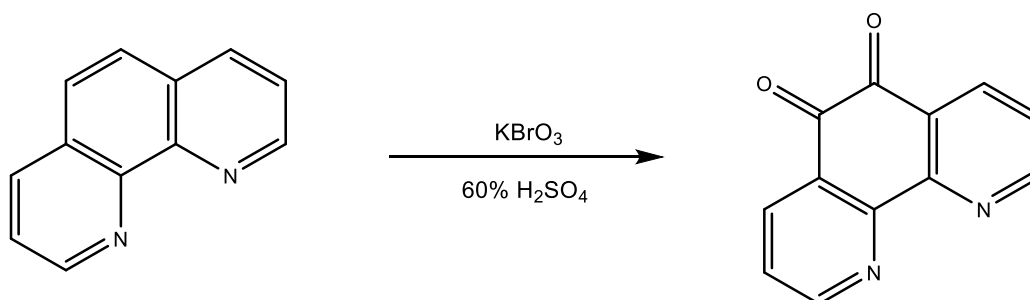
Figure 2.7 - Synthesis of dpq

2.3.4 Synthesis of dipyridophenazine (dppz)

Dppz is formed by reflux of dpq and 1,2-diaminobenzene in ethanol. The amine and quinone moieties undergo a condensation reaction the form the fused ring system of the dppz. The product is recrystallized from ethanol and obtained as cream coloured crystals.
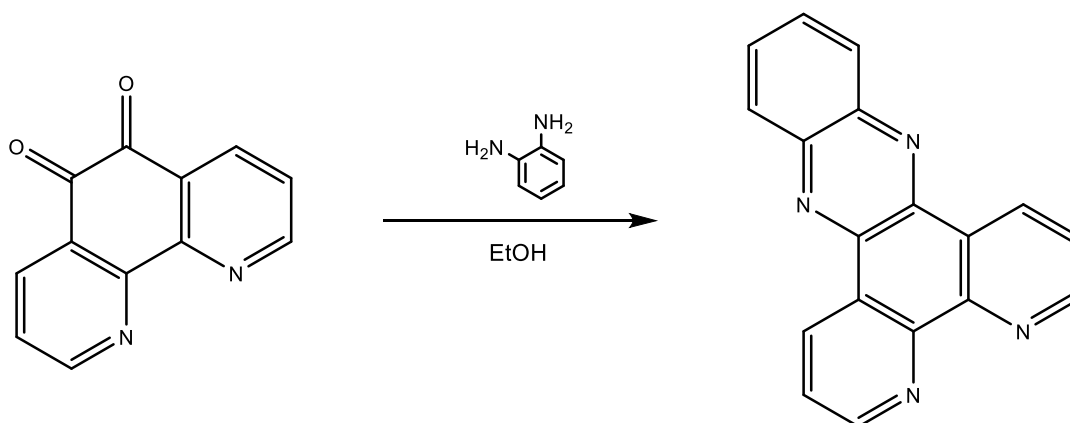
Figure 2.8 - Synthesis of dppz

2.3.5 Synthesis of [RuCl(tpm)(dppz)]⁺PF₆⁻

The dppz unit is added to the ruthenium complex using an adapted method previously reported for phen and bpy ligands. [RuCl₃(tpm)] is refluxed with the dppz unit in an ethanol:water solvent mix to solubilise both the organic ligand and the removed chloride. Triethylamine is added to aid the reduction of the ruthenium centre. The product is precipitated using saturated KPF_6 and purified using an alumina column and a 1:1 acetonitrile:toluene eluant. The product is isolated as a red solid.
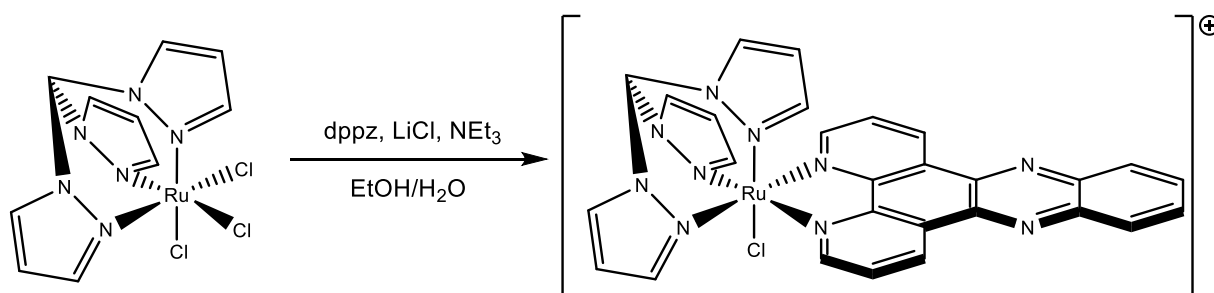
Figure 2.9 - Synthesis of [RuCl(tpm)(dppz)]⁺PF₆⁻

2.3.6 Synthesis of tris(pyrazolyl)ethanol (tpe)

The electron deficient nature of the pyrazole ring stabilises anions on the central carbon atom of tpm resulting in an acidic proton. This can be utilised to add function to the molecule, as demonstrated by Reger, *et. al.*[18] Tpm is deprotonated using with potassium tert-butoxide in anhydrous THF. This unit then undergoes nucleophilic attack of paraformaldehyde, thus adding an ethoxy moiety to the tpm molecule. The quenching and extraction of the reaction gives the product as a white solid in quantitative yield.
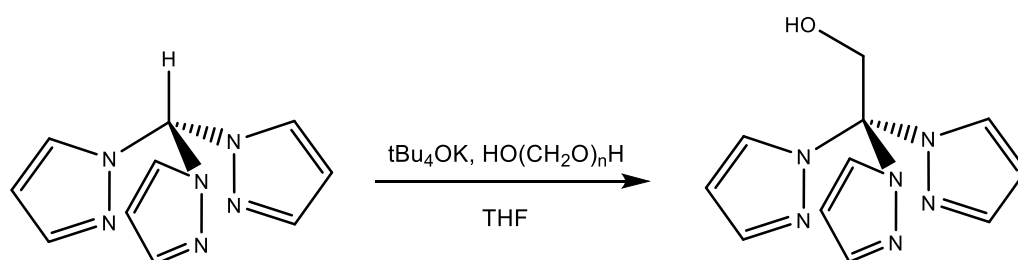
Figure 2.10 - Synthesis of tpe

2.3.7 Synthesis of tris(pyrazolyl)propynyloxyethane (tppoe)

The tpe unit acts as a building block for further functionalisation due to the presence of the alcohol moiety. Tppoe was synthesised by the method of Reger, *et. al.*[18] in which tpe is deprotonated using sodium hydride in anhydrous THF, followed by addition of propargyl bromide. The nucleophilic substitution of tpe results in a stable ether linkage to the alkyne group which could be further used for click chemistry. The extract is purified by column chromatography to giving a yellow, waxy solid.
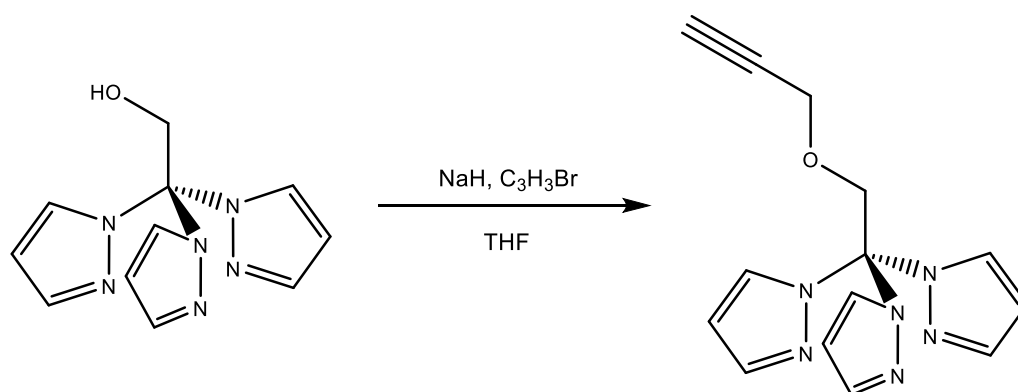
Figure 2.11 - Synthesis of tppoe

2.3.8 Synthesis of [RuCl₃(tppoe)]

In the same way that tpm is reacted with RuCl₃, attempts were made to form a ruthenium complex with the derivative tppoe. Initial attempts using ethanol did not yield a precipitate, as is observed with tpm. Alternative purification techniques also failed to yield the desired product. On the basis that the added organic structure of the ligand may be increasing the solubility of the resultant complex, the solvent was switched to propanol, yielding a brown precipitate as expected. The low solubility of the complex made characterisation difficult. Subsequent reactions using the solid as the starting material did not yield the desired complex so it is likely that the initial reaction was not a success.
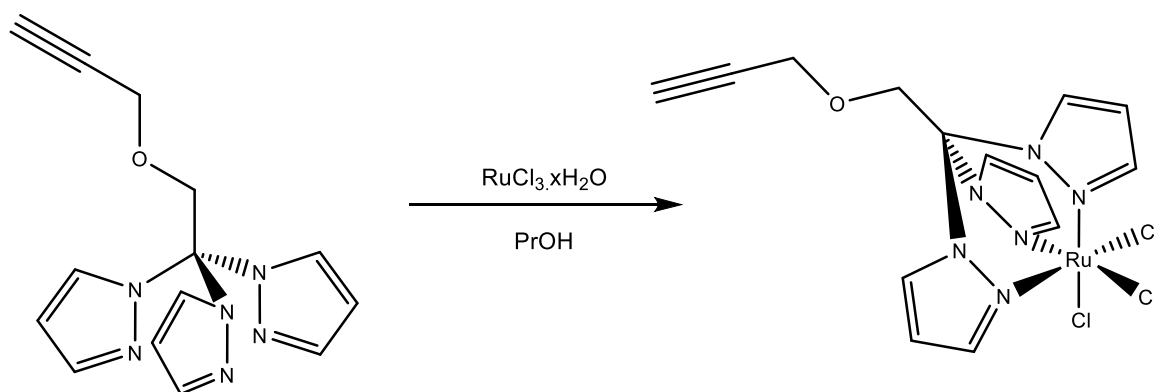
Figure 2.13 - Attempted synthesis of [RuCl₃(tppoe)]

It has been shown that ruthenium polypyridyl complexes can react with alkynes, ultimately destroying the functional group and forming a carbonyl ligand on the ruthenium centre.[25] Although RuCl₃ may not be capable of such reactions, it could be that some intermediate formed in the reaction is more active and could catalyse the destruction of the alkyne group, forming unwanted side products. Due to this potential sensitivity, other groups were investigated in an attempt to form a suitable complex.

2.3.9 Synthesis of thiolated tppoe (tppoe-SH)

One solution to the potential issue of alkyne sensitivity is the remove it prior to the complexation reaction. This can be achieved by performing the azide-alkyne cycloaddition to add the thiol group to the ligand, rather than employing it as a surface attachment reaction. As a proof of concept azidopropanethiol was synthesised to attach to tppoe. This was synthesised by refluxing chloropropanethiol with sodium azide, whereby the azide and chloro moieties switch.[26] This is only a proof of concept as the propane unit would likely not be long enough to be useful for surface attachment. As there could be a potential steric barrier to binding DNA to a surface, the binding unit would have to be held at a sufficient distance from the surface to prevent such an unfavourable interaction. However if this approach is successful with the propane unit, which is used for ease of synthesis, then a longer ligand could be developed.

The tppoe ligand and azidopropane thiol are stirred in aqueous solution in the presence of copper sulphate and sodium ascorbate to perform the cycloaddition. Whilst the 1,2 product is possible in the absence of copper, in the reaction mixture, the copper complexes to the alkyne and catalyses the reaction, directing it to form only the

1,3 substituted product.[20] The sodium ascorbate acts to keep the copper reduced in the copper (I) state. On completion the reaction was extracted to yield the product as a yellow oil. This indicates the success of the reaction as the added carbon chain will make stacking of molecules into a solid less efficient.
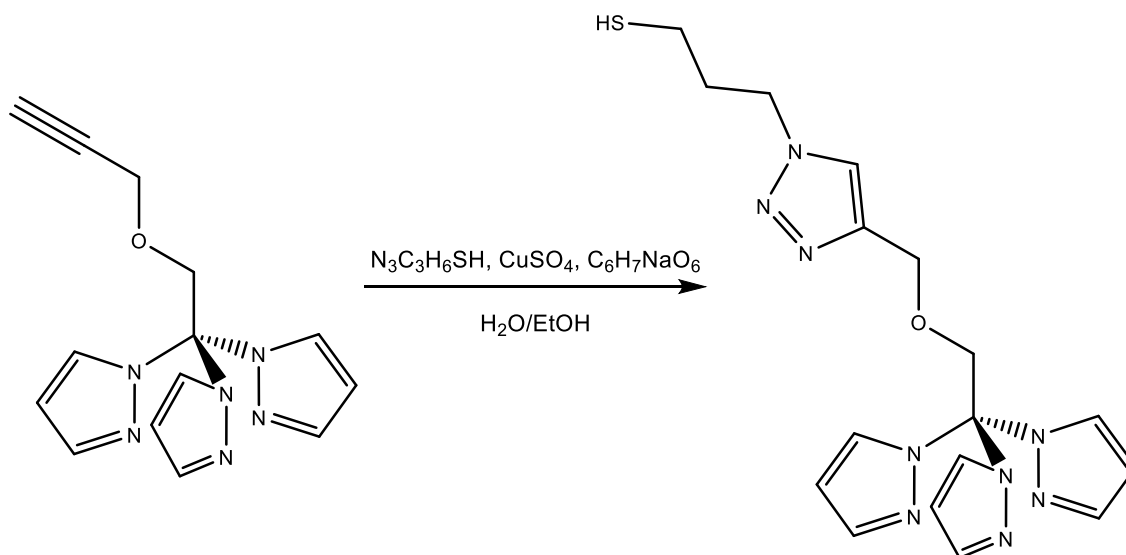
Figure 2.14 - Synthesis of tppoe-SH

2.3.10 Synthesis of bi-functional tppoe (bis-tppoe)

The alkyne unit was also removed by alkyne-azide cycloaddition and the formation of a bi-functional alkyl-azide compound. This is a molecule of interest, partly as a proof of concept, to test if the removal of the alkyne leads to successful complexation with ruthenium, but also in its own right as a linker ligand for "DNA staples". It also does not contain the thiol group present in the previous ligand that might be incompatible with a complexation reaction. DNA staple molecules are of interest based on previous work in the Thomas group[27] and may have interesting intra and inter-strand interactions with DNA.

In this instance dibromopentane was refluxed with sodium azide to form diazidopentane. Then the azide-alkyne cycloaddition was performed as with the thiolated tppoe ligand. Due to difficulties purifying and drying the diazidopentane the ratio of diazidopentane to tppoe was not precise. Initially, this led to inefficient synthesis, with some half substituted molecules formed with a pendant azide. Adjusting the ratio so that the tppoe was in excess, allowed for a fully substituted molecule to be formed as a brown oil after purification by column chromatography.
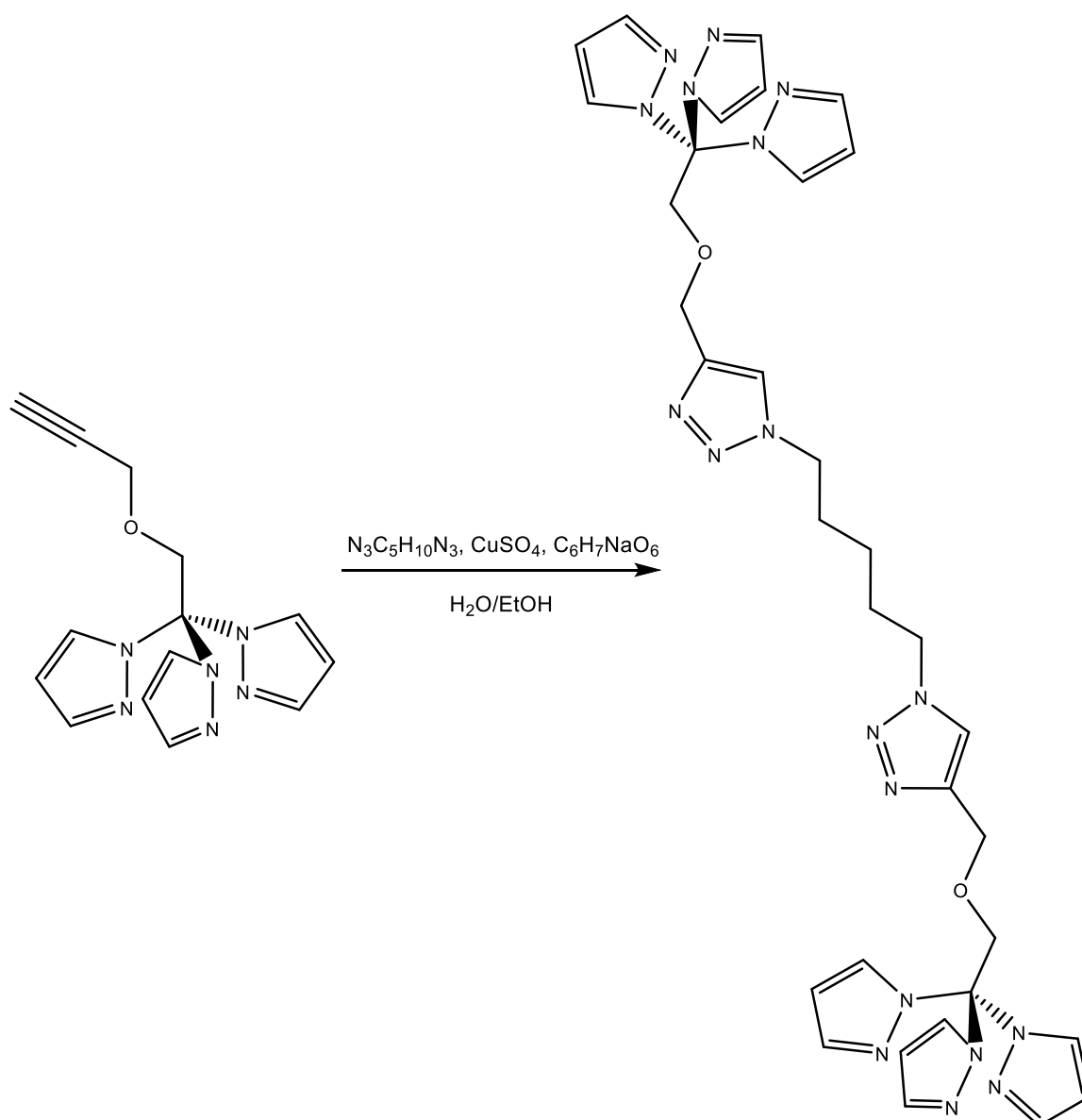
Figure 2.15 - Synthesis of bis-tppoe

2.3.11 Synthesis of tris(pyrazolyl)ethyl iodobenzoate (tpeib)

The alkyne present in the tppoe ligand has also been reacted with aryl halides in a Sonogashira cross-coupling reaction.[18,19] This is a potential alternative to the azide-alkyne cycloaddition initially planned, using an azide functional surface and alkyne functional complex. The moieties in both cases can be switched, so that the alkyne is on the surface rather than the complex. The tpeib ligand is designed to place an iodo-benzyl group on the tpm base to facilitate cross coupling with an alkyne.

Analogous to the synthesis of tppoe, tpe is initially deprotonated with sodium hydride in anhydrous THF. To this solution, the 4-iodobenzoyl chloride was added which lead to an esterification reaction, eliminating the chlorine atom and forming an ester linkage between the aryl halide and the tpm base. The extract was purified by column chromatography to give the product as a white solid.
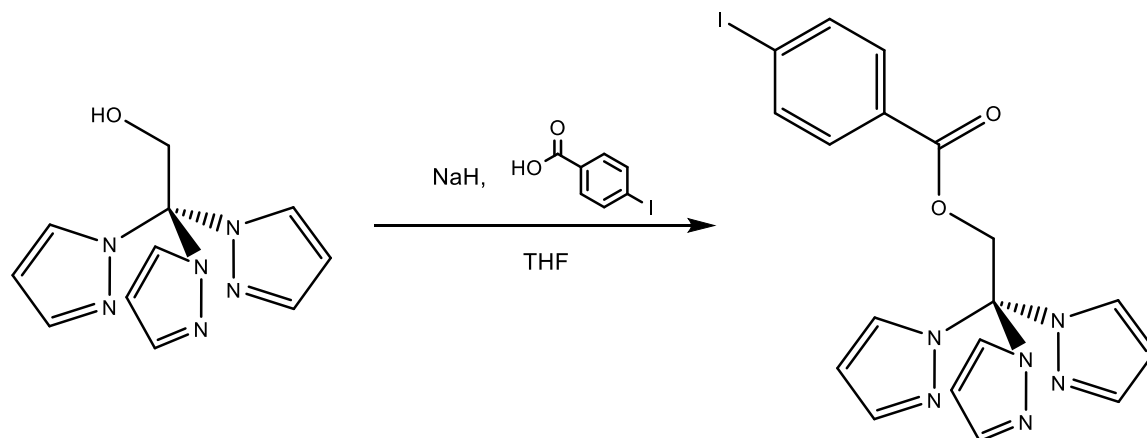
Figure 2.16 - Synthesis of tpeib

2.3.12 Synthesis of tris(pyrazolyl)bromomethylbenzyl oxyethane (tpbmb)

As part of their work into crystal engineering with tpm based molecules, Reger, *et. al.* also synthesised a bi-functional tpm based molecule.[18] This was formed by reaction of two tpe units with the para-functionalised di(bromomethyl)benzene. Based on the ease of switching halide groups for azide groups, this molecule inspired a new design for a potential surface linking ligand. It was realised that by reacting only one side of the di(bromomethyl)benzene with the tpe unit, a molecule could be produced that retained one bromo methyl group that could be further reacted.

This was achieved using the synthesis of Mitsumoto *et. al.*[28], where the dibromomethyl benzene is present in excess. Statistically therefore, in the reaction mixture, the mono-substituted molecule that forms is not likely to contact another tpe molecule to add to the opposite side as it is used up quickly and it is present in relatively low concentration. The product of this reaction was purified by column chromatography to remove the excess unreacted starting material, yielding the product as a yellow oil.
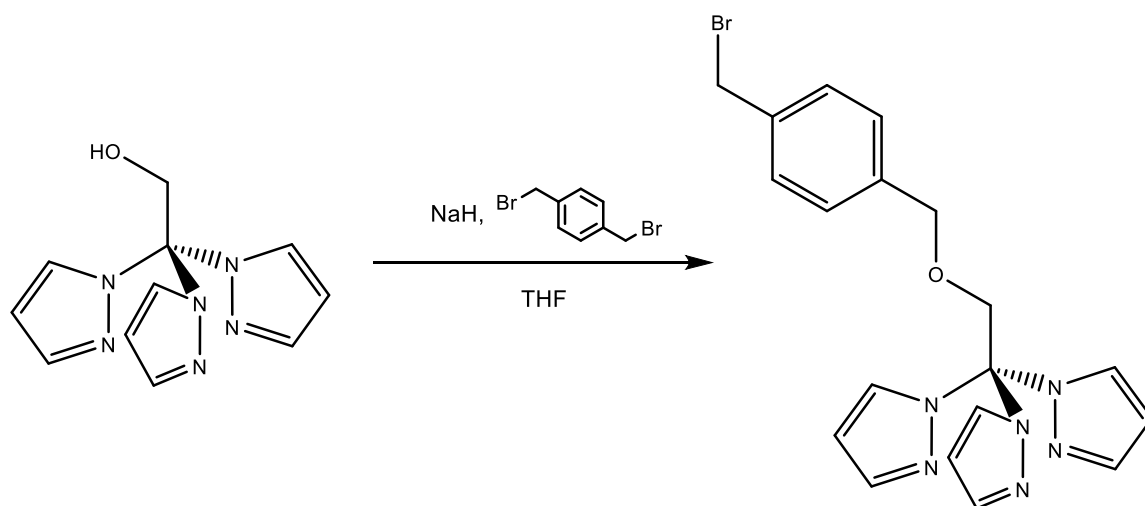
Figure 2.17 - Synthesis of tpbmb

2.3.13 Synthesis of tris(pyrazolyl)azidomethylbenzyl oxyethane (tpazb)

To form a potential link to the surface the bromine is switched for an azide group. This is achieved by reflux with sodium azide, in the same way as was employed for the alkylhalides previously. The azide group is then available for a alkyne-azide cycloaddition with an alkyne functional surface, the reverse of the original design.

The product was isolated as a brown oil. The NMR analysis showed a shift in the protons associated with the methyl group next to the bromine/azide site, due to the change in electronegativity of the moiety.
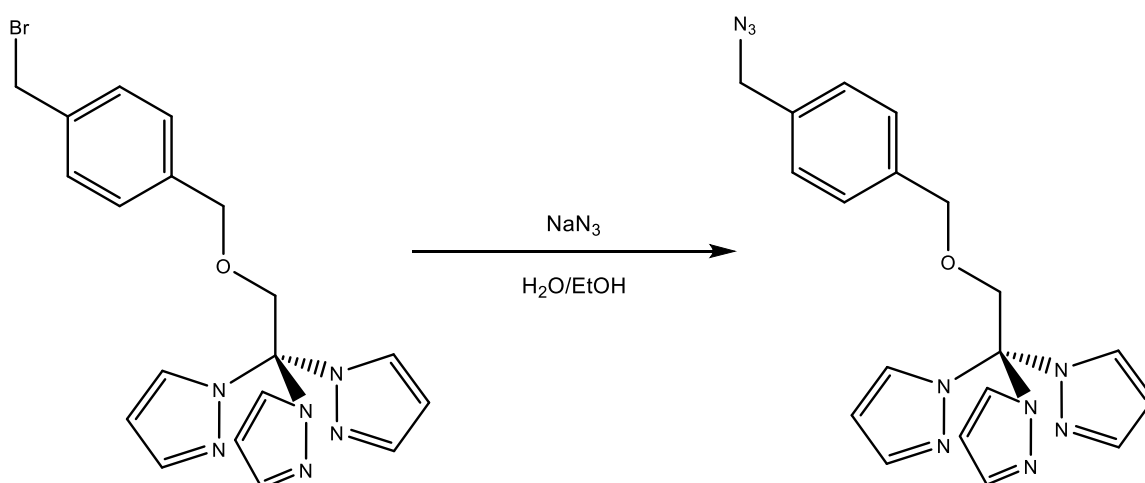
Figure 2.18 - Synthesis of tpazb

2.3.14 Synthesis of tris(pyrazolyl)aminomethylbenzyl oxyethane (tpamb)

As the azide group may be vulnerable to degradation it can be reduced to form the amine instead. As an alternative to the azide-alkyne cycloaddition, initially proposed, this could be used to link to a surface through an amine-aldehyde link. This was achieved by refluxing the tpeazb with PPh_3. The change in substituent is again observed by a shift in the proton NMR spectra due to decrease in electronegativity from azide to amine.
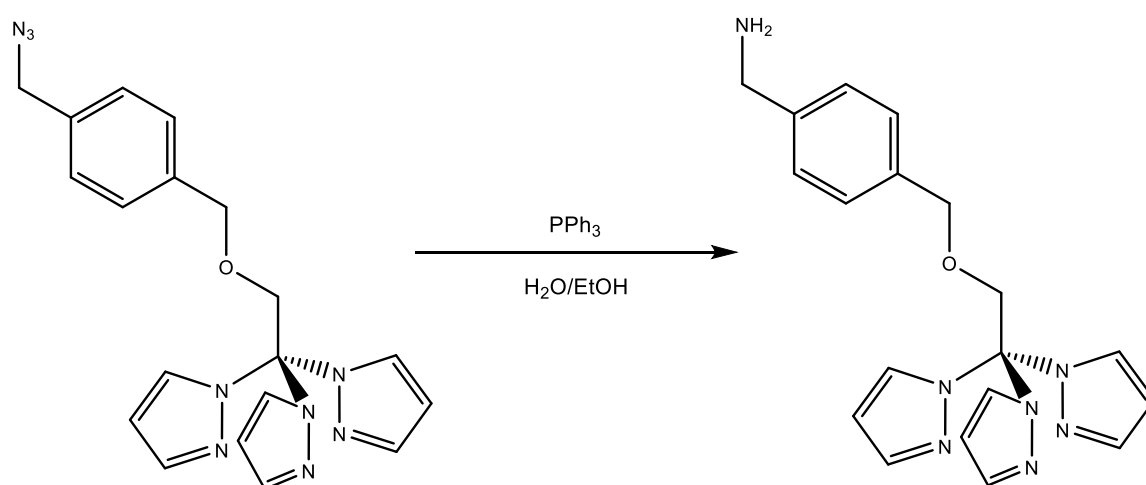
Figure 2.19 - Synthesis of tpamb

2.3.15 Synthesis of [RuCl$_2$(dmso)$_4$]

Due to the failure of attempts at synthesis with $RuCl_3$ an alternative route to synthesis was sought. One possible reason for the failed synthesis could be the oxidation of the ligand on interaction with the ruthenium. To try to counteract this, a new starting material was synthesised by reaction of the $RuCl_3$ with DMSO. The DMSO acts to reduce the ruthenium from the Ru(III) state to Ru(II) and co-ordinates to the metal centre. This may make the ruthenium less oxidising as it has already oxidised d. The complex has also been used previously to co-ordinate to tpm.[29]

Ruthenium chloride is heated in DMSO and propanol to 85 °C and the product precipitates as a yellow solid on cooling the solution. This forms the cis-isomer of the complex, whereby the two chlorine atoms are cis to each other. Lower temperatures

give the trans-isomer as the kinetic product. The identity of the complex was confirmed by IR, where the DMSO stretches were specific to a cis compound.
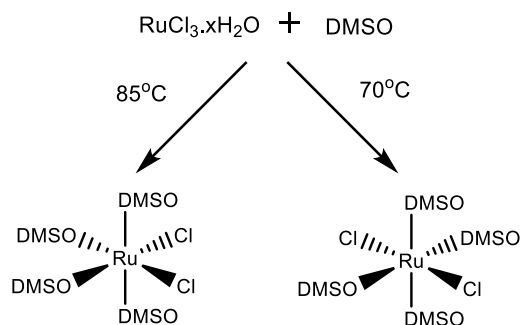
Figure 2.20 - Synthesis of [RuCl$_2$(dmso)$_4$]

2.3.16 Synthesis of complexes using [RuCl$_2$(dmso)$_4$]

The reaction of tpm with [RuCl$_2$(dmso)$_4$] has been reported, producing a facially capped [RuCl$_2$(dmso)(tpm)] precursor for further reaction.[29] Analogous to the reported reaction, the alkyne containing derivative tppoe was refluxed with [RuCl$_2$(dmso)$_4$] in ethanol. The resultant NMR spectrum shows a very complex array of peaks, suggesting multiple products are formed. Mass spectrum analysis showed only one peak with the indicative ruthenium isotope pattern, corresponding to the correct mass, however it related to an insignificantly small proportion of the submitted sample. Attempts to repeat and purify the reaction did not produce the desired compound.

When tpm is reacted with RuCl$_3$ the crude product is still sufficiently pure to function as a precursor for the dppz containing complex. With this in mind the crude product of the [RuCl$_2$(dmso)$_4$] and tppoe reaction was used in an analogous reaction with dppz. Analysis of the crude product gave an NMR that appeared to have both dppz peaks and tpm peaks but none relating to the alkyne section of the ligand. The mass spectrum did not show any mass ions relating to the desired product. Attempts to purify gave an NMR where only the dppz peaks were present, suggesting either the ligand has been removed from the complex or was not co-ordinated in the precursor.

The reaction was also attempted in the alternative solvent, CHCl$_3$, which was used by Iengo *et. al.* with tpm.[29] The isolated product showed NMR peaks relating to pyrazole but again seemed to lack those for the alkyne tail. The mass spectrum shows a peak at 665 mass units which matches to the sandwich complex [Ru(tppoe)$_2$], however it does

not appear to have a ruthenium isotope pattern. There is also a mass ion with the correct isotope pattern at 857 but it is unclear as to what this could be.

The reaction in ethanol was also attempted using the tpeib ligand, however no indication of the formation of the product was seen in the mass spectrum. As each attempt with the alternative precursor, $[RuCl_2(dmso)_4]$ failed, an alternative approach was sought.

2.3.17 Synthesis of $[RuCl_2(dmso)_2(dppz)]$

Due to the failure of previous attempts at synthesis by adding the tripodal ligand first, a new synthetic route was developed. This used the previously reported synthesis of $[RuCl_2(dmso)_2(dppz)]$ as a first step,[30] adding the bidentate ligand prior to the tridentate ligand. It was hoped that, by first occupying some of the co-ordination sites, the interaction between the tridentate ligand and the metal centre may be changed and degradation of the ligand may be averted.

The dppz ligand and $[RuCl_2(dmso)_4]$ complex are refluxed together in toluene. Neither of the reagents are soluble in toluene at room temperature and are only sparingly soluble at the high temperature of the reflux. This maintains both in a very low concentration in the reaction and so prevents multiple additions of the dppz ligand. This would occur in higher concentrations as the dmso ligands are labile so $[RuCl_2(dppz)_2]$ would likely form, similar to when dppz and $RuCl_3$ are reacted. Once formed in solution the $[RuCl_2(dmso)_2(dppz)]$ precipitates as a brown solid. The reaction mixture is filtered hot and then washed with toluene to remove any unreacted starting material. The product is isolated in near quantitative yield.
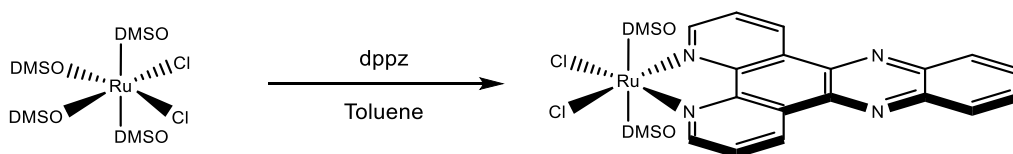
Figure 2.21 - Synthesis of $[RuCl_2(dmso)_2(dppz)]$

2.3.18 Alternative synthesis of $[RuCl(tpm)(dppz)]^+PF_6^-$

To test the suitability of the new approach, the standard tpm complex was synthesised initially using the alternative staring material. $[RuCl_2(dmso)_2(dppz)]$ and tpm were heated to 140°C in ethylene glycol. This forms a deep red solution, to which saturated

KPF$_6$ is added to precipitate the product, which is collected by filtration and then dissolved through the sinter and obtained by rotary evaporation.

The solid was purified by column chromatography with an alumina stationary phase and 1:1 acetonitrile:toluene as eluant. It was observed that the initial purple band usually present from the synthesis of [RuCl(tpm)(dppz)]$^+$PF$_6^-$, was less intense in colour from this route than the usual synthetic route. This band is assumed to be an impurity from the reaction.
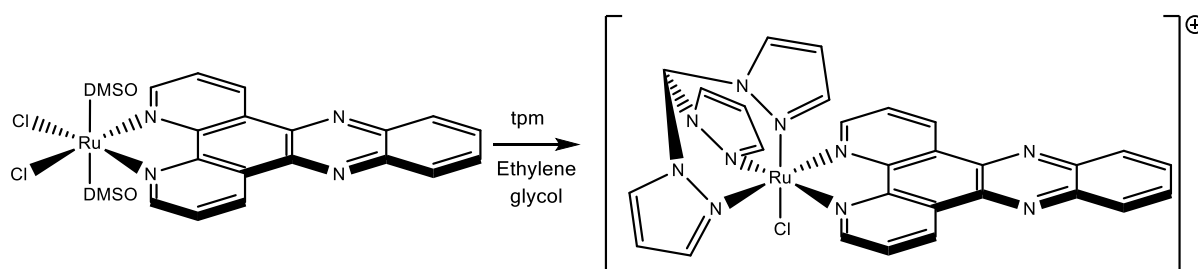
Figure 2.22 - Synthesis of [RuCl(tpm)(dppz)]$^+$PF$_6^-$

The yield achieved from the reaction was also better than the established synthetic route. Figure 2.23 shows the two alternative routes, combining the yields of each step to show the new synthesis is a far more efficient route. As far as the author is aware this procedure has not previously been reported.
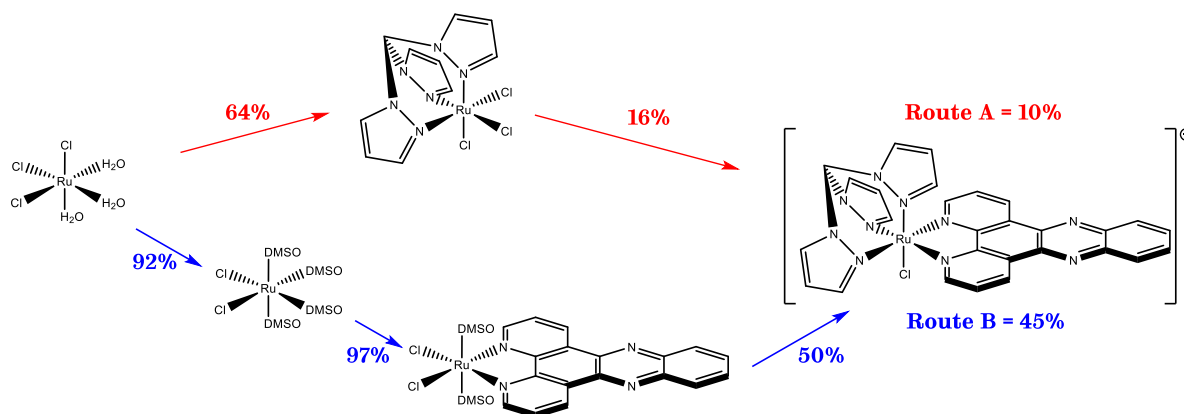
Figure 2.23 – The two alternative routes to [RuCl(tpm)(dppz)]PF$_6$, highlighting difference in reaction efficiency

74

2.3.19 Synthesis of [Ru(tpm)(dppz)(py)]$^{2+}$(PF$_6^-$)$_2$

The full synthesis of the complex was completed, using silver triflate to remove the remaining chloride ligand. This is achieved by reflux with the starting material in 3:1 ethanol:water solvent mix. The reaction is filtered through celite to remove silver chloride. An excess of pyridine is added followed by reflux overnight. The solution is cooled and the product is precipitated with saturated KPF$_6$.
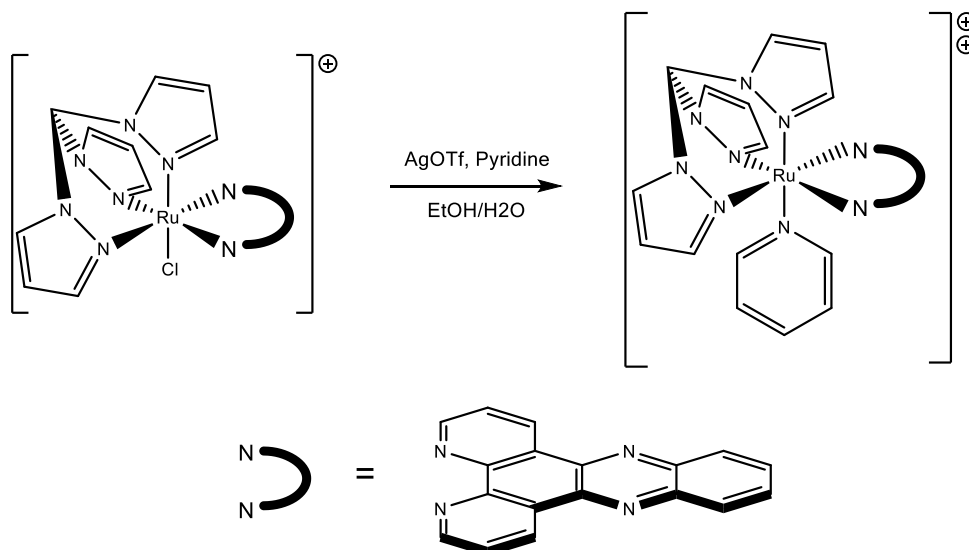
Figure 2.24 - Synthesis of [Ru(tpm)(dppz)(py)]$^{2+}$(PF$_6^-$)$_2$

2.3.20 Synthesis of complexes using [RuCl$_2$(dmso)$_2$(dppz)]

Following the success of the use of [RuCl$_2$(dmso)$_2$(dppz)] as a starting material to synthesise [RuCl(tpm)(dppz)]$^+$, the tpm derived ligands were also tested using the new method. In the same way as for the tpm method, each ligand was heated in ethylene glycol followed by precipitation with saturated KPF$_6$ and column purification on alumina.

The reaction was attempted with tpe, the building block of the originally designed linker ligand. The reaction with tpe yielded a deep red solution as with the reaction of tpm, suggesting a reaction had taken place and the increased solubility suggests a salt has been formed. The precipitated PF$_6$ salt was subjected to the same alumina column procedure as for tpm, however the resultant collected fraction was not pure as in the tpm case and showed multiple unexpected peaks, indicating a mixture of products. LC-

MS analysis indicated a small peak giving the correct mass of 663 but it formed the minor product accompanied by fractions with mass peaks of 633 and 623. The attempts made using tppoe also yielded a similar result, with many products observed in the NMR after purification. LC-MS also showed a similar picture with major component mass ions of 633 and 623 but no peak of 701, relating to the desired complex, was observed.

The reaction was also attempted with the ligands that eliminated the alkyne functionality that was thought to be a problem. As with tpe and tppoe, the reaction itself proceeded as expected giving the colour change to a deep red solution from a brown suspension. In each case, with bis-tppoe, tpeib, tpbmb and tpazb, a similar pattern was observed. The resultant NMR were very complicated with multiple peaks and very similar LC-MS peaks were observed in each case. The two key peaks of 633 and 623 were observed in each example along with a peak at 679. This points to a very similar degradation in each example. The peak at 633 is the same as would be expected for $[RuCl(tpm)(dppz)]^+$ though it is hard to imagine how this may have formed and, while the NMRs appear to contain pyrazole peaks, they do not show the 2:2:2:1:1:1 integration ratio that would suggest the presence of an asymmetric complex of tpm. Two possible degradation products are shown in figure 2.24.

Molecular Weight: 633.11

Molecular Weight: 623.06
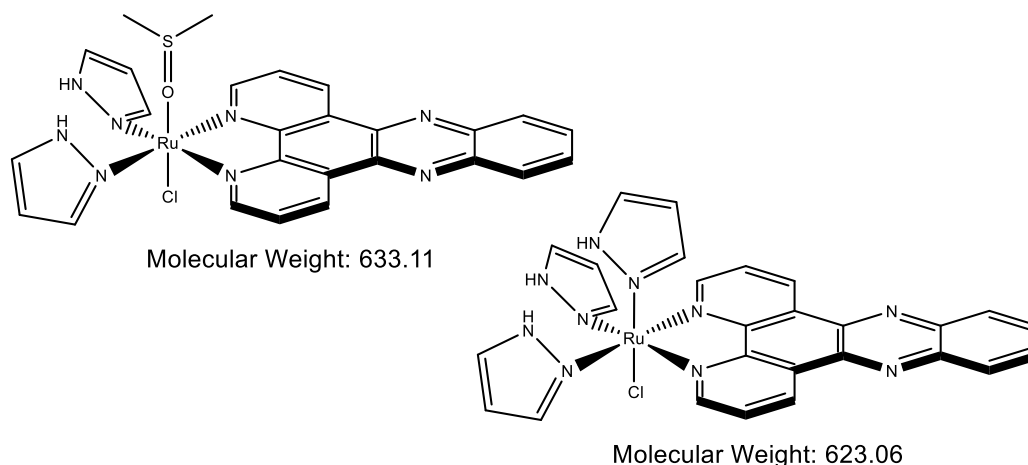
Figure 2.25 - Possible degradation products of tpm-derived ligands when reacted with $[RuCl_2(dmso)_2(dppz)]$ in ethylene glycol

The results of these experiments suggest that the stability issue with the ligand was not the presence of alkyne or other substituent, but rather an instability in the tpm unit itself. It is possible that the functionalising of the tpm makes the molecule more

susceptible to hydrolysis at the point where the pyrazole rings are joined; resulting in free pyrazole rings that can then co-ordinate to the ruthenium centre themselves. This is consistent with the work on [RuCl$_2$(dmso)$_4$] and tpm, where it was reported that in refluxing ethanol the tpm was stable and formed a single complex with the ruthenium centre. However when methanol was used, a more nucleophilic solvent, a degradation product was observed where the tpm had been hydrolysed, leaving single pyrazole rings on the ruthenium centre as shown in figure 2.25.
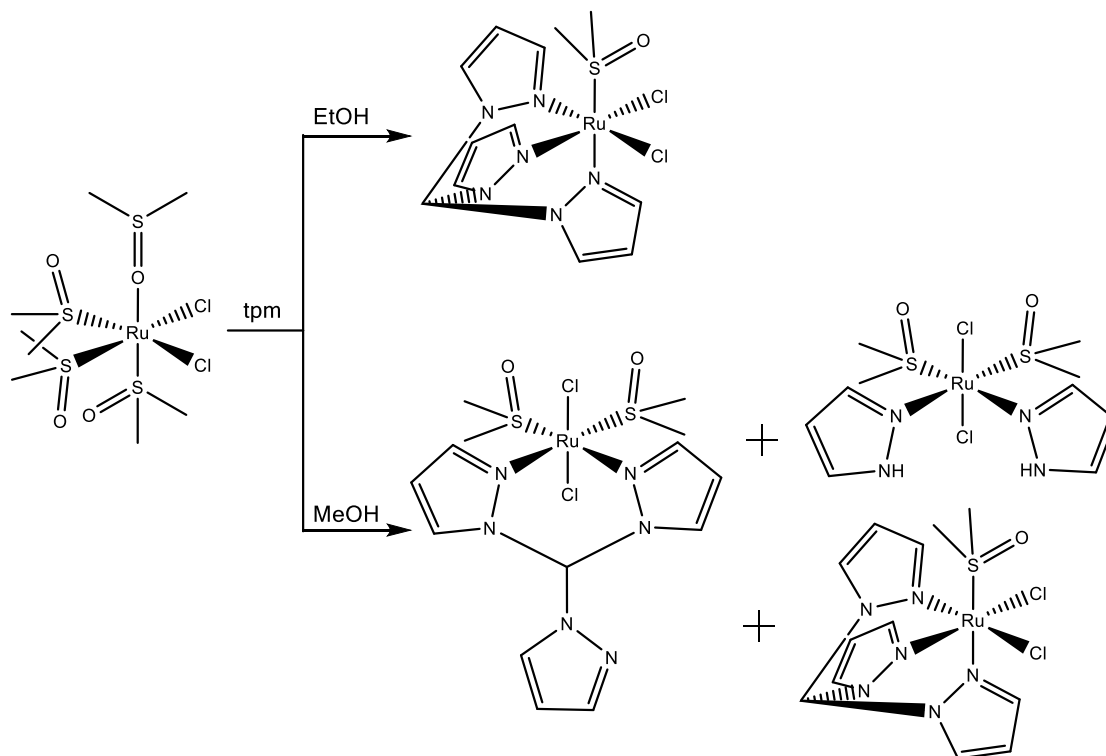
Figure 2.26 - Solvent dependant range of complexes formed from tpm and [RuCl$_2$(dmso)$_4$] as reported by Iengo *et. al.*[29]

It is also observed that, when tpm is functionalised, a shift is observed in its ^{13}C NMR spectrum. The peak relating to the methyl carbon of tpm is observed to shift downfield when the ethanol unit is added to form tpe. This suggests that the carbon is more de-shielded, thus more electron deficient which may make attack from electron rich nucleophiles more favourable. The shift is show in figure 2.26.
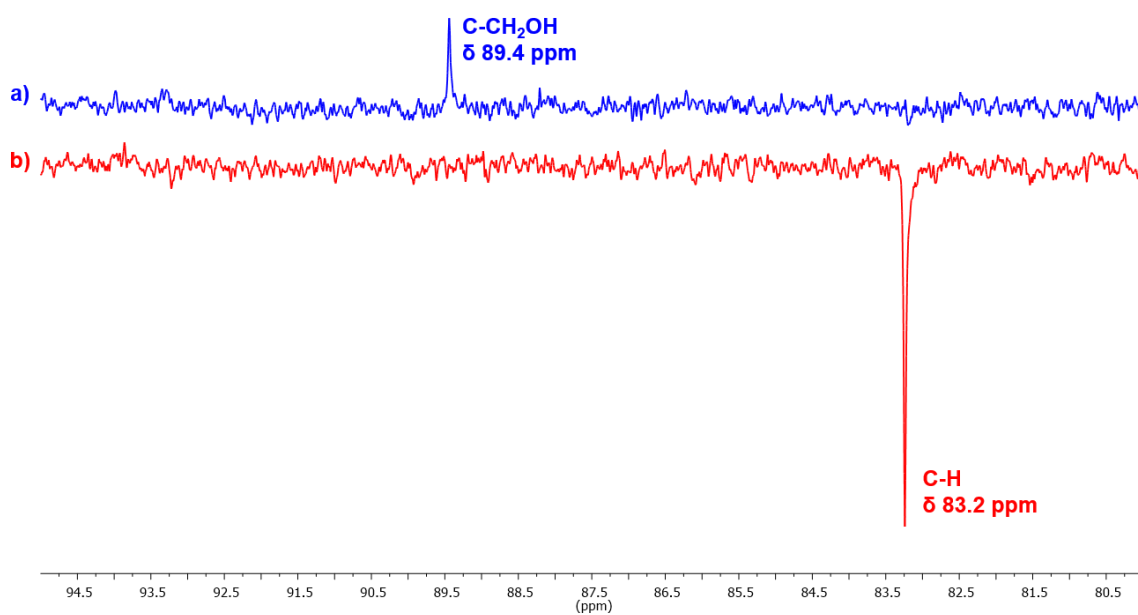
Figure 2.27 - Shift in DEPTQ ^{13}C NMR signal of the methyl carbon of tpm on functionalisation shown in the spectra of a) tpe and b) tpm

2.4 Characterisation of novel tpm derived ligands

2.4.1 ^{1}H NMR of thiolated tppoe

The ^{1}H NMR spectrum (((2,2,2-tri(1H-pyrazol-1-yl)ethoxy)methyl)-1H-1,2,3-triazol-1-yl)propanethiol (tppoe-SH), recorded in deuterated chloroform is shown in figure 2.27 with peaks labelled relating to the lettering on the molecular structure.
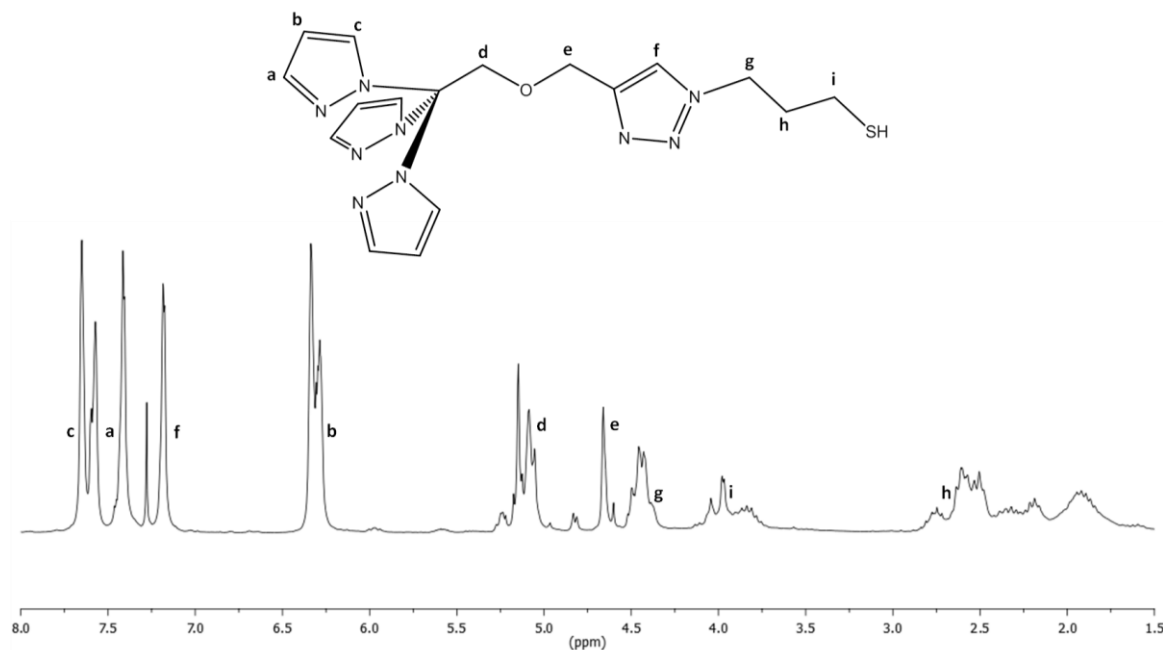
Figure 2.28 - 400 MHz ^{1}H NMR spectrum of tppoe-SH in CDCl$_3$

The NMR of tppoe-SH is poorly resolved, making assignment of the peaks challenging. The assignment is made with the help of the assignment of bis-tppoe below, as the molecules are similar. The peaks relating to the protons of the pyrazole unit (**a,b** and **c**) are distinct from the other peaks in the spectrum as they integrate to three protons, one for each pyrazole ring, while the others are one or two. The most deshielded of these will be **c** as it is closest to the more electronegative nitrogen, close the peak for **a** also next to a nitrogen atom. Proton **b** is the most upfield as it is furthest from the effect of the nitrogens. The peak for proton **f** is distinct as the only peak that integrates to a value of one. It is also the only other peak in the area of the spectrum commonly occupied by aromatic protons, it being on the triazole ring. The protons **d** and **e** are hard to distinguish and are assigned on the basis of similar ppm shift values to that of bis-tppoe described below. This is also the case for the remaining protons. Proton **g** is assigned on the basis it is nearest the triazole ring and so will be most deshielded of

the remaining peaks. Proton **i** is assigned to the next peak as it will also be deshielded by the influence of the thiol group, with the remaining **h** proton assigned to the lowest ppm shift.

2.4.2 ^{1}H NMR of bi-functional tppoe (bis-tppoe)

The ^{1}H NMR spectrum of 1,5-bis(4-((2,2,2-tri(1H-pyrazol-1-yl)ethoxy)methyl)-1H-1,2,3-triazol-1-yl)pentane (bis-tppoe), recorded in deuterated chloroform is shown in figure 2.28 with peaks labelled relating to the lettering on the molecular structure.
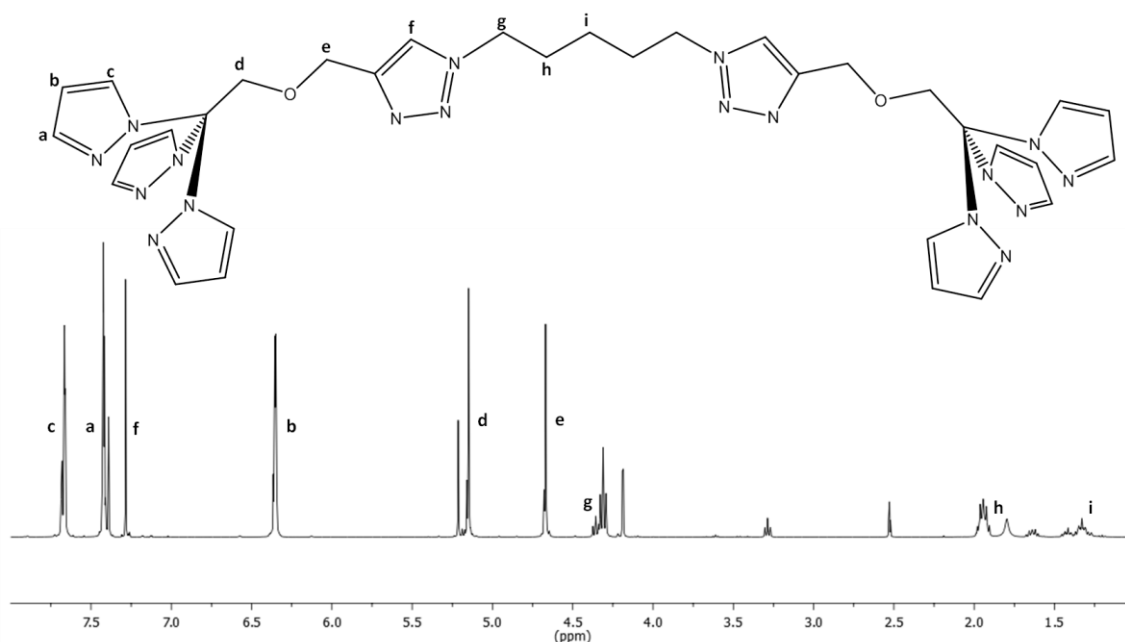
Figure 2.29 - 400 MHz ^{1}H NMR spectrum of bis-tppoe in CDCl$_3$

Protons **a**, **b** and **c** relate to the pyrazole protons on the tpm portion of the molecule and are assigned in the same way as for tppoe-SH. They are distinct as they integrate to six protons where all other peaks integrate to four or two. On this basis, environments **f** and **i** are the only peaks that integrate to two protons and differ in their splitting patterns. Peak **i** is a quintet, indicative of coupling to the four aliphatic protons that split it either side in the molecule. Peak **f** is a singlet, as the protons are isolated from coupling to other protons and also appear downfield in the spectrum owing to their aromatic environment. Of the peaks relating to four protons, **h** is identified as the quintet peak, owing to its coupling to the four protons either side of its position in the molecule. Proton environment **g** is assigned the the position next to **h** as it appears in the spectrum as a triplet, a consequence of it coupling to the two protons of **h,** but with

no further protons to couple to on the opposite side. Protons **d** and **e** are shown as singlet peaks due to electronic isolation from other protons in the molecule. Proton **d** shares a similar shift value as its equivalent in the tpe molecule which does not contain proton **e**. Thus it is assigned as the more downfield peak as it is closer to the significantly electron deficient tpm unit.

2.4.3 ^{1}H NMR of tris(pyrazolyl)ethyl iodobenzoate (tpeib)

The ^{1}H NMR spectrum of 2,2,2-tri(1H-pyrazol-1-yl)ethyl 4-iodobenzoate (tpeib), recorded in deuterated chloroform is shown in figure 2.29 with peaks labelled relating to the lettering on the molecular structure.
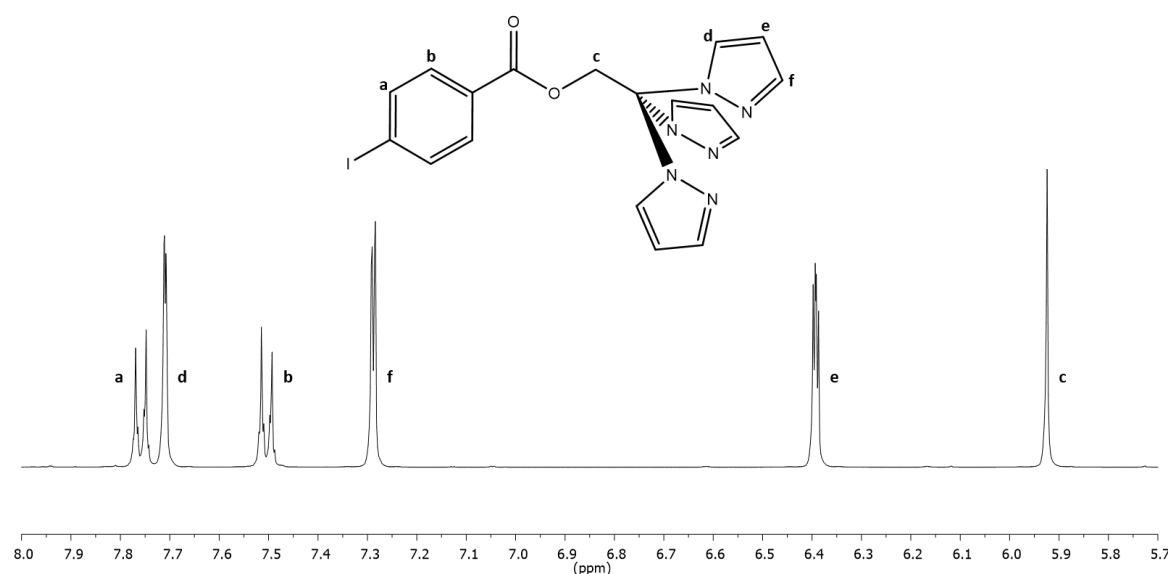
Figure 2.30 - 400 MHz ^{1}H NMR spectrum of tris(pyrazolyl)ethyl iodobenzoate in CDCl$_3$

Protons **a**, **b** and **c** are distinguished from those belonging to the tpm portion (**d**, **e** and **f**) on the basis of different integration values. The three pyrazole rings of the tpm part give each related peak an integration value of three, compared to two for the other proton environments. The ethyl protons of **c** are distinct as they are isolated from other protons in the molecule and therefore exhibit no splitting pattern. They are also the only non-aromatic protons and so relate to the least deshielded peak at lowest ppm shift. The peaks for protons **a** and **b** are distinguished on the basis of the greater electronegativity of the iodine substituent, meaning that protons closest to this

substituent are represented by the peak, **a** at the higher ppm. Assignment of **d, e** and **f** is the same as for previously described tpm based pyrazole environments.

2.4.4 X-ray crystal structure of tris(pyrazolyl)ethyl iodobenzoate (tpeib)

Crystals of tpeib were obtained *via* slow vapour diffusion of diethyl ether into a solution of tpeib in nitromethane. The produced crystals were analysed to obtain the x-ray structures shown below.
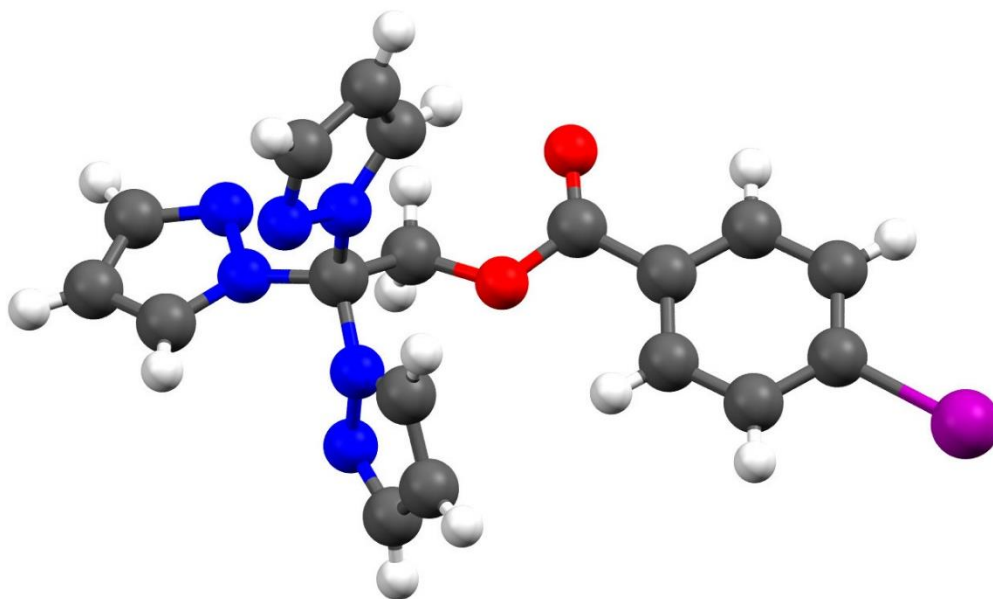
Figure 2.31 - Crystal structure of tris(pyrazolyl)ethyl iodobenzoate (tpeib)

The crystal system shows a triclinic packing structure with the space group P-1.
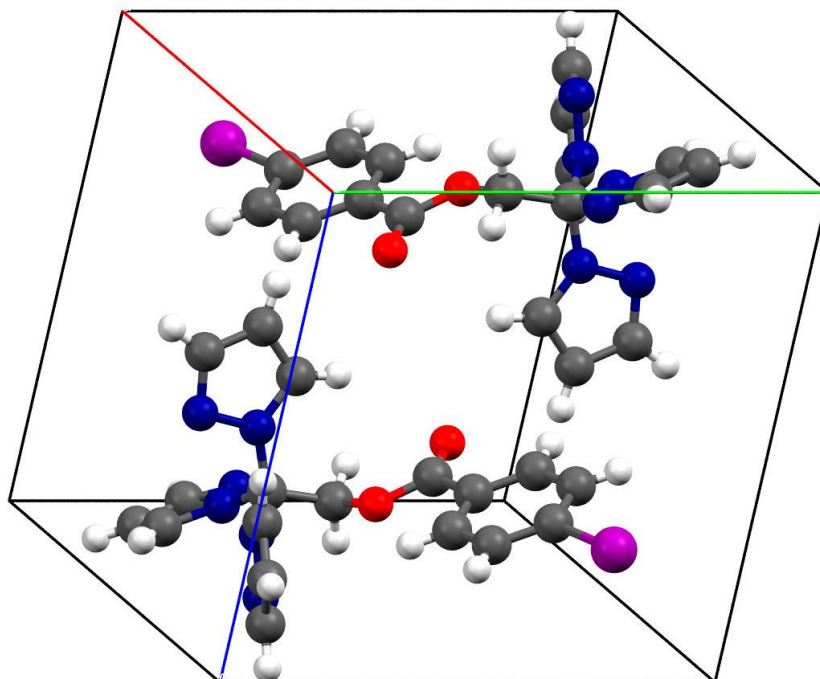
Figure 2.32 - Unit cell packing of the tpeib crystal system

A key feature of the crystal structure, which likely contributes to its stability, is the presence of halogen bonding. As shown in figure 2.32, the iodine substituent on the aromatic ring interacts with the lone pairs on the oxygen of the ester linkage of its neighbouring molecule. This interaction is not present in the similarly structured tpbmb, tpazb and tpamb which did not crystallise and were only obtained as oils.
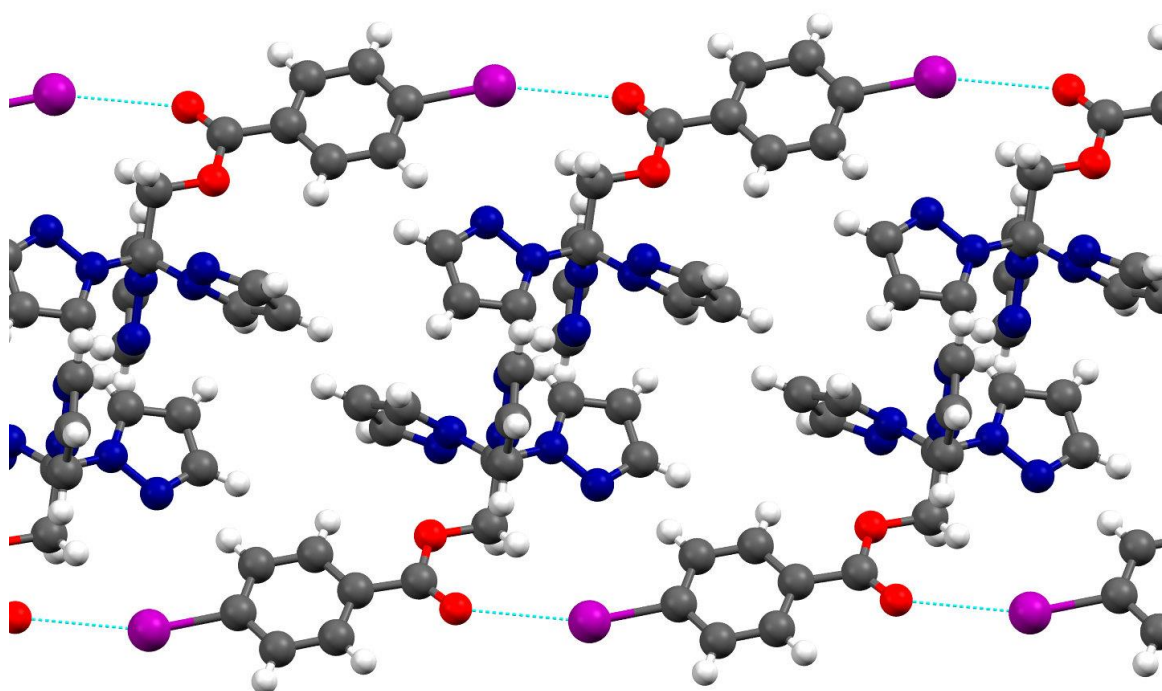
Figure 2.33 - Halogen bonding interactions present in the tpeib crystal system

2.4.5 ^{1}H NMR of tris(pyrazolyl)azidomethylbenzyl oxyethane (tpazb)

The ^{1}H NMR spectrum of tris(1H-pyrazol-1-yl)azidomethylbenzyl oxyethane (tpbmb), recorded in deuterated chloroform is shown in figure 2.33 with peaks labelled relating to the lettering on the molecular structure.
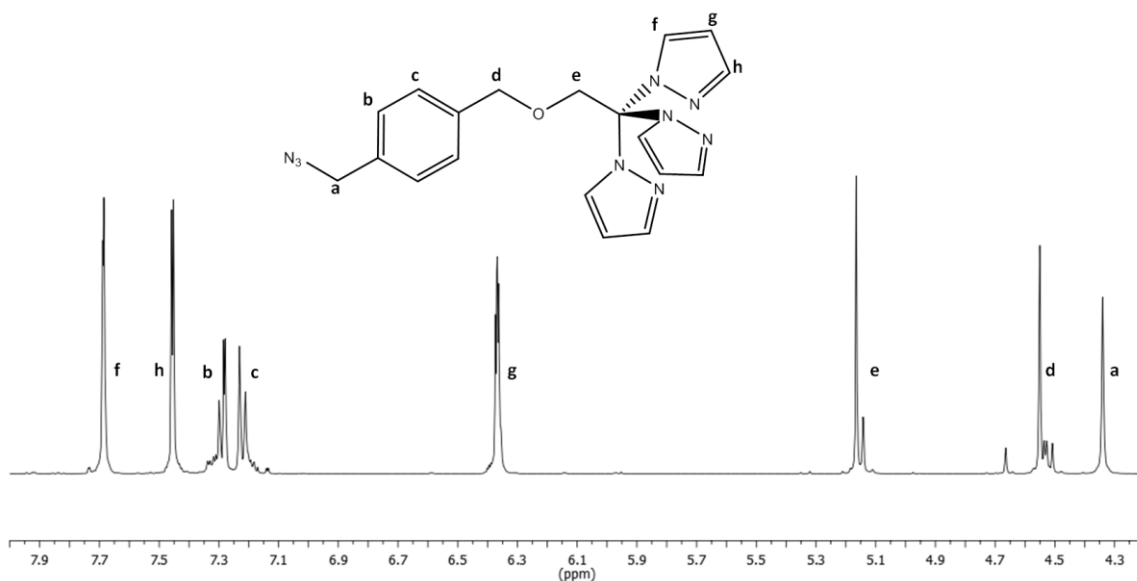
Figure 2.34 - 400 MHz ^{1}H NMR spectrum of tris(pyrazolyl)azidomethylbenzene oxyethane in CDCl$_3$

The assignment of the spectrum for tpazb is broadly similar to that for tpeib with some additional environments. Here, peaks **f**, **g** and **h** have the indicative three proton integration of the tpm unit and are assigned as previously described. Peak **e** is assigned on the basis that it shares its shift value with the same environment present in the starting material, tpe, prior to addition of the benzyl unit. Protons **d** and **a** give singlet signals in the spectrum as they are isolated from coupling to other protons. They are distinguished on the basis of their shift due to a change in substituent from bromine to azide, and then to amine. When the bromine substituent is replaced, it is peak **a** that shifts, so this signal is assumed to be the proton environment closest to the azide. Benzyl protons **b** and **c** can likewise be distinguished: after the bromine is replaced, the **b** peak is shifted furthest and so this signal is assigned to the environment closest to the azide substituent.

2.4.6 ^{1}H NMR tris(pyrazolyl)aminomethylbenzyl oxyethane (tpamb)

The ^{1}H NMR spectrum of tris(1H-pyrazol-1-yl)aminomethylbenzyl oxyethane (tpbmb), recorded in deuterated chloroform is shown in figure 2.34 with peaks labelled relating to the lettering on the molecular structure.
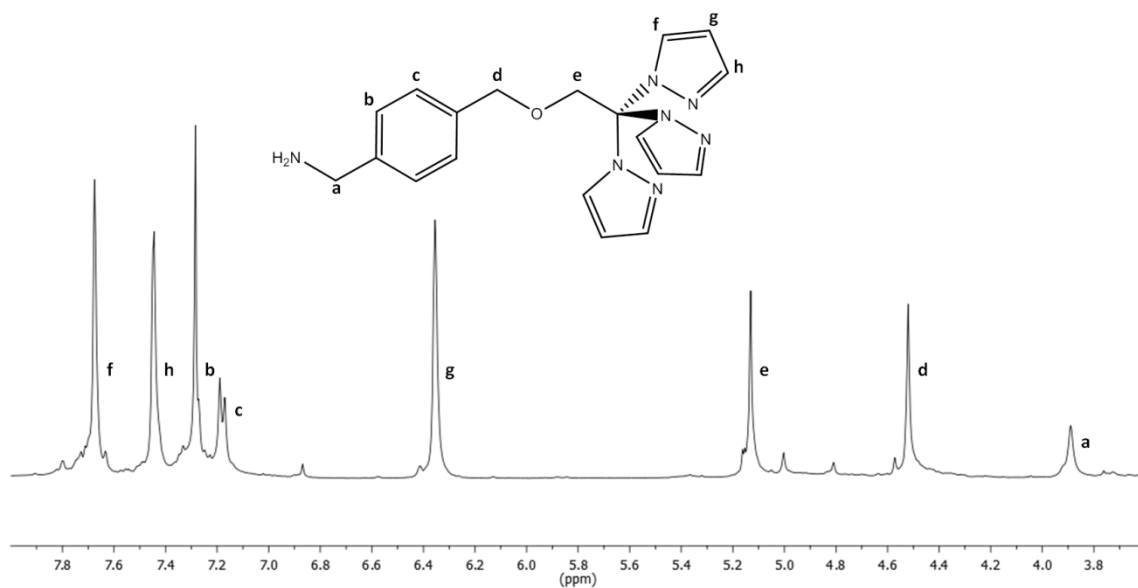
Figure 2.35 - 400 MHz ^{1}H NMR spectrum of tris(pyrazolyl)aminomethylbenzene oxyethane in CDCl$_3$

The spectrum for tpamb is less well resolved but the peaks are clear. There is no change in the number of proton environments from tpazb so the assignment remains similar. Here, there is a further shift in peak **a** from 4.34 ppm in tpazb to 3.89 ppm, owing to the lower electronegativity of the amino substituent. A small upfield shift of 0.04 ppm in peak **c** is also observed but peak **b** is obscured by the solvent peak related to CHCl$_3$.

2.5 Alternative complex design and synthesis

Due to the failed attempts at adding function to the complex through the tpm ligand, an alternative strategy was devised to attach a linker though the pyridine site. This is inherently less stable as it is only monodentate. This means that, potentially, it could be replaced by a competing ligand, whereas the chelate effect makes this tridentate ligands immune to this mechanism. In addition the use of the pyridine position may sterically impede the DNA intercalation, by obstructing the insertion of the complex into the double helix. This could weaken the binding of the π systems of the dppz and the DNA base pairs and thus weaken the overall interaction. This effect has been investigated with smaller substituents previously, with the position of the substituent on the pyridine ring shown to modulate binding strength.[17]

Whilst not ideal for the assembly of a sensor device it would still work as an interesting proof of concept to study how DNA interacts with an intercalator at a surface.

2.5.1 Synthesis of mercapto(pyridinylmethyl)undecanamide (py-SH)

The linker design was based on the previous work linking amino-phenanthroline to nanoparticles.[31] Mercapto-undecanoic acid was stirred with 1-hydroxybenzotriazole hydrate (HOBt) and N,N'-Dicyclohexylcarbodiimide (DCC) in dry DCM to form a reactive intermediate. 3-picolylamine was added to the solution, forming the amide link.
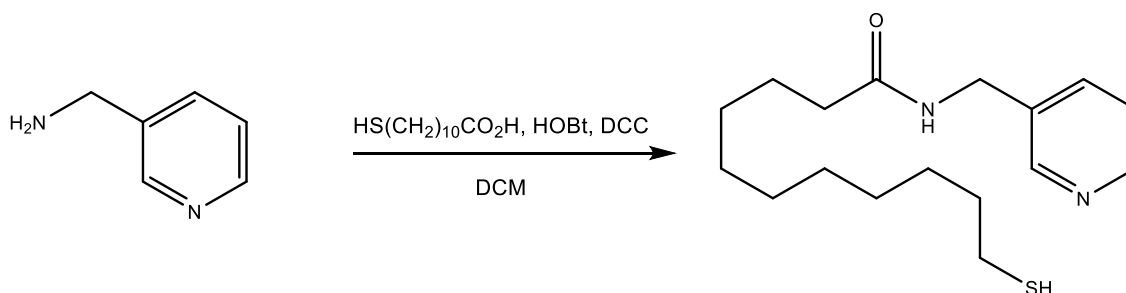
Figure 2.36 - Synthesis of py-SH

One possible issue with the applicability of this linker to the aim of the project is that it is synthetically more challenging to alter its length. As the distance of luminophores from a surface plasmon is known to have an effect on the enhancement of

luminescence[32] it would be useful to easily change this and test different distances. In this case the thiol-acid unit used is the longest that is commercially available and if a longer unit was desired then further synthetic design would be required. Attempts were made to perform this reaction after the picolylamine was co-ordinated to the Ru complex but they proved unsuccessful. This approach is therefore potentially less versatile than the previously proposed alkyne-azide click reaction approach as it may not work on the surface.

2.5.2 Synthesis of $[Ru(tpm)(dppz)(py\text{-}SH)]^{2+}(PF_6^-)_2$

To co-ordinate the newly synthesised thiol linked pyridine ligand the same procedure is followed as for the synthesis of $[Ru(tpm)(dppz)(py)]^{2+}(PF_6^-)_2$. Firstly, the last remaining chloride is abstracted from $[RuCl(tpm)(dppz)]^+PF_6^-$ using silver triflate, refluxing in a 3:1 ethanol:water solvent mix. The resultant solution is then filtered through celite to remove the precipitated AgCl. A five fold excess of the thiol linked pyridine ligand is added to the solution and heated to reflux. The product is precipitated using saturated KPF_6 and purified by preparative HPLC, to separate the formed complex from residual ligand.
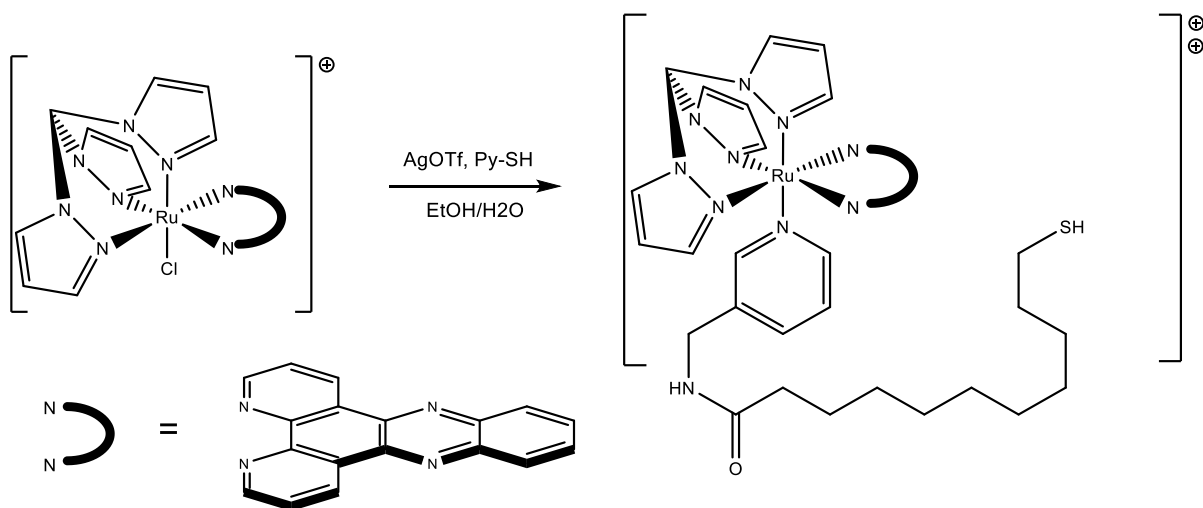
Figure 2.37 - Synthesis of $[Ru(tpm)(dppz)(py\text{-}SH)]^{2+}(PF_6^-)_2$

This molecule has the potential to both bind to DNA, through the dppz ligand, and to a surface through the thiol moiety. Pure complex was obtained however in very small quantity, in the order of milligrams. The complex was assessed for its photophysical properties however insufficient quantities could be produced for surface attachment. Attempts to scale up the reaction were limited by purification. The preparative HPLC approach results in significant loss of compound and is impractically time consuming

for the production of more than ten milligrams, short of the hundred required for further work. Attempts to purify the complex by standard column chromatography also led to loss of compound and a lack of separation with the excess ligand. In each attempt the ligand seemed to co-elute with the complex, such that suitably pure product was not obtained. Given these difficulties and the issues with the design, the complex was abandoned in favour of a new design.

2.6 Characterisation of alternative complex

2.6.1 ^{1}H NMR of mercapto(pyridinylmethyl)undecanamide (py-SH)

The ^{1}H NMR spectrum of mercapto(pyridinylmethyl)undecanamide (py-SH), recorded in deuterated methanol is shown in figure 2.37 with peaks labelled relating to the lettering on the molecular structure.
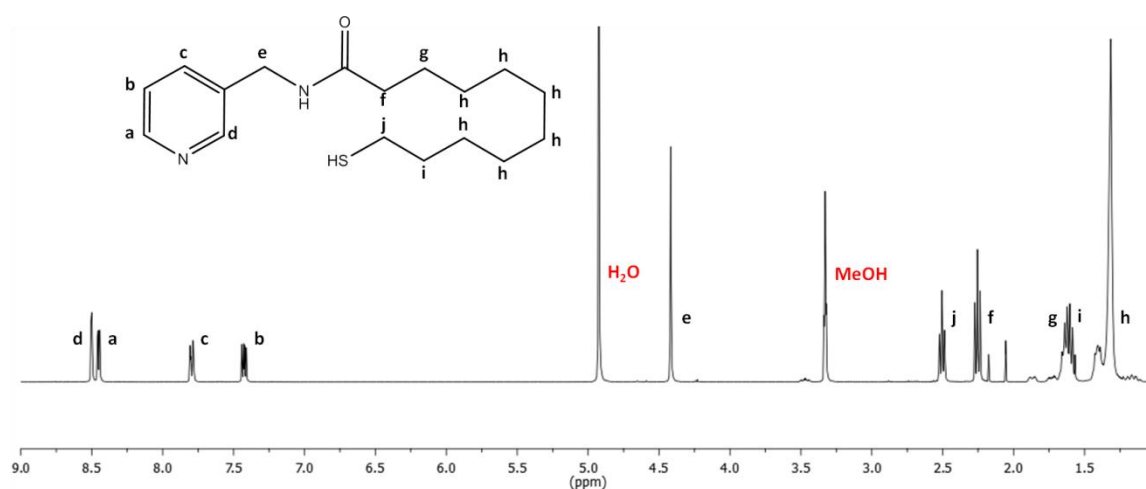
Figure 2.38 - 400 MHz ^{1}H NMR of mercapto(pyridinylmethyl)undecanamide   (py-SH) in MeOD

The NMR spectrum of py-SH exhibits peaks in the aromatic region between 7 and 9 ppm and the aliphatic region, between 4.5 and 1 ppm. The aromatic peaks relate to the aromatic protons of the pyridine ring. The pyridine is not symmetric, owing to the substitution of the 2-position. This results in four distinct proton environments, each equivalent to one proton. The presence of an electron deficient nitrogen atom

will deshield the nearest protons, moving their respective peaks to a higher ppm value. Thus, the peaks with the highest ppm values, **a** and **d,** are assigned to the protons next to the nitrogen. They are distinguished from each other by coupling values. Proton **d** is isolated from the other protons in the ring, having none in its para positions. This leads to a doublet of doublets with small coupling values of J = 2.1 Hz and 0.6 Hz. Proton **a** is para to proton **b** giving stronger coupling in a doublet of doublets with J = 4.9 Hz and 1.6 Hz. Protons **c** and **b** display ddd coupling and are assigned on the basis of ring currents. The inductive effect of the nitrogen atom will be directed to the para and ortho positions, meaning proton **c** will be more deshielded than proton **b**.

Each of the aliphatic signals relate to two protons in the molecular structure. Peak **e** is the only distinct singlet, suggesting no coupling to other protons. This is assigned to the protons between the amide and pyridine ring, where there are no protons for it to couple to. The two triplet peaks are assigned to the protons next to functional groups as they have only two protons on one side to couple to, giving the triplet pattern. Protons **f** and **j** are distinguished by the observation that in some fractions of the product, **j** appears as two peaks. This is thought to be due to the formation of dimer molecules, containing sulfide bridges. This is shown in figure 2.38, with **j** relating to protons next to a thiol and **j*** relating to protons next to a disulfide bond. These dimers are symmetrical so they do not affect the other proton environments, however the protons closest to the thiol are shifted due to the greater elecrtonegativity of a sulfide bridge compared to a thiol group. The split peaks still integrate to two protons when compared to peak **f** which would not be likely if the peak was an impurity.
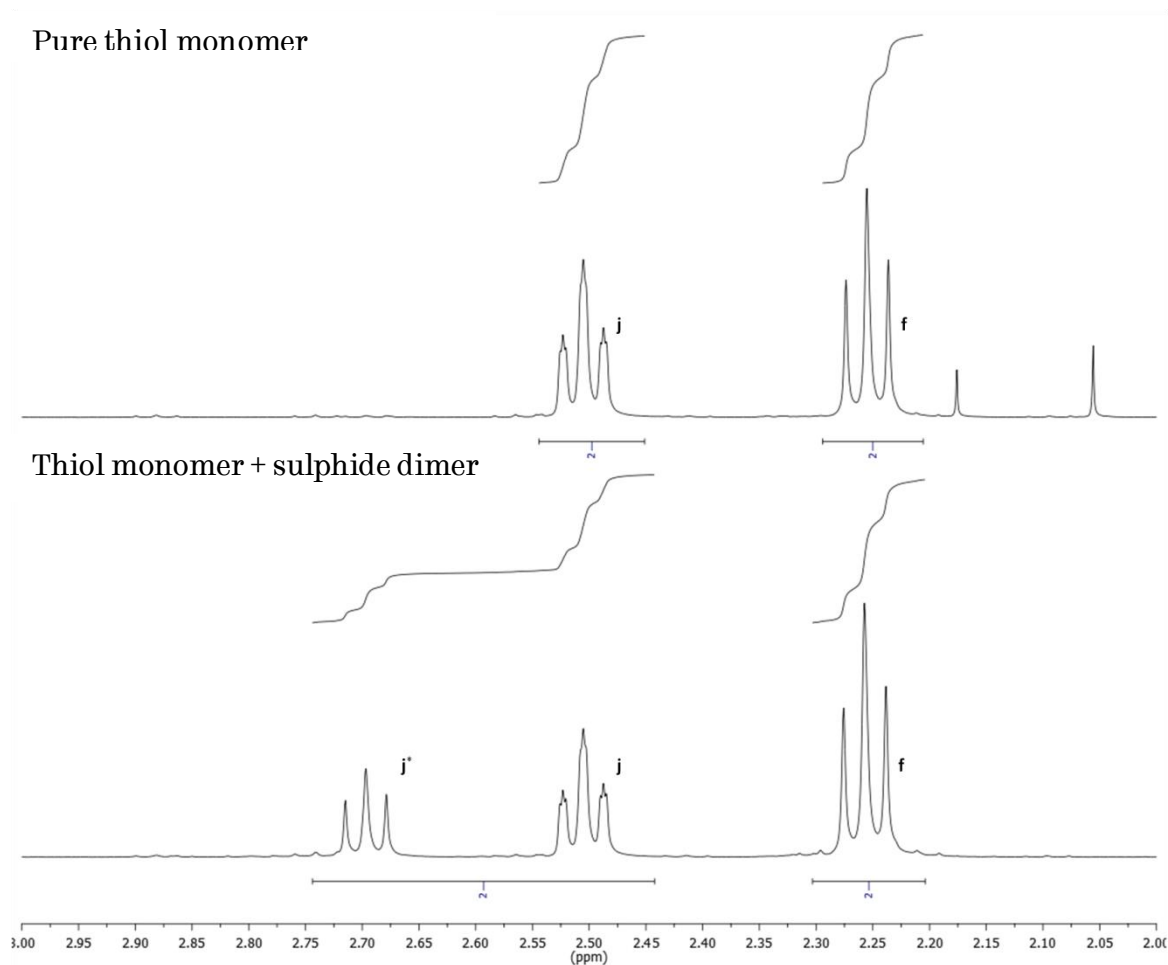
Figure 2.39 - Stacked ^{1}H NMR spectra showing the splitting of the peak closest to thiol group on sulfide formation

The remaining peaks consist of a mixed multiplet peak with an integration of 4 and a large broad singlet peak with an integration of 12. The protons **g** and **i** are closest to functional groups and so will be more deshielded and are assigned to the multiplet. The remaining broad singlet relates to the protons of the alkyl chain, **h**.

2.6.2 ^{1}H NMR of [Ru(tpm)(dppz)(py-SH)]$^{2+}$(PF$_6^-$)$_2$

The aromatic region of the ^{1}H NMR spectrum of [Ru(tpm)(dppz)(py-SH)]$^{2+}$(PF$_6^-$)$_2$, recorded in deuterated methanol is shown in figure 2.39 with peaks labelled relating to the lettering on the molecular structure. The lettering is colour coded to the different ligands for clarity.
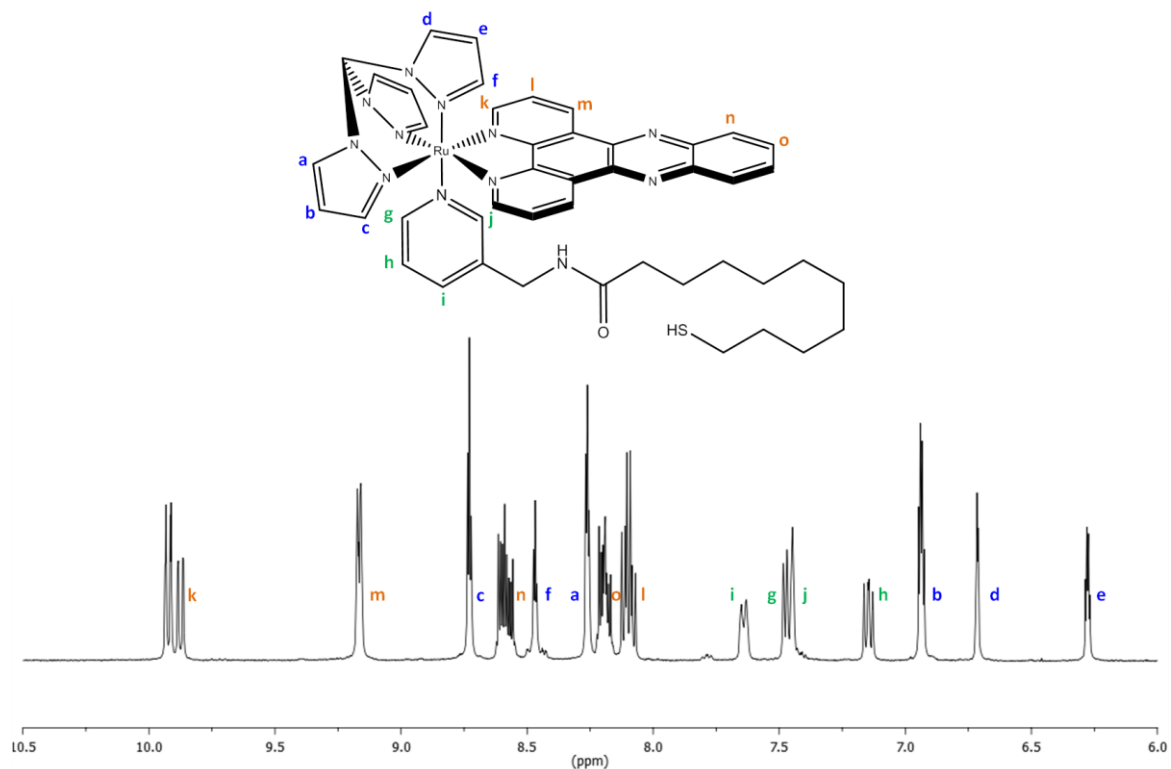
Figure 2.40 - Aromatic region of the 400 MHz ^{1}H NMR of
[Ru(tpm)(dppz)(py-SH)]$^{2+}$(PF$_6$)$_2$ in MeOD

The assignment of the NMR of [Ru(tpm)(dppz)(py-SH)]$^{2+}$ is aided by the assignment of similar tpm based complexes.[33] On co-ordination to a ruthenium centre the tpm unit is split by the plane of symmetry of the molecule and so its protons are no longer equivalent. This enables the protons of the axial pyrazole to be assigned on the basis that they integrate to one proton per environment. Proton **f** is assigned to the most deshielded peak due to its presence next to the most electronegative nitrogen. Proton **d** is then closest to the less electronegative nitrogen and the least deshielded peak is assigned to proton **e**. The protons of the equatorial tpm pyrazole rings are assigned to the only remaining peaks that exhibit triplet splitting, as they couple to the two other protons of the pyrazole ring. In the same fashion as the axial ring, **c** is most deshielded due to proximity to co-ordinated nitrogen, **a** is close to the other nitrogen and **b** is most shielded of the peaks.

The peaks relating to the pyridine ligand all exhibit the same splitting pattern as observed for the un-coordinated ligand. The peaks are all shifted upfield on co-ordination to ruthenium and switch positions relative to one another. The peak for proton **i** becomes the most deshielded, exhibiting doublet splitting due to its single

neighbouring proton. Protons **j** and **g** are close in ppm shift owing to their proximity to the co-ordinated nitrogen, which **j** distinguished by its singlet coupling. This leaves **h** as the remaining peak, with dd coupling due to non-equivalent neighbour protons.

The peaks relating to the dppz unit each integrate to two protons. They are distinguished based on their proximity to nitrogen atoms and their splitting pattern. Protons **k** and **m** are doublets due to coupling to **l** and are assigned on the basis that **k** is more deshielded being closer to the nitrogen. It is not clear why **k** appears to have been split into two peaks, whilst the integration value remains correct. It could be due to the affect of the sulphide dimer formation, but it is odd that this proton would be affected more than others. Protons **n** and **o** have more complicated splitting due to magnetic non-equivalence. They are also assigned on the basis that **n** is closer to nitrogen. The remaining peak is proton **l**.

The aliphatic region of the ^{1}H NMR spectrum of [Ru(tpm)(dppz)(py-SH)]$^{2+}$(PF$_6^-$)$_2$, recorded in deuterated methanol is shown in figure 2.40 with peaks labelled relating to the lettering on the molecular structure.
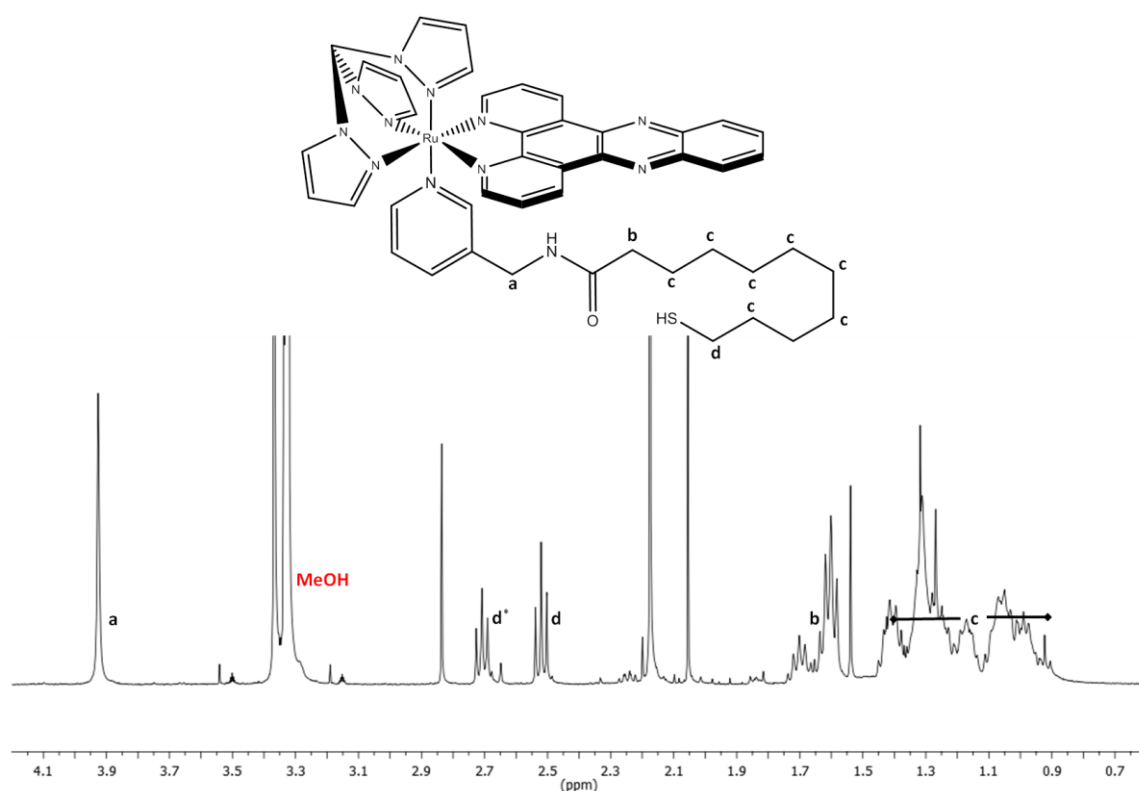
Figure 2.41 - Aliphatic region of the 400 MHz ^{1}H NMR of
[Ru(tpm)(dppz)(py-SH)]$^{2+}$(PF$_6^-$)$_2$ in MeOD

As with the protons on the pyridine, some proton signals in the ligand tail have been shielded by co-ordinating to the ruthenium centre. The singlet of proton **a** is the only proton without neighbours to couple to. Proton **d** is assigned on the basis that it also exhibits two peaks due to the formation of a sulphide dimer, as described for the ligand. Proton **b** is assigned to the only distinguishable triplet remaining in the aliphatic region. It is not possible to further assign protons relating to **c** as the signals are not sufficiently resolved.

2.6.3 UV/Vis spectrum of $[Ru(tpm)(dppz)(py\text{-}SH)]^{2+}(PF_6^-)_2$

The UV-visible absorption spectrum for $[Ru(tpm)(dppz)(py\text{-}SH)](PF_6)_2$ is shown in figure 2.41. The key peaks are summarised in table 2.1, alongside the assignment of each to a transition in the complex.
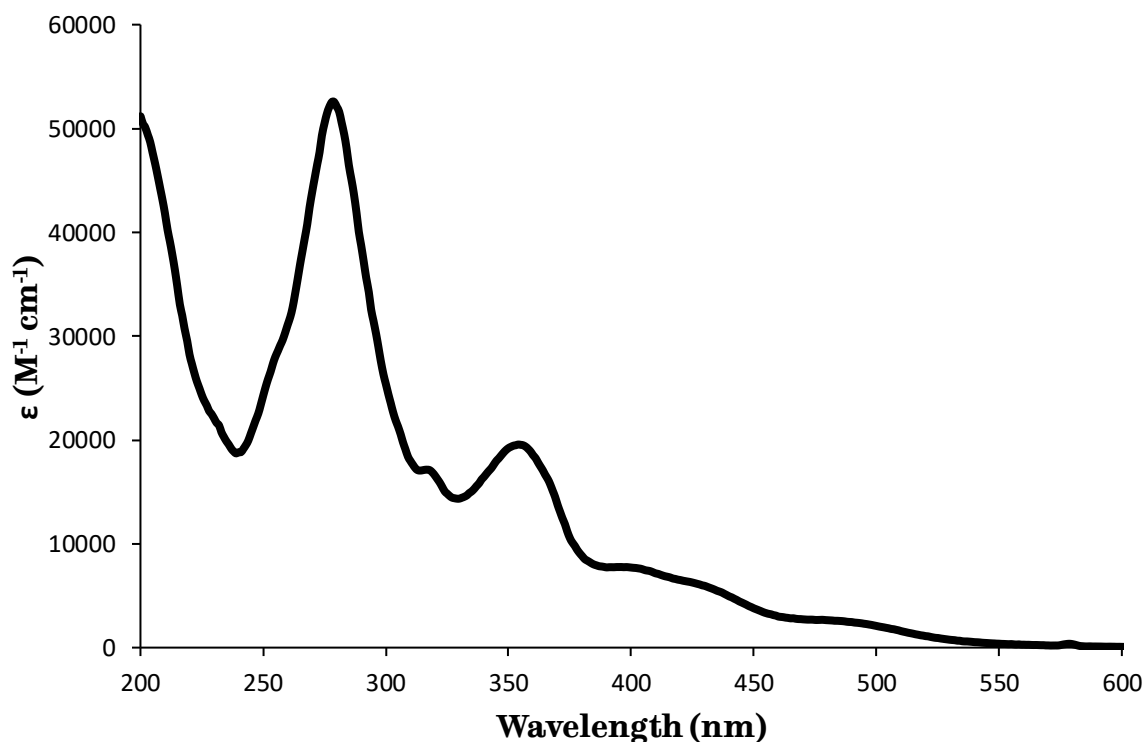
Figure 2.42 - UV-visible spectra of $[Ru(tpm)(dppz)(py\text{-}SH)]^{2+}$ in acetonitrile solution

λ_{max} (nm)	ε_{max} (M^{-1} cm^{-1})	Assignment
258 (sh)	29607	$\pi - \pi^*$
280	52064	$\pi - \pi^*$
318	17086	$\pi - \pi^*$
354	19557	$\pi - \pi^*$
396	7760	MLCT
426 (sh)	6207	MLCT
478 (sh)	2676	MLCT

Table 2.1 - Summary of UV-Visible data for [Ru(tpm)(dppz)(py-SH)](PF$_6$)$_2$ in acetonitrile. (sh = shoulder)

[Ru(tpm)(dppz)(py-SH)](PF$_6$)$_2$ predictably displays very similar photophysical properties to the parent compound Ru(tpm)(dppz)(py)](PF$_6$)$_2$.[16] The high energy bands from 250 nm to 300 nm are typical of ruthenium polypyridyl complexes and assigned to $\pi - \pi^*$ transitions of the N-donor ligands. The dppz ligand alone exhibits absorption bands at 367 and 379 nm in DCM,[34] and bands from 340 nm to 379 nm in DMF,[35] assigned to $\pi - \pi^*$ transitions of the dppz ligand. Thus the band at 354 nm is assigned to the $\pi - \pi^*$(dppz) transition, as for the parent compound.[16] The complex also exhibits an MLCT band with a maxima at 396 and shoulders at 426 and 478 nm in the region typical for such bands to be observed, and of similar energy to the parent compound that displays such bands at 398 and 484 nm.[16]

2.6.4 Luminescent emission spectrum of [Ru(tpm)(dppz)(py-SH)]$^{2+}$(PF$_6^-$)$_2$

The emission spectrum for [Ru(tpm)(dppz)(py-SH)](PF$_6$)$_2$ is shown in figure 2.42.
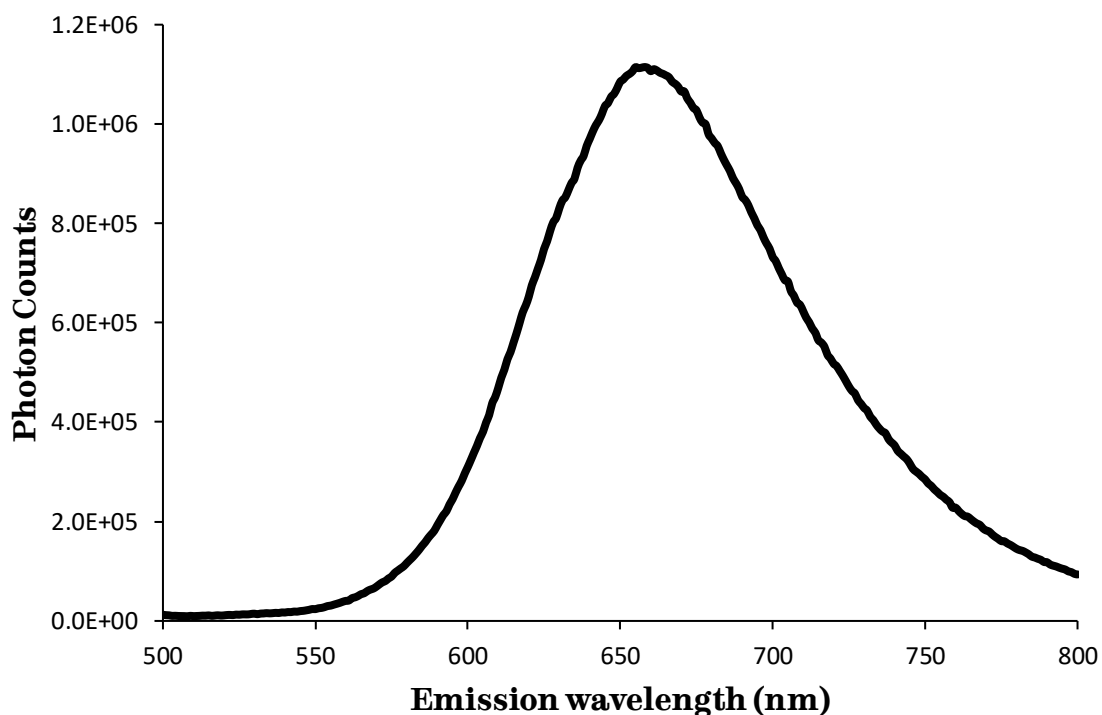
Figure 2.43 - Emission spectra of [Ru(tpm)(dppz)(py-SH)]$^{2+}$ in acetonitrile solution. Excited at 426 nm

The emission spectra of the complex was recorded in acetonitrile as a solution of the hexaflurophosphate salt. The complex was exited at 426 nm, which is part of the MLCT band, as shown in the previous UV-visible absorbance study. The complex shows and emission maxima at 657 nm. This is nearly the same as was reported for the parent compound, [Ru(tpm)(dppz)(py)]$^{2+}$, which is reported to have a maximal emission at 656 nm.[16] This is promising for the suitability of the complex as a sensor as the altering of the pyridine ligand appears to have not significantly affected the emissive properties of the complex. A study of the quantum yield of the complex would also be helpful to check the intensity of emission is similar.

2.7 Conclusion

This chapter describes the synthesis of multiple tpm derived ligands which potentially possess the ability to link a ruthenium metal complex to a surface. The synthesis of the desired ruthenium complex from these tpm derived ligands ultimately proved unsuccessful, possibly due to an inherent instability in the tpm unit after it has been functionalised. While the ligands developed did not prove useful for the overall aim of the project, they could be repurposed for other applications, such as crystal engineering.

In the process of trying to develop a successful synthesis using the novel tpm derived ligands, an improved synthesis of $[Ru(tpm)(dppz)(py)]^{2+}$ was discovered. This was achieved by adding a single dppz ligand to the ruthenium centre prior to the addition of the tridentate tpm ligand. This is the reverse of the usual technique, which adds the tpm first. The new synthesis improved the overall yield of the synthesis from 10% to 45%. The new route also opens the possibility of constructing novel Ru-dppz complexes with alternative mono, tri or tetra dentate ligands. This route is utilised in the next chapter to prepare a range of pyridyl based ruthenium complexes that may not have been possible when using the previous tpm based method.

An alternative to the initial plan of attaching a ruthenium complex to a surface *via* the tpm ligand has also been developed. This involves creating a linker through the pyridine ligand. This solution is less versatile and possibly less stable, due to the lack of chelate effect, than the original aim to connect through the tpm. The complex was successfully synthesised and purified by preparative HPLC. The complex shows expected MLCT absorption bands in its UV-visible spectrum. The complex exhibits a strong emission at 657 nm in acetonitrile, which is similar to the parent compound where the pyridine is not altered. These initial photophysical measurements suggest that the complex could be suitable for the sensor applications desired.

Further work is needed to assess the DNA binding ability of the complex, which could be adversely affected by substituting the pyridine ligand. This would also test if the complex retains the light switch effect, observed for the parent complex. An assessment of the quantum yield would also confirm if the complex has suitable photophysical properties to be used as a sensor. Key in enabling this work to take place is improving on the purification step that currently loses a lot of material and yields

very little pure complex. Due to the difficulties experienced in obtaining the pure compound, an alternative approach was sought, that is described in the subsequent chapter.

2.8 References

1   M. R. Gill and J. A. Thomas, *Chem. Soc. Rev.*, 2012, **41**, 3179.

2   A. E. Friedman, J. K. Barton, J. C. Chambron, J. P. Sauvage, N. J. Turro and J. K. Barton, *J. Am. Chem. Soc.*, 1990, **112**, 4960–4962.

3   F. E. Poynton, J. P. Hall, P. M. Keane, C. Schwarz, I. V. Sazanovich, M. Towrie, T. Gunnlaugsson, C. J. Cardin, D. J. Cardin, S. J. Quinn, C. Long and J. M. Kelly, *Chem. Sci.*, 2016, **7**, 3075–3084.

4   G. Li, L. Sun, L. Ji and H. Chao, *Dalton Trans.*, 2016, **45**, 13261–13276.

5   J. P. Hall, D. Cook, S. R. Morte, P. McIntyre, K. Buchner, H. Beer, D. J. Cardin, J. A. Brazier, G. Winter, J. M. Kelly and C. J. Cardin, *J. Am. Chem. Soc.*, 2013, **135**, 12652–12659.

6   N. J. Rogers, S. Claire, R. M. Harris, S. Farabi, G. Zikeli, I. B. Styles, N. J. Hodges and Z. Pikramenou, *Chem. Commun.*, 2014, **50**, 617–619.

7   Y. Zhang, K. Aslan, S. N. Malyn and C. D. Geddes, *Chem. Phys. Lett.*, 2006, **427**, 432–437.

8   W. W. Brandt and G. F. Smith, *Anal. Chem.*, 1949, **21**, 1313–1319.

9   S. Serroni, S. Campagna, F. Puntoriero, C. Di Pietro, N. D. McClenaghan and F. Loiseau, *Chem. Soc. Rev.*, 2001, **30**, 367–375.

10   A. Juris, V. Balzani, F. Barigelletti, S. Campagna, P. Belser and A. Von Zelewsky, *Coord. Chem. Rev.*, 1988, **84**, 85–277.

11   J. K. Barton, *Science*, 1986, **233**, 727–734.

12   E. Tuite, P. Lincoln and B. Norden, *J. Am. Chem. Soc.*, 1997, **119**, 239–240.

13   J. P. Hall, P. M. Keane, H. Beer, K. Buchner, G. Winter, T. L. Sorensen, D. J. Cardin, J. A. Brazier and C. J. Cardin, *Nucleic Acids Res.*, 2016, **44**, 9472–9482.

14   J. K. Barton, L. a Basile, A. Danishefsky and A. Alexandrescu, *Bioinorg. Med. Chem.*, 1992, **114**, 8946–8952.

15   C. S. Burke and T. E. Keyes, *RSC Adv.*, 2016, **6**, 40869–40877.

16   S. P. Foxon, C. Metcalfe, H. Adams, M. Webb and J. A. Thomas, *Inorg. Chem.*, 2007, **46**, 409–416.

17   P. Waywell, V. Gonzalez, M. R. Gill, H. Adams, A. J. H. M. Meijer, M. P. Williamson and J. A. Thomas, *Chem. - Eur. J.*, 2010, **16**, 2407–2417.

18   D. L. Reger, J. R. Gardinier, R. F. Semeniuc, U. H. F. Bunz and M. D. Smith, *New J. Chem.*, 2005, **29**, 1035–1043.

19   H. Pfeiffer, A. Rojas, J. Niesel and U. Schatzschneider, *Dalton Trans.*, 2009, 4292–4298.

20   J. E. Moses and A. D. Moorhouse, *Chem. Soc. Rev.*, 2007, **36**, 1249–1262.

21   H. C. Kolb, M. G. Finn and K. B. Sharpless, *Angew. Chemie - Int. Ed.*, 2001, **40**, 2004–2021.

22   C. W. Tornøe, C. Christensen and M. Meldal, *J. Org. Chem.*, 2002, **67**, 3057–3064.

23   N. K. Devaraj and J. P. Collman, *QSAR Comb. Sci.*, 2007, **26**, 1253–1260.

24   D. L. Reger, T. C. Grattan, K. J. Brown, C. A. Little, J. J. S. Lamba, A. L. Rheingold and R. D. Sommer, *J. Organomet. Chem.*, 2000, **607**, 120–128.

25   N. Zabarska, D. Sorsche, F. W. Heinemann, S. Glump and S. Rau, *Eur. J. Inorg. Chem.*, 2015, **2015**, 4869–4877.

26   M. N. Tahir, N. Lämmerhardt and P. Mischnick, *Carbohydr. Polym.*, 2012, **88**, 154–164.

27   H. K. Saeed, I. Q. Saeed, N. J. Buurma and J. A. Thomas, *Chem. Eur. J.*, 2017, **23**, 5467–5477.

28   K. Mitsumoto, H. Nishikawa, G. N. Newton and H. Oshio, *Dalton Trans.*, 2012, **41**, 13601.

29   E. Iengo, E. Zangrando, E. Baiutti, F. Munini and E. Alessio, *Eur. J. Inorg. Chem.*, 2005, 1019–1031.

30   C. M. Shade, R. D. Kennedy, J. L. Rouge, M. S. Rosen, M. X. Wang, S. E. Seo, D. J. Clingerman and C. A. Mirkin, *Chem. - Eur. J.*, 2015, **21**, 10983–10987.

31   R. B. P. Elmes, K. N. Orange, S. M. Cloonan, D. C. Williams and T. Gunnlaugsson, *J. Am. Chem. Soc.*, 2011, **133**, 15862–15865.

32   S. A. M. Osborne and Z. Pikramenou, *Faraday Discuss.*, 2015, **185**, 219–231.

33   M. G. Walker, PhD Thesis, University of Sheffield, 2013.

34   M. R. Waterland, K. C. Gordon, J. J. Mcgarvey and P. M. Jayaweera, 1998, **10**, 609–616.

35   J. Fees, W. Kaim, M. Moscherosch, W. Matheis, J. Klima, M. Krejcik and S. Zalis, *Inorg. Chem.*, 1993, **32**, 166–174.

3.0 Synthesis of pyridyl based complexes

3.1 Introduction

The apparent instability of ligands derived from the base tpm molecule described in the previous chapter showed that the initial approach was not suitable. A surface linker could not be realised using derivatives of the tpm molecule due to the instability of the pyrazolyl unit. Thus, an alternative ligand was sought. As was described in the previous chapter the ideal design consists a tripodal ligand in combination with the known intercalator, dppz. This eliminates the chirality of any resultant complex, which simplifies understanding of the binding mechanism to DNA, and ultimately the photophysics of the complex. The other advantage of this approach is that the tridentate nature of the ligand will take advantage of the chelate effect. This means that it is entropically unfavourable for the ligand to be replaced by another. As the tridentate ligand occupies three co-ordination sites, even if one is replaced by a competing ligand, the tridentate ligand will still be held in place by two attachment points. It is then more likely that the tridentate ligand will displace the competing ligand, rather than be displaced from the complex itself.

One possible candidate considered for the role of surface linker was 4-ethynylterpyridine, shown in figure 3.1. This ligand has the potential to bind to ruthenium, through the pyridine moieties, and to a surface *via* click chemistry with the alkyne group. This approach has been demonstrated in linking a ruthenium complex to a metal organic framework.[1] The parent ligand, terpyridine, has already been used alongside dppz to form an intercalating ruthenium complex.[2] The study of binding did not show a light switch effect as is required to make a sensor device. It has been suggested that this lack of emission is due to the bite angle that the terpyridine ligand confers on ruthenium complexes.[3] This bite angle causes a distortion from ideal octahedral geometry so that the non-emissive *d-d* excited state is close enough in energy to the MLCT state that they are in equilibrium. This provides a non-emissive route to deactivating the usually luminescent MLCT excited state. It is not likely that the addition of an alkyne group would alter this, thus it is not a suitable candidate. It did however lead to consideration of alternative pyridyl based ligands that could offer the potential for surface linkage without affecting the photophysics adversely.

tris(2-pyridyl)methanamine (tpyma)   tris(2-pyridyl)carbinol (tpyc)
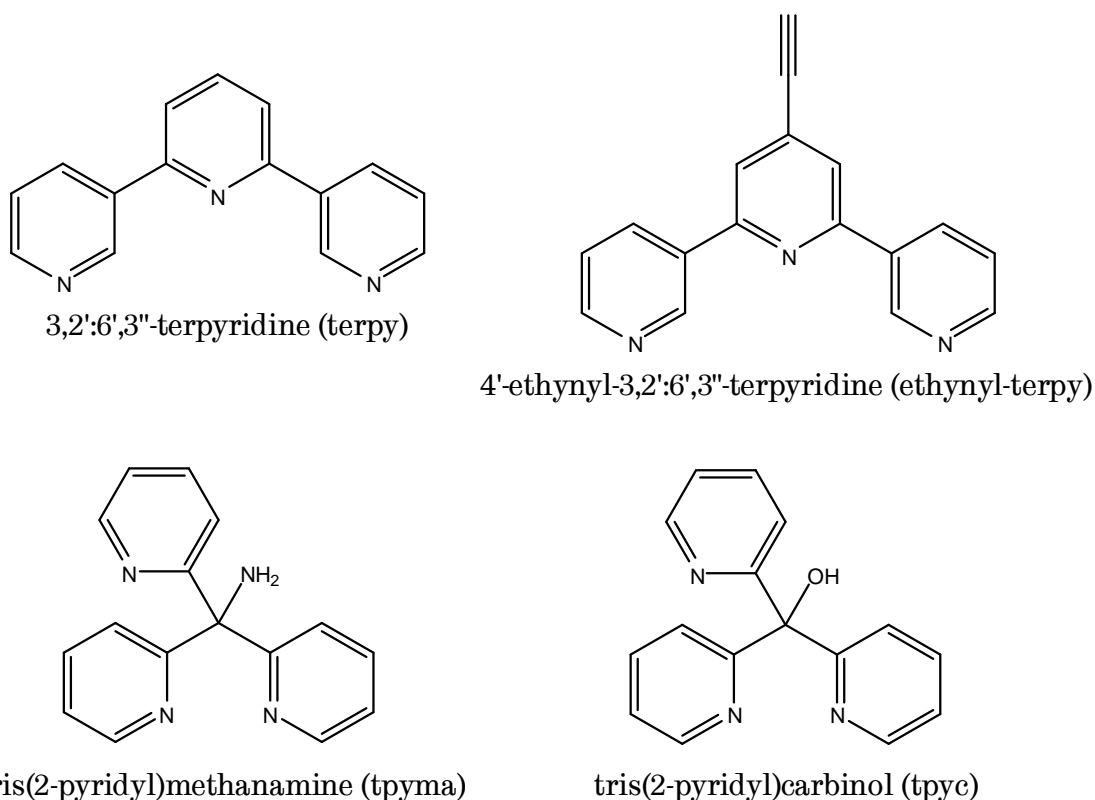
Figure 3.1 - Potential pyridyl based ligands with surface linker potential

An alternative to linking three pyridine rings directly, as in the case of terpyridine, is to link them through a central carbon atom, similar to the construction of tpm. This addition of a methyl spacer should make the ligand more flexible, to avoid issues around strain and bite angle. Two examples of this approach, tris(2-pyridyl)methylamine (tpyma) and tris(2-pyridyl)carbinol (tpyc) are shown in figure 3.1. Both molecules offer a tripodal binding site through the pyridyl nitrogens, and a functional group that can be used to add a linker to the molecule. Complexes synthesised with the tpyc ligand were first reported in 1980.[4] These studies showed that the ligand can display two different binding modes, dependant on the metal. The ligand has also been altered to introduce ether linkages into the molecule.[5] This is of interest as it may be possible to introduce a surface linker with this kind of method.

In comparison the tpyma ligand has received much less research attention, as it is a more recent innovation, being first reported in 1998.[6] Interestingly, this initial paper points to this ligand's potential for derivitisation. When co-ordinated as part of a copper(II) sulfato complex the amine group of the ligand is free for further reaction. This amine could be used to link to a surface. Attempts to take advantage of these features of both the tpyma and tpyc ligands are described in this chapter.

3.2 Complex design

The design considerations remain the same as those that were discussed in the previous chapter. The complex must contain a ruthenium centre for its photophysical properties, a DNA intercalator in the form of dppz, a surface linking ligand and an ancillary ligand to complete the complex. The complex detailed in this chapter is analogous to that described in the previous chapter, with a pyridyl ligand replacing the pyrazolyl ligand tpm. All other ligands will remain the same. The methodology of attachment to the surface changes from the click chemistry designed in the previous chapter, to amide formation. This is achieved through reaction of an aldehyde based self assembled monolayer (SAM) with the pendant amine of the tpyma ligand. This has previously been described for other amines and aldehyde functional gold surfaces.[7] The new complex and desired surface attachment are illustrated in figure 3.2.
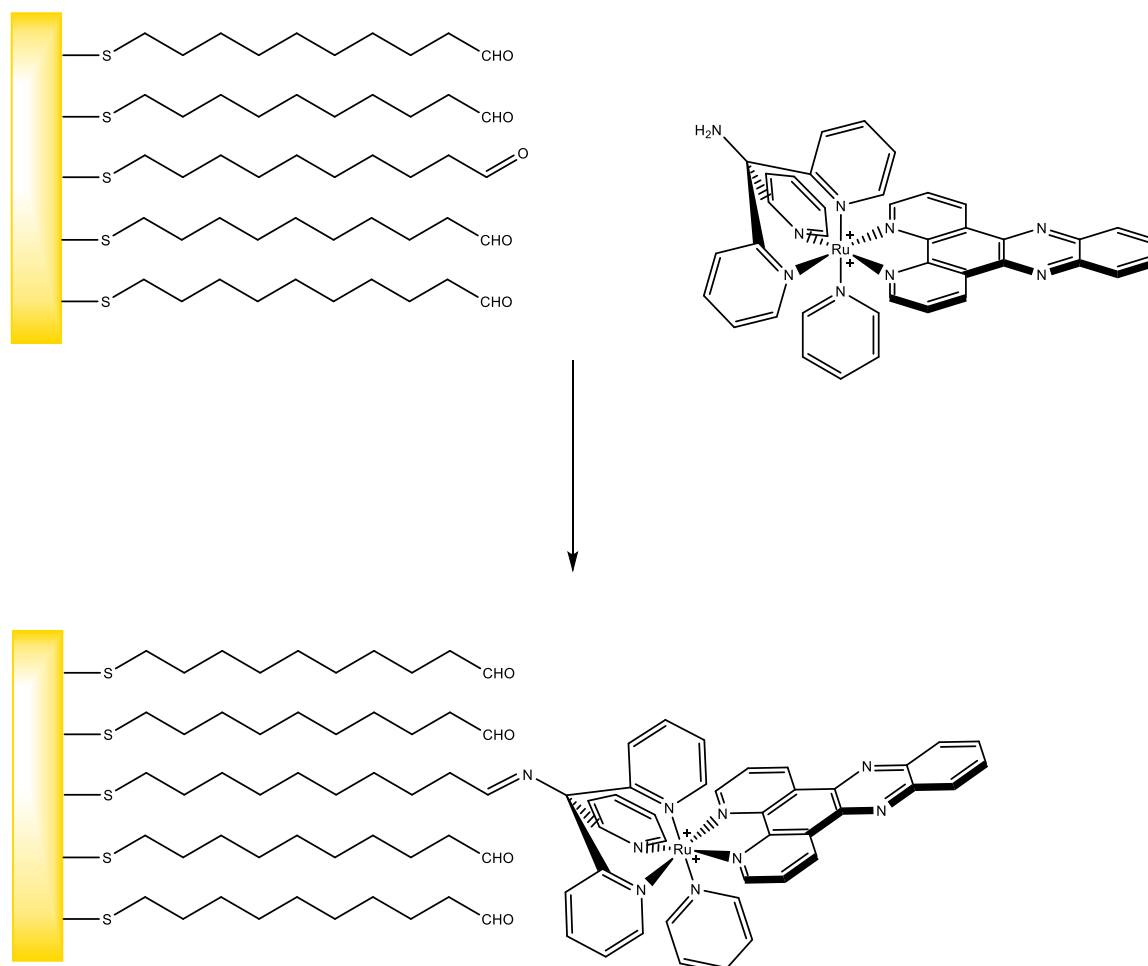
Figure 3.2 - Illustration of a the proposed surface bound, intercalating ruthenium complex

3.3 Tris(pyridyl) complex synthesis

3.3.1 Synthesis of tris(2-pyridyl)methylamine (tpyma)

Tris(pyridyl)methylamine is synthesised using the method of Arnold *et. al.*[8], first metallating 2-picolyamine with n-butyl lithium in dry THF. 2-bromopyridine is introduced into the reaction and adds to the methyl group of the picolylamine, initially forming di(2-pyridyl)methylamine as an intermediate which can be isolated. On addition of another equivalent of bromopyridine tris(pyridyl)methylamine is formed. On extraction the product was obtained as a brown oil which formed crystals over a period of months. The crude product was sufficiently pure for subsequent reaction.
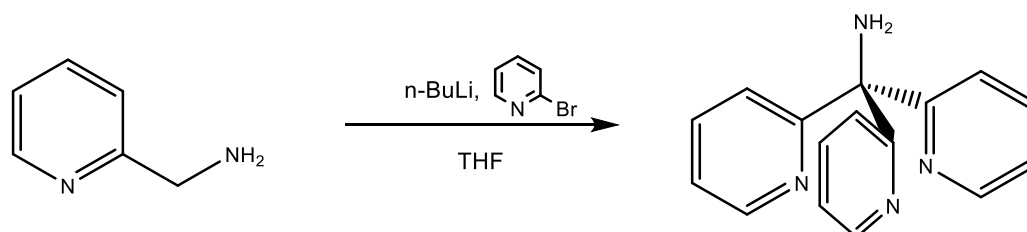
Figure 3.3 - Synthesis of tpyma

3.3.2 Synthesis of tris(2-pyridyl)carbinol (tpyc)

The synthesis of tris(pyridyl)carbinol was achieved using the method reported by Jonas and Stack.[9] The initial step is to lithiate 2-bromopyridine with n-butyl lithium in dry THF. This can then react with the carbonyl of di(2-pyridyl)ketone when it is added to the reaction, forming tpyc. The product is extracted and recrystalised to form off white crystals.
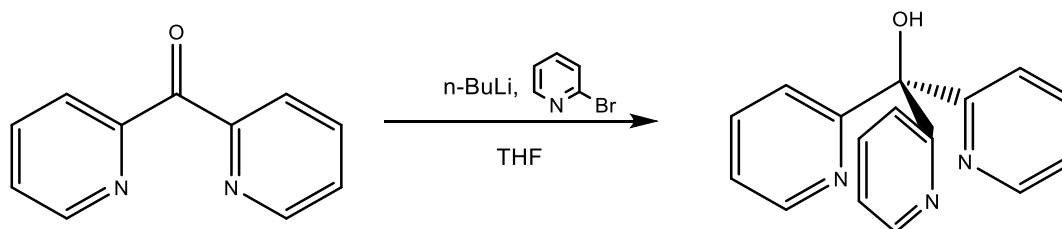
Figure 3.4 - Synthesis of tpyc

3.3.3 Synthesis of mercapto(tris(2-pyridyl)methyl)undecanamide (tpyma-SH)

The attraction of using tpyma is that it contains a free amine group that can be derivitised. Ideally this would be reacted with the surface after co-ordination to the ruthenium metal centre, but to test its suitability it was reacted prior to addition of ruthenium. This was achieved using the same reagents and conditions as was used to synthesise mercapto(pyridinylmethyl)undecanamide (py-SH) (Section 2.5.1). The mercapto-undecanoic acid is initially stirred with 1-hydroxybenzotriazole hydrate (HOBt) and N,N'-Dicyclohexylcarbodiimide (DCC) in dry DCM prior to the introduction of tpyma. This forms a reactive species that forms an amide linkage with the amine of tpyma. The resultant product was extracted and purified by column chromatography on silica.
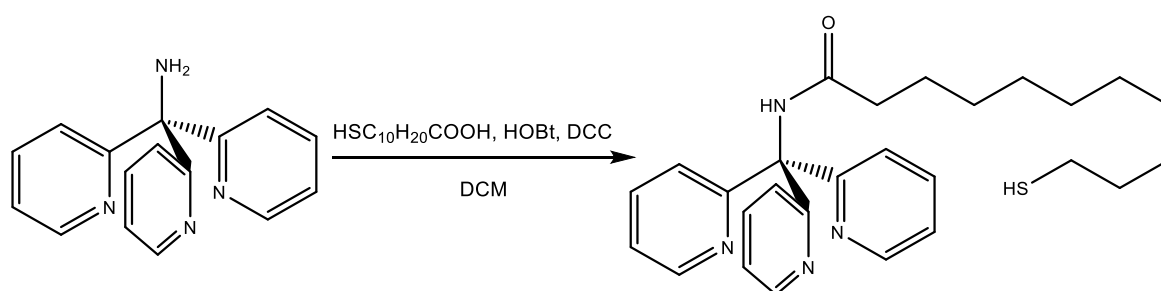
Figure 3.5 - Synthesis of tpyma-SH

3.3.4 Synthesis of tris(2-pyridyl)methylazide (tpyaz)

An alternative to the use of an amide linkage to a surface is the azide-alkyne cycloaddition described in chapter 2. In order to offer a potential alternative route, if there were any problems with the amine coupling, a ligand containing an azide moiety was designed. The synthesis was achieved by adapting a procedure reported for the synthesis of azospermine,[10] which relies on switching an amine for an azide moiety.

Triflic anhydride and sodium azide are first stirred in dry acetonitrile under ice to form triflic azide. This solution is added to a separate solution containing the tpyma alongside copper sulphate and triethylamine which act to catalyse the transformation. The product is extracted as a black solid and purified by column chromatography.
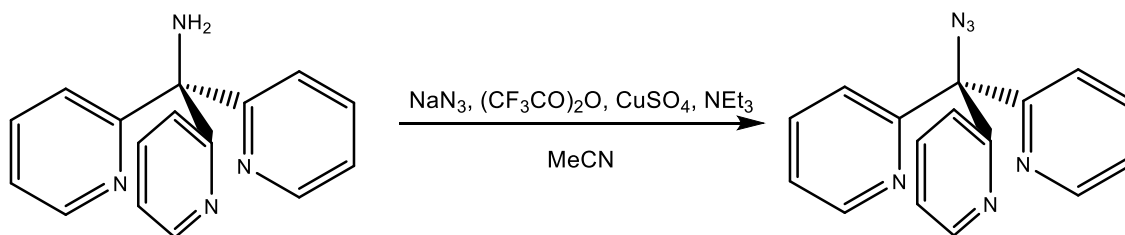
Figure 3.6 - Synthesis of tpyaz

3.3.5 Synthesis of [RuCl(tpyma)(dppz)]$^+$PF$_6$$^-$

Using the same procedure that was developed for the synthesis of [RuCl(tpm)(dppz)]$^+$ described in chapter 2 (section 2.3.18), tpyma was added to [RuCl$_2$(dmso)$_2$(dppz)]. The ligand was heated with the ruthenium complex in ethylene glycol forming the expected deep red solution. Saturated KPF$_6$ solution was used to precipitate the product which was then collected and purified using an alumina column and 1:1 acetonitrile:toluene as the eluent. The brown band was collected and re-precipitated.

Figure 3.7 - Synthesis of [RuCl(tpyma)(dppz)]$^+$

3.3.6 Synthesis of [Ru(tpyma)(dppz)(py)]$^{2+}$(PF$_6$$^-$)$_2$
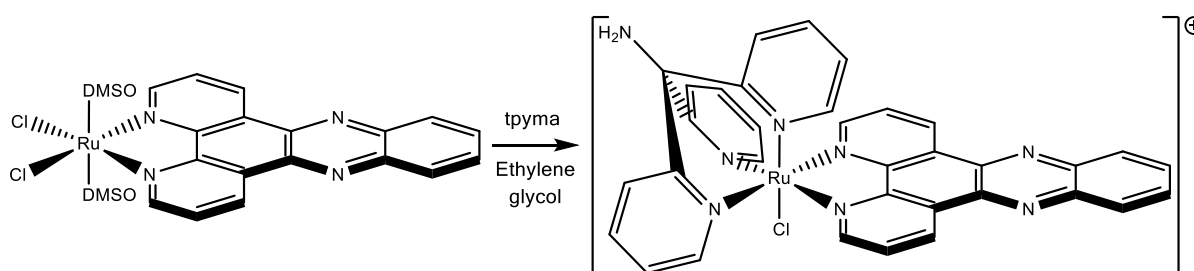
To complete the synthesis of the target complex the remaining chloride ligand was removed and replaced with pyridine. This was achieved by the same method previously discussed (section 2.3.19) whereby silver triflate abstracts the chloride ion forming insoluble AgCl. The pyridine is then added in excess to co-ordinate to the ruthenium centre.
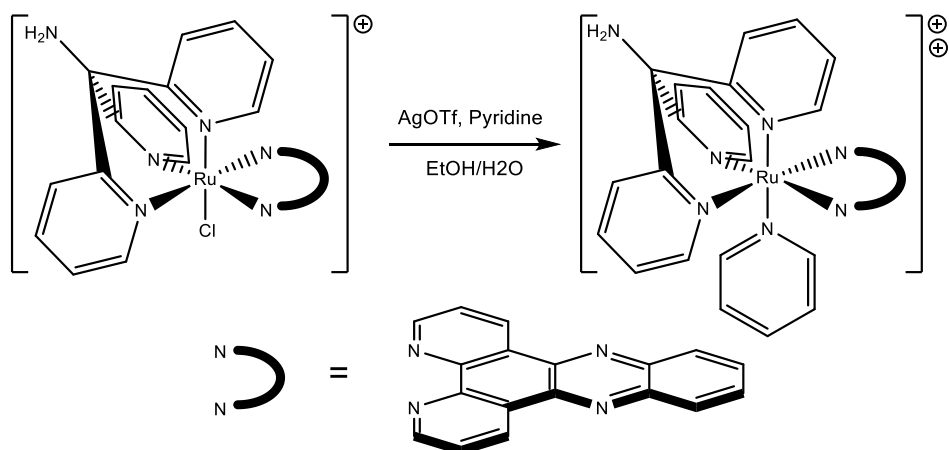
Figure 3.8 - Synthesis of [Ru(tpyma)(dppz)(py)]$^{2+}$

The complex was designed for the amine to be free to further react and form amide linkage with other molecules and ultimately a surface monolayer. Attempts were made to link the complex with mercaptoundecanoic acid using the same successful method as with the synthesis of tpyma-SH (section 3.3.3). In addition, iodobenzoyl chloride was stirred with the complex to try and form an amide link. This was the same starting material used to form the tpeib ligand (section 2.2.13) and could be used for aryl halide based cross coupling. Neither of these reactions proved to yield the desired amide link.

Subsequently it was found that the reason for these failures may have been that the amine moiety was not available as proposed. The x-ray crystal structure showed that the amine was in fact co-ordinated to the ruthenium centre, with one of the pyridines exposed instead. The actual structure is illustrated in figure 3.9.
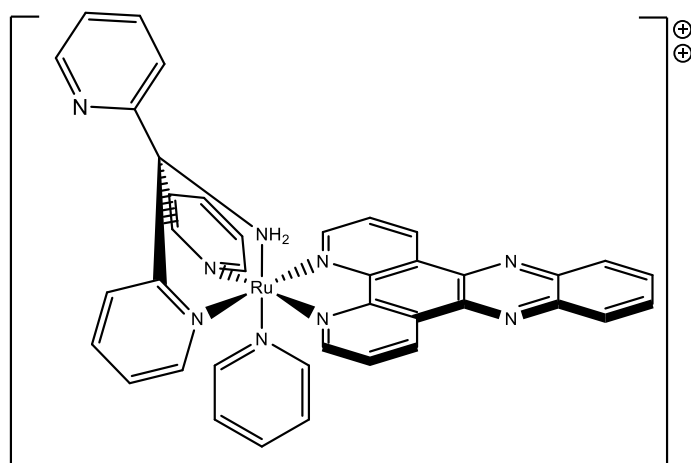
Figure 3.9 – Actual binding mode of tpyma as discovered by x-ray crystallography

This renders the complex ineffective for the desired application; however it does open the possibility of switching the exposed pyridine for an alternative moiety that could be used for a surface linker. Attempts to construct such a complex are described later in this chapter.

3.3.7 Synthesis of [RuCl(tpyc)(dppz)]$^+$PF$_6^-$

Analogous to the reaction of tpyma, tpyc was heated with [RuCl$_2$(dmso)$_2$(dppz)] in ethylene glycol to form [RuCl(tpyc)(dppz)]$^+$. The complex was precipitated as a PF$_6$ salt and purified by alumina column chromatography with 1:1 acetonitrile:toluene as eluent. The product formed as a darker, black solid, opposed to the deep red of RuCl(tpyma)(dppz)]$^+$.
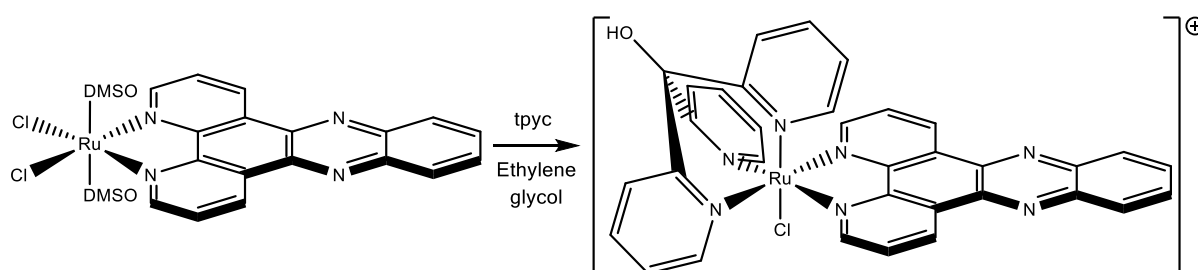
Figure 3.10 - Synthesis of [RuCl(tpyc)(dppz)]$^+$

3.3.8 Synthesis of [Ru(tpyc)(dppz)(py)]$^{2+}$(PF$_6^-$)$_2$

The remaining chloride ligand of [RuCl(tpyc)(dppz)]$^+$ was removed by abstraction with silver triflate. Excess pyridine was added to form [Ru(tpyc)(dppz)(py)]$^{2+}$. The precipitated PF$_6$ salt was again darker than the tpyma equivalent. It was not possible to grow crystals of sufficient quality to analyse the compound by xray crystallography and assess the co-ordination mode of tpyc. It may be that the ligand co-ordinates through the alcohol in the same way that the amine co-ordinates in the case of tpyma. It has been previously reported that the ligand can exhibit both modes, as in the case of [Ru(tpyc)$_2$]$^+$.[11]
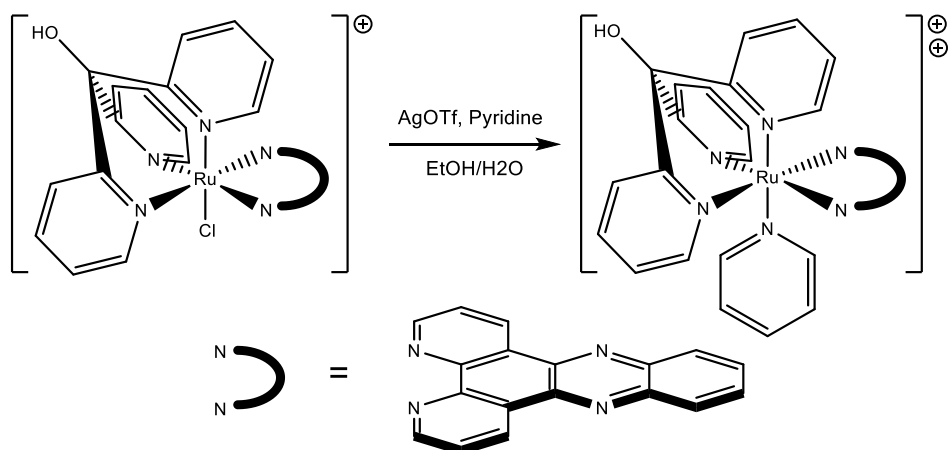
Figure 3.11 - Synthesis of $[Ru(tpyc)(dppz)(py)]^{2+}$

3.3.9 Synthesis of $[RuCl(tpyma-SH)(dppz)]^{+}PF_6^{-}$

The thiol linked ligand tpyma-SH was heated with $[RuCl_2(dmso)_2(dppz)]$ in ethylene glycol in an attempt to co-ordinate the ligand. The solution became deep red as is expected, however on analysis it seemed that the ligand had not co-ordinated. LC-MS analysis showed that mainly the free ligand was present in the extracted product. It is possible that the formation of the amide prevents the co-ordination of the ligand as it is the amine that co-ordinates. There was no evidence of the desired complex in the LC-MS analysis.
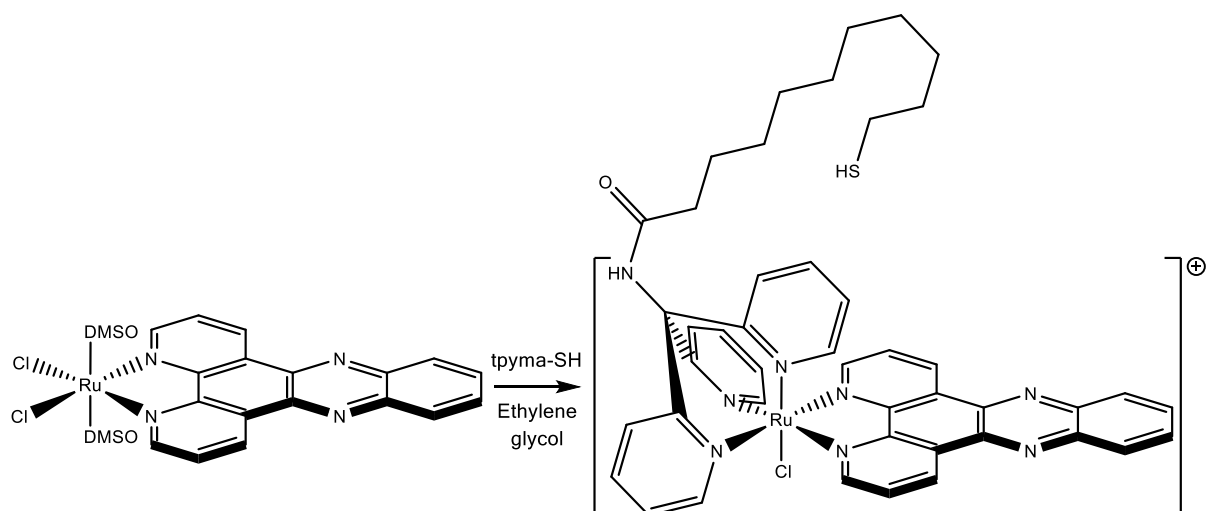
Figure 3.12 - Synthesis of $[RuCl(tpyma-SH)(dppz)]^{+}$

3.3.10 Synthesis of $[RuCl(tpyaz)(dppz)]^{+}PF_6^{-}$

On reaction with $[RuCl_2(dmso)_2(dppz)]$ the tpyaz ligand also formed a deep red solution and precipitated as a PF_6 salt as would be expected. On analysis of the resulting

precipitate the LC-MS did not show a mass ion relating to the desired product. There was however a peak relating to [RuCl(tpyma)(dppz)]⁺. It would seem that the azide formed on the tpyaz ligand is converted back to the amine moiety on interaction with ruthenium. Although x-ray crystallography analysis was not performed, it is likely that the same binding mode is present with the amine co-ordinated to the ruthenium. This is therefore not a useful route to a surface binding complex.
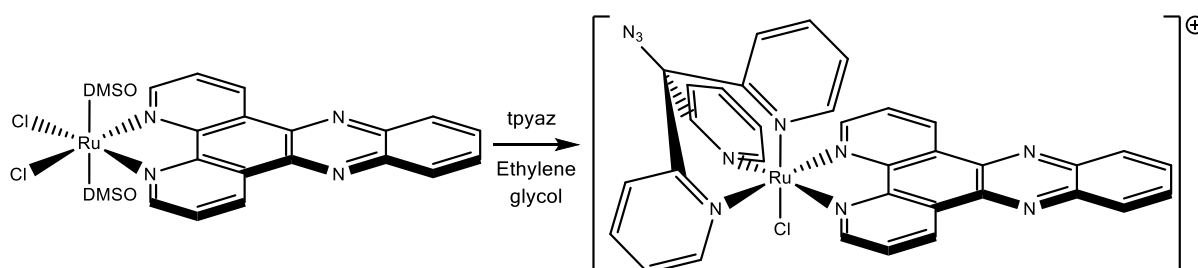
Figure 3.13 - Synthesis of [RuCl(tpyaz)(dppz)]⁺

3.3.11 Synthesis of dipyridoquinoxaline (dpqx)

In conducting a study of the suitability of the tpyma ligand to DNA binding a range of ligands were employed. The range involves extending the bi-pyridine (bpy) ligand with aromatic rings to form a range of lengths of ligand up to the extended dppn ligand. The dpqx ligand forms part of the series, being one aromatic ring shorter than the dppz ligand, of which the synthesis was described previously (section 2.3.4).

Dpqx is formed by refluxing ethylene diamine with dpq in ethanol. The amines form a condensation reaction with the ketones forming a pyrazine ring. The product is recrystalised from ethanol and obtained as a cream coloured solid.
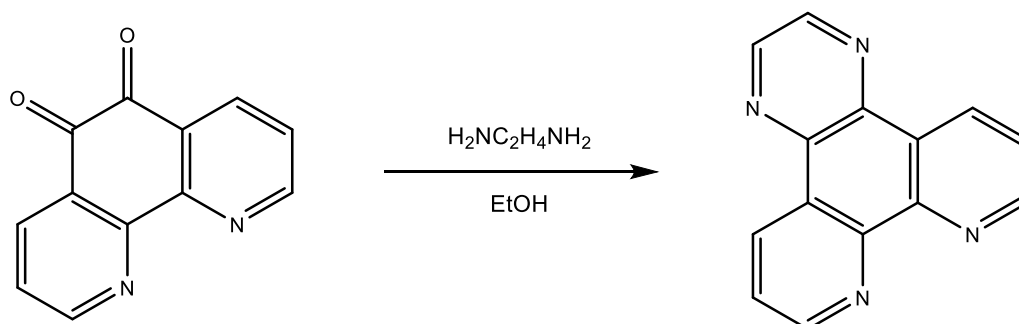
Figure 3.14 - Synthesis of dpqx

3.3.12 General synthesis of [RuCl$_2$(dmso)$_2$(NN)]

To construct the range needed to investigate the DNA binding of tpyma based complexes, the starting materials need to be synthesised in the same way as for dppz, previously described (section 2.3.17). In each case, the bidentate portion of the complex was refluxed in toluene with [RuCl$_2$(dmso)$_4$], replacing two of the dmso ligands with only one bidentate ligand. This was performed with bpy, phen, dpqx and dppn in addition to the previously synthesised dppz. The isolated precipitate varied in shades of brown depending on the ligand used.
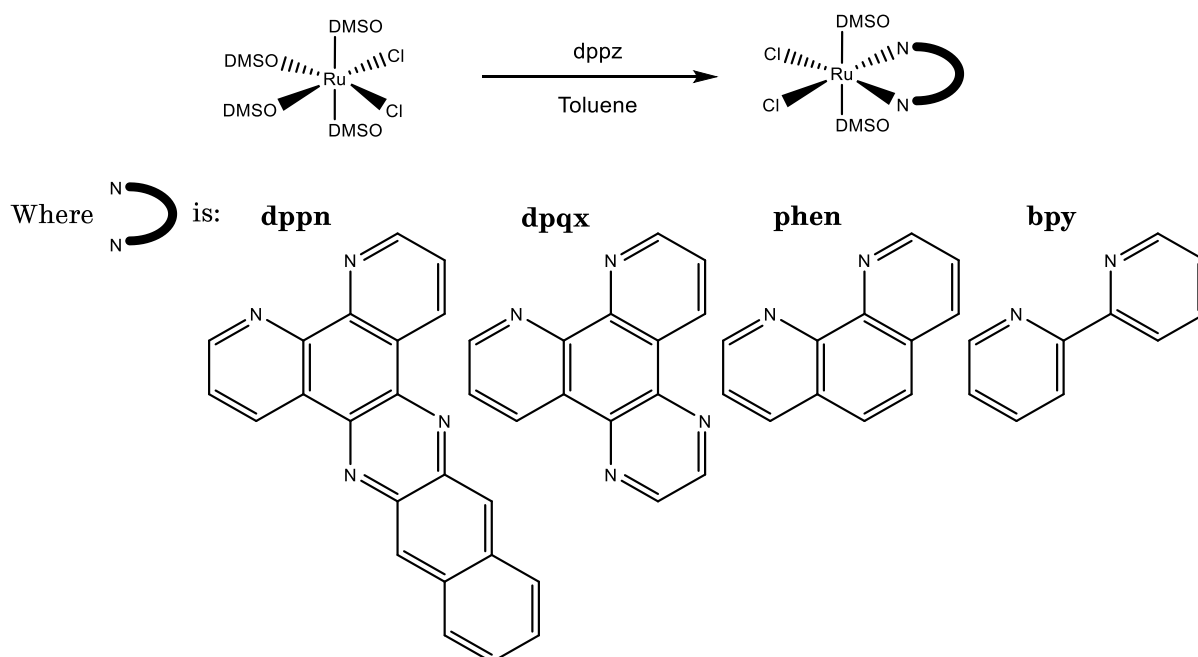
Figure 3.15 - Synthesis of [RuCl$_2$(dmso)$_2$(NN)]

3.3.13 General synthesis of [RuCl(tpyma)(NN)]$^+$PF$_6^-$

The tpyma ligand was introduced into each of the complexes described in section 3.3.12 by heating the ligand and respective ruthenium complex in ethylene glycol. The product was precipitated by addition of saturated KPF$_6$ solution. In each case the

product was purified by alumina column chromatography using 1:1 acetonitrile:toluene as the eluent. This synthesis is analogous to that for [RuCl(tpyma)(dppz)] (section 3.3.5).
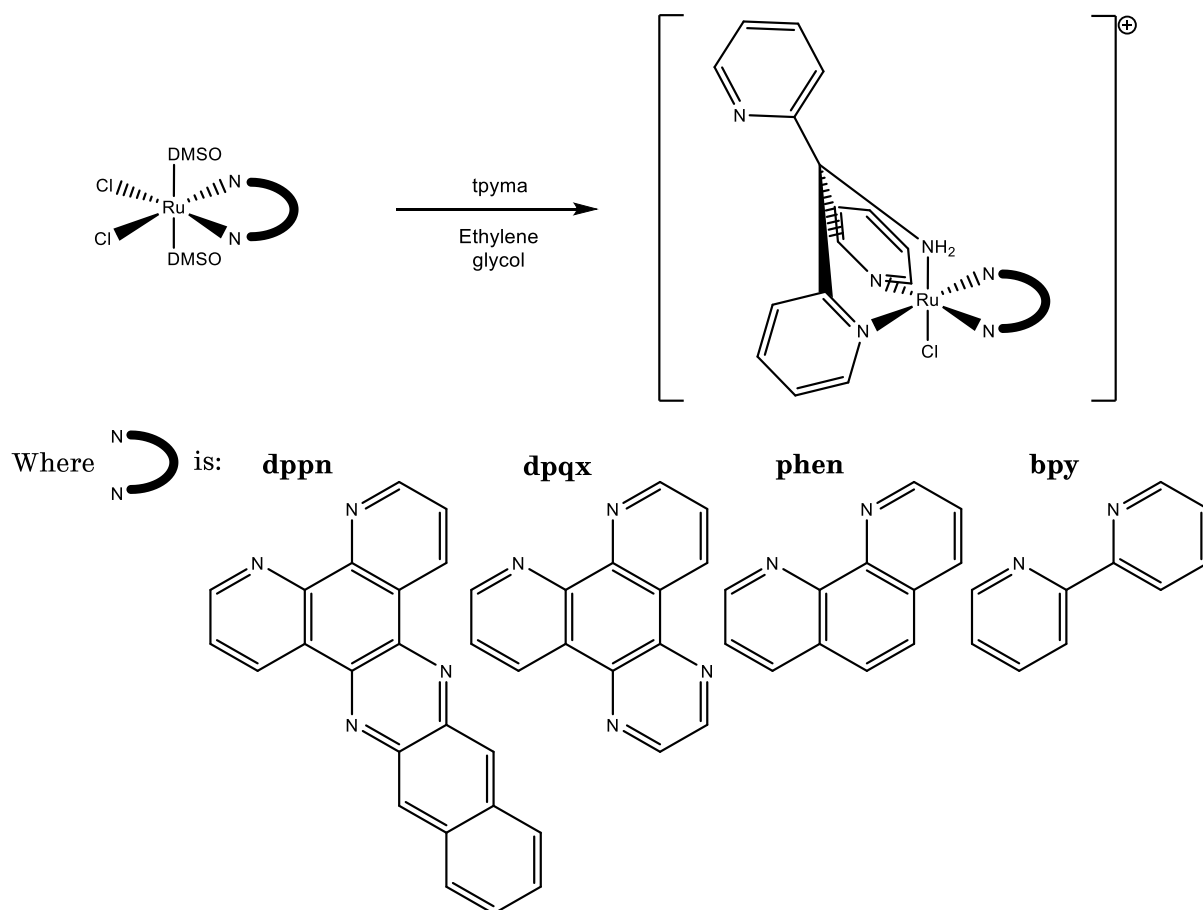
Figure 3.16 - Synthesis of [RuCl(tpyma)(NN)]$^+$

3.3.14 General synthesis of [Ru(tpyma)(NN)(py)]$^{2+}$(PF$_6^-$)

The synthesis of tpyma based complexes was completed by the abstraction of the remaining chloride ligand with silver triflate and replacement by the addition of excess pyridine. The product was obtained by precipitation as a PF$_6$ salt.
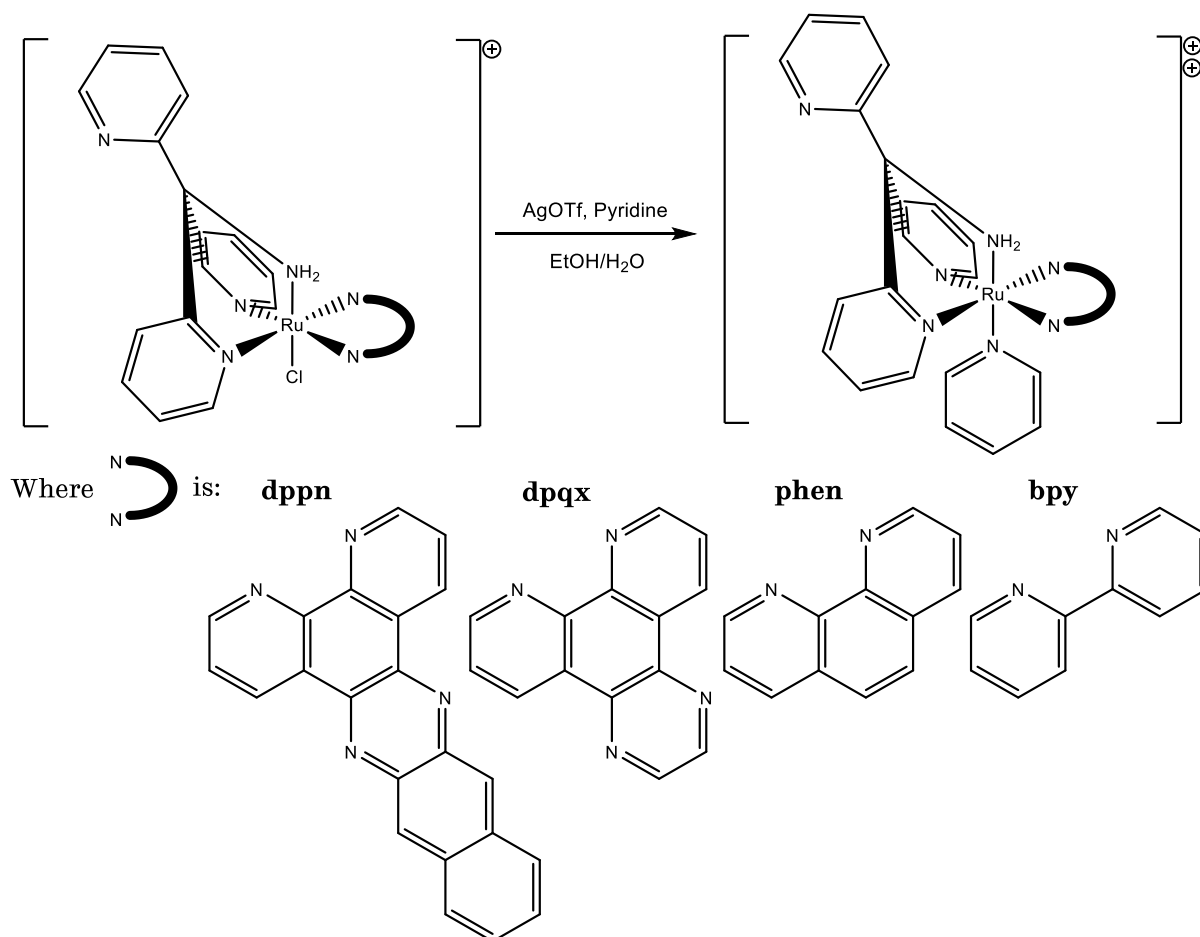
Figure 3.17 - Synthesis of [Ru(tpyma)(NN)(py)]$^{2+}$

The synthesis was successful for all but the [Ru(tpyma)(dpqx)(py)]$^{2+}$ ligand. In this instance the LC-MS indicated that there were two different molecules present in the final product. Attempts were made to purify the complex by converting from the PF$_6$ salt to a chloride salt and employing a magic mix eluent (98:1:1, acetonitrile:water:saturated KNO$_3$) with silica gel stationary phase. Although separation was observed on the column, the LC-MS analysis remained unchanged.

The ^{1}H NMR spectrum of the compound contained too many hydrogen environments for the sample to be pure. It was possible to grow crystals of the compound by slow diffusion of diethyl ether into a solution of the complex in nitromethane. Analysis by x-ray crystallography suggested that a single molecule was present, possessing a

similar structure to that which was expected, with a large amount of electron density in the 3-position of dpqx. It is thought to be consistent with a halide attached to the ligand. It is unclear as to how this could be possible. The structure is shown in figure 3.18.
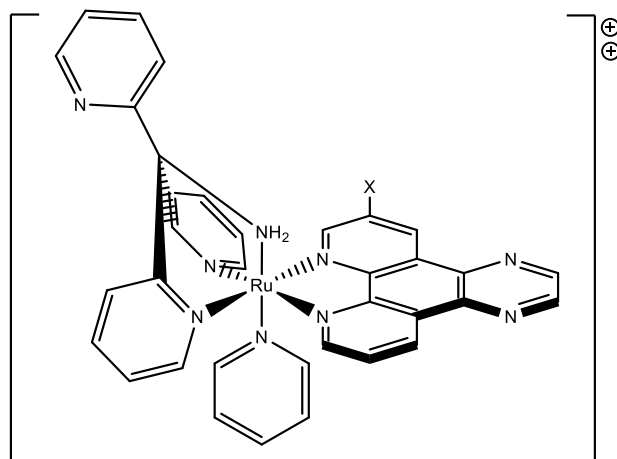
Figure 3.18 - Possible structure formed on attempted synthesis of [Ru(tpyma)(dpqx)(py)]$^{2+}$ with group X demonstrating the position of electron density observed by x-ray crystallography

3.4 NMR studies of tris(pyridyl) complexes

3.4.1 ¹H NMR of mercapto(tris(2-pyridyl)methyl)undecanamide (tpyma-SH)

The ¹H NMR spectrum of mercapto(pyridinylmethyl)undecanamide (py-SH), recorded in deuterated acetone is shown in figure 3.19 with peaks labelled relating to the lettering on the molecular structure.
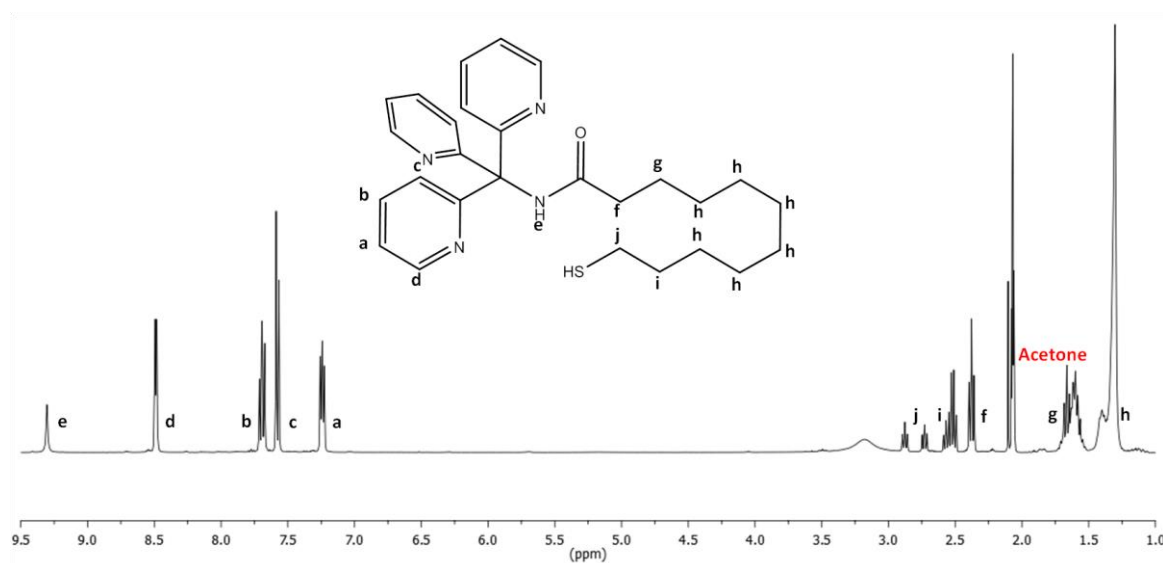
Figure 3.19 - 400 MHz ¹H NMR of mercapto(tris(2-pyridyl)methyl)undecanamide (tpyma-SH) in d_6-acetone

The ¹H NMR spectrum of tpyma-SH exhibits peaks in both the aromatic and aliphatic regions. Protons **a-d** of the pyridine portion of the molecule give the aromatic peaks. These protons are assigned based on their splitting pattern and proximity to the electron deficient nitrogen atom. Being closest to the nitrogen, proton **d** is assigned to the most deshielded of these protons at 8.5 ppm and gives a doublet peak due to the coupling to the single proton, **a**. Proton **c** is assigned as the only other doublet in the region as it also only has one proton neighbour, while the remaining protons have more. Protons **a** and **b** give doublet of doublet signals as they are both neighboured by two non equivalent protons. Proton **a** is primarily coupled to **d** and is assigned based on the fact the peaks share a coupling constant of 4.8 Hz. Likewise, **b** and **c** share a coupling constant of 8.1 Hz. The amide proton **e** is assigned to the broad singlet at 9.4

ppm. It is only present as the acetone solvent used is aprotic and so the proton does not switch with deuterium ions in the solution.

As seen and described for py-SH, the protons, **j,** nearest the thiol is split into two small triplet peaks due to disulfide formation. The other triplet in the aliphatic region is assigned to protons **f** as it is the only other protons with only two neighbour protons. Protons **i** and **g** are assigned on the basis that they are closest to the functional groups and so are more deshielded. The remaining protons **h** are assigned to the large broad signal at lowest ppm shift.

3.4.2 ^{1}H NMR of [Ru(tpyma)(bpy)(py)]$^{2+}$(PF$_6^-$)$_2$

The ^{1}H NMR spectrum of [Ru(tpyma)(bpy)(py)]$^{2+}$(PF$_6^-$)$_2$, recorded in deuterated acetone is shown in figure 3.20 with peaks labelled relating to the lettering on the molecular structure. The lettering is colour coded to the different aromatic ring systems for clarity.
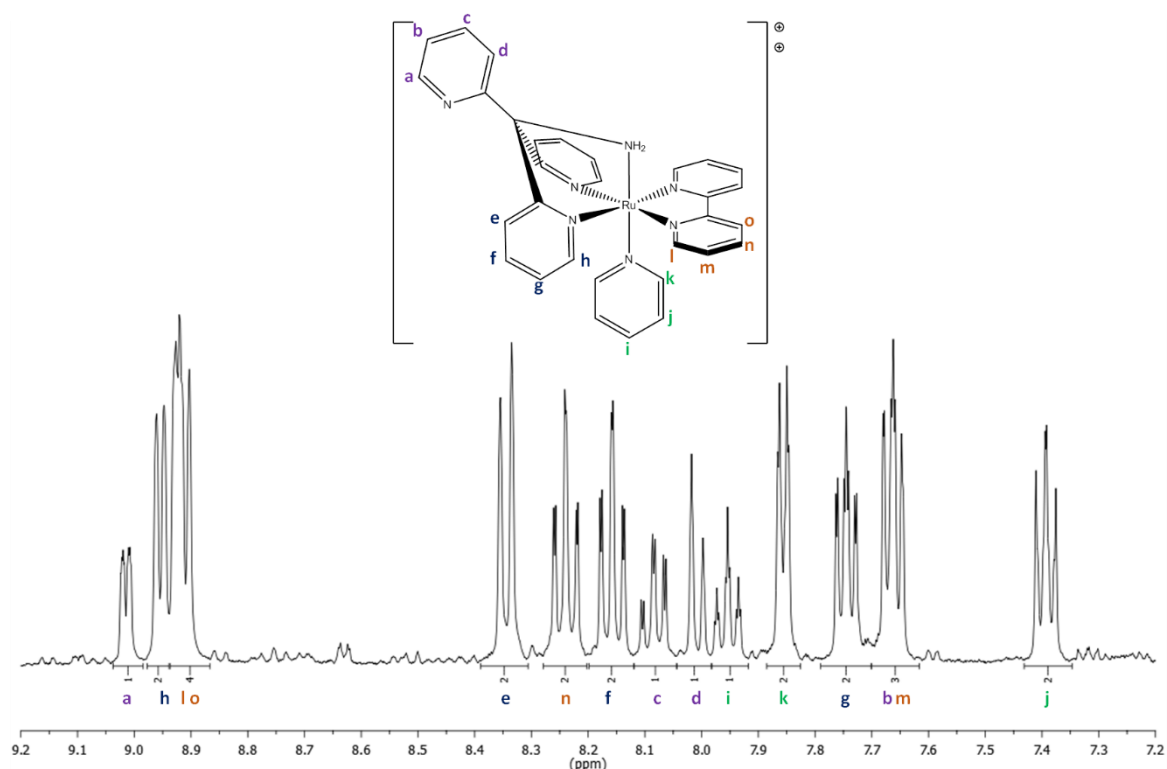
Figure 3.20 - 400 MHz ^{1}H NMR of [Ru(tpyma)(bpy)(py)]$^{2+}$(PF$_6^-$)$_2$ in d$_6$-acetone

The spectrum of [Ru(tpyma)(bpy)(py)]$^{2+}$(PF$_6^-$)$_2$ was assigned with the aid of a 2D COSY NMR experiment, the spectrum of which is shown in figure 3.21. The COSY NMR

indicates which protons are coupled as they are displayed as cross peaks. Connecting these cross peaks allows for the distinguishing of the different aromatic ring systems present in the different ligands of the complex. This has been done with colour coded lines, relating to the molecular structure shown in the figure. Once these coupling patterns have been established, the protons of each aromatic ring are more easily assigned.

Protons **a** – **d** were assigned on the basis that it is the only ring system in the molecule to consist entirely of single proton environments, due to it being bisected by the plane of symmetry on the molecule. The other ring system that also sits in the plane of symmetry is the single pyridine ligand. Its protons, **i** – **k** are distinguished as the only ring system that exhibits only three proton environments, where all others have four. It also is the only system to have and integration pattern of 2:2:1. In isolation it is difficult to distinguish between the remaining tpyma signals and the bpy proton signals. They both share four signals that all integrate to two protons and exhibit the same splitting pattern. Therefore, the ring systems are assigned by comparison with the other complexes synthesised, where the tpyma ligand remains the same but the bpy ligand is extended.

Protons **a** – **d** are distinguished from each other on the basis of splitting pattern, coupling constants and proximity to the nitrogen atom. As the closest proton to the nitrogen **a** will be most deshielded and is assigned to the peak at highest ppm shift. The primary coupling to proton **b** forms a doublet, though some smaller coupling interaction with other protons can be seen with very small coupling constants. The only other proton in the ring system that has one neighbour, thus forming a doublet, is proton **d**. Using the COSY NMR, the only other signal in this ring to exhibit a doublet exists at 8.0 ppm shift and is thus assigned to **d**. The protons neighbouring each other will share a primary coupling value. The peak assigned to proton **d** shares a coupling value of 8.1 Hz with the triplet at 8.1 ppm shift. Thus, the triplet is assigned to proton **c**, the proton that neighbours **d** in the molecular structure. The remaining proton **b** is assigned to the last peak in the ring system, however it cannot be confirmed that it shares a coupling constant of 4.8 Hz with proton **a** as it is mixed with another signal.

Protons **e** – **h** are assigned in a very similar way to **a** – **d**, as they exhibit the same splitting and coupling patterns. Protons **e** and **h** are assigned to the doublet peaks at 8.9 ppm and 8.3 ppm shift, with proton **h** assigned to the more deshielded peak owing

to its proximity to the nitrogen atom. The peak of proton **h** exhibits a coupling constant of 5.2 Hz which it shares with the pseudo triplet peak at 7.7 ppm shift, thus this is assigned to its neighbour proton **g**. The remaining peak in the system shares a coupling value of 8.0 Hz with **e** confirming that it is the remaining proton **f**.

Protons **i** – **k** are easily assigned on the basis of integral value and splitting pattern. Proton **i** is assigned to the only peak in the ring system with an integral value of one, as the other protons on the ring have an equivalent partner opposite, resulting in an integral value of two. Proton **k** is assigned to the pseudo doublet peak of the three in the ring system as that only has one neighbour to form significant coupling with, although some smaller coupling is seen as the peak is not strictly a doublet peak. This leaves proton **j** as the pseudo triplet as it couples to both **i** and **k**.

Protons **l** – **o** are more difficult to assign as three of the four peaks related to the ring system are overlapping with another signal. This means that coupling constants and splitting patterns cannot be established. The assumption is made that the protons will act in a very similar fashion to the protons opposite on the equatorial pyridyl rings of the tpyma portion. Therefore the protons **l** and **o** in the 1 and 4 positions on the ring are assigned to the peaks at highest ppm shift of 8.9 ppm, similar to **e** and **h**. Proton **n** in the 3 position is assigned to the triplet at a shift of 8.2 ppm similar to **f**. Proton **m** in the 2 position is assigned to the lowest ppm shift peak in the ring system, similar to **g**.
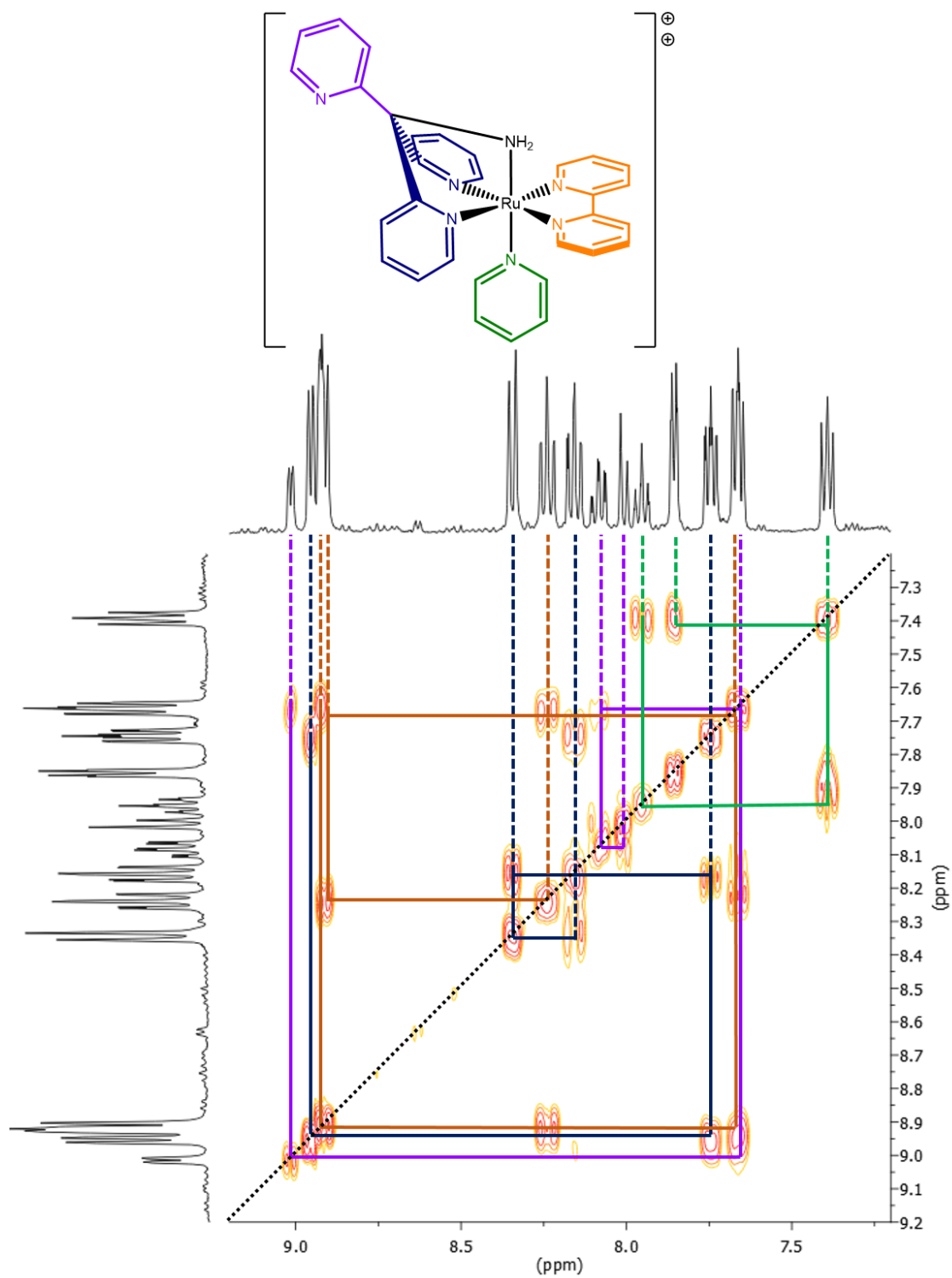
Figure 3.21 - 400 MHz COSY ^{1}H NMR of [Ru(tpyma)(bpy)(py)]$^{2+}$(PF$_6^-$)$_2$ in d$_6$-acetone with coupled protons connected by lines

3.4.3 ^{1}H NMR of $[Ru(tpyma)(phen)(py)]^{2+}(PF_6^-)_2$

The ^{1}H NMR spectrum of $[Ru(tpyma)(phen)(py)]^{2+}(PF_6^-)_2$, recorded in deuterated acetone is shown in figure 3.22 with peaks labelled relating to the lettering on the molecular structure. The lettering is colour coded to the different aromatic ring systems for clarity.
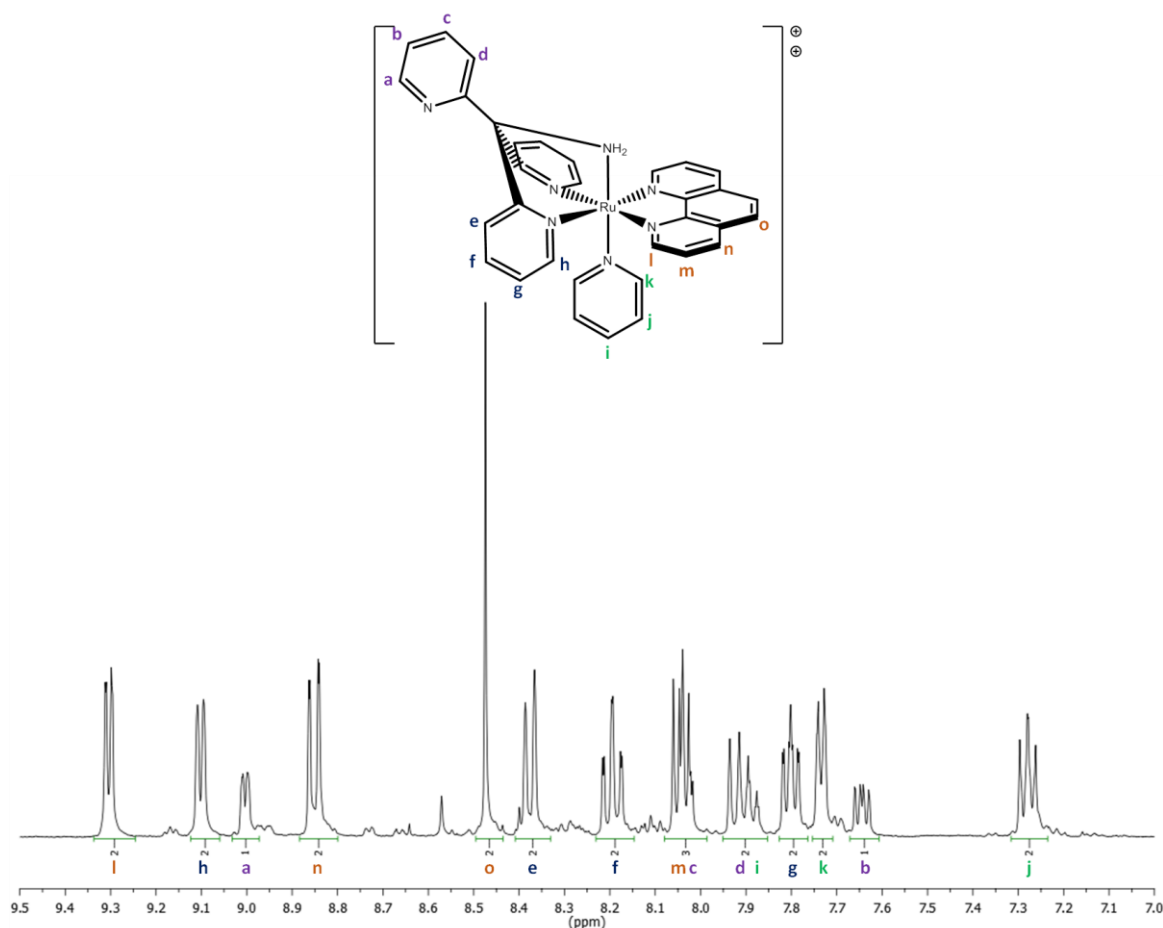
Figure 3.22 - 400 MHz ^{1}H NMR of $[Ru(tpyma)(phen)(py)]^{2+}(PF_6^-)_2$ in d_6-acetone

The assignment of the protons is broadly similar to that of $[Ru(tpyma)(bpy)(py)]^{2+}(PF_6^-)_2$, with the exception of the protons of the bidentate ligand. The COSY interpretation is more straightforward as each ring has a unique number of proton environments or integration values. Protons **a** − **d** are a distanced from the change made in the molecule and as such the ppm shifts of the peaks are relatively unaffected. Proton **a** exhibits the same shift at 9.0 ppm, while **c, d** and **b** are all to lower values by approximately 0.1 ppm. Similarly, protons **i** − **k** appear in the spectrum in the same order and are all shifted to lower ppm by approximately 0.1 ppm. Of the remaining tpyma protons, **h** is the most

affected being deshielded to appear above **a** in the spectrum unlike in the case of the bpy complex. However **e**, **f** and **g** all have very similar shift values to the bpy complex.

The change from bpy to phen is most obvious in the appearance of a large singlet peak assigned to proton **o,** which has no neighbours on the ring system to couple with, resulting in its unique splitting pattern. The peak also shows no cross peak in the COSY NMR, leading to a coupling set of only three proton environments. These are distinguished from the four signal coupling of the tpyma protons. The peaks are more clearly distinguished than in the bpy case as now only the signal for proton **m** is mixed with another signal. The doublet representing proton **l** is more deshielded than its bpy counterpart, while proton **n** appears as a doublet at similer ppm value.
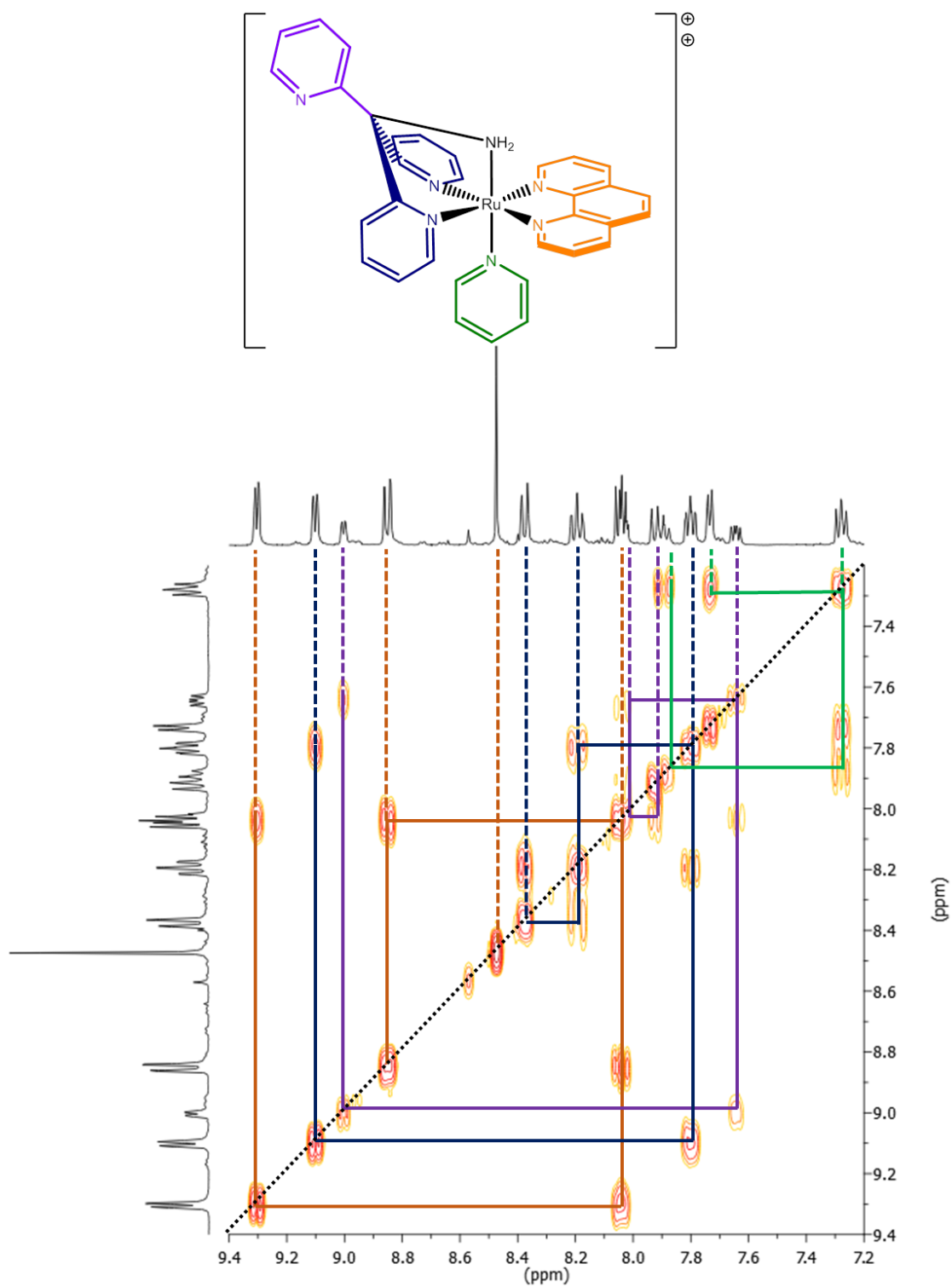
Figure 3.23 - 400 MHz COSY ^{1}H NMR of [Ru(tpyma)(phen)(py)]$^{2+}$(PF$_6^-$)$_2$ in d$_6$-acetone with coupled protons connected by lines

3.4.4 ^{1}H NMR of [Ru(tpyma)(dppz)(py)]$^{2+}$(PF$_6^-$)$_2$

The ^{1}H NMR spectrum of [Ru(tpyma)(dppz)(py)]$^{2+}$(PF$_6^-$)$_2$, recorded in deuterated acetone is shown in figure 3.24 with peaks labelled relating to the lettering on the molecular structure. The lettering is colour coded to the different aromatic ring systems for clarity.
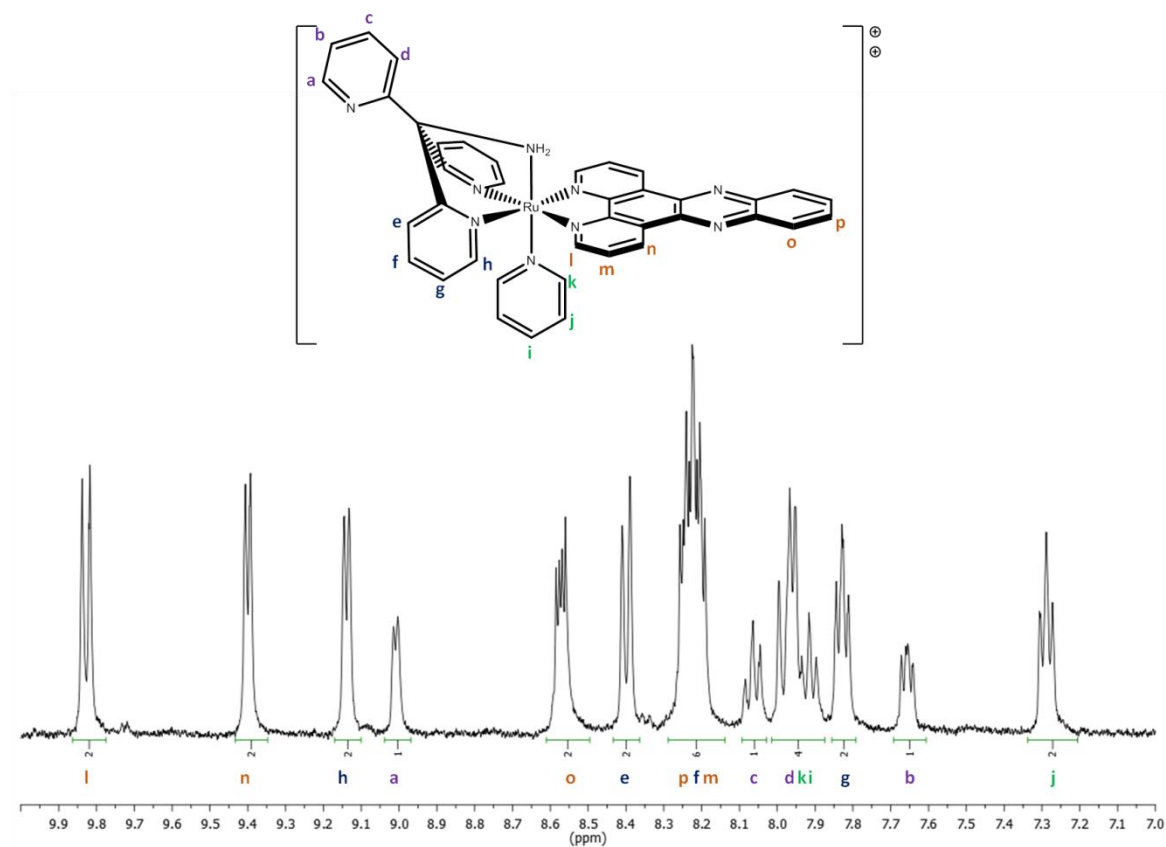
Figure 3.24 - 400 MHz ^{1}H NMR of [Ru(tpyma)(dppz)(py)]$^{2+}$(PF$_6^-$)$_2$ in d$_6$-acetone

The additions made to the bidentate ligand to form the dppz also have very little effect on the peak positions of the other ligands in the molecule. The peaks **a** – **h** relating to the tpyma ligand are almost totally unchanged in their ppm shift values when compared to the spectrum of the phen complex. The only significant shift is a deshielding of the proton **k**, which is the closest proton to the dppz ligand on the pyridine ligand. It is moved downfield by a shift of 0.2 ppm and is subsequently mixed with the peak for the proton **i** and **d.**

The additions made to form the dppz ligand have a large effect on the protons **l** and **n** relative to their equivalents in the phen complex. Both are shifted downfield by a value of 0.5 ppm, while the proton **m** between them is shifted by 0.2 ppm downfield. The added proton environments in the form of **o** and **p,** are assigned on the basis of their proximity to the nitrogen atoms, with **o** being the most deshielded at higher ppm. They exhibit a different form of splitting pattern that is related to the magnetic non-equivalence of the protons. This is observed for the peak relating to **o** but not for **p** which is part of a mixed signal.
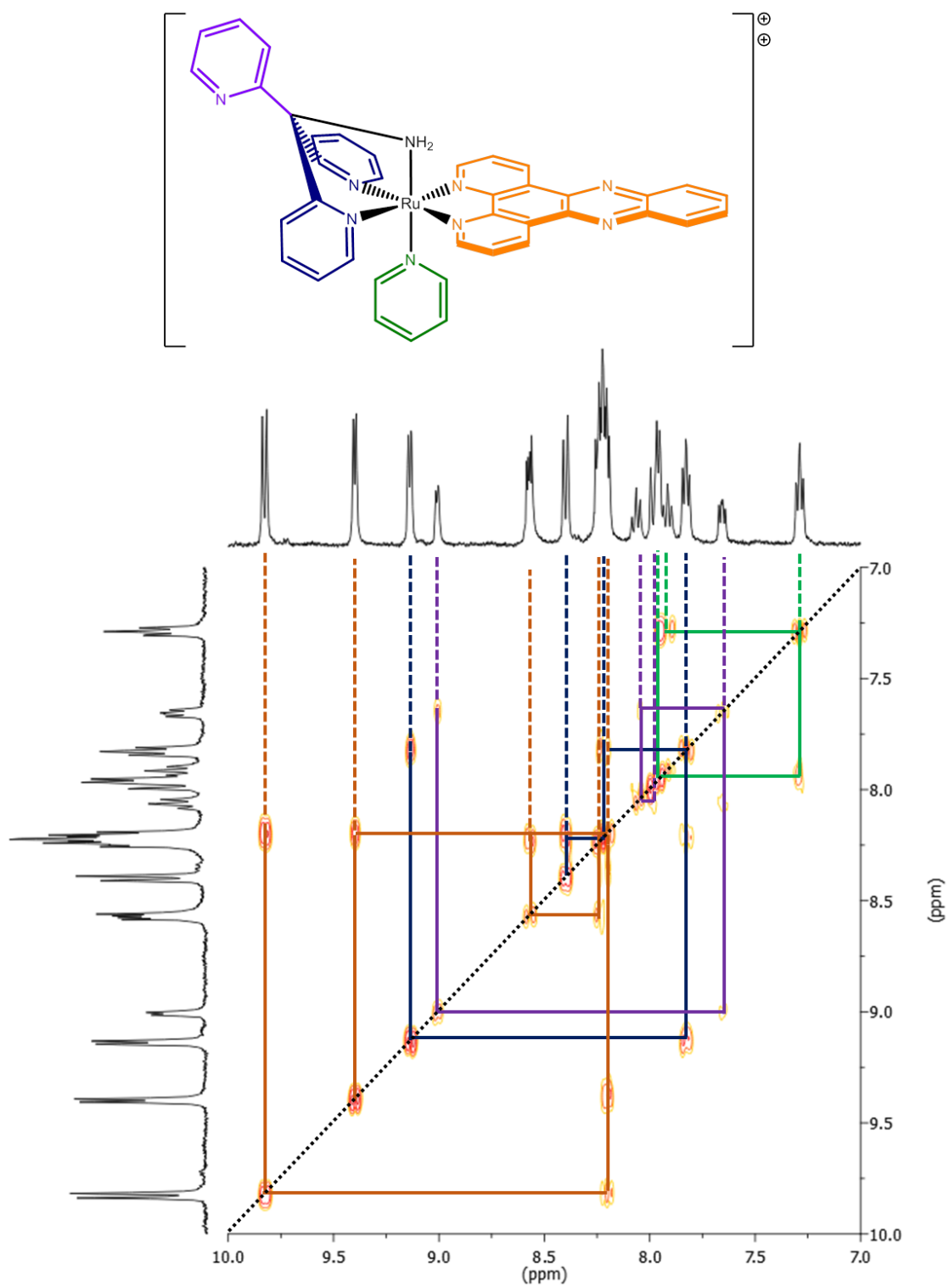
Figure 3.25 - 400 MHz COSY ^{1}H NMR of [Ru(tpyma)(dppz)(py)]$^{2+}$(PF$_6$)$_2$ in d$_6$-acetone with coupled protons connected by lines

3.4.5 ^{1}H NMR of [Ru(tpyma)(dppn)(py)]$^{2+}$(PF$_6^-$)$_2$

The ^{1}H NMR spectrum of [Ru(tpyma)(dppn)(py)]$^{2+}$(PF$_6$)$_2$, recorded in deuterated acetone is shown in figure 3.26 with peaks labelled relating to the lettering on the molecular structure. The lettering is colour coded to the different aromatic ring systems for clarity.
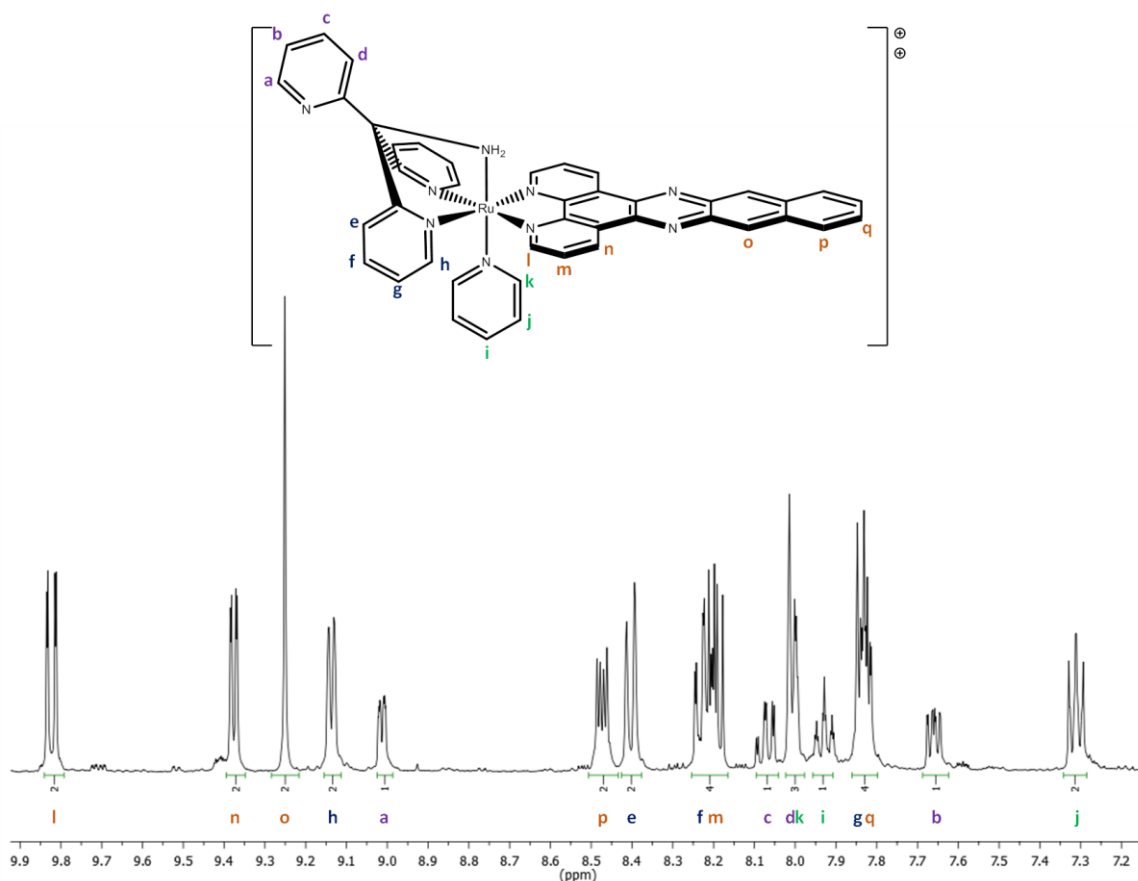
Figure 3.26 - 400 MHz ^{1}H NMR of [Ru(tpyma)(dppn)(py)]$^{2+}$(PF$_6$)$_2$ in d$_6$-acetone

On changing the bidentate ligand to dppn, the tpyma protons **a – h** remain unchanged when compared to the dppz complex. A further shift downfield of proton **k**, the pyridine proton nearest the changed ligand, is observed such that it becomes distinct from the signal of proton **i**. The protons **l – n** are also not moved compared to their equivalent protons in the dppz complex. The key difference between the spectra of the two complexes is the introduction of a large singlet signal at 9.2 ppm. This is assigned to proton **o** that is isolated from the coupling effects of other protons. Proton **p** shares a similar shift value and splitting pattern with proton **o** in the dppz complex. Proton **q**

is also an added signal to the spectrum. The splitting pattern is not observed due to mixing with the signal of proton **g**.
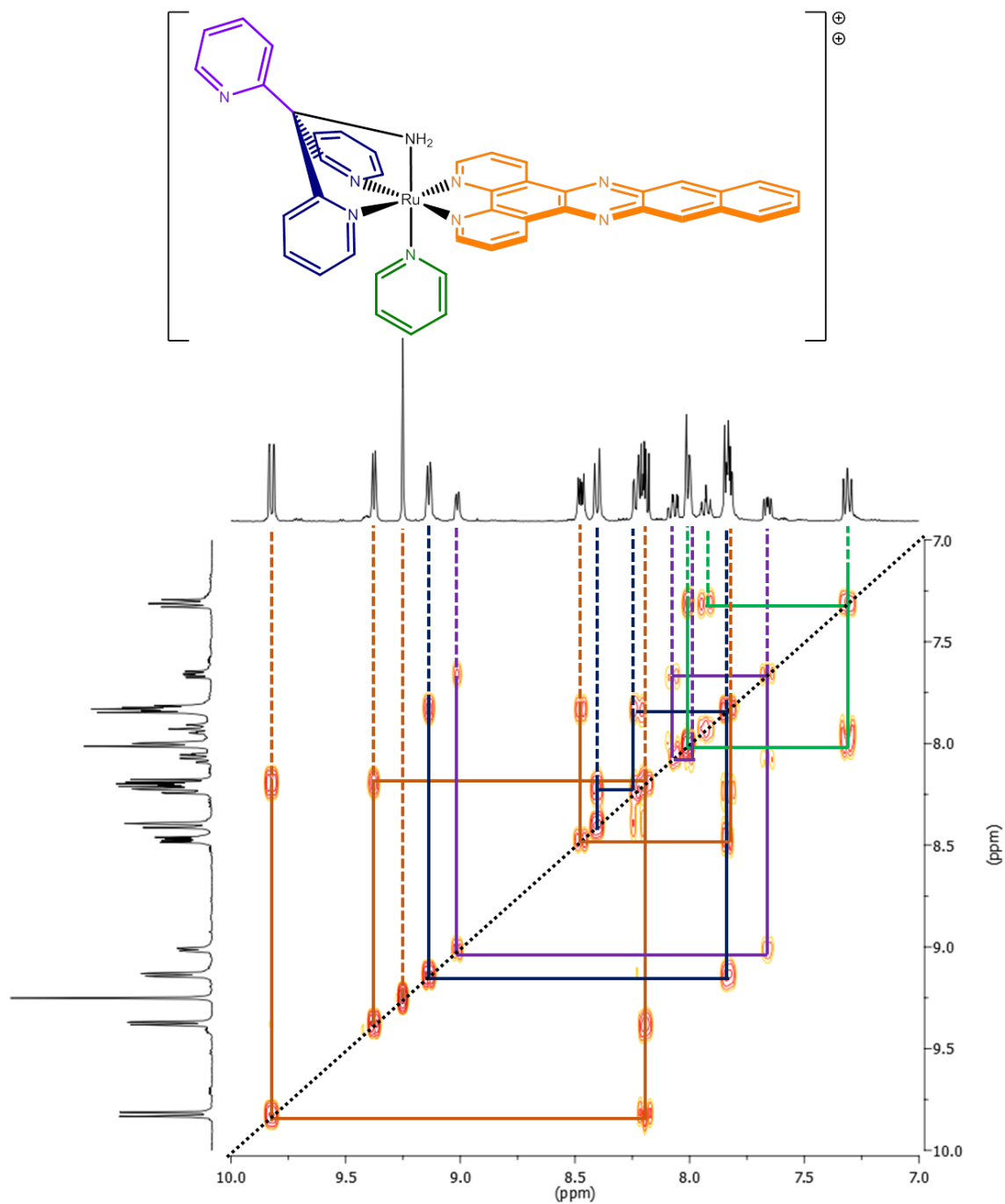
Figure 3.27 - 400 MHz COSY ^{1}H NMR of [Ru(tpyma)(dppn)(py)]$^{2+}$(PF$_6^-$)$_2$ in d$_6$-acetone with coupled protons connected by lines

3.4.6 ^{1}H NMR of [Ru(tpyc)(dppz)(py)]$^{2+}$(PF$_6^-$)$_2$

The ^{1}H NMR spectrum of [Ru(tpyma)(dppz)(py)]$^{2+}$Cl$^-_2$, recorded in deuterated methanol is shown in figure 3.28.
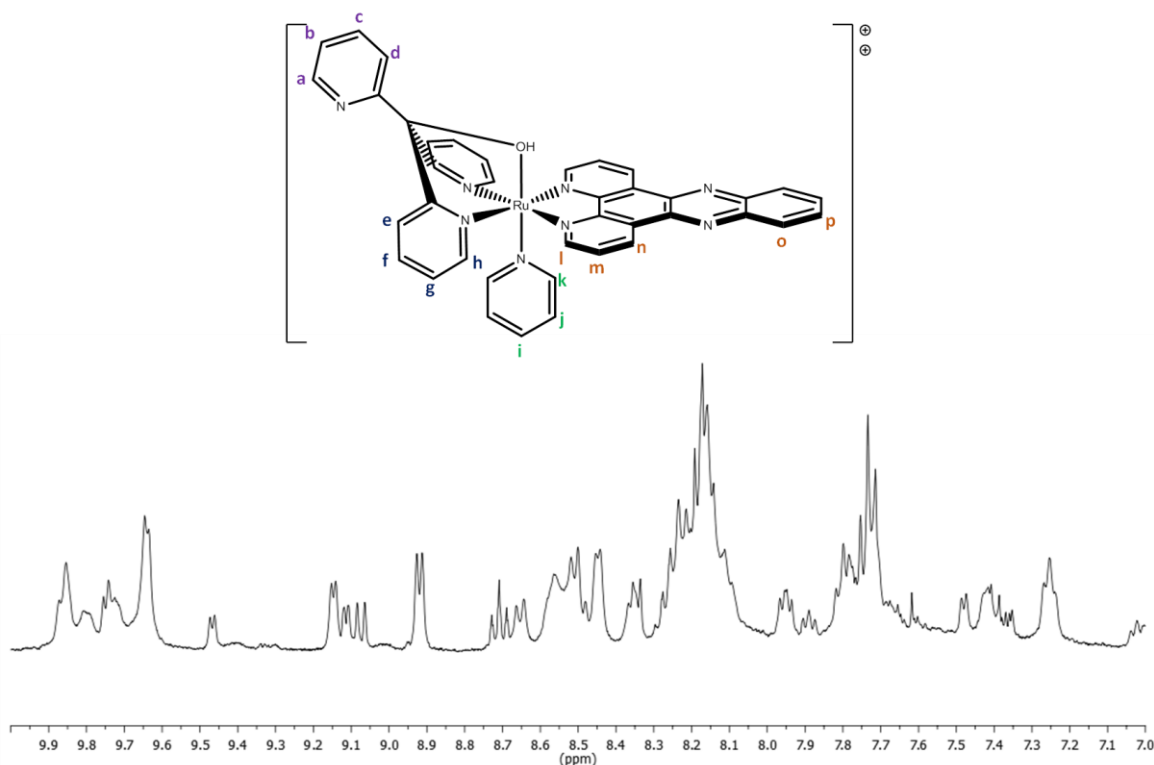
Figure 3.28 - 400 MHz ^{1}H NMR of [Ru(tpyc)(dppz)(py)]$^{2+}$Cl$^-_2$ in d$_3$-MeOD

The NMR of [Ru(tpyc)(dppz)(py)]$^{2+}$ would be expected to be similar to that of [Ru(tpyma)(dppz)(py)]$^{2+}$ with some shift due to the replacement of the amine with a hydroxyl group. Multiple attempts were made to obtain an NMR spectrum that was clear and could be assigned. This included attempts with both the PF$_6$ salt and the chloride salt, whose spectrum is shown in figure 3.28. The spectra observed were all poorly resolved, with broad peaks making integration difficult. The chloride salt provided the best spectrum. This broadening may point to a problem in solubility in the sample. The complex nature of the spectrum may also be due to multiple isomers being present, due to multiple binding modes of tpyc. Alternatively there may be a stability issue with the complex, and it is degrading in solution, possibly due to photoinstability.

3.5 Photophysical Studies of tris(pyridyl) complexes

3.5.1 UV-Visible absorption of [Ru(tpyma)(NN)(py)]$^{2+}$

The UV-Visible spectra of the [Ru(tpyma)(NN)(py)]$^{2+}$ series were recorded in both acetonitrile (as hexafluorophosphate salts) and buffer solution (as chloride salts). The spectra are shown in figure 3.29 and figure 3.30. The data obtained for each complex is summarised in table 3.1 and table 3.2.
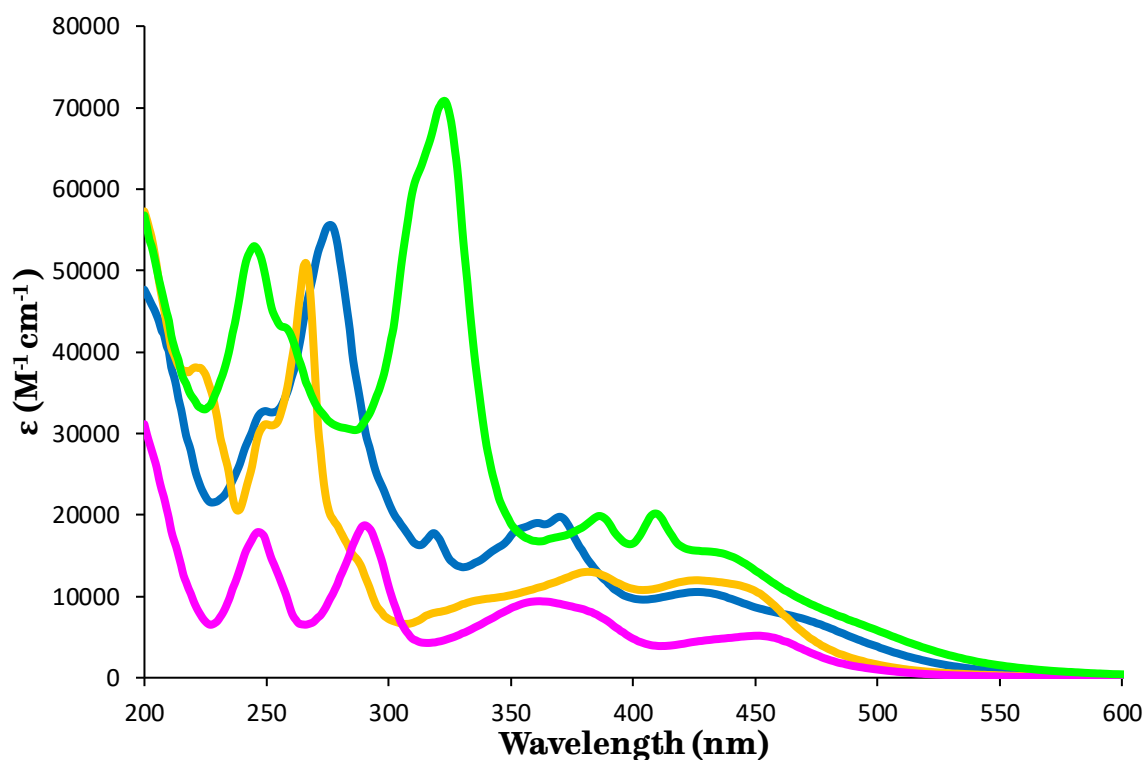
Figure 3.29 - UV-visible absorption spectrum of the series [Ru(tpyma)(NN)(py)](PF$_6$)$_2$ recorded in acetonitrile, where NN = bpy (■), phen (■), dppz (■) or dppn (■)

Complex	λ_{max} (nm)	ε_{max} (M^{-1} cm^{-1})	Assignment
[Ru(tpyma)(bpy)(py)](PF$_6$)$_2$	247	17866	$\pi - \pi^*$
	290	18708	$\pi - \pi^*$
	362	9390	$\pi - \pi^*$
	452	5154	MLCT
[Ru(tpyma)(phen)(py)](PF$_6$)$_2$	221	38105	$\pi - \pi^*$
	250	31121	$\pi - \pi^*$
	266	50935	$\pi - \pi^*$
	382	12996	MLCT
	426	11965	MLCT
[Ru(tpyma)(dppz)(py)](PF$_6$)$_2$	249	32719	$\pi - \pi^*$
	276	55588	$\pi - \pi^*$
	318	17730	$\pi - \pi^*$
	352 (sh)	18007	$\pi - \pi^*$
	361	18993	$\pi - \pi^*$
	370	19759	$\pi - \pi^*$
	426	10527	MLCT
	472 (sh)	7007	MLCT
[Ru(tpyma)(dppn)(py)](PF$_6$)$_2$	244	52988	$\pi - \pi^*$
	257 (sh)	42891	$\pi - \pi^*$
	322	70798	$\pi - \pi^*$
	385	19857	$\pi - \pi^*$
	408	20157	$\pi - \pi^*$
	436 (sh)	15233	MLCT

Table 3.1 - Summary of the maximal absorption of the UV-Visible spectra of [Ru(tpyma)(NN)(py)](PF$_6$)$_2$ recorded in acetonitrile (sh = shoulder)

All the complexes in the series possess strong absorbance bands below 350 nm, with the spectra exhibiting sharp, well defined peaks in this region. These are commonly assigned to $\pi - \pi^*$ in the polypyridyl ligands. They also share lower intensity broader bands above this region, common to metal to ligand charge transfer (MLCT) states commonly seen in ruthenium complexes. This gives all the complexes a red/orange colour in solution.

The spectrum of [Ru(tpyma)(bpy)(py)](PF$_6$)$_2$ shares common features with the reported spectrum of [Ru(bpy)$_3$]$^{2+}$. The main similarity between the spectra is the band at 290 nm which is comparable to the 285 nm band reported for the tris-bpy complex.[12] This is assigned to $\pi - \pi^*$ transitions of the bpy ligand itself and is assigned in the same manner for the tpyma complex reported here. The other dominant band at 247 nm is in a region that is assigned to *d-d* transitions in [Ru(bpy)$_3$]$^{2+}$, which are characterised by low absorption intensity.[12] This cannot be said of the band in the tpyma-bpy complex as it is equal to the bpy transition in intensity. It can also be seen that a peak is present at very similar wavelength in each of the spectra for the tpyma complex series. It is therefore likely to result from a feature that each complex shares, either $\pi - \pi^*$ of the tpyma ligand or the pyridine ligand. The peak at 362 nm is also not shared by the tris-bpy complex and is also assigned to a $\pi - \pi^*$ transition in one of the ligands. The broad band observed at 452 nm shares its maximum with the MLCT band reported for the tris-bpy complex,[12] and as such is assigned to an MLCT transition in the tpyma complex.

The spectrum obtained for the [Ru(tpyma)(phen)(py)](PF$_6$)$_2$ exhibits its strongest absorption at 266 nm. There is a shoulder at 221 nm. This double peak feature appears very similar to that reported for the un-coordinated phenanthroline ligand and is assigned to a $\pi - \pi^*$ in the ligand itself.[13] Thus the same assignment is made for the tpyma complex. As alluded to previously, the spectrum shares a similar peak with bpy complex at 250 nm, possibly a $\pi - \pi^*$ of tpyma. The broader, less intense bands at 382 and 426 nm are assigned to MLCT transitions as they are similar to those reported for [Ru(phen)$_3$]$^{2+}$.[14]

The [Ru(tpyma)(dppz)(py)](PF$_6$)$_2$ complex shows a more intense absorption than the phen and bpy equivalents, with a generally greater extinction co-efficient. The main peak at 276 nm is close to the main peak at 285 nm reported for [Ru(dppz)$_3$]$^{2+}$ in DMF.[15] This is assigned to $\pi - \pi^*$ in the dppz ligand. There is also a small peak prior to the main absorbance at 249 nm that is assigned to the tpyma $\pi - \pi^*$ in a similar position to both the bpy and phen complexes. The broader band from $350 - 370$ nm exhibiting multiple maxima, is also a feature of the dppz ligand. A very similar pattern of absorptions is observed for the un-coordinated ligand in DMF, with a band from 340 -380 nm.[16] The main MLCT band is observed at 426 nm with a slight shoulder at 472 nm. These bands

are assigned in the same way as the MLCT band of [Ru(dppz)$_3$]$^{2+}$ in DMF, which exhibits a band at 436 nm and shoulder at 460 nm.[15]

The [Ru(tpyma)(dppn)(py)](PF$_6$)$_2$ complex gives a spectrum containing a double hump absorption which is distinctive to dppn containing species. These appear in the spectrum at 244 and 322 nm which is very similar to the absorption bands reported for [Ru(tpm)(dppn)(py)]$^{2+}$, which shows the double hump at 243 and 322 nm.[17] Along with the peaks nearby these are assigned to the $\pi - \pi^*$ of the dppn ligand. The MLCT band is seen with a shoulder at 436 nm with a long tail off, that may contain a second shoulder ~500 nm similar to that reported for the tpm complex.[17]
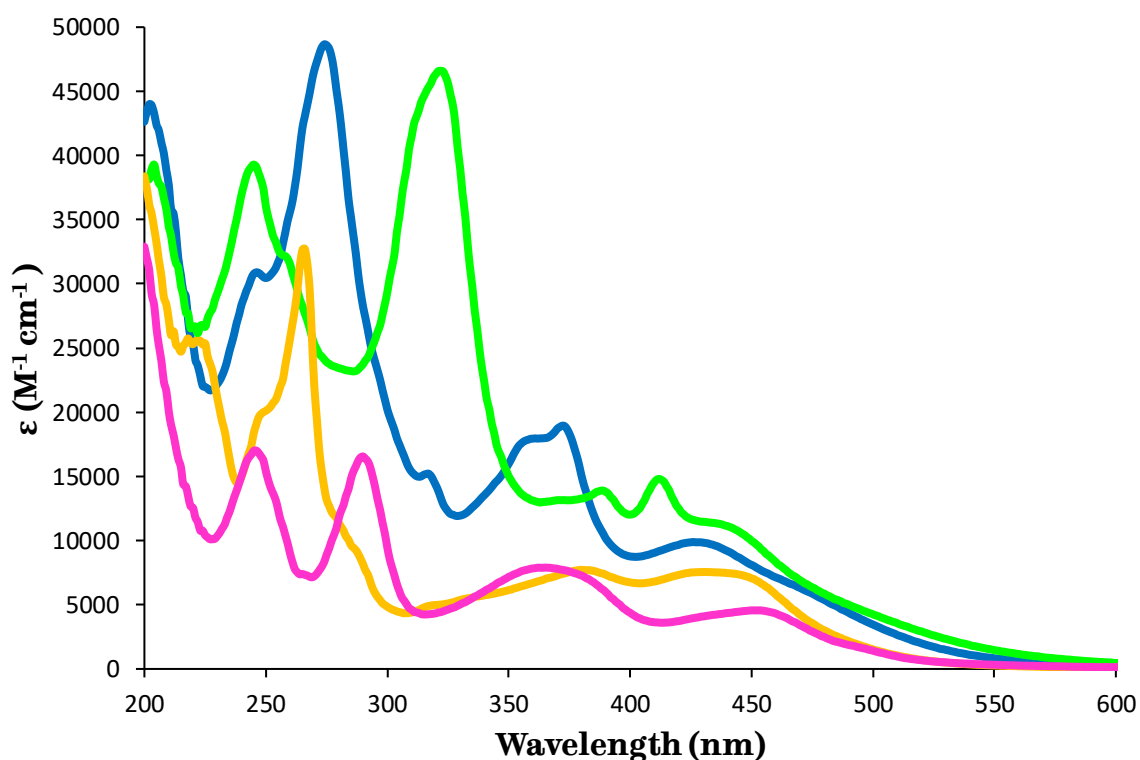
Figure 3.30 - UV-visible absorption spectrum of the series [Ru(tpyma)(NN)(py)]Cl$_2$ recorded in buffer solution, where NN = bpy (■), phen (■), dppz (■) or dppn (■)

Complex	λ_{max} (nm)	ε_{max} (M^{-1} cm^{-1})	Assignment
[Ru(tpyma)(bpy)(py)]Cl$_2$	246	17015	$\pi - \pi^*$
	290	16555	$\pi - \pi^*$
	365	7893	$\pi - \pi^*$
	453	4565	MLCT
[Ru(tpyma)(phen)(py)]Cl$_2$	218	25748	$\pi - \pi^*$
	248 (sh)	19912	$\pi - \pi^*$
	266	32733	$\pi - \pi^*$
	380	7719	MLCT
	431	7555	MLCT
[Ru(tpyma)(dppz)(py)]Cl$_2$	203	43999	$\pi - \pi^*$
	247	30901	$\pi - \pi^*$
	275	48655	$\pi - \pi^*$
	318	15215	$\pi - \pi^*$
	362	17963	$\pi - \pi^*$
	373	18944	$\pi - \pi^*$
	427	9887	MLCT
[Ru(tpyma)(dppn)(py)]Cl$_2$	204	39288	$\pi - \pi^*$
	245	39296	$\pi - \pi^*$
	258 (sh)	32257	$\pi - \pi^*$
	322	46604	$\pi - \pi^*$
	389	13889	$\pi - \pi^*$
	412	14801	$\pi - \pi^*$
	443 (sh)	10893	MLCT

Table 3.2 - Summary of the maximal absorption of the UV-Visible spectra of [Ru(tpyma)(NN)(py)]Cl$_2$ recorded in buffer solution (sh = shoulder)

The spectra of the chloride salts recorded in aqueous environment are broadly similar to those recorded in acetonitrile for the PF$_6$ salts. The extinction co-efficient is lower in some cases, most notably in the case of the dppn ligand. The maximal absorption are generally at the same energy with a few of the peaks shifting 1-3 nm.

3.5.2 Luminescent emission of [Ru(tpyma)(NN)(py)]²⁺

The emission spectra of the [Ru(tpyma)(NN)(py)]²⁺ series were recorded in acetonitrile and buffer solution. The spectra are shown in figure 3.31.
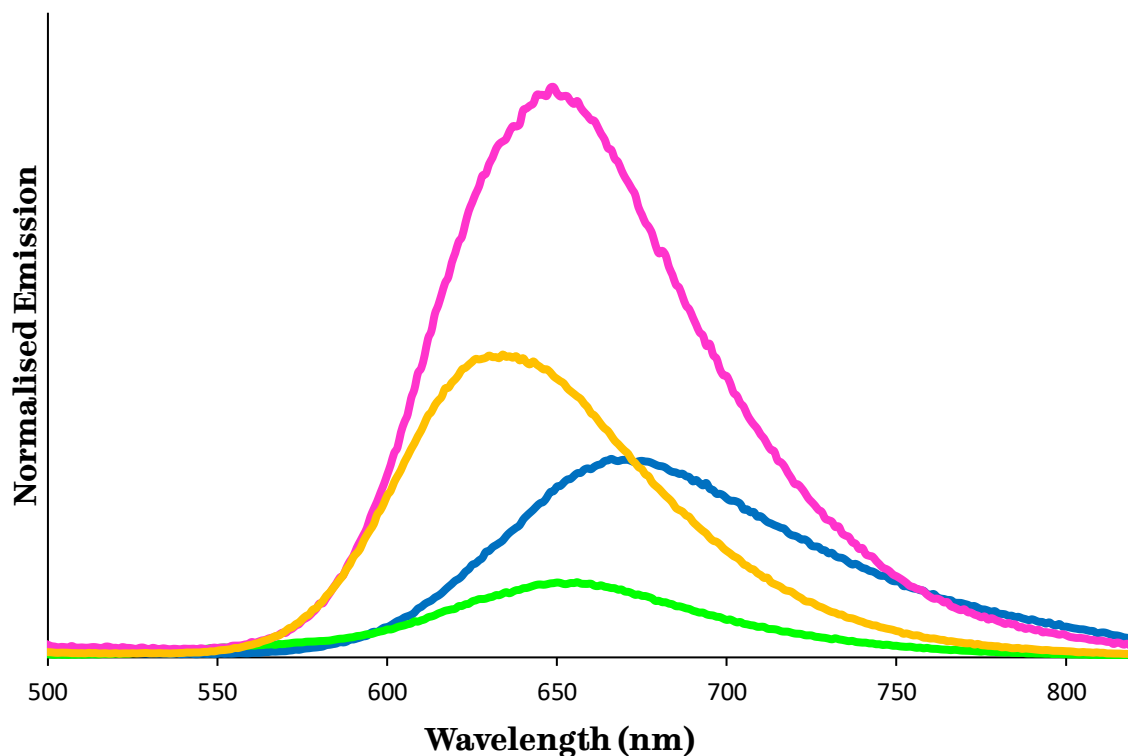
Figure 3.31 - Luminescent emission spectra of the series [Ru(tpyma)(NN)(py)](PF$_6$)$_2$ recorded in acetonitrile, where NN = bpy (■), phen (■), dppz (■) or dppn (■). Complexes excited at 426 nm.

Each of the complexes were made up to the same concentration and excited at the same wavelength. The emission was then normalised by dividing the photon count by the extinction co-efficient of each complex at 426 nm. This allows for a rough comparison of the emission intensity, accounting for the complexes different absorptions. It is not as reliable as comparison of the quantum yield of each complex due to differences in excitation maxima which have not been considered. By this measure the series in order of emission is phen > bpy > dppz > dppn.

The noise in the data made the determination of the max emission energy difficult. To combat this issue the data was fitted using software and the wavelength of the

maximum emission was estimated using the fitted data. The emission maxima are summarised in table 3.3.

Complex	λ_{max} (nm)
[Ru(tpyma)(bpy)(py)](PF$_6$)$_2$	648
[Ru(tpyma)(phen)(py)](PF$_6$)$_2$	633
[Ru(tpyma)(dppz)(py)](PF$_6$)$_2$	670
[Ru(tpyma)(dppn)(py)](PF$_6$)$_2$	655

Table 3.3 Emission maxima for the series [Ru(tpyma)(NN)(py)](PF$_6$)$_2$

3.5.3 UV-Visible absorption of [Ru(NNN)(dppz)(py)]$^{2+}$

The UV-Visible spectrum of the [Ru(tpyc)(dppz)(py)]$^{2+}$ was recorded in acetonitrile, with the spectra shown in figure 3.32 alongside the spectrum for the tpyma complex for comparison. The data obtained for the complex is summarised in table 3.4.
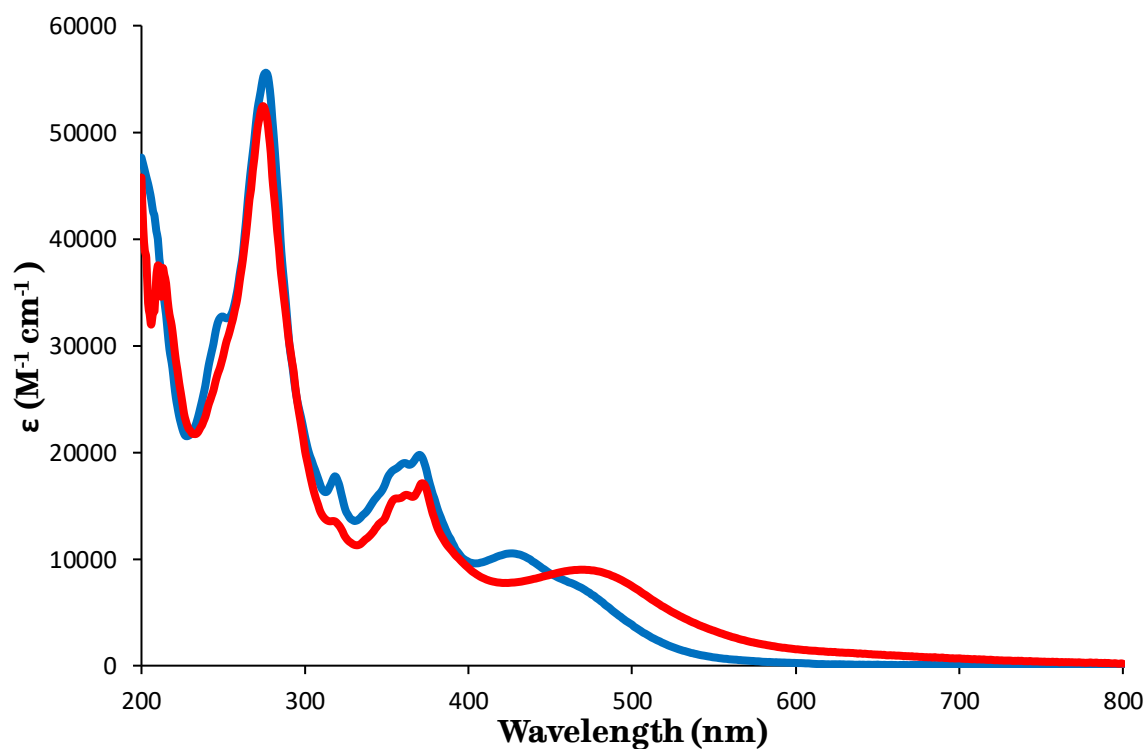
Figure 3.32 - UV-visible absorption spectrum of complexes [Ru(NNN)(dppz)(py)](PF$_6$)$_2$ recorded in acetonitrile, where NNN = tpyma (■) or tpyc (■)

Complex	λ_{max} (nm)	ε_{max} (M^{-1} cm^{-1})	Assignment
[Ru(tpyc)(dppz)(py)](PF$_6$)$_2$	210	37522	$\pi - \pi^*$
	274	52440	$\pi - \pi^*$
	317 (sh)	13557	$\pi - \pi^*$
	361	16016	$\pi - \pi^*$
	372	17088	$\pi - \pi^*$
	469	8996	MLCT

Table 3.4 - Summary of the maximal absorption of the UV-Visible spectra of [Ru(tpyc)(dppz)(py)](PF$_6$)$_2$ recorded in acetonitrile (sh = shoulder)

The absorption bands for the tpyc complex are observed to be broadly similar to the tpyma complex. Interestingly the band 247 nm has been lost in the change to tpyc, adding to the evidence that the band is due to the $\pi - \pi^*$ of the tpyma ligand. The assignments of the absorption bands are made in the same way as for the tpyma complex. The tpyc spectrum also includes a peak at 210 nm which could be due to $\pi - \pi^*$ in the tpyc ligand. The other key difference is the shift in the MLCT which becomes much lower in energy, shifting to 469 nm. This is also observed visually as, when dissolved the compound appears as a much darker coloured solution compared to the tpyma equivalent. The change to the tpyc ligand also seems to have affected the absorbance of the complex given that the extinction co-efficient is slightly lower.

3.5.4 Luminescent emission of [Ru(NNN)(dppz)(py)]$^{2+}$

The emission spectrum of the [Ru(tpyc)(dppz)(py)]$^{2+}$ was recorded in acetonitrile, with the spectra shown in figure 3.33, alongside the spectrum for the tpyma complex for comparison.
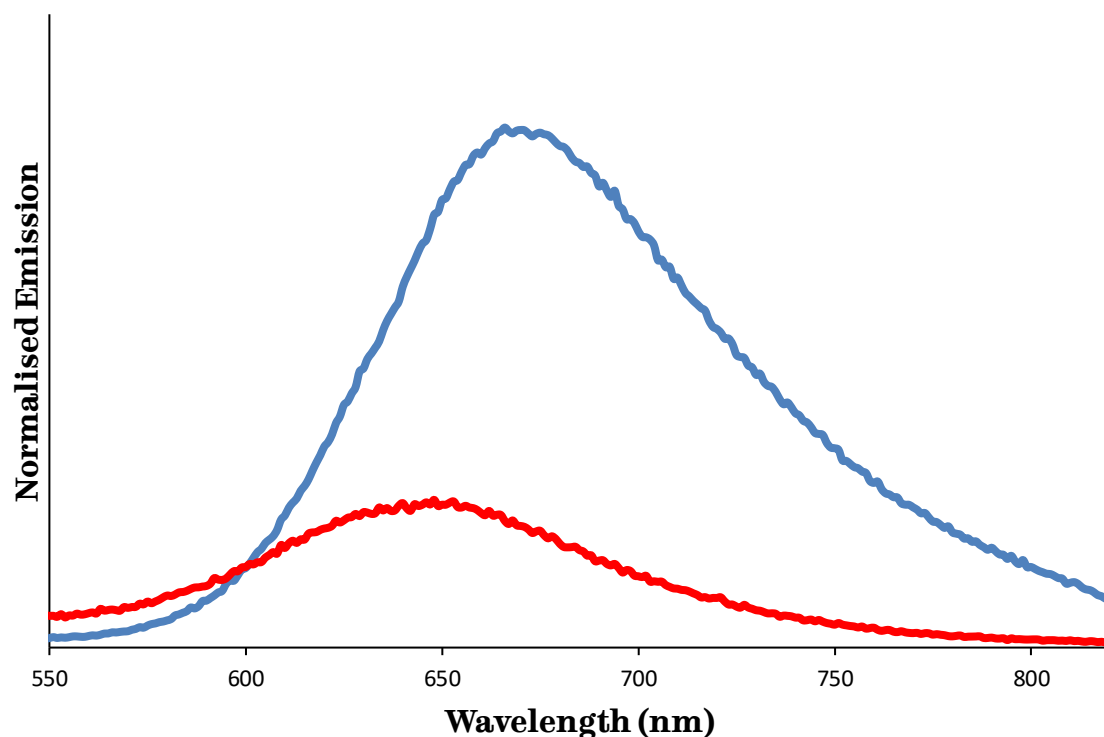
Figure 3.33 - Luminescent emission spectra of complexes [Ru(NNN)(dppz)(py)](PF$_6$)$_2$ recorded in acetonitrile, where NNN = tpyma (▬) or tpyc (▬). Complexes excited at 426 nm.

The change from tpyma to tpyc has resulted in a marked shift in the emission of the complex. The emission maxima shifts from 670 nm for the tpyma complex to 647 nm for the tpyc complex. There also appears to be a much lower emission from the tpyc complex, as it results in lower photon counts for a similar concentration, although this comparison is less reliable than the quantum yield measurement that would shed more light on this change. This measurement should be considered before attempts to use the tpyc ligand as a surface attachment as it may be rendering the complex less emissive, which would make it less suited to sensor applications.

3.6 Electrochemical Studies of tris(pyridyl) complexes

Cyclic voltammetry of each of the [Ru(tpyma)(NN)(py)](PF$_6$)$_2$ complexes (where NN = bpy, phen, dppz, dppn) and the [Ru(tpyc)(dppz)(py)](PF$_6$)$_2$ complex was studied in DMF solution. The oxidation and reduction potentials were measured using a scan rate of 100 mV s^{-1} against a Ag/AgCl reference electrode and a background electrolyte of Bu$_4$N(PF$_6$) at 0.1 M concentration. The results are summarised in table 3.5 where the potentials are quoted as estimated half-wave potential based on the anodic and cathodic potentials. The separation between these peaks is indicated in mV in brackets.

Complex	Oxidation		Reduction
	E$_{1/2}$	Fc/Fc$^+$	E$_{1/2}$
[Ru(tpyma)(bpy)(py)](PF$_6$)$_2$	0.92 (50)	0.53 (7)	-1.36 (11)
[Ru(tpyma)(phen)(py)](PF$_6$)$_2$	0.83 (38)	0.53 (7)	-1.36 (9)
[Ru(tpyma)(dppz)(py)](PF$_6$)$_2$	0.84 (38)	0.51 (10)	-0.88 (11)
[Ru(tpyma)(dppn)(py)](PF$_6$)$_2$	1.07 [a]	0.53 (7)	-0.45 [a], -0.76 (7), -1.24 [a], -1.43 [a]
[Ru(tpyc)(dppz)(py)](PF$_6$)$_2$	0.50 (6)	-	-0.89 (8)

Table 3.5 - Summary of data obtained from cyclic voltammetry measurements of the series [Ru(tpyma)(NN)(py)](PF$_6$)$_2$ in volts vs. Ag/AgCl. All measurements made in DMF with 0.1 M Bu$_4$NPF$_6$. [a] Non reversible redox

The single reversible oxidation measured for the bpy, phen and dppz complexes can be assigned to the Ru(II)/Ru(III) redox couple as has been done previously for ruthenium complexes including the tpm ligand,[17] and a similar series of compounds.[18] The values of E$_{1/2}$ for similar ruthenium complexes has been rationalised on considering the σ- and π-donating capability of the ligands. This potentially gives an interesting insight into the co-ordination mode of tpyc. While it could not be determined by X-ray crystallography the CV results suggest that the oxygen is co-ordinated. As the oxidation potential is related to the oxidation state of the ruthenium centre, the stark difference in E$_{1/2}$ likely points to a different co-ordination sphere. It may be that the oxygen atom binding to the ruthenium centre does not share the stabilising effect of the nitrogen atom when it is bound. If the three pyridines were co-ordinated in the cases of both tpyma and tpyc, a large difference in E$_{1/2}$ would not be expected. It is also unlikely that three pyridines are co-ordinated as pyridine is a good π-acceptor and thus would be expected to stabilise Ru(II) by taking electron density from the Ru centre.[17]

The reduction potentials can be attributed to the bidentate ligand that is varied across the series. This is seen where the two complexes that share the dppz ligand, also share the same reduction potential. The values of these reductions are similar to those reported for a similar series of compounds.[18] The dppz and dppn ligands are more readily reduced due to a lower lying π^* energy level of the phenazine unit, when compared with phen and bpy.[17] The cyclic voltammetry curves for all tested compounds are shown in figure 3.34 to 3.38
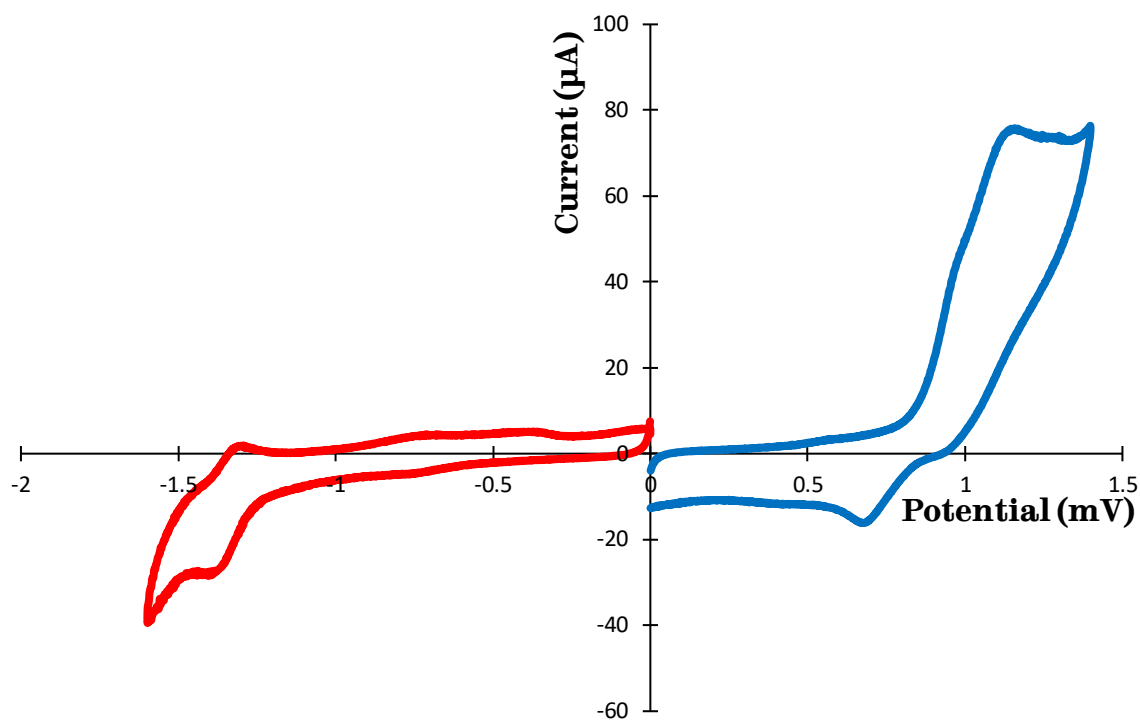
Figure 3.34 – Cyclic voltammetary curve of [Ru(tpyma)(bpy)(py)](PF$_6$)$_2$ measured in DMF at 100mV/s
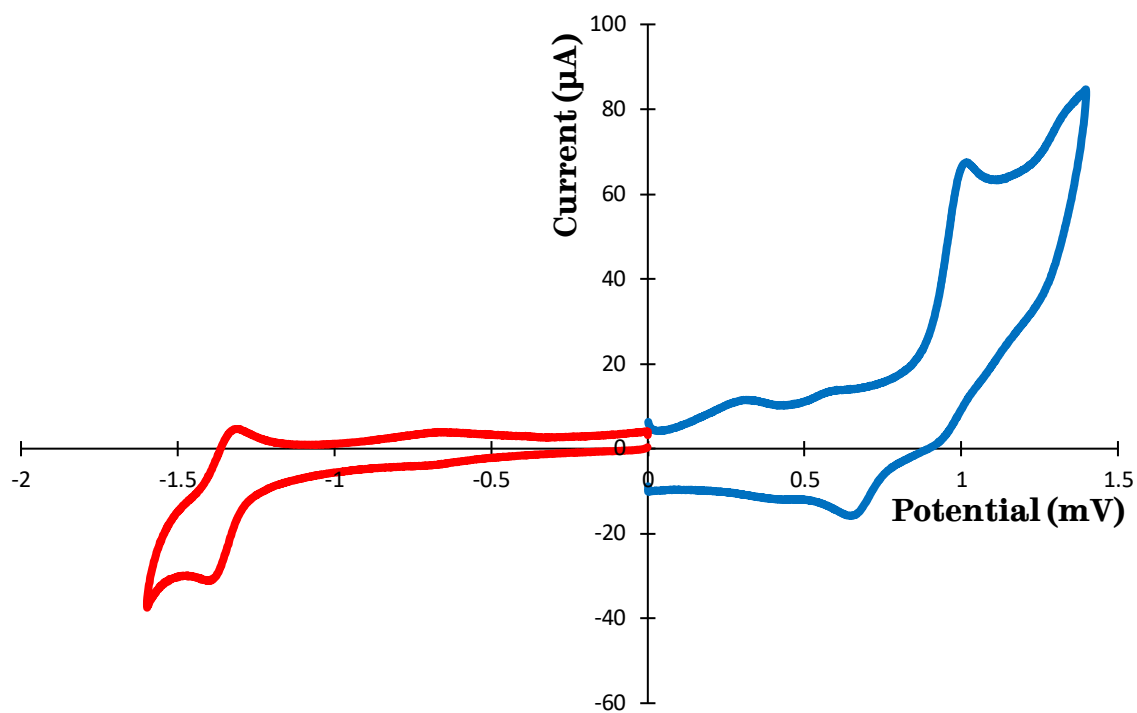
Figure 3.35 – Cyclic voltammetary curve of [Ru(tpyma)(phen)(py)](PF$_6$)$_2$ measured in DMF at 100mV/s
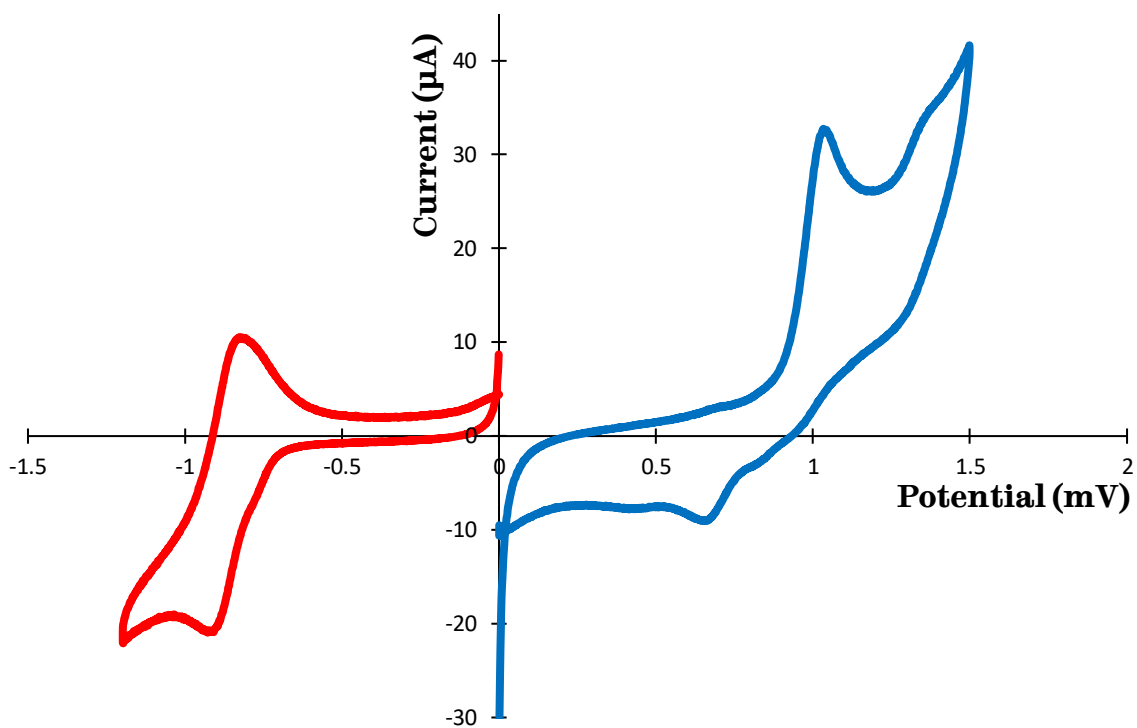
Figure 3.36 – Cyclic voltammetary curve of [Ru(tpyma)(dppz)(py)](PF$_6$)$_2$ measured in DMF at 100mV/s
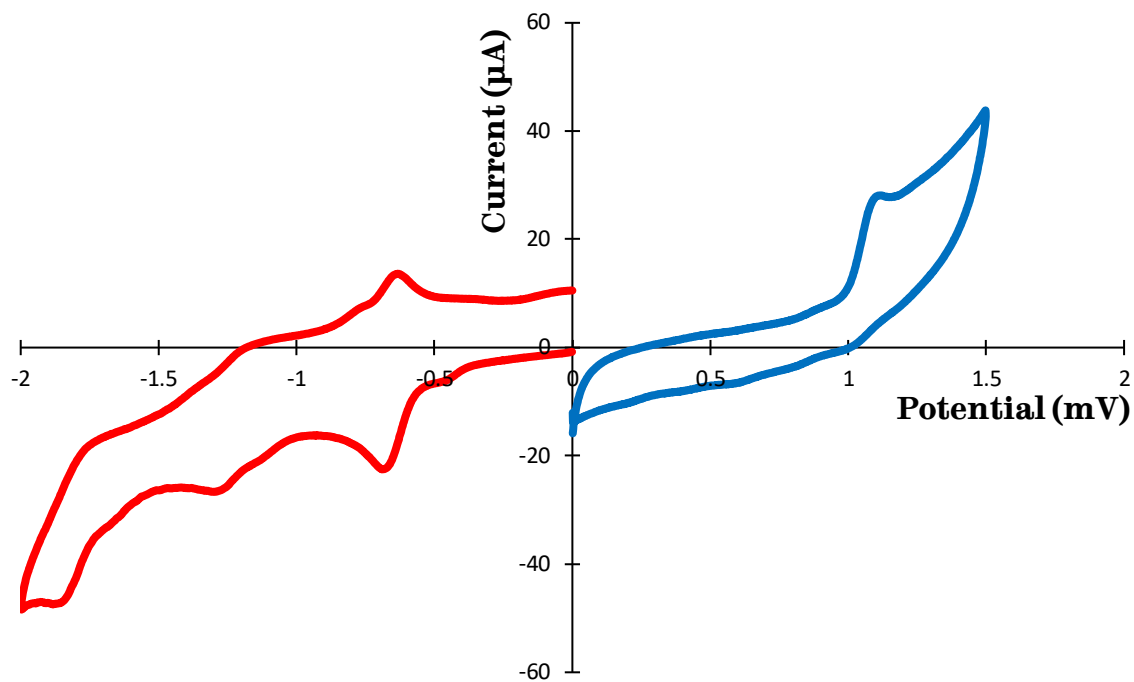
Figure 3.37 – Cyclic voltammetary curve of [Ru(tpyma)(dppn)(py)](PF$_6$)$_2$ measured in DMF at 500mV/s
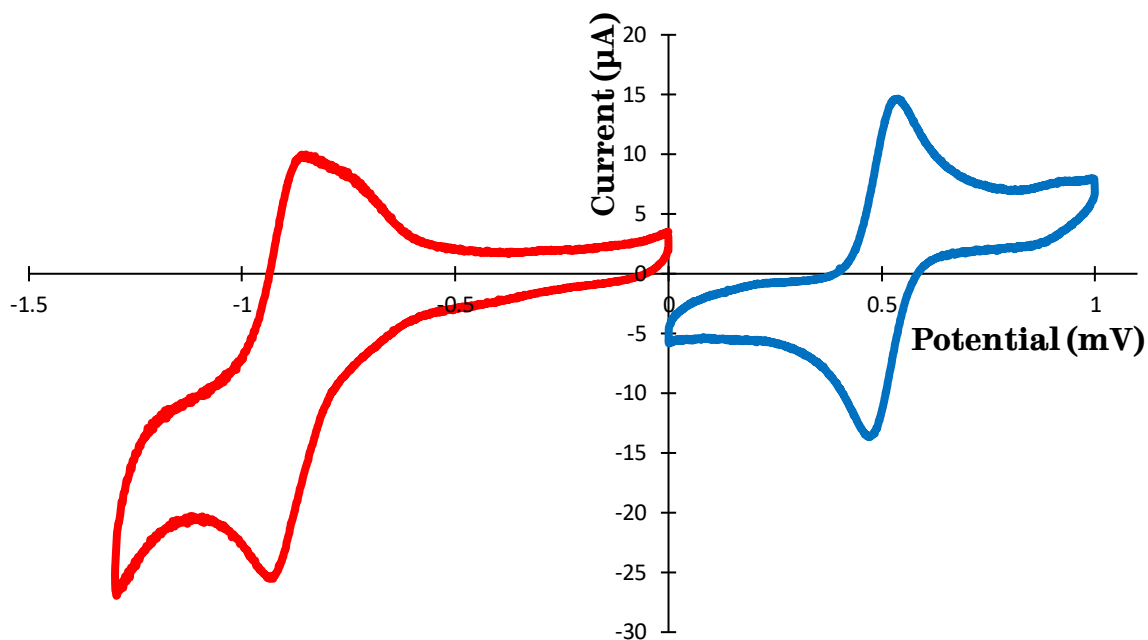
Figure 3.38 – Cyclic voltammetary curve of [Ru(tpyc)(dppz)(py)](PF$_6$)$_2$ measured in DMF at 100mV/s

3.7 Synthesis of di(pyridyl) based complexes

Due to the unexpected binding mode of tris(pyridyl) ligands, a new approach was devised, to try and replace the pendant pyridine with a moiety capable of coupling to a surface. First di(pyridyl)methylamine (dpyma) was synthesised and reacted with [RuCl$_2$(dmso)$_2$(dppz)] in the same was as for tpyma to assess whether it would co-ordinate in the same fashion. Subsequently the dpyma unit was altered to introduce an alkyne moiety, in a similar way to that which was introduced to tpm in the ligand initially designed for the project. This should retain tripodal co-ordination, through two pyridines and the amine group, whilst adding alkyne function to the complex for use in a coupling reaction with an azide functional surface.

3.7.1 Synthesis of di(2-pyridyl)oxime

Di(2-pyridyl)oxime is synthesised by the method of Rana *et. al.*,[19] as a precursor in the making of di(2-pyridyl)methylamine. Di(2-pyridyl)ketone is heated in the presence of aqueous hydroxylamine hydrochloride. The hydroxylamine reacts with the ketone portion, eliminating the oxygen to form the oxime. On cooling the oxime precipitates from the solution. Purification is achieved by a recrystallisation from water and acetone.
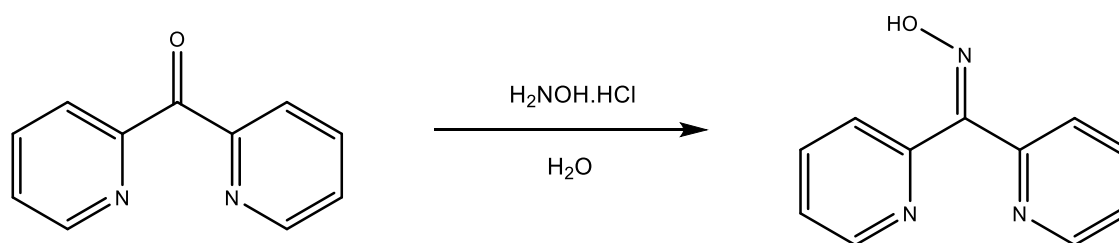
Figure 3.39 - Synthesis of di(2-pyridyl)oxime

3.7.2 Synthesis of di(2-pyridyl)methylamine

The reduction of the oxime to an amine in di(2-pyridyl)methylamine is achieved by the method of Rana *et. al.*[19] The oxime is reacted with ammonium acetate and ammonia in the presence of zinc powder as a heterogeneous catalyst. This is performed in refluxing ethanol. The product is treated with NaOH solution to deprotonated the amine and ensure it is extracted in DCM. The product is obtained as an oil which is crystallised by cooling in acetone. The yellow crystals obtained turn black on drying in a vacuum oven and slowly becomes an oil over time.
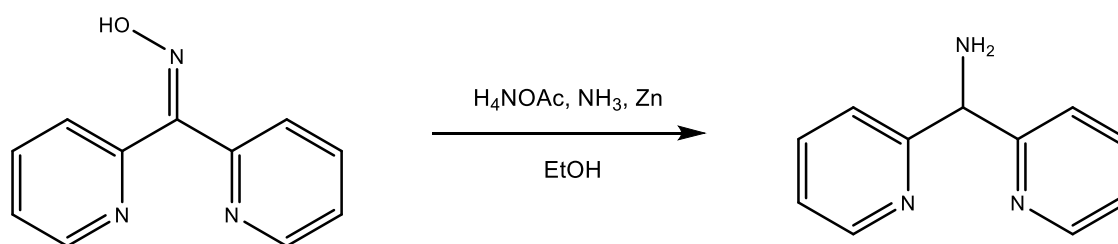
Figure 3.40 - Synthesis of di(2-pyridyl)methylamine

3.7.3 Synthesis of [RuCl(dpyma)(dppz)]⁺PF₆⁻

Analagous to the reaction for tpyma, dpyma is heated with $[RuCl_2(dmso)_2(dppz)]$ in ethylene glycol forming a deep red solution. The product is collected as a PF_6 salt and purified by alumina column using a 1:1 acetonitrile:toluene eluent.
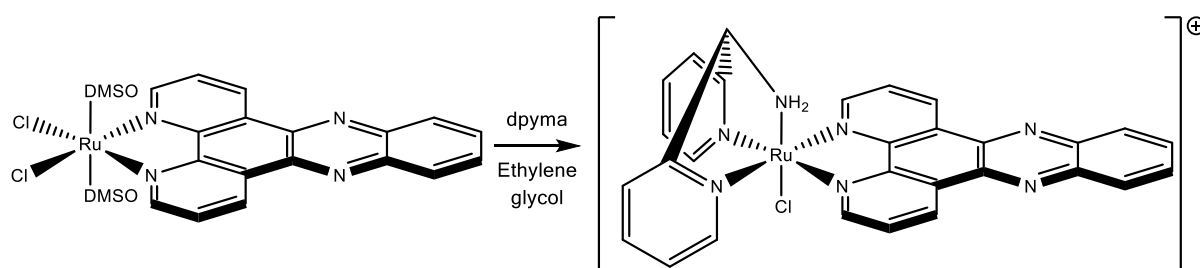
Figure 3.41 - Synthesis of [RuCl(dpyma)(dppz)]⁺

3.7.4 Synthesis of [Ru(dpyma)(dppz)(py)]²⁺(PF₆⁻)₂

The full complex is completed by the abstraction of the remaining chloride ligand with silver triflate, leading to a silver chloride precipitate. Refluxing the resultant complex with excess pyridine yields the final product, precipitated as a PF_6 salt.
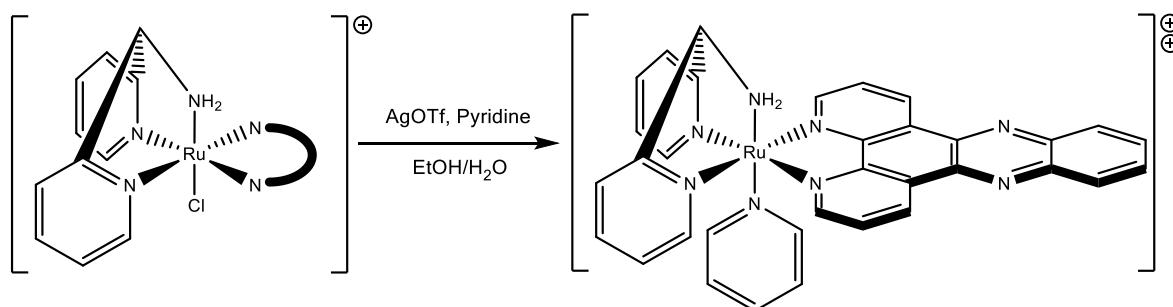
Figure 3.42 - Synthesis of [Ru(dpyma)(dppz)(py)]²⁺

3.7.5 Synthesis of di(2-pyridyl)-1-amino-3-butyne

As the synthesis of the complex containing dpyma proved to be a success, attempts were made to functionalise in a similar fashion to that for the tpm molecule. Unlike the tpm molecule, the proton on the methyl group connecting the pyridine moieties is less acidic. The synthesis was designed on the basis of previous work where lithiation of the dpyma molecule allowed for the introduction of alkyl groups.[20]

Dpyma was lithiated with n-butyl lithium and subsequently reacted with propargyl bromide, allowing for the lithiated species to displace the bromide, thus introducing an alkyne moiety to the product. Purification of the compound was attempted by preparative HPLC. It was not possible to achieve sufficient material to produce an NMR spectrum. The only evidence of the success of the reaction comes from the correct mass ion of 224 [MH+] being present in the mass spectrum analysis.
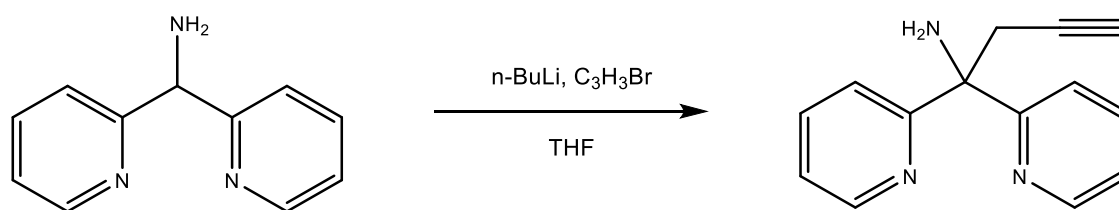
Figure 3.43 - Synthesis of di(2-pyridyl)-1-amino-3-butyne

3.8 Characterisation of di(pyridyl) complexes

3.8.1 ^{1}H NMR of [Ru(dpyma)(dppz)(py)]$^{2+}$(PF$_6$)$_2$

The ^{1}H NMR spectrum of [Ru(tpyma)(dppz)(py)]$^{2+}$(PF$_6$)$_2$, recorded in deuterated acetone is shown in figure 3.44 with peaks labelled relating to the lettering on the molecular structure. The lettering is colour coded to the different aromatic ring systems for clarity.
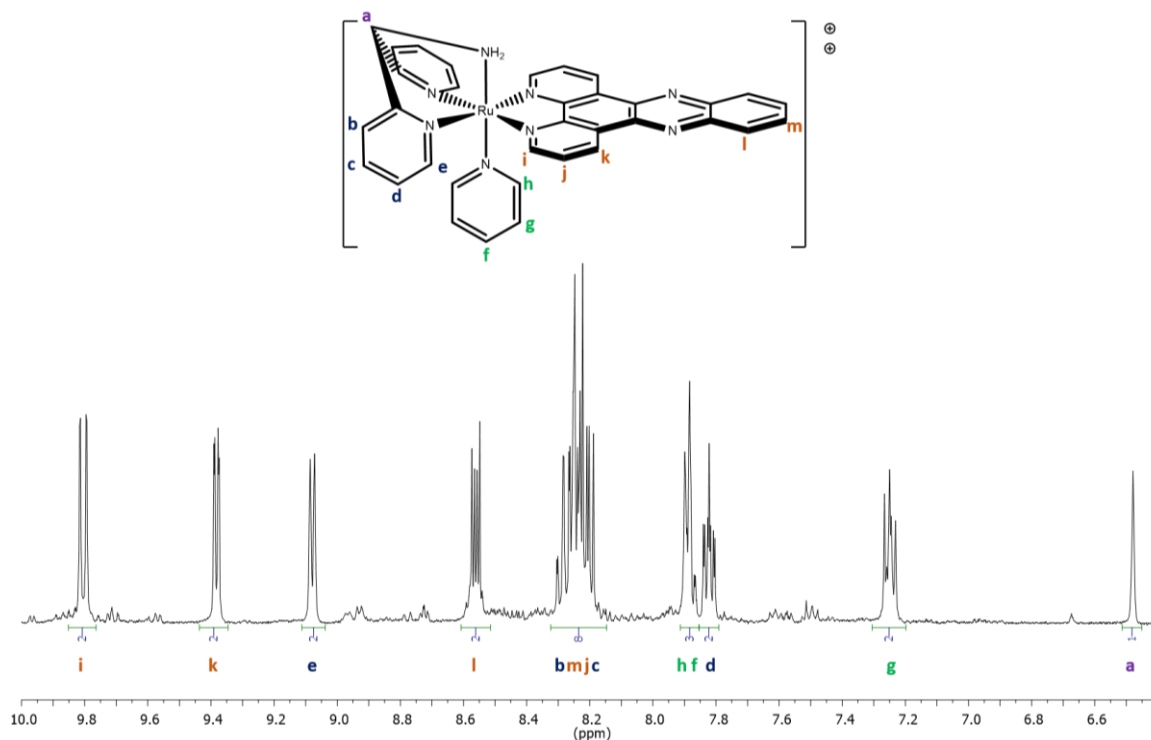
Figure 3.44 - 400 MHz ^{1}H NMR of [Ru(dpyma)(dppz)(py)]$^{2+}$(PF$_6^-$)$_2$ in d$_6$-acetone

The ^{1}H NMR spectrum of [Ru(dpyma)(dppz)(py)]$^{2+}$ is effectively a simplified version of the spectrum of [Ru(tpyma)(dppz)(py)]$^{2+}$. The signals for the third pyridine of the tpyma ligand have been removed, while the remaining signals are relatively unchanged. The only significant differences are the introduction of proton **a** in place of the missing pyridine ring, and the slight shift of proton **b**. Proton **a** appears as a distinct signal at 6.5 ppm shift, integrating to one proton, and is a singlet signal as it has no neighbouring protons to couple with. Proton **b** is closest to the change in the dpyma ligand and is shifted slightly upfield, due to a lesser inductive effect, resulting in it mixing with the signals of proton **m**, **j** and **c** giving an eight proton multiplet, where it is a separate signal in the tpyma complex.

The COSY NMR, shown in figure 3.45 is also very similar to that of the tpyma complex. The pyridine ring can now be distinguished as the only ring system containing a signal that integrates to one proton, proton **f**. Protons **f** to **g** are shifted very slightly from the tpyma complex, but their relative position, and splitting pattern, remain the same. The protons (**i** to **m**) of the dppz ligand also remain in the same positions as for the tpyma complex. The remaining protons of the dpyma ligand (**c** to **e**) are also in the same positions.

145
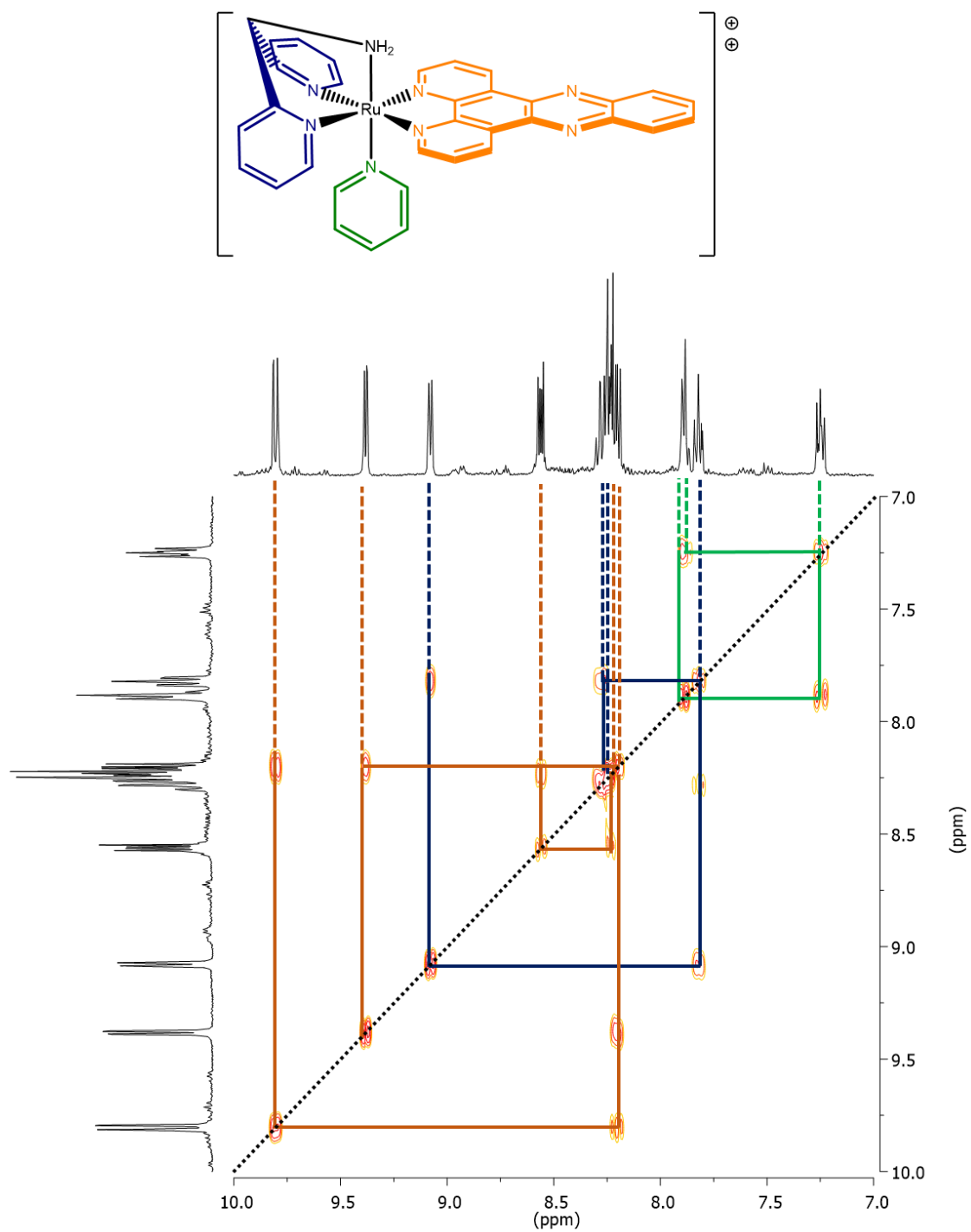
Figure 3.45 - 400 MHz COSY ^{1}H NMR of [Ru(dpyma)(dppz)(py)]$^{2+}$(PF$_6^-$)$_2$ in d$_6$-acetone with coupled protons connected by lines

3.9 Synthesis of other ruthenium-dppz complexes

The alternative approach used in the construction of ruthenium-dppz complexes, whereby the dppz ligand is added to the ruthenium centre first, allowed for the construction of other complexes that were not useful for the main aim of the project but of interest for other studies within the group. The synthesis of these compounds is detailed in this section.

3.9.1 Synthesis of $[Ru(tpya)(dppz)]^{2+}(PF_6^-)_2$

The three pyridine rings of the tpyma ligand do not preferentially bind to the ruthenium centre, with the ligand co-ordinating through two pyridines and the amine group instead. It is thought that this could be due to steric constraints which lead to a bite angle for the pyridine groups that is not as stable as the bite angle of two pyridine ligands and the amine group. Adding more flexibility to the ligand could alter the sterics sufficiently to allow for a different binding mode.

The tris(2-pyridylmethyl)amine (tpya) ligand was employed to test this theory. The ligand contains three pyridine rings that are bound to a nitrogen atom with a methyl spacer between them. The methyl spacer makes the ligand more flexible than tpyma which has no spacer between the pyridine rings and the point of attachment. The tpyc ligand is not suitable for further functionalisation as the nitrogen used to attach to the rings is saturated, however if the approach is successful, an alternative ligand may be designed to alter this.

The synthesis was performed by heating the ligand with $[RuCl_2(dmso)_2(dppz)]$ in ethylene glycol as in previous examples. Subsequently the product was purified by alumina column chromatography with eluent of 1:1 acetonitrile:toluene. This yielded a clear separation of two bands, red and orange. On analysis the LC-MS indicated that the red band contained the expected product where one chlorine ligand remained while the subsequent orange band contained $[Ru(tpya)(dppz)]^{2+}$ where the ligand was tetradentate and all other ligands were removed.
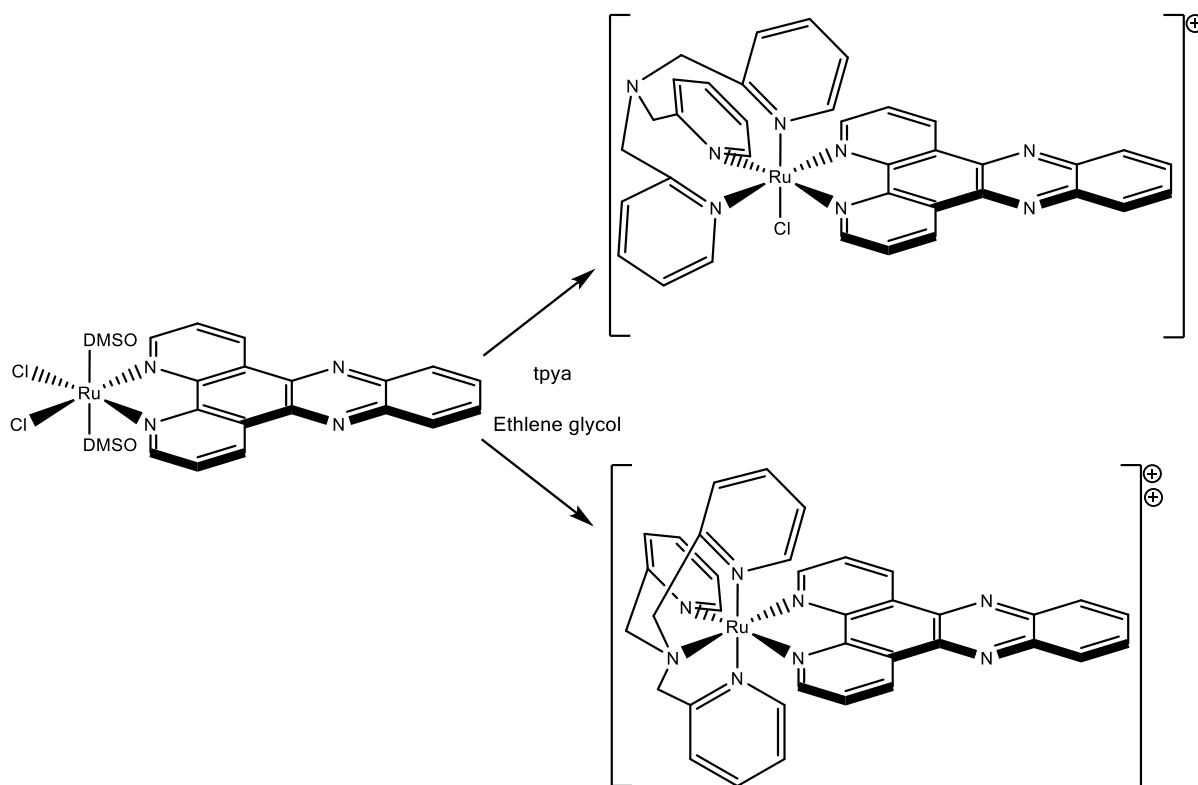
Figure 3.46 - Synthesis of [RuCl(tpya)(dppz)]$^+$ and [Ru(tpya)(dppz)]$^{2+}$

X-ray quality crystals of the tridentate tpya complex could not be obtained to confirm the co-ordination mode, however crystals of [Ru(tpya)(dppz)]$^{2+}$ were analysed. As far as the author is aware this is the only example of a ruthenium complex where the dppz unit is coupled with a tetradentate ligand. Although not useful to the aim of this project it is a molecule of interest in the wider field of DNA binding. The molecule is chiral as the amine could be oriented in either of the equatorial co-ordination sites, forming non-equivalent enantiomers. This should form enantiomers of significantly different shape, as there is little steric bulk behind the amine, unlike the pyridine. The molecule could display different binding modes to DNA or different uptake into cells which have been observed in other examples.

3.9.2 Synthesis of [Ru(py)$_4$(dppz)]$^{2+}$(PF$_6^-$)$_2$

The approach using [RuCl$_2$(dmso)$_2$(dppz)] as a starting material also allows for easy synthesis of compounds containing dppz and four monodentate ligands. This may be more challenging if the monodentate ligands were added first as it could be difficult to control how many ligands attach to the ruthenium centre. This may not leave sufficient binding sites for a dppz ligand to be added.

$[Ru(py)_4(dppz)]^{2+}$ was synthesised by refluxing $[RuCl_2(dmso)_2(dppz)]$ in pyridine alongside silver triflate. The silver triflate abstracts the final chloride ligand, forming silver chloride, to allow for the ruthenium to be saturated with pyridine ligands. In the absence of silver triflate $[RuCl(py)_3(dppz)]^+$ was formed. The complex has been previously synthesised as a perchloride salt *via* an alternative method.[21]
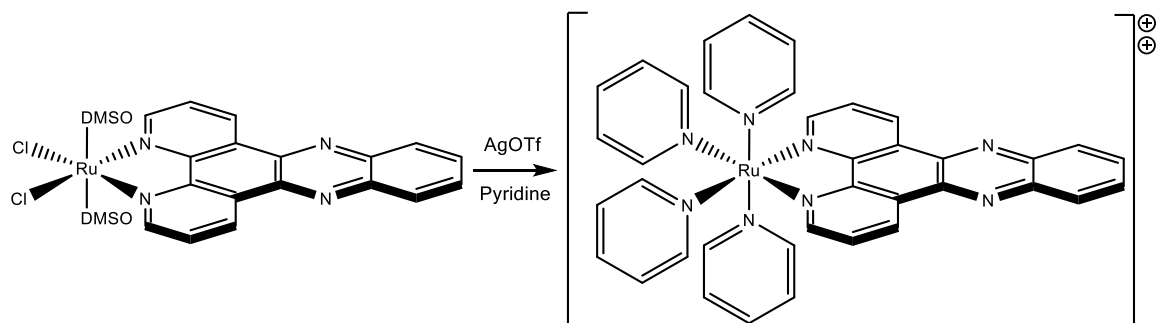
Figure 3.47 - Synthesis of $[Ru(dppz)(py)_4]^{2+}$

3.9.3 Synthesis of $[Ru(MeCN)_3(dmso)(dppz)]^{2+}(PF_6^-)_2$

Analogous to the synthesis of $[Ru(py)_4(dppz)]^{2+}$, $[RuCl_2(dmso)_2(dppz)]$ was refluxed in acetonitrile with silver triflate. The aim of this reaction was to synthesise $[Ru(MeCN)_4(dppz)]$ to assess the DNA binding of a complex where there the ancillary ligands are minimal in size and should have little influence over the binding. This may allow the dppz unit to insert into the DNA more easily and bind more strongly.

The synthesis resulted in a marked colour change from brown to bright yellow. LC-MS analysis appeared to confirm the synthesis of the target complex, by presence of a mass ion peak of the expected mass. However, when crystals were grown and analysed by x-ray crystallography it was discovered that one dmso remained on the complex.
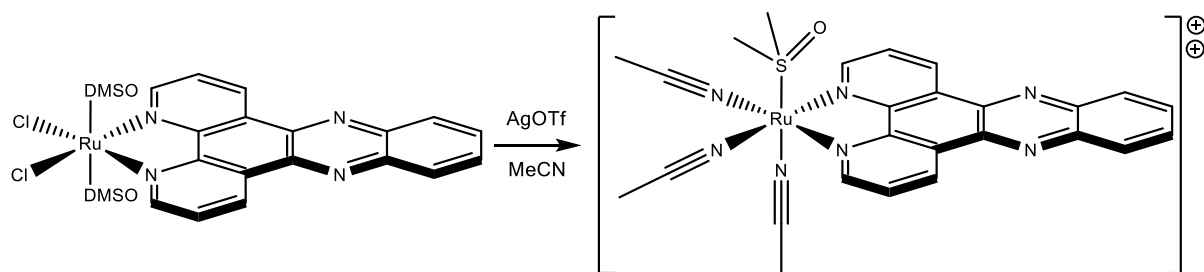
Figure 3.48 - Synthesis of $[Ru(MeCN)_3(dmso)(dppz)]^{2+}$

3.10 Characterisation of other ruthenium complexes

3.10.1 ^{1}H NMR of [Ru(tpya)(dppz)]$^{2+}$(PF$_6^-$)$_2$

The ^{1}H NMR spectrum of [Ru(tpya)(dppz)]$^{2+}$(PF$_6^-$)$_2$, recorded in deuterated acetone is shown in figure 3.49 with peaks labelled relating to the lettering on the molecular structure. The lettering is colour coded to the different aromatic ring systems for clarity. Peaks labelled with an apostrophe are referring to the equivalent proton opposite the label in the dppz ligand.
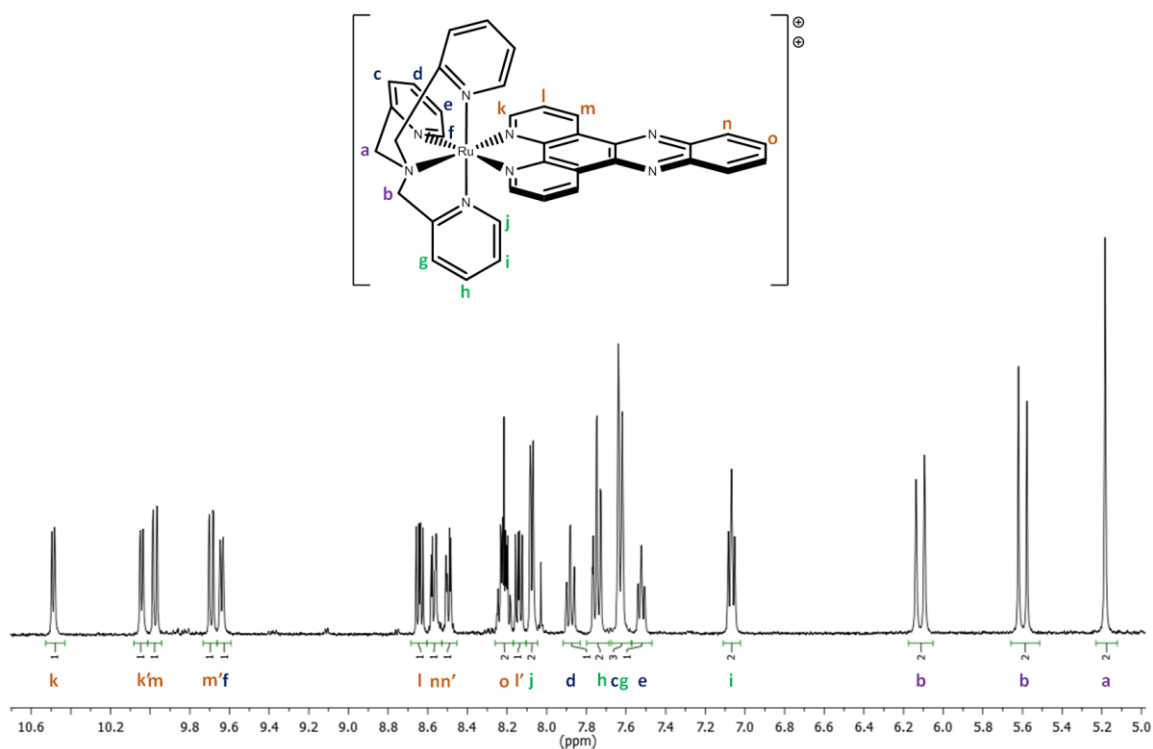
Figure 3.49 - 400 MHz ^{1}H NMR of [Ru(tpya)(dppz)]$^{2+}$(PF$_6^-$)$_2$ in d$_6$-acetone

Unlike similar, previously assigned, pyridyl complexes, the line of symmetry of [Ru(tpya)(dppz)]$^{2+}$ runs parallel to the dppz ligand, rather than bisecting it. The leads to a more complex spectrum as the protons on the two sides of the dppz ligand are not equivalent. In figure 3.49 this is shown by the apostrophe, such that **k'** is the proton environment opposite **k**. These protons are assigned in the same order as for previous examples, with proximity to the nitrogen atom and splitting pattern indicating which proton is which. Proton **o** is very close to its opposite, so exhibits a multiplet signal rather than two distinct signals. It is likely that the more deshielded protons are closest to the equatorial pyridine and its ring current is affecting their chemical shift.

This cannot be confirmed without further NMR experiments that would show spacial coupling between the pyridine and dppz protons.

Another interesting feature of the spectrum is the coupling exhibited in proton environment **b**. This displays as a large coupling value of 17.1 Hz, indicative of geminal coupling. This coupling is not seen in the free ligand as rotation around the bond results in the equivalence of the two protons. However, when the ligand is bound to ruthenium this rotation is restricted, effectively forming an 8 membered ring. This leads to the two protons pointing towards, and away from, the third pyridine ring resulting in differing shift values. As with the dppz protons, a spacial NMR experiment is needed to confirm which is which. Coupling is not seen in proton **a** as it is in the plane of symmetry.

The remaining protons of the pyridine rings are distinguished using the COSY NMR, shown in figure 3.50, as they exist as separate, non coupled ring systems. The ring system of **c** – **f** are distinct from **g** – **j** as the latter integrates to twice the number of protons. They are assigned in the same way as previously, with the most deshielded signal assigned to the proton nearest the nitrogen. The other doublet in the system is assigned to the proton opposite. The most deshielded triplet is assigned to the proton opposite the nitrogen, with the remaining signal assigned to the proton in the meta-position.
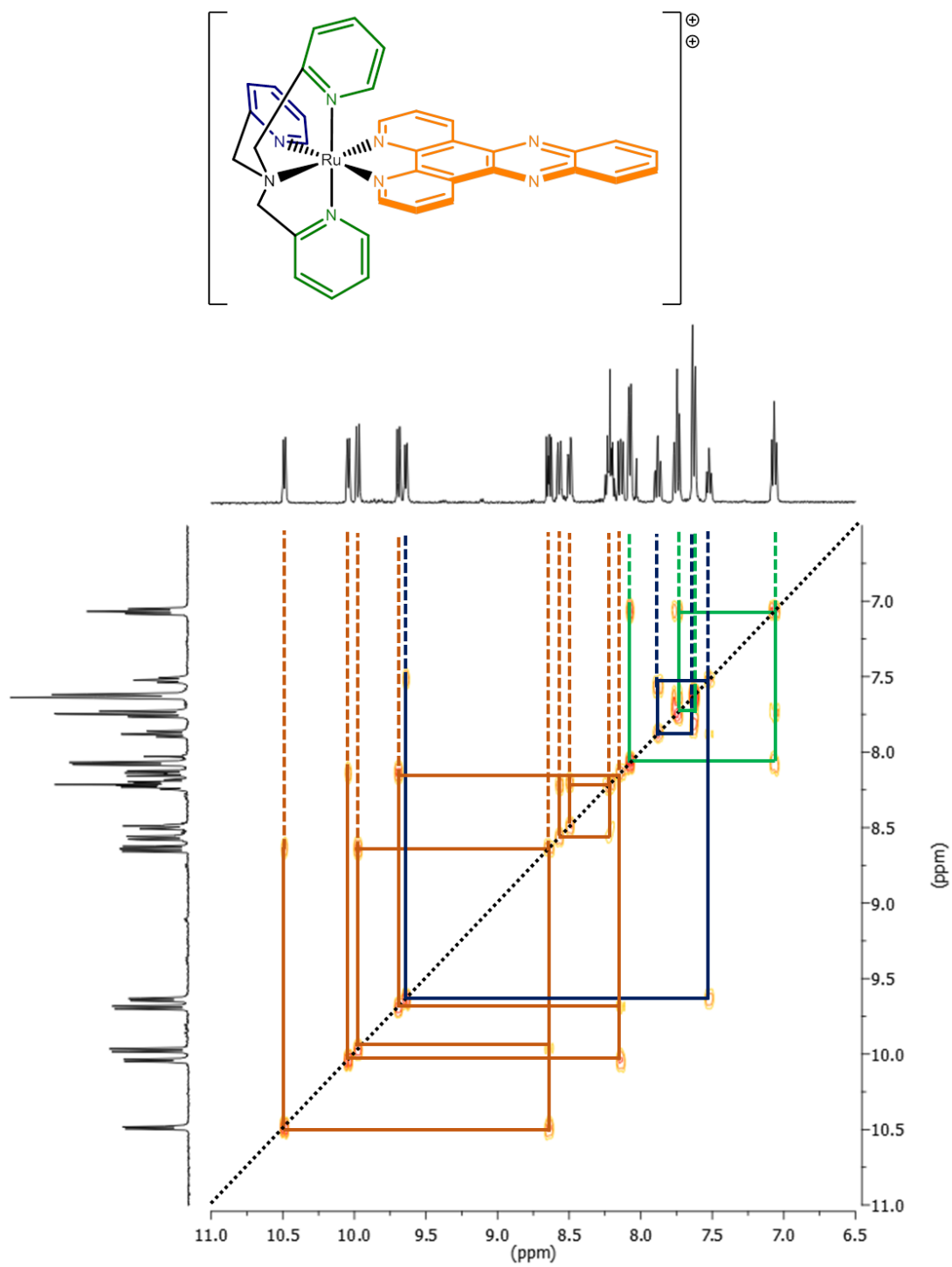
Figure 3.50 - 400 MHz COSY ^{1}H NMR of [Ru(tpya)(dppz)]$^{2+}$(PF$_6^-$)$_2$ in d$_6$-acetone with coupled protons connected by lines

3.10.2 ^{1}H NMR of [Ru(dppz)(MeCN)$_3$(dmso)]$^{2+}$(PF$_6^-$)$_2$

The ^{1}H NMR spectrum of [Ru(tpyma)(dppz)(py)]$^{2+}$(PF$_6^-$)$_2$, recorded in deuterated acetone is shown in figure 3.51 with peaks labelled relating to the lettering on the molecular structure.
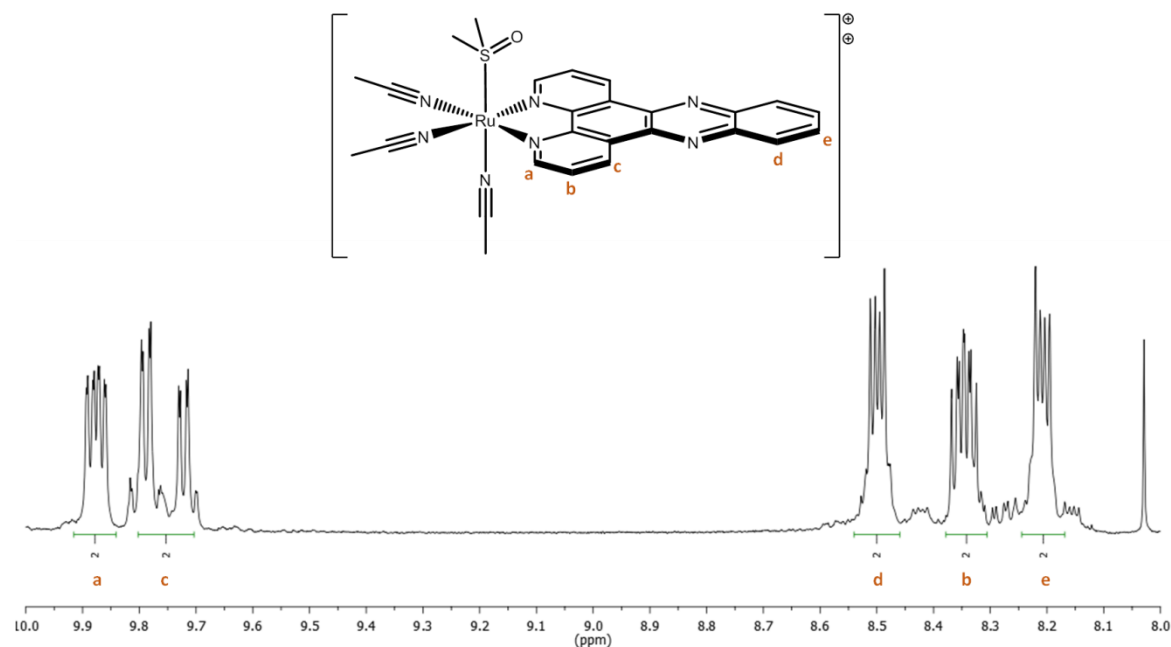
Figure 3.51 - 400 MHz ^{1}H NMR of [Ru(dppz)(MeCN)$_3$(dmso)]$^{2+}$(PF$_6^-$)$_2$ in d$_6$-acetone

The NMR of Ru(dppz)(MeCN)$_3$(dmso)]$^{2+}$ is more simple than related Ru-dppz complexes in this chapter due to only one aromatic ring system co-ordinated to the metal centre. The COSY 2D NMR shown in figure 3.52 shows the coupled protons on the phenanthroline portion of the ligand and a separate coupling pattern for the phenazine portion. These two sections are separated by the nitrogen atoms in the centre of the ligand, thus there is no coupling between them. The peaks are assigned in a similar fashion to previous examples containing the dppz ligand. The key difference is observed in the added splitting of the doublet peaks expected for protons **a** and **c**. It may be that there are two or more isomers of the product present in the sample that have caused this phenomena. The peaks are assigned on the basis that **a** is closer to the electron deficient nitrogen and so will be the more deshielded peak, followed by **c**. The remaining peak in the coupling set, shown by COSY, is assigned to the proton **b** between **a** and **c**. Protons **d** and **e** are also assigned on the basis of proximity to nitrogen atoms. They display more complex splitting patterns due to magnetic non-equivalence.

The protons relating to the acetonitrile and dmso ligands are not assigned as they could not be distinguished from residual solvent peaks in the aliphatic region of the NMR spectrum.
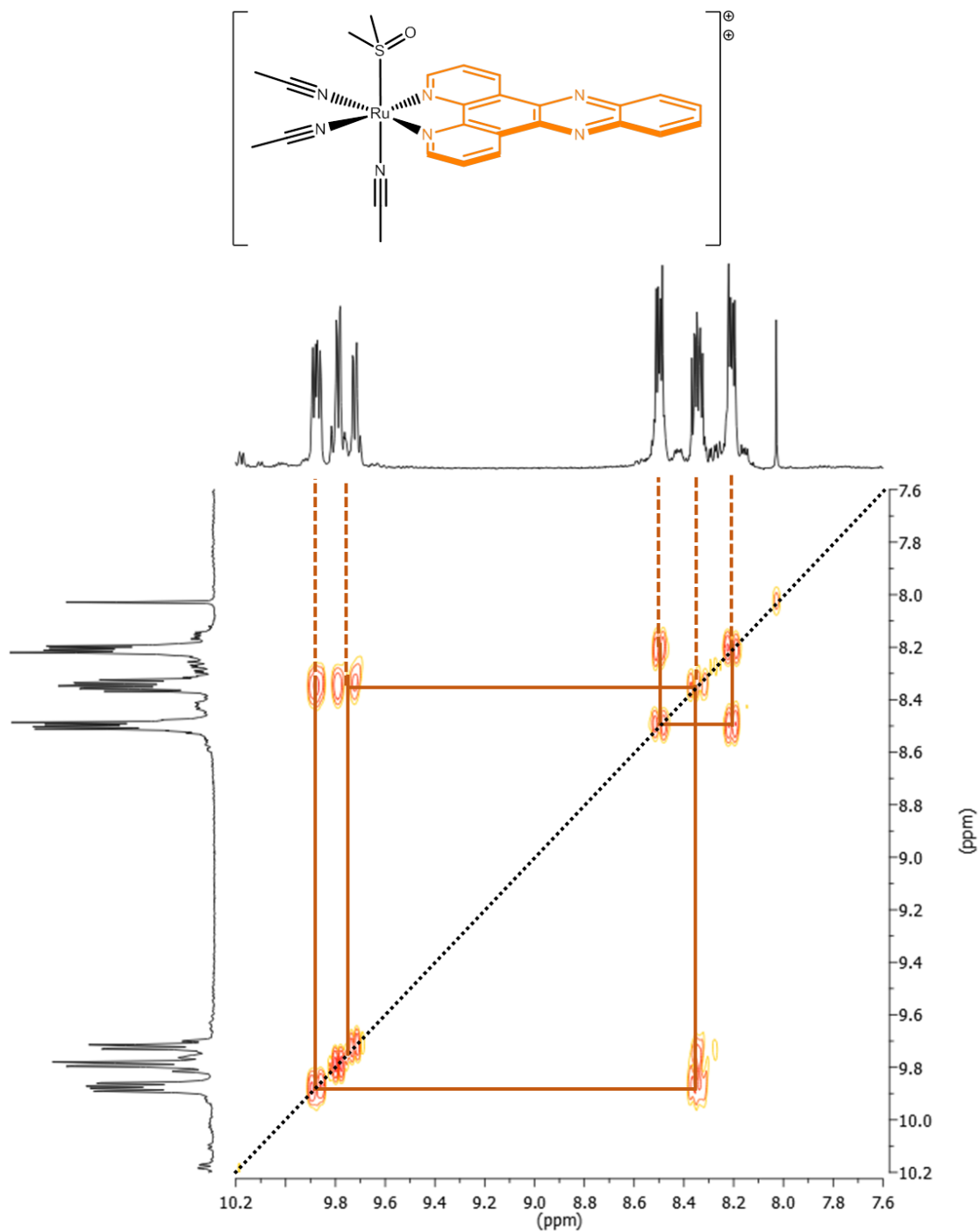
Figure 3.52 - 400 MHz COSY ^{1}H NMR of [Ru(dppz)(MeCN)$_3$(dmso)]$^{2+}$(PF$_6^-$)$_2$ in d$_6$-acetone with coupled protons connected by lines

3.10.3 UV-Visible absorption of other ruthenium complexes

The UV-Visible spectrum of $[Ru(tpya)(dppz)]^{2+}$ and $[Ru(dppz)(MeCN)_3(dmso)]^{2+}$ were recorded in acetonitrile, with the spectra shown in figure 3.53. The data obtained for the complexes is summarised in table 3.6.
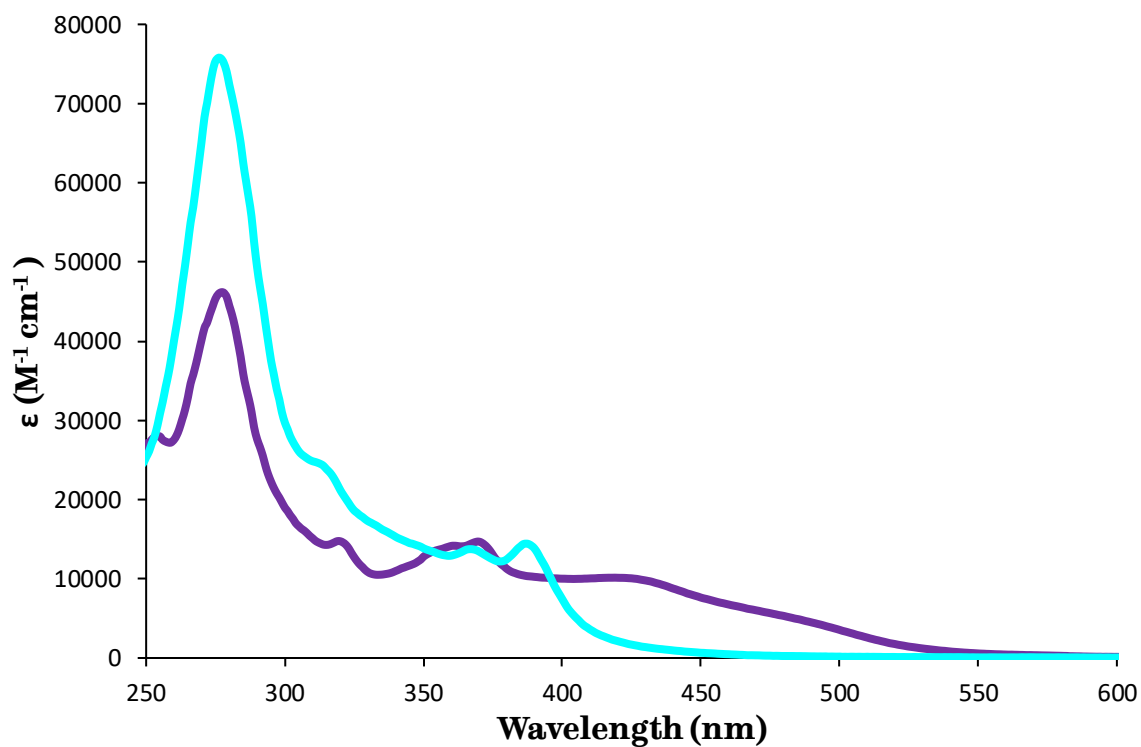
Figure 3.53 - UV-visible absorption spectra of complexes $[Ru(tpya)(dppz)](PF_6)_2$ (■) and $[Ru(dppz)(MeCN)_3(dmso)](PF_6)_2$ (■) recorded in acetonitrile

Complex	λ_{max} (nm)	ε_{max} (M^{-1} cm^{-1})	Assignment
[Ru(tpya)(py)](PF$_6$)$_2$	277	46168	$\pi - \pi^*$
	319	14756	$\pi - \pi^*$
	361 (sh)	14173	$\pi - \pi^*$
	370	14689	$\pi - \pi^*$
	419	10141	MLCT
	493 (sh)	4233	MLCT
[Ru(dppz)(MeCN)$_3$(dmso)](PF$_6$)$_2$	276	75775	$\pi - \pi^*$
	315 (sh)	23838	$\pi - \pi^*$
	367	13741	$\pi - \pi^*$
	387	14436	MLCT

Table 3.6 - Summary of the maximal absorption of the UV-Visible spectra of Ru-dppz complexes recorded in acetonitrile (sh = shoulder)

The appearance of the spectrum of [Ru(tpya)(py)](PF$_6$)$_2$ is similar to the previously reported Ru-dppz complexes. The distinctive and most intense absorption, relating to the dppz $\pi - \pi^*$ transition, is observed at 277 nm and is slightly less intense than the previous examples reported for the tpyma and tpyc complexes. The double hump band at 360-370 nm, indicative of dppz, is also observed along with the MLCT band at 419 nm. The MLCT is slightly higher in energy than the tpyma complex and is also a relatively intense absorption. There is also a more significant tail to the MLCT band with a shoulder observed at 493 nm.

In the spectrum of [Ru(dppz)(MeCN)$_3$(dmso)](PF$_6$)$_2$ a peak at 276 nm, correlating to the dppz $\pi - \pi^*$ is much more intense than other examples, possibly as it is the only section of the complex to have an extended aromatic system. The characteristic double hump band of dppz is slightly obscured, by the blue shifted MLCT at 387 nm. The MLCT band does not display a long tail in this case and the absorbance falls away immediately after the maximum. This is also observed on inspection of the solution, as it forms a bright yellow colour, rather than the orange/red of other dppz complexes.

3.11 Conclusion

This chapter reports the investigation of alternative, pyridyl based ligands, with potential to act as surface linkages for a DNA binding ruthenium complex. Initially the tpyc and tpyma ligands, which contain a hydroxyl and amine group respectively, were investigated due to their free functional groups that could be used to add function to a complex. This could be achieved either through the formation of ester or amide linkages. The ligands were successfully co-ordinated to ruthenium, facilitated by the method developed in the previous chapter, whereby the bidentate ligand is added to the ruthenium before a tridentate ligand is added. This lead to the formation of a series of compounds containing tpyma of the form $[Ru(tpyma)(NN)(py)]^{2+}$ where NN is bpy, phen, dppz or dppn alongside the $[Ru(tpyc)(dppz)(py)]^{2+}$ complex. This work was in the hope that the complex formed would be able to link to other moieties post co-ordination. Efforts were also made to create linkages with the ligand prior to co-ordination to ruthenium, as a possible alternative approach. This led to the linkage of tpyma to mercaptoundecanoic acid, resulting in a potential ligand that could attach to a surface through its thiol moiety.

The synthesised complexes were characterised by mass spectrometry and ^{1}H NMR spectroscopy. The photophysics were also studied but recording the UV-visible absorption spectrum and the luminescent emission in acetonitrile. Each of the complexes exhibited high energy absorptions, attributed to the $\pi - \pi^*$ of their respective polypyridyl ligands, alongside lower energy MLCT absorptions owing to the presence of the ruthenium centre. These absorptions were similar to those of previously reported ruthenium complexes containing the bidentate ligands. Each complex showed strong emission in the $630 - 670$ nm range, with the exception of the tpyc complex which showed minimal emission. Coupled with the very low oxidation potential from cyclic voltammetry measurements, this may be due to co-ordination of the hydroxyl group to the ruthenium centre, rather than the expected route through the pyridines. X-ray crystallography, discussed in the subsequent chapter, shows that the tpyma ligand co-ordinates in a similar fashion, through the amine and two pyridines. This renders the complexes unsuitable as linkers, as the group that would be used to add function to the complex is no longer available for reaction.

Due to the problems with the use of tris(pyridyl) ligands, a new approach was devised utilising the newly discovered co-ordination mode. The di(pyridyl) analogue of tpyma,

dpyma, was synthesised to assess if it would co-ordinate as a tripodal ligand in its own right. The synthesis of the complex [Ru(dpyma)(dppz)(py)]$^{2+}$ proved successful, with the tripodal co-ordination mode confirmed by x-ray crystallography. Based on this, an alternative method of adding the alkyne, used in the previous chapter, to the dpyma ligand was devised. While the reaction appeared successful my LCMS analysis, it was not possible to achieve an NMR to confirm this. Further work is required to develop a purification protocol for the compound before attempts to co-ordinate it in the same way as dpyma.

The method of Ru-dppz complex synthesis, that adds the dppz first, also allowed for the synthesis of other novel complexes. One such complex incorporated the tetradentate, tris(2-pyridylmethyl)amine ligand, which may be the first example of a tetradentate ligand coupled with dppz on a ruthenium centre. While not useful for the aim of the project, this is an interesting use of the method developed from the project. This method could be further used to develop novel DNA binding molecules that incorporate other tri- and tetra-dentate ligands.

3.12   References

1   S. Wu, L. Chen, B. Yin and Y. Li, *Chem. Commun.*, 2015, **51**, 9884–9887.

2   A. K. F. Mårtensson and P. Lincoln, *Dalton Trans.*, 2015, **44**, 3604–3613.

3   J. M. Calvert, J. V. Caspar, R. A. Binstead, T. D. Westmoreland and T. J. Meyer, *J. Am. Chem. Soc.*, 1982, **104**, 6620–6627.

4   R. K. Boggess and S. J. Boberg, *J. Inorg. Nucl. Chem.*, 1980, **42**, 21–26.

5   M. Bette, T. Kluge, J. Schmidt and D. Steinborn, *Organometallics*, 2013, **32**, 2216–2227.

6   P. Arnold, S. C. Davies, J. R. Dilworth, M. C. Durrant, D. V. Griffiths, D. L. Hughes and R. L. Richards, *Inorg. Chem. Commun.*, 1998, **1**, 43–45.

7   R. C. Horton, T. M. Herne and D. C. Myles, *J. Am. Chem. Soc.*, 1997, **119**, 12980–12981.

8   P. J. Arnold, S. C. Davies, J. R. Dilworth, M. C. Durrant, D. V Griffiths, D. L. Hughes, R. L. Richards and P. C. Sharpe, *J. Chem. Soc. Trans.*, 2001, 736–746.

9   R. T. Jonas and T. D. P. Stack, *Inorg. Chem.* , 1998, **37**, 6615–6629.

10   T. Yamada, C. G. Peng, S. Matsuda, H. Addepalli, K. N. Jayaprakash, M. R. Alam, K. Mills, M. A. Maier, K. Charisse, M. Sekine, M. Manoharan and K. G. Rajeev, *J. Org. Chem.*, 2011, **76**, 1198–1211.

11   F. R. Keene, D. J. Szalda and T. A. Wilson, 1987, 2211–2216.

12   K. Kalyanasundaram, *Coord. Chem. Rev.*, 1982, **46**, 159–244.

13   G. Accorsi, A. Listorti, K. Yoosaf and N. Armaroli, *Chem. Soc. Rev.*, 2009, **38**, 1690–1700.

14   L. Luzuriaga and M. F. Cerdá, 2012, **2012**, 262–267.

15   J. Fees, M. Ketterle, A. Klein, J. Fiedler and W. Kaim, *J. Chem. Soc. Dalton Trans.*, 1999, 2595–2600.

16   J. Fees, W. Kaim, M. Moscherosch, W. Matheis, J. Klima, M. Krejcik and S. Zalis, *Inorg. Chem.*, 1993, **32**, 166–174.

17   S. P. Foxon, C. Metcalfe, H. Adams, M. Webb and J. A. Thomas, *Inorg. Chem.*, 2007, **46**, 409–416.

18   M. G. Walker, PhD Thesis, University of Sheffield, 2013.

19   S. Rana, A. Dey and D. Maiti, *Chem. Commun.*, 2015, **51**, 14469–14472.

20   A. R. McDonald, Y. Guo, V. V. Vu, E. L. Bominaar, E. Münck and L. Que, *Chem. Sci.*, 2012, **3**, 1680.

21   P. Naishadham, P. Pallavi, K. L. Reddy and S. S, *J. Chem. Pharm. Res.*, 2012, **6**, 3309–3318.

4.0 Structural studies of novel ruthenium-pyridyl complexes

4.1 Introduction

X-ray crystallography was developed at the turn of the 20th century as a method for determining the molecular structure of compounds. Based on the initial observations of Max von Laue that crystals diffract x-rays, father and son William H Bragg and William L Bragg were able to discern the arrangement of atoms based on the diffraction pattern, resulting in the report of the structure of crystal lattices such as NaCl.[1] The technique has been aided by advancement in technology that has resulted in higher quality x-ray sources and computing that can analyse the resulting diffraction patterns with ease. This allowed for the determination of much more complex molecular solids.

In the field of co-ordination chemistry this technique is particularly useful. While many other methods of characterisation exist, such as mass spectrometry and NMR, they cannot provide the same detailed structural information realised through crystallography. In co-ordination chemistry this can be important, as when dealing with ligands that can co-ordinate in multiple ways, crystallography may be the only reliable method of confirming a structure. For example, in the case of isomers, mass spectra can be the same and even NMR spectra can be identical if the resulting isomers are symmetric; however, crystallography affords the definitive positions of atoms, allowing for identification of the isomer formed.

The structure of packing in a crystal can provide insights into the manner in which a molecule may bind to DNA. In particular, if $\pi - \pi$ stacking between putative DNA binding ligands is observed in a structure, this suggests that similar forces may drive intercalative stacking with base pairs of a DNA duplex.

This chapter reports the crystal structures of several of the novel ruthenium compounds described in the previous chapter. In particular, these studies detail the unexpected co-ordination mode of the tpyma ligand. The first reported structure, of $[Ru(dppz)(py)_4]^{2+}$, has unhindered pyridines coordinated to ruthenium; by comparing it to structures in which the pyridines are linked, the strain introduced by these connections can be assessed.

4.1.1 Sample preparation

The crystals grown for analysis were obtained by a vapour diffusion technique, in which the sample is first dissolved in a solvent and then an anti-solvent is diffused into the solution, inducing crystallisation. In this study, where PF_6 salts have been used, the sample is dissolved in nitromethane and the anti-solvent is diethyl ether. All samples were grown in a refrigerator, to slow the diffusion of the anti-solvent and encourage the growth of larger crystals, allowing for a better resolution on analysis.

4.1.2 X-ray crystal structure of $[Ru(dppz)(py)_4](PF_6)_2$

The X-ray crystal structure of $[Ru(dppz)(py)_4](PF_6)_2$ is shown in figure 4.1 with a summary of the data collected in table 4.1.
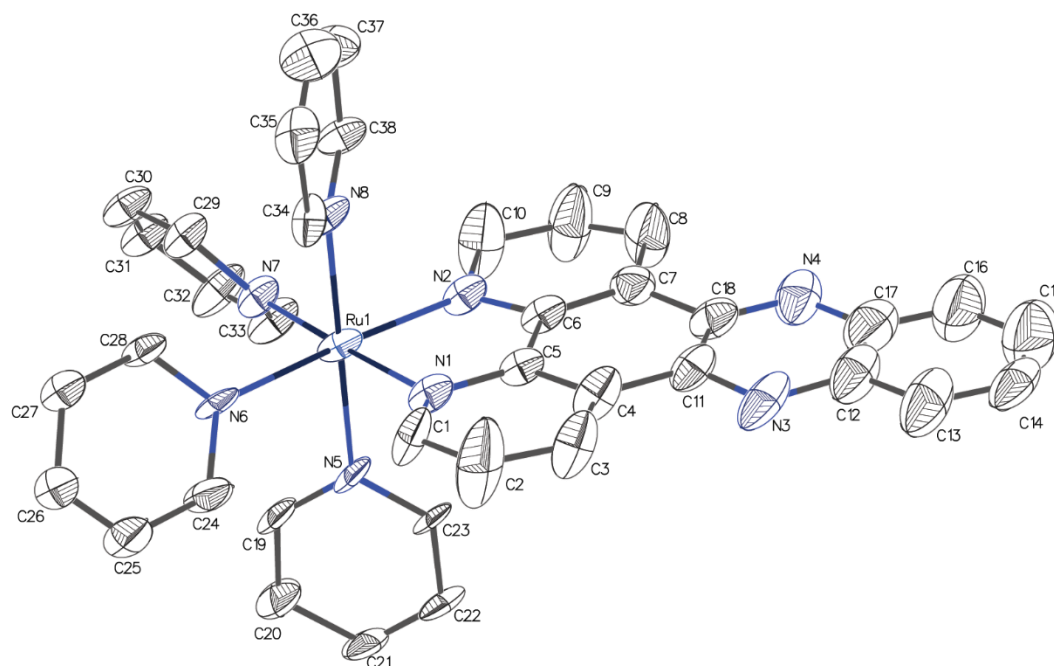
Figure 4.1 - ORTEP crystal structure of $[Ru(dppz)(py)_4](PF_6)_2$

Metal coordination in the crystal structure of $[Ru(dppz)(py)_4](PF_6)_2$ is close to a perfect octahedron, as the pyridine ligands are not connected and therefore unhindered in their co-ordination to the ruthenium centre. The bond angles between the pyridines are close to the 90° as expected for an octahedral complex, with N-Ru-N angles ranging from 87.21° to 92.30°. The only major distortion in the co-ordination sphere is observed around the dppz ligand, which forces the co-ordinating nitrogen atoms closer together than they are when freely co-ordinated. The angle between the two Ru-N bonds of the

dppz is 79.87°, much tighter than the ideal 90°. The bond lengths of this near ideal complex are between 2.15 Å and 2.23 Å for the Ru-N(py) bonds and 2.10 Å and 2.13 Å for the Ru-N(dppz) bonds.

Also of interest that the two axial pyridines in figure 4.1 are perpendicular to each other and not both bisecting the equatorial pyridines. This could point to why the tpyma ligand co-ordinates through the amine, as the same steric interactions forcing the pyridines into this formation may make the attachment of the third pyridine of tpyma unfavourable.

Complex	$[Ru(dppz)(py)_4]^{2+}$
Empirical formula	$C_{38}H_{30}F_{12}N_8P_2Ru$
Formula weight	989.71
Temperature/K	100
Crystal system	triclinic
Space group	P-1
a/Å	10.75(3)
b/Å	10.79(4)
c/Å	22.30(9)
α/°	81.02(5)
β/°	79.58(5)
γ/°	62.38(8)
Volume/Å^3	2246(15)
Z	2
ρ_{calc}g/cm^3	1.463
μ/mm^{-1}	0.507
F(000)	992.0
Crystal size/mm^3	0.4 × 0.4 × 0.15
Radiation	MoKα (λ = 0.71073)
2Θ range for data collection/°	1.864 to 54.27
Index ranges	-13 ≤ h ≤ 12, -13 ≤ k ≤ 12, -28 ≤ l ≤ 28
Reflections collected	34724
Independent reflections	8909 [R_{int} = 0.1333, R_{sigma} = 0.1819]
Data/restraints/parameters	8909/561/520
Goodness-of-fit on F^2	1.042
Final R indexes [I>=2σ (I)]	R_1 = 0.1814, wR_2 = 0.4299
Final R indexes [all data]	R_1 = 0.2452, wR_2 = 0.4680
Largest diff. peak/hole / e Å^{-3}	3.34/-2.45

Table 4.1 - Summary of crystal structure data for $[Ru(dppz)(py)_4](PF_6)_2$

The unit cell of $[Ru(dppz)(py)_4](PF_6)_2$, displayed in figure 4.2 contains two ions, alongside four PF_6 counter ions that are omitted from the figure for clarity. The unit is triclinic, having the least symmetry of the crystal groups. The two ions appear stacked on top of one another, presumably due to the favourable π-π interactions of the dppz moiety. They are also stacked end to end with one ruthenium centre opposite to the

other. In the extended packing, as shown in figure 4.3, t a PF_6^- molecule sits below the dppz, preventing further stacking between dppz units. The unit cells are arranged in a slightly offset fashion, with the top unit positioned between two units below it.
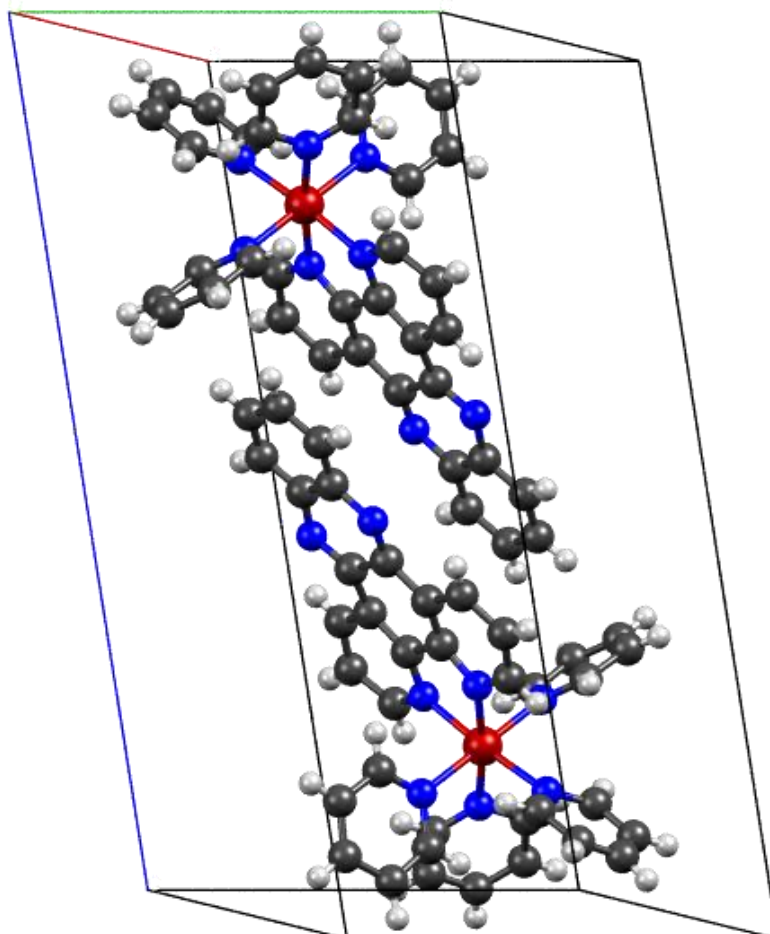
Figure 4.2 - Unit cell of the [Ru(dppz)(py)$_4$](PF$_6$)$_2$ crystal. Counter ions removed for clarity.
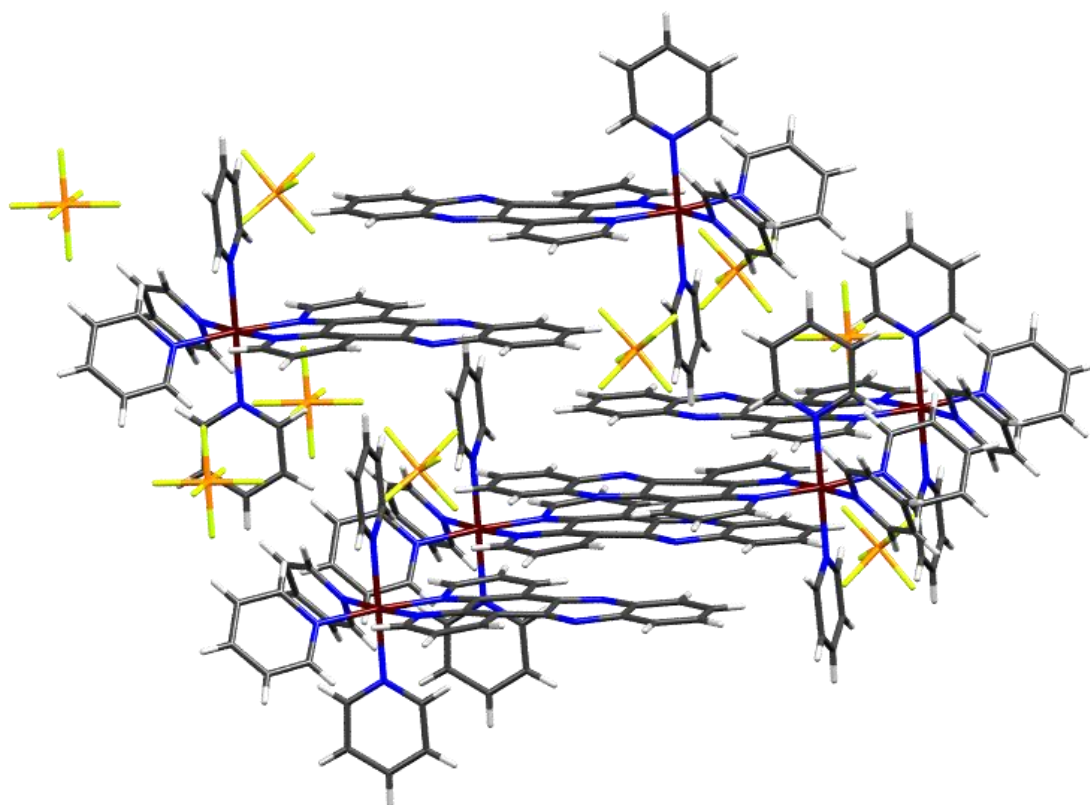
Figure 4.3 – Extended packing of the [Ru(dppz)(py)$_4$](PF$_6$)$_2$ crystal with counter ions included.

4.2 Structural studies of tris(pyridyl) ruthenium complexes

4.2.1 X-ray crystal structure of [Ru(tpyma)(bpy)(py)](PF$_6$)$_2$

The X-ray crystal structure of [Ru(tpyma)(bpy)(py)](PF$_6$)$_2$ is shown in figure 4.3 with a summary of the data collected in table 4.2.
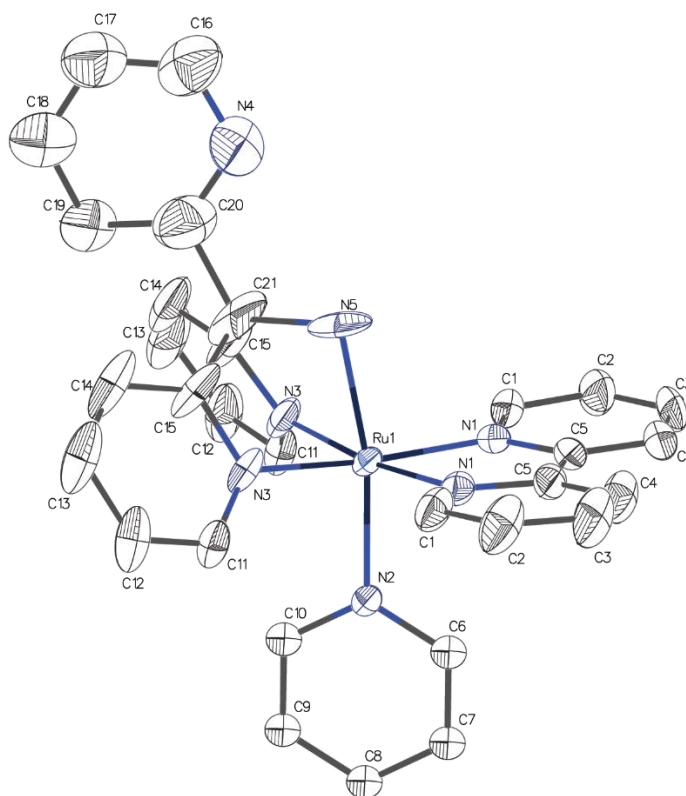
Figure 4.4- Single Cation ORTEP crystal structure of [Ru(tpyma)(bpy)(py)](PF$_6$)$_2$

The x-ray structure of [Ru(tpyma)(bpy)(py)](PF$_6$)$_2$ is highly disordered. There are multiple cations present in the structure and the ORTEP structure in figure 4.3 shows only one of these. The calculated solution of the structure contains multiple positions for some of the atoms in the molecule, particularly the tpyma portion. The unit cell is not displayed for this reason, as the positions of atoms are not particularly clear and the image is chaotic. This crystal structure does however confirm the co-ordination mode of the tpyma ligand is through two of the pyridine ligands and the amine group.

It is not valid to comment on the distortion of bond lengths and angles due to the multiple atom positions.

Complex	$[Ru(tpyma)(bpy)(py)]^{2+}$
Empirical formula	$C_{31}H_{27}F_{18}N_7P_3Ru$
Formula weight	1033.57
Temperature/K	100
Crystal system	Orthorhombic
Space group	Pnma
a/Å	25.430(5)
b/Å	13.211(2)
c/Å	11.297(2)
α/°	90
β/°	90
γ/°	90
Volume/Å³	3795.2(12)
Z	4
ρ_{calc}g/cm³	1.809
μ/mm⁻¹	0.665
F(000)	2052.0
Crystal size/mm³	0.5 × 0.3 × 0.08
Radiation	MoKα (λ = 0.71073)
2Θ range for data collection/°	3.204 to 55.012
Index ranges	-27 ≤ h ≤ 33, -17 ≤ k ≤ 17, -10 ≤ l ≤ 14
Reflections collected	23088
Independent reflections	4545 [R_{int} = 0.0523, R_{sigma} = 0.0411]
Data/restraints/parameters	4545/550/362
Goodness-of-fit on F²	1.539
Final R indexes [I>=2σ (I)]	R_1 = 0.1160, wR_2 = 0.3411
Final R indexes [all data]	R_1 = 0.1397, wR_2 = 0.3662
Largest diff. peak/hole / e Å⁻³	2.77/-2.06

Table 4.2 - Summary of crystal structure data for $[Ru(tpyma)(bpy)(py)](PF_6)_2$

4.2.2 X-ray crystal structure of [Ru(tpyma)(phen)(py)](PF$_6$)$_2$

The X-ray crystal structure of [Ru(tpyma)(phen)(py)](PF$_6$)$_2$ is shown in figure 4.5 with a summary of the data collected in table 4.3.
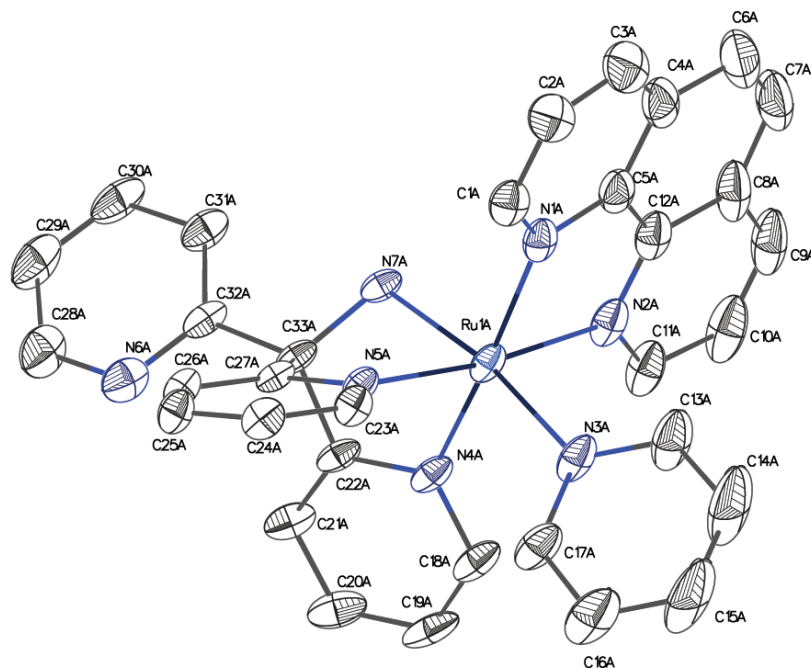
Figure 4.5 - ORTEP crystal structure of [Ru(tpyma)(phen)(py)](PF$_6$)$_2$

Extending the aromatic structure of the bpy ligand to form phen seems to improve the stacking in the crystal. This leads to a more defined crystal structure with a single cation throughout. The unit cell, shown in figure 4.6, contains four complex ions alongside ten PF$_6^-$ counterions, some of which are shared with neighbouring units. Both the unit cell and the structure shown in figure 4.7 show some stacking of the phen ligands. There is some curvature induced in the ligand, particularly visible in figure 4.7. The phen units are π-π stacking, showing a slight overlap of the ligands. This may explain the differences between the bpy and phen complexes on DNA binding, as the phen complex displays more pronounced stacking in its crystal form and perhaps can interact with DNA in a similar way, while the bpy complex is disordered and does not bind to DNA. As with the [Ru(dppz)(py)$_4$](PF$_6$)$_2$ structure shown in section 4.1.2, the stacking of the ligands does not extend through the crystal as it is disrupted by the PF$_6$ counter ions.

Complex	$[Ru(tpyma)(phen)(py)]^{2+}$
Empirical formula	$C_{33}H_{27}F_{12}N_7P_2Ru$
Formula weight	912.62
Temperature/K	100
Crystal system	Triclinic
Space group	P-1
a/Å	11.4223(6)
b/Å	17.4299(10)
c/Å	21.4205(12)
α/°	106.488(3)
β/°	104.315(3)
γ/°	104.296(3)
Volume/Å^3	3724.3(4)
Z	4
ρ_{calc}g/cm^3	1.628
μ/mm^{-1}	0.603
F(000)	1824.0
Crystal size/mm^3	0.25 × 0.25 × 0.15
Radiation	MoKα (λ = 0.71073)
2θ range for data collection/°	2.11 to 55.056
Index ranges	-14 ≤ h ≤ 14, -22 ≤ k ≤ 22, -27 ≤ l ≤ 27
Reflections collected	120760
Independent reflections	17121 [R_{int} = 0.0637, R_{sigma} = 0.0472]
Data/restraints/parameters	17121/145/1024
Goodness-of-fit on F^2	1.065
Final R indexes [I>=2σ (I)]	R_1 = 0.0542, wR_2 = 0.1334
Final R indexes [all data]	R_1 = 0.0816, wR_2 = 0.1512
Largest diff. peak/hole / e Å^{-3}	2.44/-0.88

Table 4.3 - Summary of crystal structure data for $[Ru(tpyma)(phen)(py)](PF_6)_2$

Compared to [Ru(dppz)(py)$_4$], co-ordination of tpyma produces significantly more distortion away from ideal octahedral geometry. The N-Ru-N bond angles within the ligand show a restrictive bite angle, with angles much more acute than the ideal octahedral 90°. Between the two pyridines the angle is 84.72°, while angles involving py-NH$_2$ are 77.82° and 77.85°. The trans angle from NH$_2$ to the pyridine ligand also reflects this distortion, being 169.83°, reduced from 179.28° when the pyridines are unhindered in [Ru(dppz)(py)$_4$](PF$_6$)$_2$. The Ru-N bond lengths for each on the tridentate sites are similar, ranging from 2.06 Å to 2.09 Å. These are significantly shorter than those observed for the unconnected pyridines, which ranged from 2.15 Å to 2.23 Å. This indicates that connecting the pyridines is forcing them to adopt closer bonds with the Ru(II) centre.
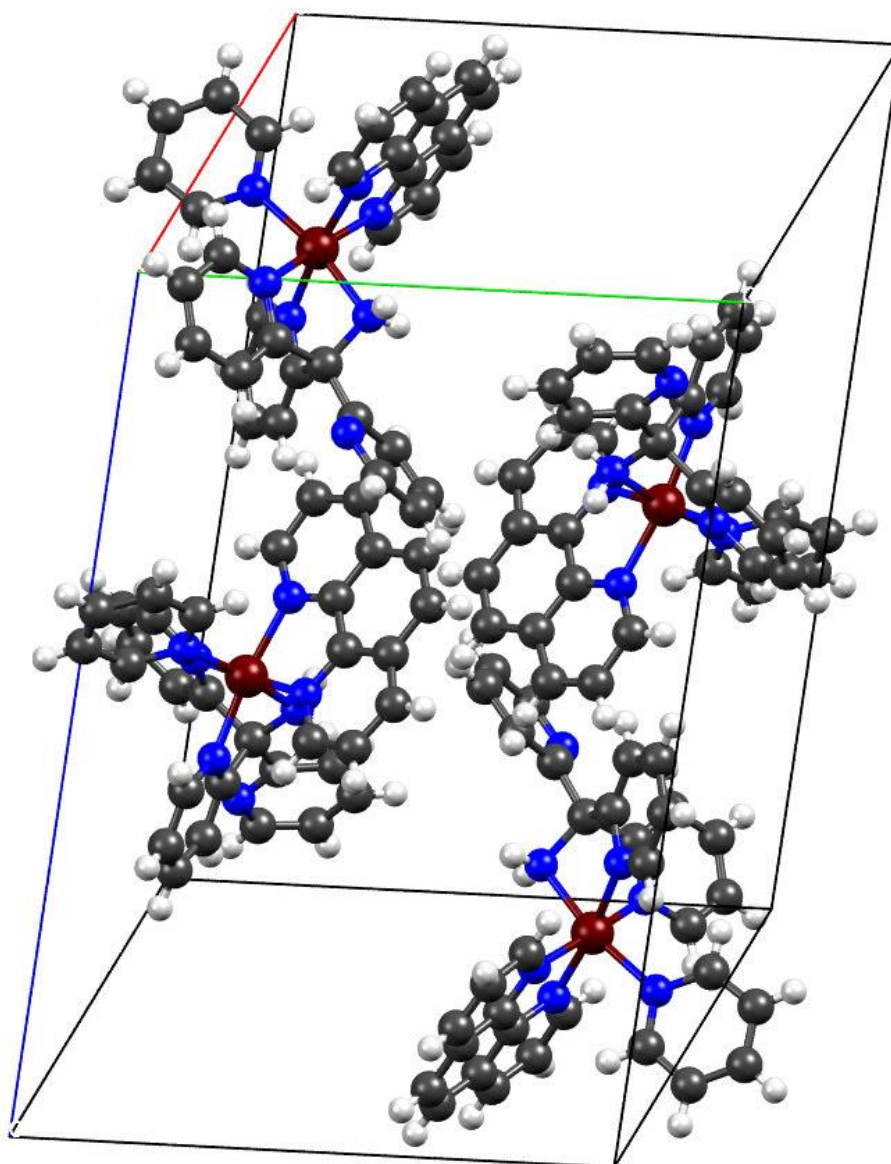
Figure 4.6 - Unit cell of the [Ru(tpyma)(phen)(py)](PF$_6$)$_2$ crystal. Counter ions removed for clarity.

The phen ligand is effectively a shortened version of dppz, presenting the same molecular shape at the point that it co-ordinates to the Ru(II) centre. Therefore, as would be expected, the N-Ru-N bite angle is very similar, at 78.82° compared to 78.87° for the dppz in section 4.1.2. At 2.07 Å and 2.08 Å the bond lengths are also similar, being only 0.02 Å to 0.06 Å shorter.

The py ligand has an Ru-N bond distance of 2.09 Å, shorter than that observed in [Ru(dppz)(py)$_4$], but similar to the other complexes containing the tpyma ligand. This may be due to an inductive effect of the amine trans to the pyridine. As the amine is a good σ-donor, its donation of electron density may increase back bonding to the π-acceptor pyridine ligand, thus increasing bond strength and decreasing length. The N-Ru-N bond angle to the phen ligand are close to ideal at 89.46° and 91.47° while, as previously seen, the pyridines of the tpyma ligand appear be distorted away from ideal as the N-Ru-N angle is increased to 93.98° and 95.96°.
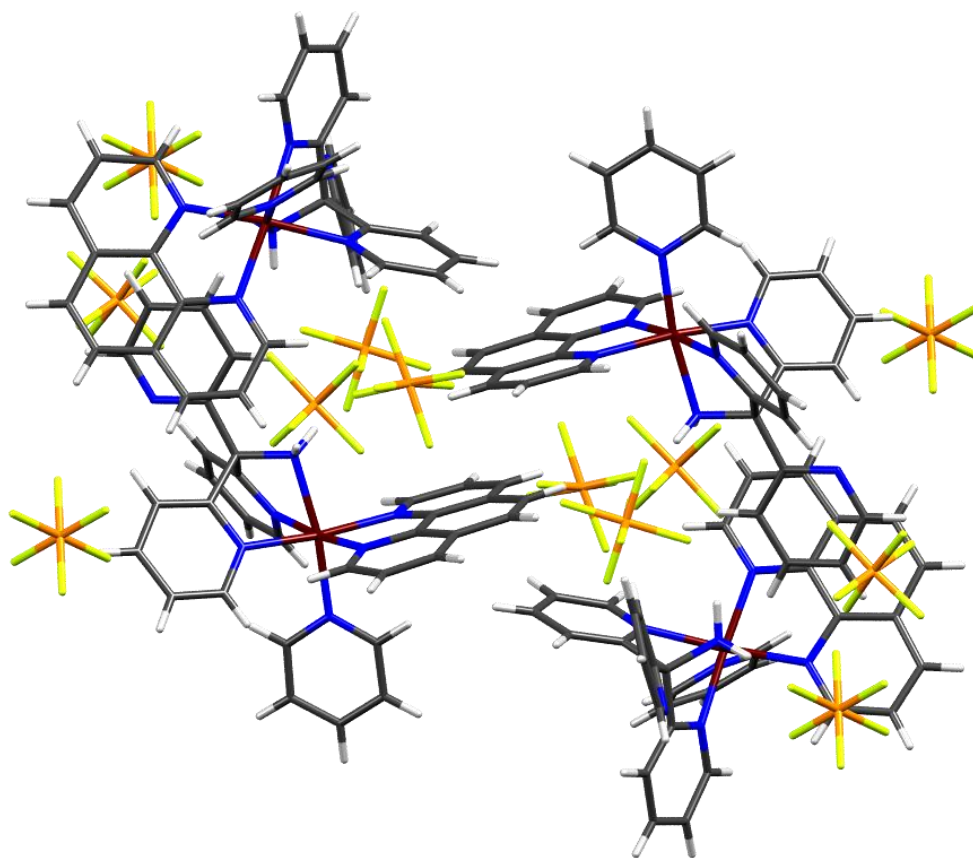
Figure 4.7 – Extended structure of the [Ru(tpyma)(phen)(py)](PF$_6$)$_2$ crystal, including PF$_6$ counter ion positions

4.2.3 X-ray crystal structure of [Ru(tpyma)(dpqx)(py)](PF$_6$)$_2$

The X-ray crystal structure of [Ru(tpyma)(dpqx)(py)](PF$_6$)$_2$ is shown in figure 4.8 with a summary of the data collected in table 4.4.
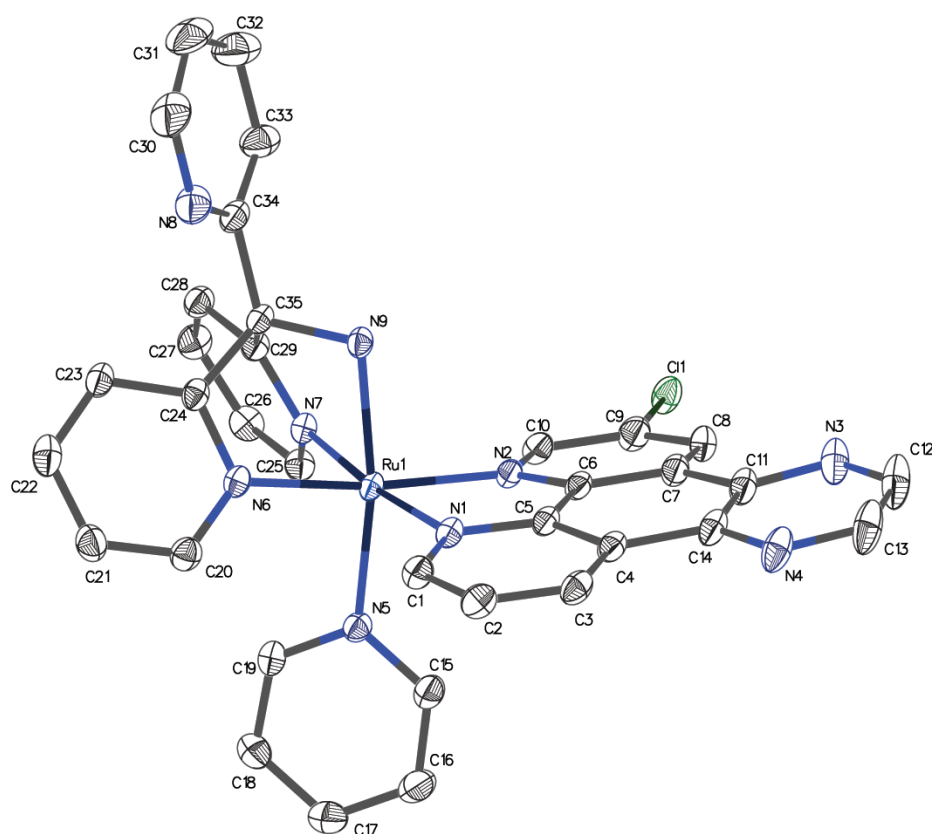
Figure 4.8 - ORTEP crystal structure of [Ru(tpyma)(dpqx)(py)](PF$_6$)$_2$

The [Ru(tpyma)(dpqx)(py)]$^{2+}$ complex shows additional, unexpected electron density next to the dpqx ligand. Efforts to solve the crystal indicated that only one ion was present, such that the electron density is not likely due to an impurity in the crystal. The feature is too close to be a counter ion and is within bonding distance of the ligand. The only way this could be explained is with a halide atom, as with the Cl atom in the ORTEP diagram of figure 4.8. This however does not make chemical sense and was not observed in the mass spectrum. It was unclear what this feature is and it was not possible to further purify the complex. This compound was not used for DNA binding for this reason. It was not possible to investigate this phenomena further in the course of the project.

Complex	$[Ru(tpyma)(dpqx)(py)]^{2+}$
Empirical formula	$C_{36}H_{29}ClF_{12}N_{10}O_2P_2Ru$
Formula weight	1060.15
Temperature/K	100
Crystal system	Triclinic
Space group	P-1
a/Å	11.3429(6)
b/Å	13.2446(6)
c/Å	14.3449(7)
α/°	105.714(2)
β/°	90.292(3)
γ/°	110.408(3)
Volume/Å^3	1932.44(17)
Z	2
ρ_{calc}g/cm^3	1.822
μ/mm^{-1}	0.667
F(000)	1060.0
Crystal size/mm^3	0.4 × 0.1 × 0.06
Radiation	MoKα (λ = 0.71073)
2Θ range for data collection/°	2.968 to 61.286
Index ranges	-16 ≤ h ≤ 16, -18 ≤ k ≤ 18, -20 ≤ l ≤ 20
Reflections collected	79721
Independent reflections	11881 [R_{int} = 0.0582, R_{sigma} = 0.0415]
Data/restraints/parameters	11881/3/588
Goodness-of-fit on F^2	1.068
Final R indexes [I>=2σ (I)]	R_1 = 0.0440, wR_2 = 0.1008
Final R indexes [all data]	R_1 = 0.0617, wR_2 = 0.1093
Largest diff. peak/hole / e Å^{-3}	1.94/-0.70

Table 4.4 - Summary of crystal structure data for [Ru(tpyma)(dpqx)(py)](PF$_6$)$_2$

4.2.4 X-ray crystal structure of [Ru(tpyma)(dppz)(py)](PF$_6$)$_2$

The X-ray crystal structure of [Ru(tpyma)(dppz)(py)](PF$_6$)$_2$ is shown in figure 4.9 with a summary of the data collected in table 4.5.
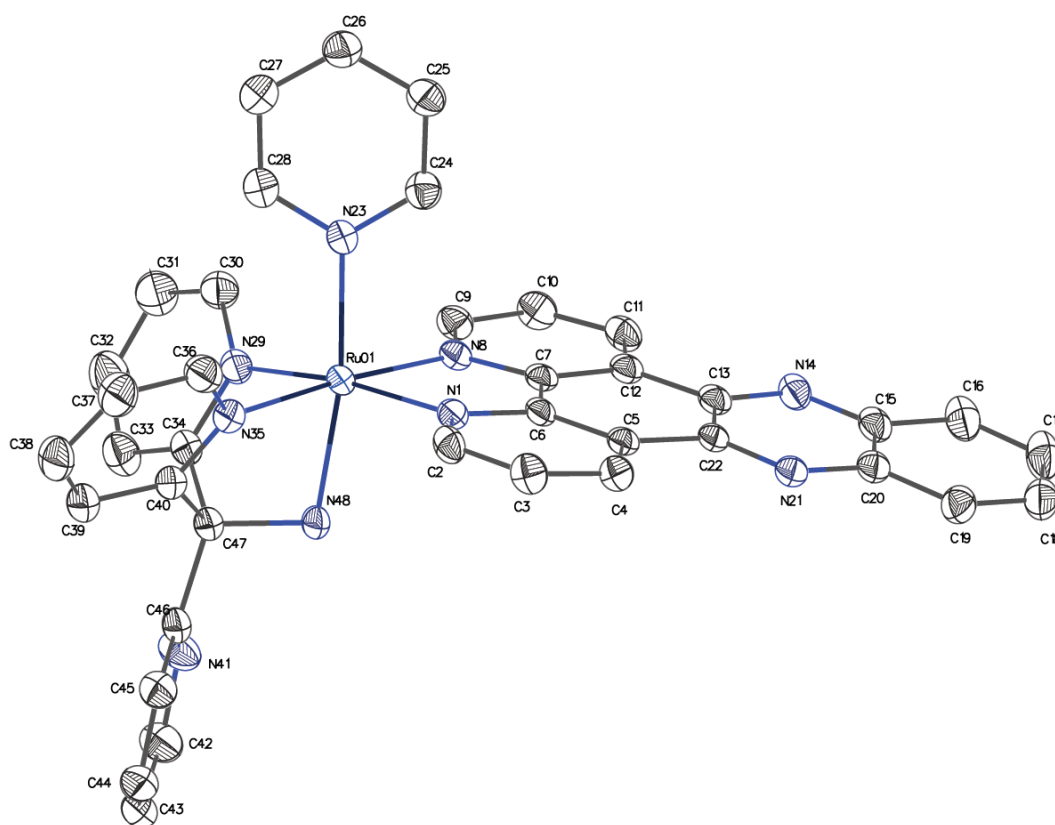
Figure 4.9 - ORTEP crystal structure of [Ru(tpyma)(dppz)(py)](PF$_6$)$_2$

The dppz complex shows more stacking between the cations than previous examples. The unit cell in figure 4.10 contains eight cations alongside sixteen PF$_6$ counterions. The unit cell shows the dppz stacked on top of each other, slightly offset from each other. The stacking causes a slight bend in the ligand as it overhangs the ligand stacked beneath it. The π-π interactions result in pillars of dppz ligands stacked on top of one another, running through the crystal. This is illustrated in figure 4.11.

Complex	$[Ru(tpyma)(dppz)(py)]^{2+}$
Empirical formula	$C_{39}H_{29}F_{12}N_9P_2Ru$
Formula weight	1014.72
Temperature/K	99.99
Crystal system	monoclinic
Space group	C2/c
a/Å	32.6903(14)
b/Å	15.0788(7)
c/Å	17.6527(8)
α/°	90
β/°	92.982(2)
γ/°	90
Volume/Å^3	8689.8(7)
Z	8
$\rho_{calc}g/cm^3$	1.551
μ/mm^{-1}	4.448
F(000)	4064.0
Crystal size/mm^3	$0.3 \times 0.2 \times 0.05$
Radiation	CuKα (λ = 1.54178)
2Θ range for data collection/°	5.414 to 133.424
Index ranges	$-38 \le h \le 38, -17 \le k \le 17, -21 \le l \le 21$
Reflections collected	61540
Independent reflections	7688 [R_{int} = 0.0388, R_{sigma} = 0.0205]
Data/restraints/parameters	7688/660/605
Goodness-of-fit on F^2	1.079
Final R indexes [I>=2σ (I)]	R_1 = 0.0362, wR_2 = 0.0889
Final R indexes [all data]	R_1 = 0.0389, wR_2 = 0.0903
Largest diff. peak/hole / e Å^{-3}	1.40/-0.75

Table 4.5 - Summary of crystal structure data for $[Ru(tpyma)(dppz)(py)](PF_6)_2$

The structural arrangement of the tpyma ligand is comparable to that observed for the phen ligand. The internal N-Ru-N angles are very similar, with py-py angle of 83.94° and py-NH$_2$ angles of 77.18° and 78.61°. The angle across the molecule, between the tpyma NH$_2$ and separate pyridine ligand, is only slightly wider than the phen equivalent, at 170.64°. The Ru-N bond lengths are also similar, having the same 2.06 – 2.09 Å range as with the phen complex. The dppz complex also exhibits the same short Ru-py bond distance as the phen complex, possibly due to an inductive effect of the NH$_2$, as previously discussed.

The geometry of the dppz ligand is slightly different to that of $[Ru(dppz)(py)_4]^{2+}$, with a wider N-Ru-N angle of 79.24° but the Ru-N bond lengths at 2.08 and 2.07 Å are the same.
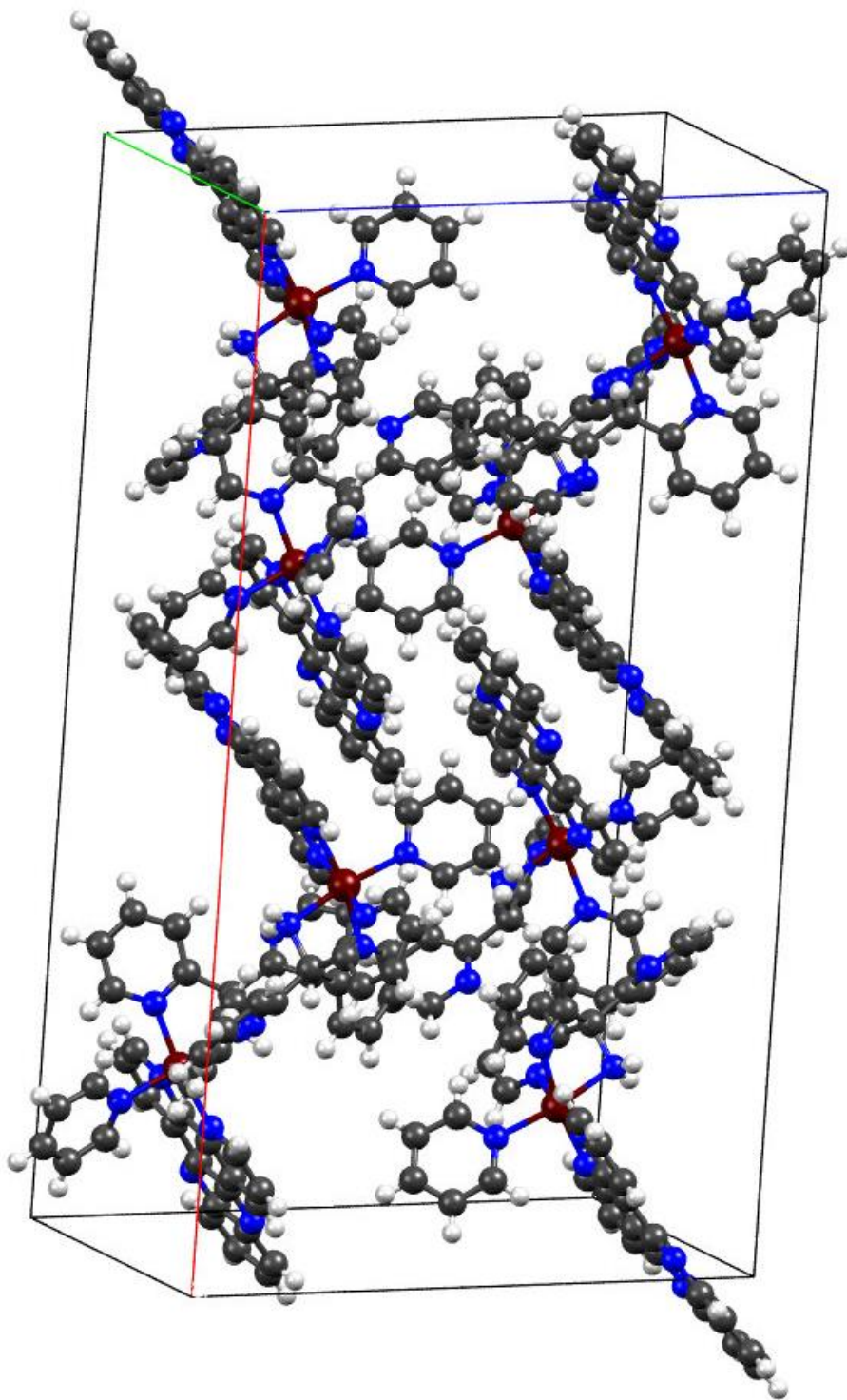
Figure 4.10 - Unit cell of the [Ru(tpyma)(dppz)(py)](PF$_6$)$_2$ crystal. Counter ions removed for clarity.
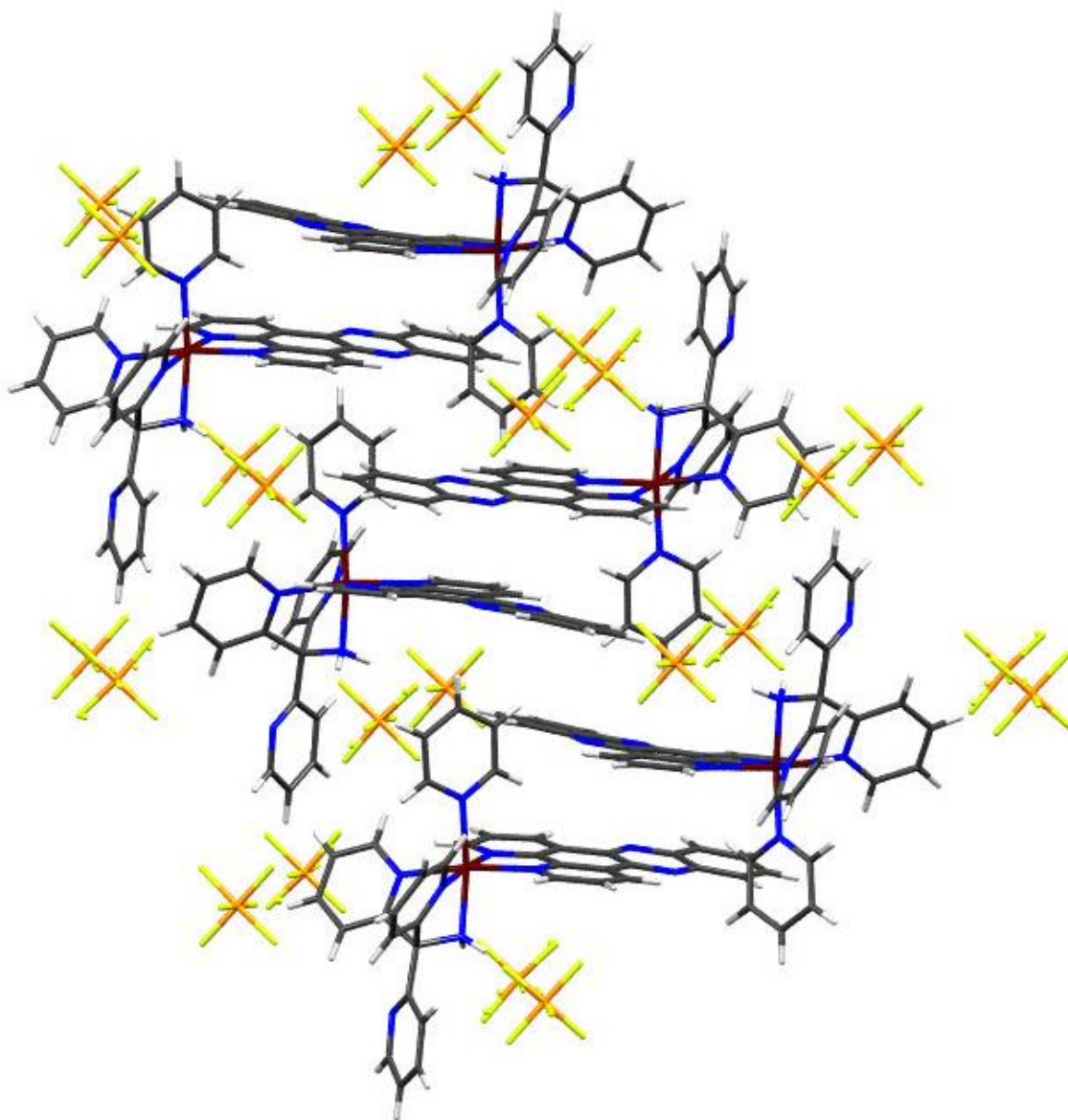
Figure 4.11 - Extended structure of the [Ru(tpyma)(dppz)(py)](PF$_6$)$_2$ crystal, including PF$_6$ counter ion positions

The key feature of the [Ru(tpyma)(dppz)(py)](PF$_6$)$_2$ crystal structure that sets it apart from the phen complex is the stacking that runs through the crystal. This is most clearly shown by figure 4.11. Here, each complex is stacked atop another, while being slightly rotated, presumably to avoid the clash of the end of the dppz ligand with the tpyma ligand of the neighbouring complex. The stacking also appears to have induced a slight twist in the dppz ligand. As a fused system of aromatic rings the dppz would be expected to be planer in geometry, however this is clearly not the case in the crystal. It appears as though the dppz is bending over the edge of the dppz ligand of its neighbour complex in the crystal. This stacking is not as offset as is seen with the [Ru(dppz)(py)$_4$](PF$_6$)$_2$ crystal.

4.2.5 X-ray crystal structure of [Ru(tpyma)(dppn)(py)](PF)$_6$

The X-ray crystal structure of [Ru(tpyma)(dppn)(py)](PF$_6$)$_2$ is shown in figure 4.12 with a summary of the data collected in table 4.6.
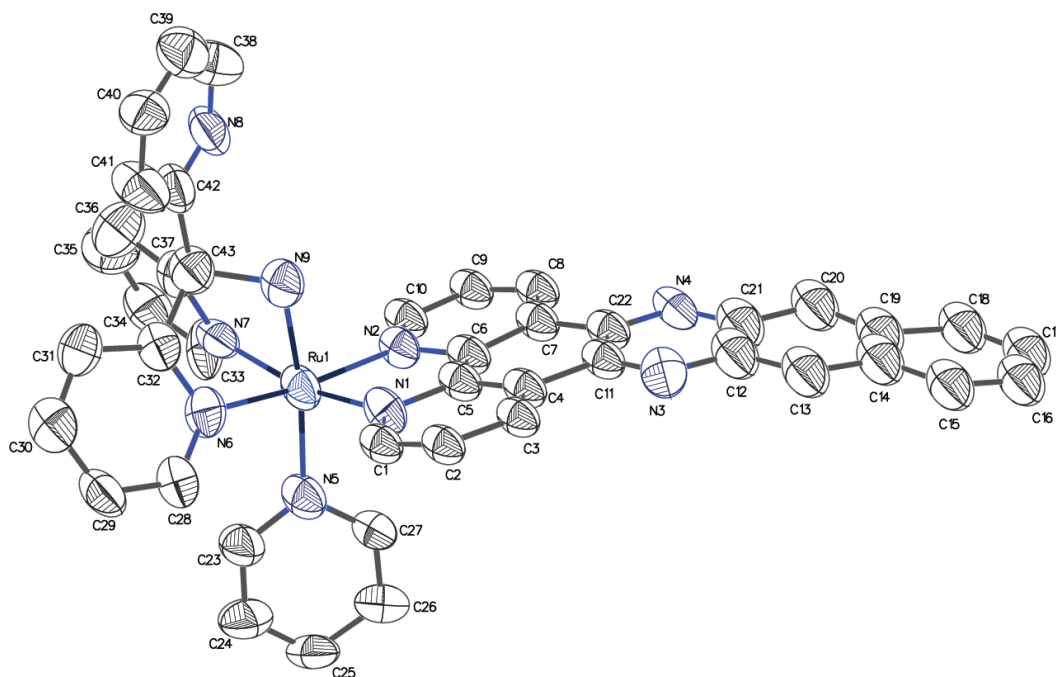
Figure 4.12 - ORTEP crystal structure of [Ru(tpyma)(dppn)(py)](PF$_6$)$_2$

The unit cell of the crystal structure of [Ru(tpyma)(dppn)(py)](PF$_6$)$_2$ initially appears a lot less ordered than the previous dppz and phen complexes, with inter ligand stacking not clear. However the expanded structure shown in figure 4.14 demonstrates that there is significant stacking present throughout the structure. The unit cell contains 8 complex cations alongside 20 PF$_6^-$ ions, some shared with neighbouring unit cells. The individual complex cations are far more distorted than both phen and dppz complexes. The dppn ligand, which is expected to be planar, displays a significant curvature, greater than that observed for the dppz ligand. It appears as though the cause of this curvature is the steric interaction with the tpyma ligand on the ruthenium centre when the complexes are stacked end to end.

Complex	$[Ru(tpyma)(dppn)(py)]^{2+}$
Empirical formula	$C_{344}H_{248}F_{102}N_{72}P_{17}Ru_8$
Formula weight	8663.18
Temperature/K	99.98
Crystal system	Triclinic
Space group	P-1
a/Å	13.581(2)
b/Å	16.739(3)
c/Å	37.537(5)
α/°	93.738(9)
β/°	99.354(10)
γ/°	97.994(11)
Volume/Å^3	8305(2)
Z	1
ρ_{calc}g/cm^3	1.732
μ/mm^{-1}	4.772
F(000)	4341.0
Crystal size/mm^3	0.08 × 0.05 × 0.05
Radiation	CuKα (λ = 1.54178)
2Θ range for data collection/°	4.79 to 81.874
Index ranges	-11 ≤ h ≤ 11, -13 ≤ k ≤ 14, -31 ≤ l ≤ 31
Reflections collected	54381
Independent reflections	10360 [R_{int} = 0.4687, R_{sigma} = 0.2461]
Data/restraints/parameters	10360/2598/2128
Goodness-of-fit on F^2	1.051
Final R indexes [I>=2σ (I)]	R_1 = 0.1062, wR_2 = 0.2290
Final R indexes [all data]	R_1 = 0.2133, wR_2 = 0.2778
Largest diff. peak/hole / e Å^{-3}	1.20/-0.54

Table 4.6 - Summary of crystal structure data for $[Ru(tpyma)(dppn)(py)](PF_6)_2$

The internal angles of the co-ordinated tpyma ligand share similar values with previous examples, with a slightly narrower N-Ru-N angle between pyridines of 82.93° and py-NH$_2$ angles of 77.71° and 78.67°. The axial angle from NH$_2$ and pyridine is closer to the unhindered pyridine example than the phen and dppz complexes, at a value of 172.35°. The Ru-N distances from the tpyma ligand are shorter than the previous examples with the distance to the co-ordinated amine at only 1.99 Å and the pyridine distances of 2.04 Å and 2.02 Å.

The bite angle of the dppn ligand itself is similar to the dppz example, with an N-Ru-N angle of 79.83°. The Ru-N distances for the dppn seem to indicate the distortion of the ligand as the one side of the ligand is held at a distance of 2.00 Å while the other is 2.08 Å suggesting the ligand is somewhat twisted, unlike the dppz example where there was only a 0.01 Å difference between the two Ru-N distances. The py-Ru bond is also shorter than in the phen and dppz examples, with an Ru-N distance of only 2.06 Å.
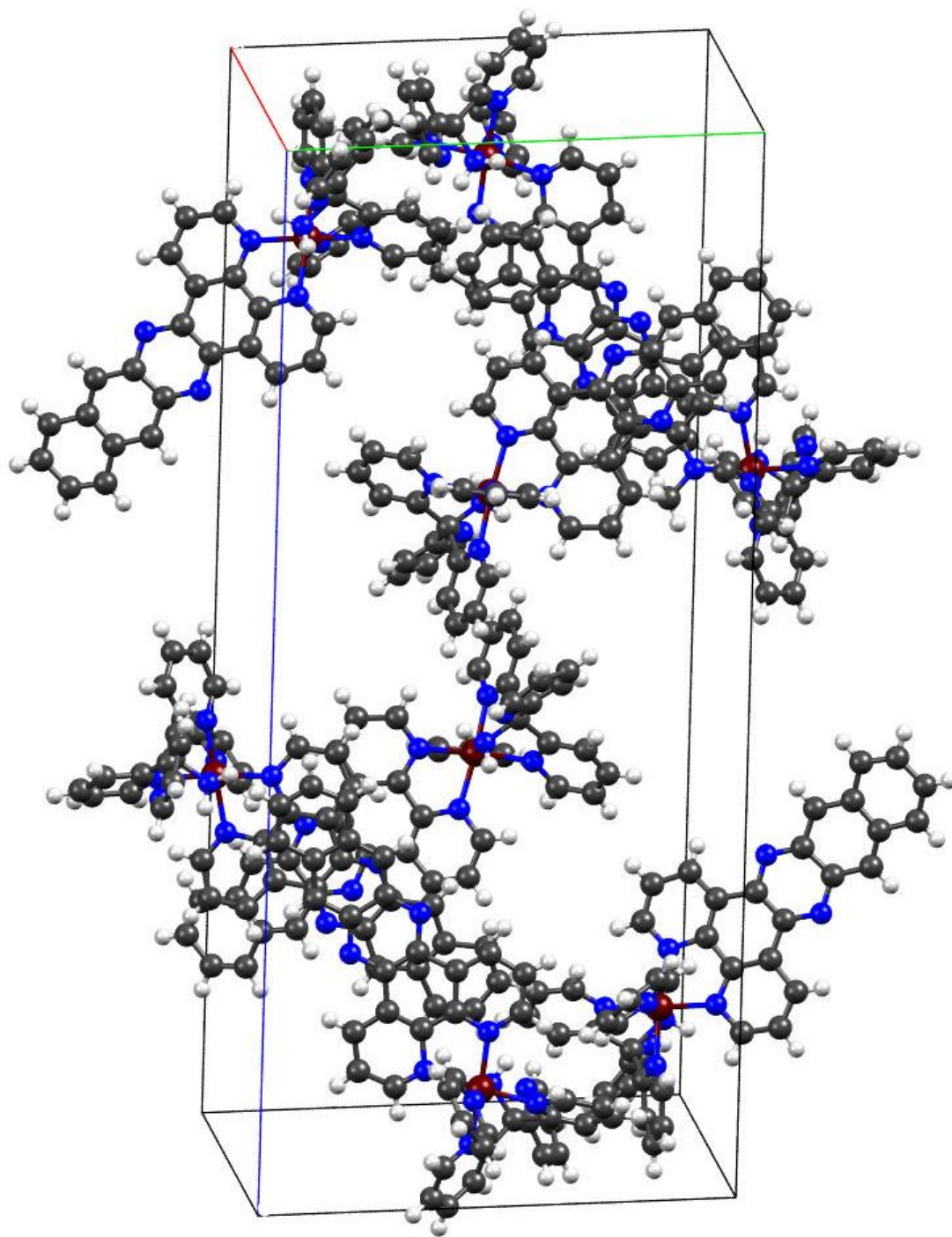
Figure 4.13 - Unit cell of the [Ru(tpyma)(dppn)(py)](PF$_6$)$_2$ crystal. Counter ions removed for clarity.
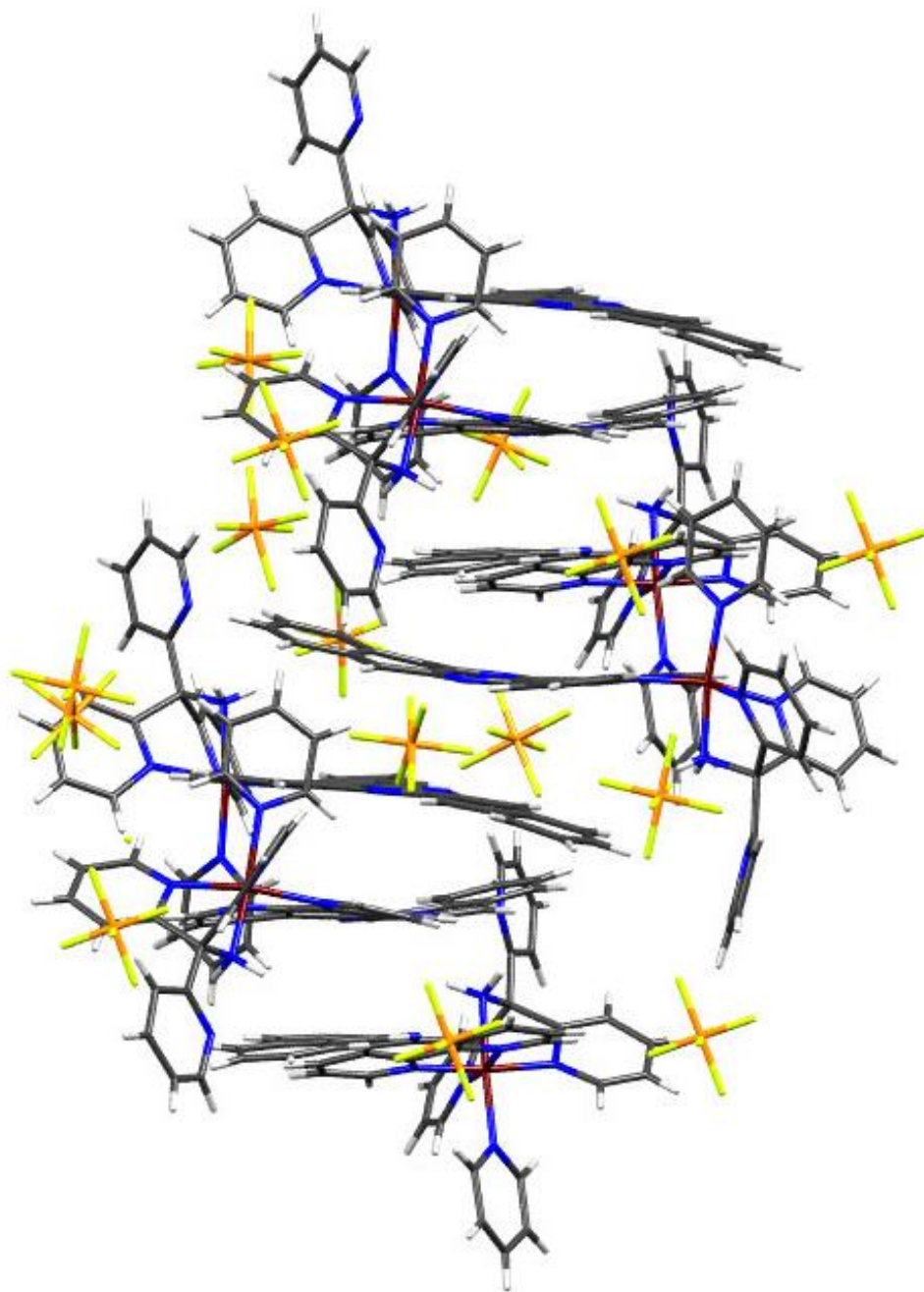
Figure 4.14 - Extended structure of the [Ru(tpyma)(dppn)(py)](PF$_6$)$_2$ crystal, including PF$_6$ counter ion positions

The stacking of the dppn units, shown in figure 4.14, is similar to that observed for the dppz complex. The complexes appear to be stacked in pairs with two units π-π stacking end to end, very slightly offset and curved to avoid clash with the ruthenium centre at the opposite end. There is then a stacked pair above and below which are rotated 90º with respect to the pair below. This also makes it appear that the dppn ligand is bending around the unit stacked below it. The curvature of the dppn ligand is greater than that of the dppz, possibly owing to its greater length, however it does not seem to display the equatorial twist that was seen in the dppz example.

4.3 Structural studies of di(pyridyl) ruthenium complexes

4.3.1 X-ray crystal structure of [Ru(dpyma)(dppz)(py)](PF$_6$)$_2$

The X-ray crystal structure of [Ru(dpyma)(dppz)(py)](PF$_6$)$_2$ is shown in figure 4.15 with a summary of the data collected in table 4.7.
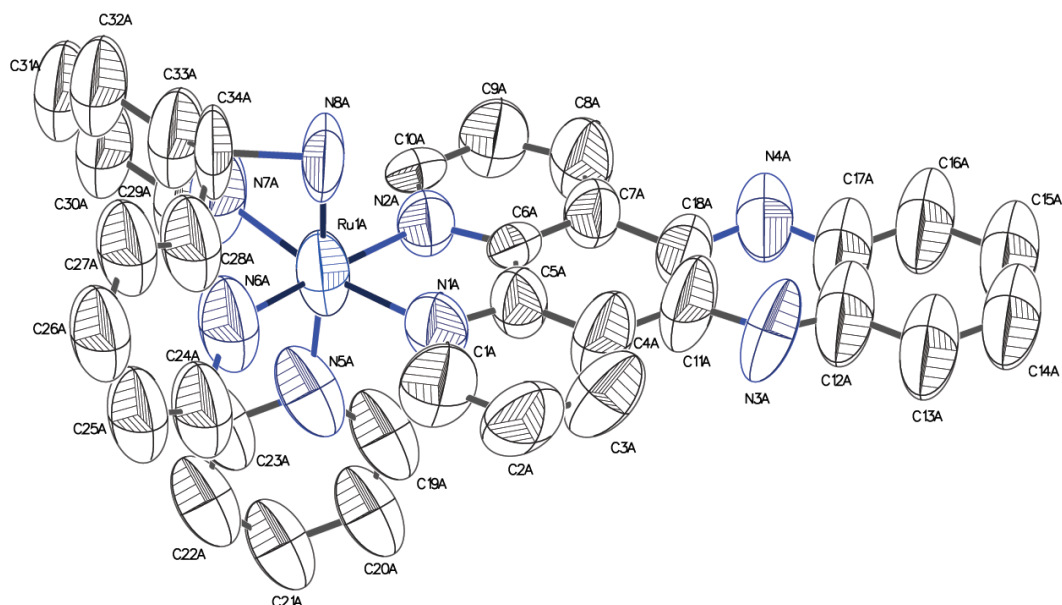
Figure 4.15 - ORTEP crystal structure of [Ru(dpyma)(dppz)(py)](PF$_6$)$_2$

The ORTEP diagram in figure 4.15 showing the dpyma complex exhibits large ellipsoids, hinting at the low quality of the crystal and subsequent data collection. The unit cell shows a very similar stacking arrangement of the compound as it found for the equivalent tpyma-containing complex. The unit cell shown in figure 4.16 contains 8 units alongside 16 PF$_6^-$ counterions, the same as the tpyma complex. It also shares a monoclinic crystal system with the tpyma complex but has a different space group. The stacking in the structure, best illustrated in figure 4.17, is similar to that of the tpyma complex, although it appears that the removal of the pendant pyridine has allowed for closer packing. There is some twist induced in the dppz ligand but it appears less pronounced than for the tpyma complex.

Complex	$[Ru(dpyma)(dppz)(py)]^{2+}$
Empirical formula	$C_{34}H_{26}F_{12}N_8P_2Ru$
Formula weight	937.64
Temperature/K	100
Crystal system	monoclinic
Space group	$P2_1/c$
a/Å	18.11(3)
b/Å	13.85(2)
c/Å	31.10(5)
α/°	90
β/°	105.450(15)
γ/°	90
Volume/Å^3	7520(20)
Z	8
ρ_{calc}g/cm^3	1.656
μ/mm^{-1}	0.600
F(000)	3744.0
Crystal size/mm^3	0.2 × 0.1 × 0.05
Radiation	MoKα (λ = 0.71073)
2Θ range for data collection/°	2.332 to 32.018
Index ranges	-14 ≤ h ≤ 13, -10 ≤ k ≤ 10, -24 ≤ l ≤ 23
Reflections collected	23454
Independent reflections	3667 [R_{int} = 0.2943, R_{sigma} = 0.1606]
Data/restraints/parameters	3667/1268/482
Goodness-of-fit on F^2	1.457
Final R indexes [I>=2σ (I)]	R_1 = 0.1766, wR_2 = 0.4257
Final R indexes [all data]	R_1 = 0.3052, wR_2 = 0.5013
Largest diff. peak/hole / e Å^{-3}	2.17/-0.55

Table 4.7 - Summary of crystal structure data for $[Ru(dpyma)(dppz)(py)](PF_6)_2$

The internal N-Ru-N angles of the dpyma ligand are close to that of the tpyma ligand, with a larger 88.66° between the two pyridines, and 77.51° and 82.27° from the two pyridines to the amine. The axial angle from the NH_2 group to the separate pyridine ligand is 173.11° illustrating that although there is a distortion from the octahedral 180°, it is closer to the ideal than the 170° of the tpyma equivalent example. The Ru-N bond distances for dpyma are 2.08 Å for Ru-NH_2, with 2.06 Å and 2.10 Å for the Ru-py distances, which are in a very similar range to those observed for the tpyma complex. It seems that the removal of the pendant pyridine has had little effect on the internal structure of the ligand, apart from a slight reduction in the overall distortion of the complex.

The dppz ligand in this case has a slightly wider N-Ru-N bite angle of 80.56° and Ru-N distances of 2.04 Å and 2.06 Å; indicating that the dppz is bonded slightly closer to the ruthenium centre, although this could be an artefact of the lower quality data due to

poor resolution. The Ru-py bond distance is the shortest of all the examples at only 2.04 Å.
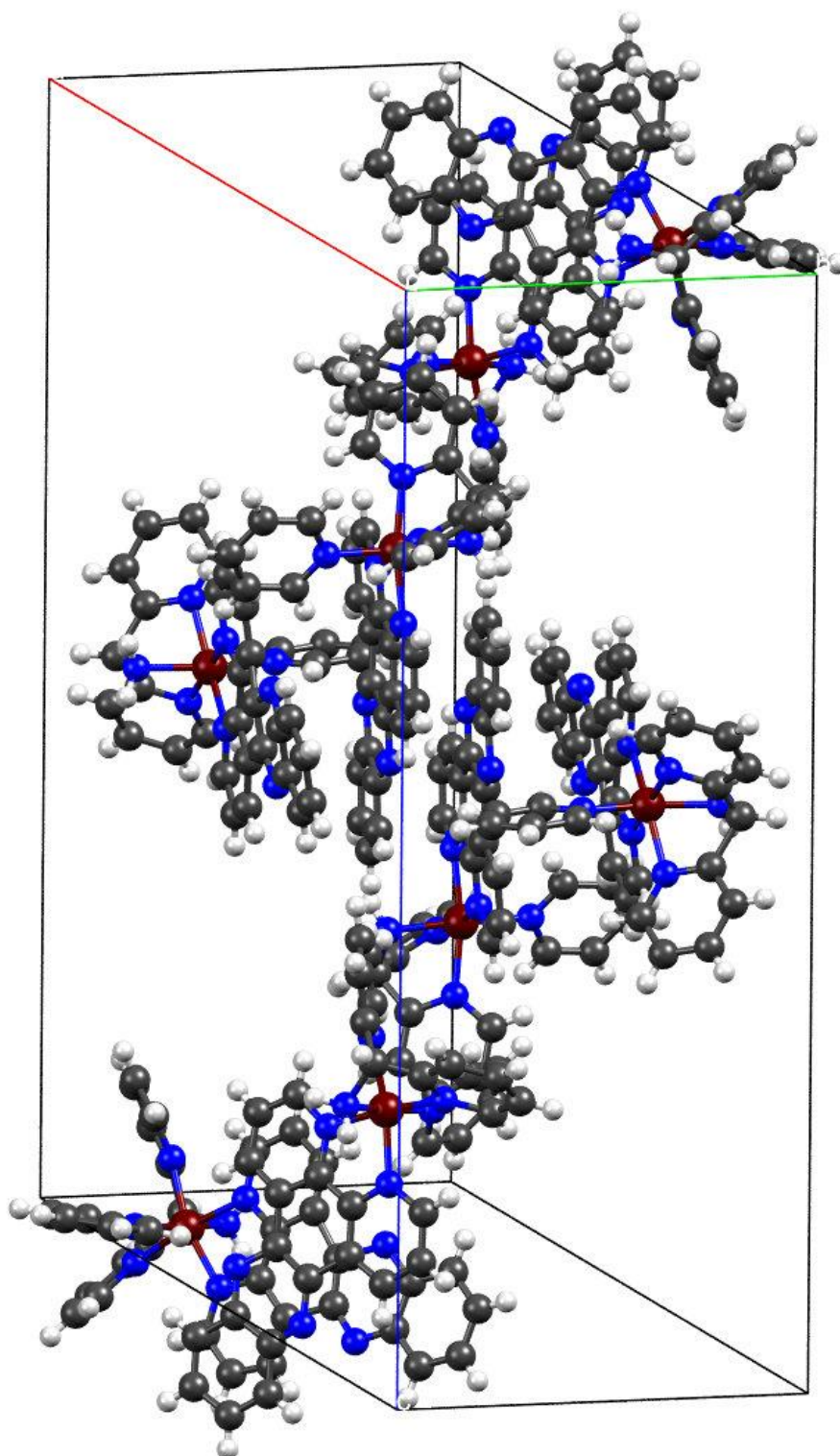
Figure 4.16 - Unit cell of the [Ru(dpyma)(dppz)(py)](PF$_6$)$_2$ crystal. Counter ions removed for clarity.
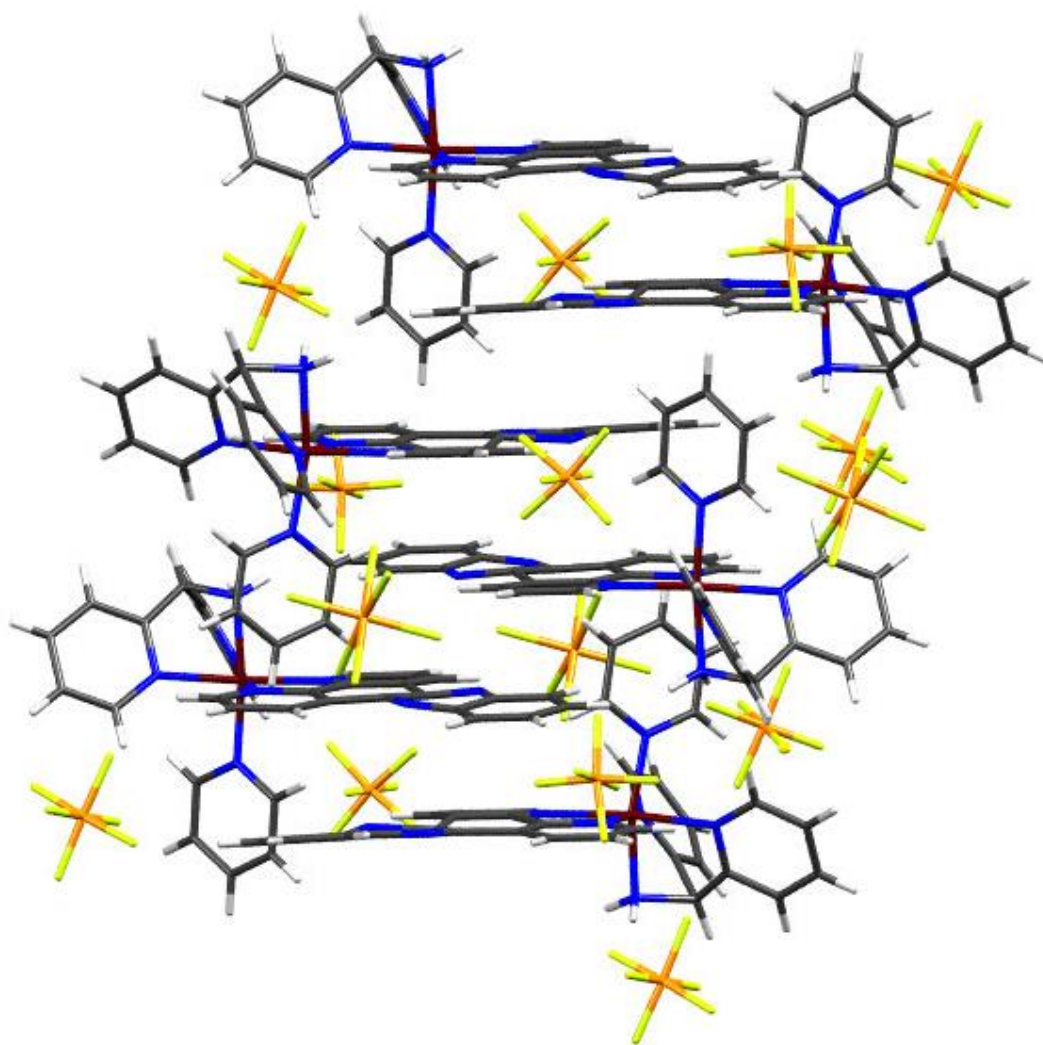
Figure 4.17 - Extended structure of the [Ru(dpyma)(dppz)(py)](PF$_6$)$_2$ crystal, including PF$_6$ counter ion positions

As previously alluded to, the stacking shown in figure 4.17 appears more ordered, with less distortion of the dppz ligand. It is closer to the planar state that would be preferable if it were not under any strain in the crystal. This is likely because the removal of the extra pyridine to form dpyma from tpyma has resulted in less steric strain induced throughout the crystal. There is still some twist in the dppz but it seems less significant than in the tpyma example. Although it is difficult to accurately measure, it also appears that the units are positioned closer together than in the tpyma crystal.

4.4 Structural studies of other ruthenium complexes

4.4.1 X-ray crystal structure of [Ru(tpya)(dppz)](PF$_6$)$_2$

The X-ray crystal structure of [Ru(tpya)(dppz)](PF$_6$)$_2$ is shown in figure 4.13 with a summary of the data collected in table 4.8.
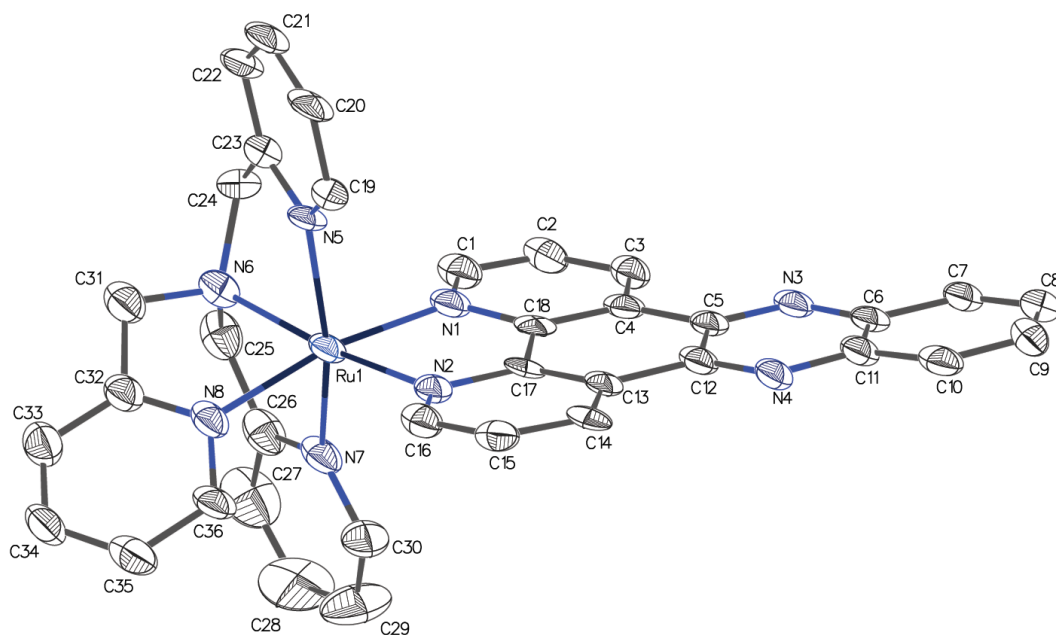
Figure 4.18 - ORTEP crystal structure of [Ru(tpya)(dppz)](PF$_6$)$_2$

The unit cell of the [Ru(tpya)(dppz)](PF$_6$)$_2$ crystal is very similar to the structure of the [Ru(tpyma)(dppz)(py)](PF$_6$)$_2$ crystal. There are eight units per unit cell alongside sixteen PF$_6^-$ counterions and four nitromethane solvent molecules. The crystal system is monoclinic which is in common with the tpyma and dpyma examples and the unit cell shares a P2$_1$/n space group with the dpyma complex. Visually, the dppz stack shown in figure 4.20 is very similar to that of the tpyma ligand, with some twist seemingly induced in the dppz ligand to avoid clash with the end of the complex that it is stacked with. There is more twist than the dpyma ligand as the amine group has been replaced by a pyridine, leading to greater steric interaction.

Complex	$[Ru(tpya)(dppz)]^{2+}$
Empirical formula	$C_{36.5}H_{29.5}F_{12}N_{8.5}OP_2Ru$
Formula weight	994.19
Temperature/K	100
Crystal system	monoclinic
Space group	$P2_1/n$
a/Å	15.0449(15)
b/Å	18.0960(19)
c/Å	31.139(3)
α/°	90
β/°	97.542(5)
γ/°	90
Volume/Å^3	8404.2(15)
Z	8
ρ_{calc}g/cm^3	1.571
μ/mm^{-1}	0.544
F(000)	3984.0
Crystal size/mm^3	0.25 × 0.25 × 0.1
Radiation	MoKα (λ = 0.71073)
2Θ range for data collection/°	2.608 to 54.97
Index ranges	$-19 \leq h \leq 19$, $-22 \leq k \leq 21$, $-40 \leq l \leq 40$
Reflections collected	86693
Independent reflections	18132 [R_{int} = 0.0887, R_{sigma} = 0.0857]
Data/restraints/parameters	18132/145/1100
Goodness-of-fit on F^2	1.019
Final R indexes [I>=2σ (I)]	R_1 = 0.0954, wR_2 = 0.2509
Final R indexes [all data]	R_1 = 0.1416, wR_2 = 0.2917
Largest diff. Peak/hole / e Å^{-3}	3.02/-2.72

Table 4.8 – Summary of crystal structure data for [Ru(tpya)(dppz)](PF$_6$)$_2$

Connecting pyridine rings to form the tpya ligand, via the amine, leads to a lot of strain in the ligand, distorting it away from the ideal octahedral geometry. When the pyridines are unhindered, as in [Ru(dppz)(py)$_4$](PF$_6$)$_2$, the N-Ru-N angle is at most 2.8° away from the octahedral 90°. The internal strain of the tpya ligand leads to the most extreme N-Ru-N angle between one of the pyridines and the tertiary amine at 11° tighter than the ideal 90°. The N-Ru-N angles between the pyridines and the amine range from 79.01° to 83.22°, while the py-py angles are 82.59° and 96.68°. The Ru-N bond distances for each of the tetradentate nitrogens of the tpya are similar, being either 2.08 Å or 2.09 Å. These are held much closer than the unhindered pyridines of [Ru(dppz)(py)$_4$](PF$_6$)$_2$ but are close to the distances observed for the tpyma and dpyma ligands. The distortion is also observed in the fact that the equatorially co-ordinated nitrogens in tpya do not sit in the same plane as the nitrogens of the dppz ligand.
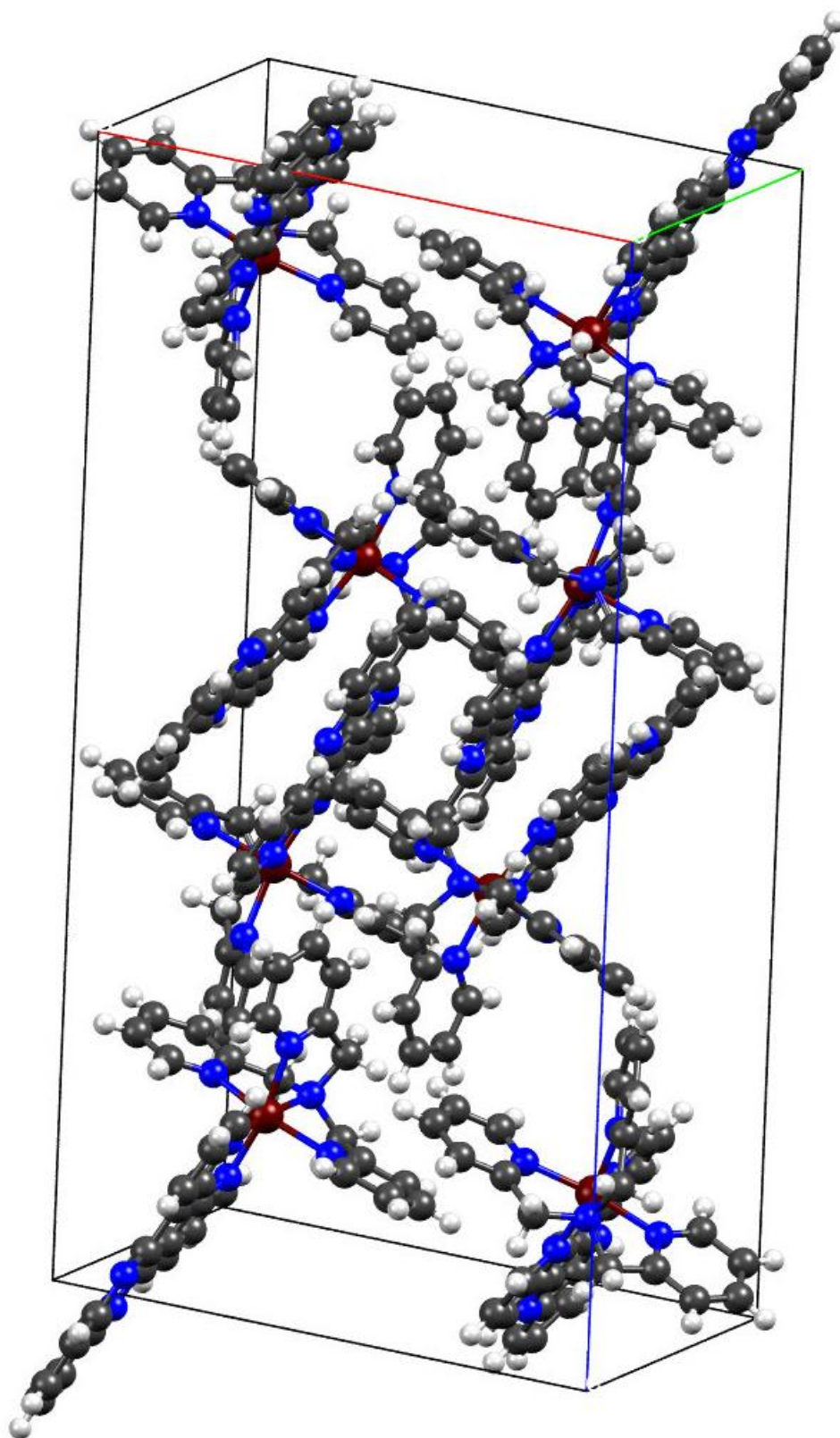
Figure 4.19 - Unit cell of the [Ru(dpya)(dppz)](PF$_6$)$_2$ crystal. Counter ions removed for clarity.
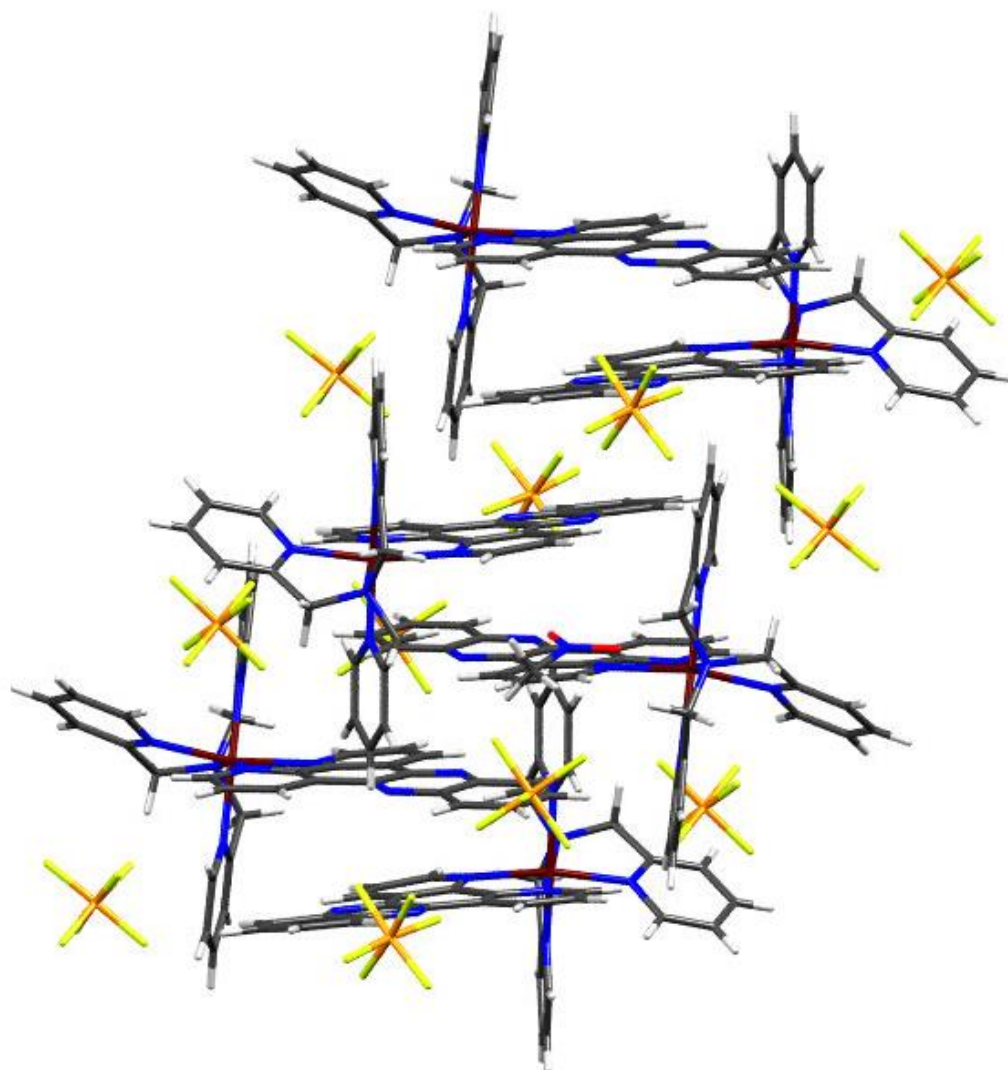
Figure 4.20 - Extended structure of the [Ru(tpya)(dppz)](PF$_6$)$_2$ crystal, including PF$_6$ counter ion positions

The dppz itself has similar co-ordination geometry to the previous examples, with an N-Ru-N bite angle of 77.85°, 1° tighter than for [Ru(dppz)(py)$_4$](PF$_6$)$_2$, with similar Ru-N distances of 2.09 Å and 2.10 Å.

The stacking of the dppz ligands, shown in figure 4.20, shows a strong resemblance to the stacking observed for the tpyma complex. Again the pattern in which two slightly offset units stack end to end is observed, with the units above and below the stacked pair are rotated roughly 90°, resulting in columns of stacked dppz ligands running through the structure. As with the tpyma example a clear curvature has been induced

in the dppz ligand. This is presumably to minimise the steric interactions with the tpya ligand at the other end of the stacked pair.

4.4.2 X-ray crystal structure of [Ru(dppz)(MeCN)$_3$(dmso)](PF$_6$)$_2$

The X-ray crystal structure of [Ru(tpya)(dppz)](PF$_6$)$_2$ is shown in figure 4.21 with a summary of the data collected in table 4.9.
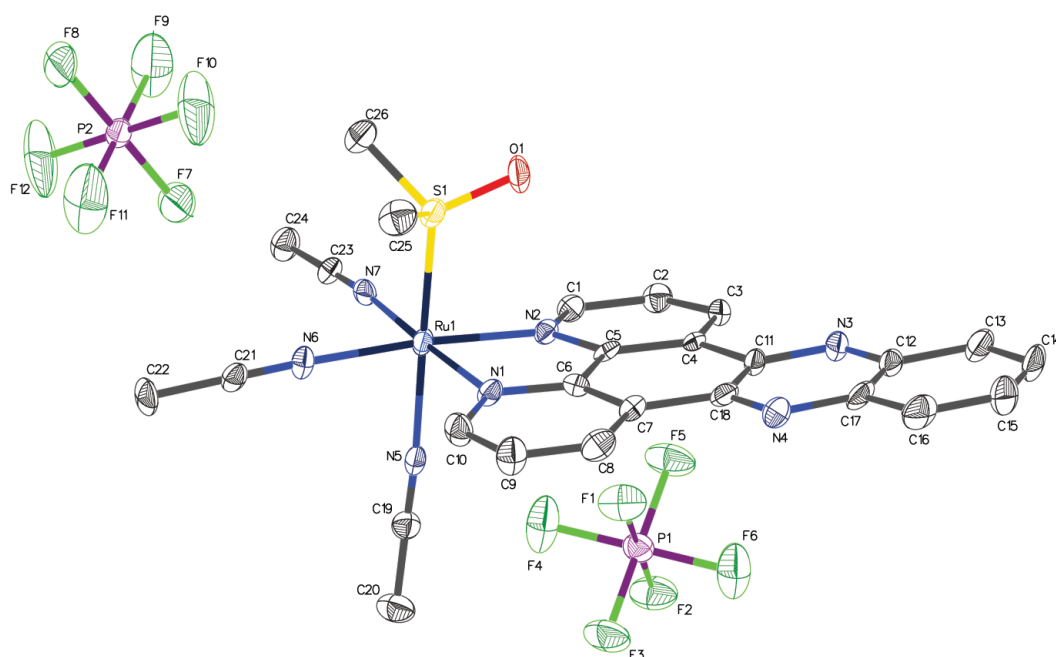
Figure 4.21 - ORTEP crystal structure of [Ru(dppz)(MeCN)$_3$(dmso)](PF$_6$)$_2$

The crystal of [Ru(dppz)(MeCN)$_3$(dmso)](PF$_6$)$_2$ displays a very similar structure to that of [Ru(dppz)(py)$_4$](PF$_6$)$_2$. The unit cell contains only two cations alongside four PF$_6^-$ counterions. The unit cell shares both the triclinic crystal system and the P-1 space group with the [Ru(dppz)(py)$_4$](PF$_6$)$_2$ crystal. The dimensions of the unit cell are also similar at 8.27 Å x 10.41 Å x 20.72 Å compared with the slightly larger cell of [Ru(dppz)(py)$_4$](PF$_6$)$_2$ at 10.75 Å x 10.79 Å x 22.30 Å, likely owing to the larger pyridine ligands. The unit cell also demonstrates the π-π stacking of the dppz ligands, with less distortion than previous examples, due to the smaller ancillary ligands resulting in less disruptive steric interactions.

Complex	$[Ru(dppz)(MeCN)_3(dmso)]^{2+}$
Empirical formula	$C_{26}H_{25}F_{12}N_7OP_2RuS$
Formula weight	874.60
Temperature/K	100
Crystal system	triclinic
Space group	P-1
a/Å	8.2726(18)
b/Å	10.412(2)
c/Å	20.720(5)
$\alpha/°$	86.756(9)
$\beta/°$	87.523(9)
$\gamma/°$	86.169(9)
Volume/Å^3	1776.4(7)
Z	2
ρ_{calc}g/cm^3	1.635
μ/mm^{-1}	0.686
F(000)	872.0
Crystal size/mm^3	0.4 × 0.21 × 0.05
Radiation	MoKα (λ = 0.71073)
2Θ range for data collection/°	3.926 to 54.868
Index ranges	-10 ≤ h ≤ 10, -13 ≤ k ≤ 13, -26 ≤ l ≤ 21
Reflections collected	23725
Independent reflections	7950 [R_{int} = 0.0817, R_{sigma} = 0.1285]
Data/restraints/parameters	7950/0/456
Goodness-of-fit on F^2	1.034
Final R indexes [I>=2σ (I)]	R_1 = 0.0656, wR_2 = 0.1346
Final R indexes [all data]	R_1 = 0.1201, wR_2 = 0.1546
Largest diff. peak/hole / e Å^{-3}	1.00/-0.92

Table 4.8 - Summary of crystal structure data for [Ru(dppz)(MeCN)$_3$(dmso)](PF$_6$)$_2$

As the ancillary ligands are not connected they are closer to the ideal octahedral geometry than previous examples. The angles between the acetonitrile ligands range from 87.22° to 88.00° and angles of 92.41° and 93.35° from the acetonitrile to dimethylsulfoxide ligand. The bond distances in the complex are also very consistent, with all Ru-N bonds, for both dppz and MeCN ligands, measuring 2.06 Å. The Ru-S bond is held at 2.27 Å, possibly due to the fact the ligand is S-bound which reduces back-bonding that would shorten the bond if it were O-bound. The dppz shows has a bite angle of 79.07° which is consistent with the [Ru(dppz)(py)$_4$](PF$_6$)$_2$ complex, where the dppz also appeared the least disrupted and closest to a planar formation.
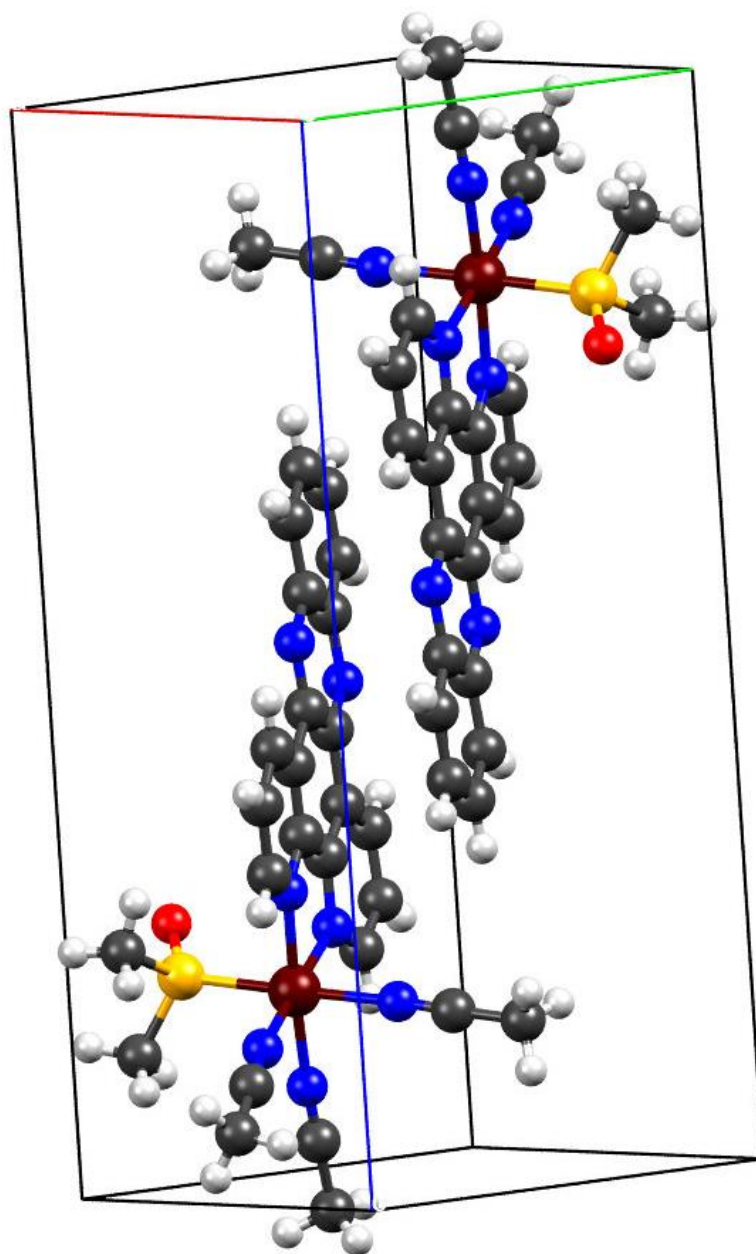
Figure 4.22 - Unit cell of the [Ru(dppz)(MeCN)₃(dmso)](PF₆)₂ crystal. Counter ions removed for clarity.

4.5 Conclusion

A number of crystal structures have been reported, demonstrating various symmetries and space groups. The technique provided confirmation that the binding mode of tpyma, was not as initially expected. This means that the amine, desired for functionalising the complex further, is actually co-ordinated to the ruthenium centre. This prevents the use of the complex for surface attachment. The study also confirms that removing the pendant pyridine to form the dpyma ligand does not change the co-ordination mode, with a tridentate ligand formed. This suggests that synthetic adjustments made to the ligand to introduce a surface attachment could be successful.

4.6 References

1   W. L. Bragg, *Proc. R. Soc. London. Ser. A*, 1913, **89**, 248 LP-277.

5.0 DNA Binding Studies

5.1 Introduction

The previous chapter described the synthesis of novel ruthenium complexes containing the tris(2-pyridyl)methylamine (tpyma) and di(2-pyridyl)methylamine (dpyma) ligands. In the case of tpyma containing complexes, a series of compounds were synthesised whereby the length of bidentate ligand was varied by extension of the aromatic system, from bpy to dppn. It is these planar bidentate ligands that primarily affect the nature of the DNA binding of the complex. Complexes containing bpy generally do not bind to DNA, while extending to phen leads to groove binding and dppz and dppn lead to intercalative interactions. Employing this series allows assessment of how the tpyma, as an ancillary ligand, affects DNA binding by comparison with these expected interactions. It could contribute to binding, whereby bpy complexes may bind to DNA, have no effect or disrupt binding, whereby dppz and dppn complexes would no longer intercalate. Figure 5.1 illustrates the series used for this study.
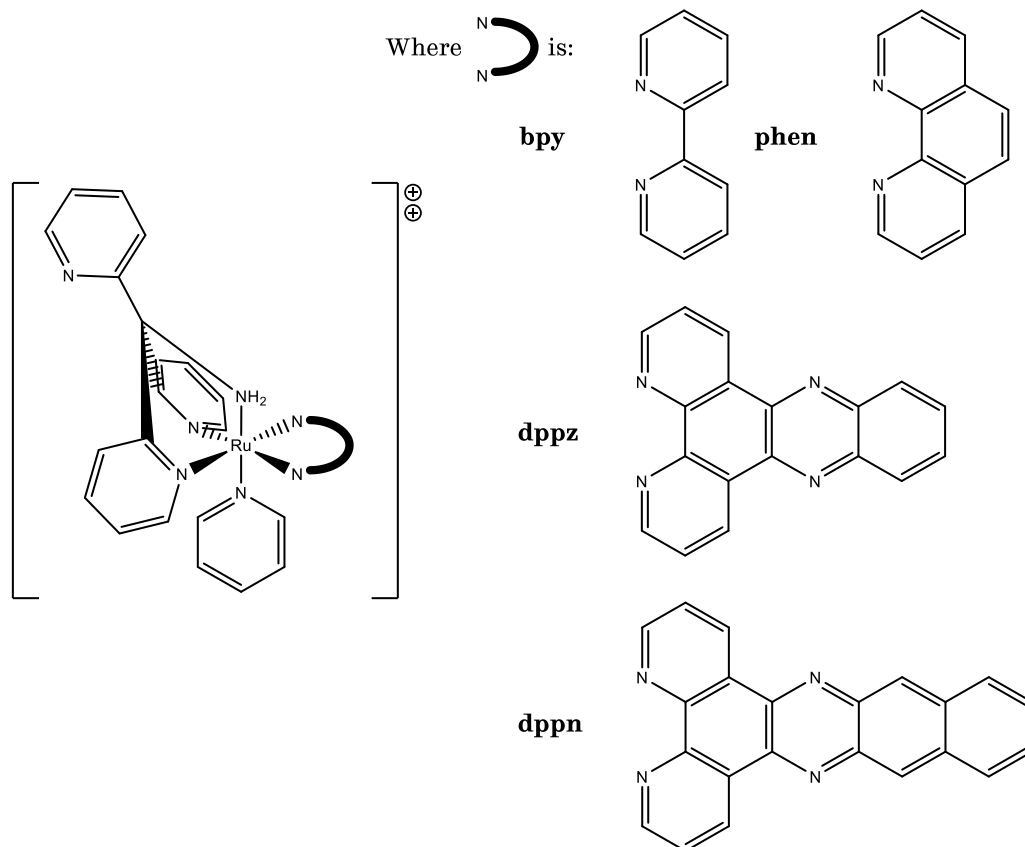
Figure 5.1 - The series of tpyma containing Ru(II) complexes studied in this chapter

As described in the previous chapter, the co-ordination mode of tpyma, discovered by x-ray crystallography makes it unsuitable for the desired surface attachment. Thus attempts were made to alter the ligand by replacing the pendant pyridine with a moiety capable of attaching to a surface. The first step in this was to study whether dpyma would co-ordinate and bind to DNA in a similar fashion to tpyma. Then dpyma could then be extended to add the required surface binding functionality. The study of DNA binding of $[Ru(dpyma)(dppz)(py)]^{2+}$, shown in figure 5.2, is also described in this chapter.
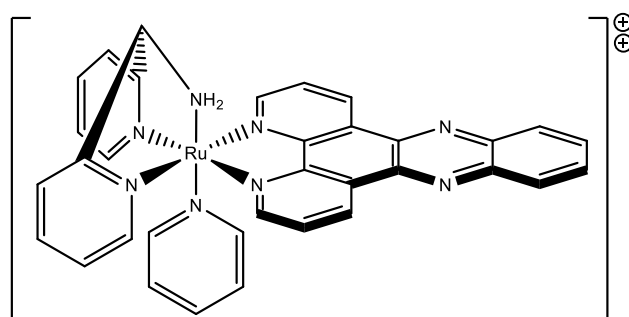
Figure 5.2 - Molecular structure of $[Ru(dpyma)(dppz)(py)]^{2+}$

The techniques described in this chapter to study DNA interaction are UV-Visible titration, luminescent titration and viscosity measurements.

5.1.1 DNA titration techniques

Ruthenium polypyridyl complexes possess photophysical properties that make them of interest in probing macromolecules. The two key features that confer this interest are the metal to ligand charge transfer (MLCT) state, which gives rise to a strong absorption[1] and strong emission from the lowest triplet MLCT state,[2] alongside low lying triplet d-d states, which may be accessed thermally from the MLCT state.[3] The interplay between these states governs the absorption and emission profiles of the ruthenium complex. The transfer of energy from MLCT to d-d state makes the complex emission sensitive to changes in solvent[1] and microenvironment.[2]

In the presence of DNA, when bound the ruthenium polypyridyl complex has transitioned from an aqueous solution into a hydrophobic environment within the DNA base pairs. This transition alters the energy levels such that changes are observed

in both the absorption and emission spectra. In the case of the UV-visible absorption of Ru-polypyridyl complexes this is often observed as a decrease in intensity within the visible region, otherwise known as a hypochromic shift. It is also possible that a bathochromic shift is observed in the MLCT state, whereby the absorption shifts to longer wavelength.

Changes are also observed in the emission profile as the MLCT state can be quenched *via* a non-emissive pathway in polar solvent. This is especially true in the case of dppz, which can hydrogen bond to water molecules through the nitrogens of the phenazine portion of the molecule. These bound water molecules couple with the vibrational states of the dppz to quench emission from the complex.[4] Thus when the bound dppz unit intercalates into the DNA duplex, it is protected from the effects of the water and becomes emissive, as it is in less-polar, aprotic solvent.

These behaviours of ruthenium polypyridyl complexes can be utilised to monitor their binding to DNA. Whilst the magnitude of the change in either absorption or emission is not important, the point at which the change stops can be used to estimate binding constants. This is due to the fact that, when DNA is titrated into a solution of complex, the point at which the spectra no longer changes indicates the point the DNA is saturated with bound complex. Using this point, the fraction of drug bound the complex can be calculated for each addition, and thus the concentration of bound drug is known. This is then used to construct a binding isotherm, from which a binding constant can be estimated. This process is described below.

In the case of a hypochromic shift in the UV-visible absorption, the observed intensity decrease is converted to fraction of complex bound (χ) using equation 5.1:

$$\chi = \frac{A_f - A_{obs}}{A_f - A_b}$$

Equation 5.1

Where A_f is the absorbance of the free complex, A_b is the absorbance of the fully bound complex and A_{obs} is the absorbance of the point for which the fraction of binding is being calculated.

Similarly the change in emission can also be converted to fraction of binding, however as an increase, rather than decrease is observed, they calculation is reversed, giving:

$$\chi = \frac{I_{obs} - I_f}{I_b - I_f}$$

Equation 5.2

Where I_f is the emission of the free complex, I_b is the emission of the fully bound complex and I_{obs} is the emission of the point for which the fraction of binding is being calculated.

Using the calculated fraction bound it is possible to determine the point of saturation. This is achieved by plotting χ against the mixing ratio (R), which is defined as:

$$R = \frac{[DNA]}{[Complex]}$$

Equation 5.3

The subsequent plot forms a saturation curve, if binding has occurred, where the fraction bound, χ, increases to plateau. At this point no more complex is binding despite the increase in DNA concentration and thus saturation has been achieved. An example of this type of plot is shown in figure 5.3.
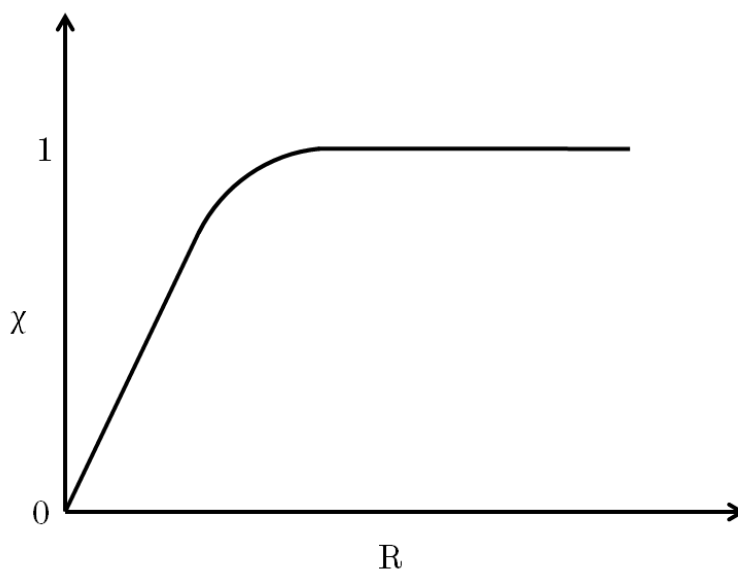
Figure 5.3 - Example of a binding plot showing a saturation curve

In the titration the initial concentration (C_i) of the complex remains the same throughout as DNA is added with an insignificant increase in overall volume. This

allows the concentration of bound complex (C_b) to be calculated, using the initial concentration and the fraction bound as:

$$C_b = \chi . C_i$$

Which in turn gives the concentration of the free complex (C_f) as, self evidently:

$$C_f = C_i - C_b$$

It is also possible, using the known concentration of DNA added to the solution, to calculate the binding ratio (r) defined as:

$$r = \frac{C_b}{[DNA]}$$

In order to use this data in the estimation of a binding constant it is necessary to construct a Scatchard plot. This method was developed by Scatchard in 1949, in an attempt to further understand the binding interactions of the many newly discovered examples of small molecules binding to proteins.[5] The method relies on the use of the Scatchard equation:

$$\frac{r}{C_f} = K_i(n - r)$$

Where K_i represents the binding constant and n is the number of binding sites occupied by the small molecule studied. Thus, plotting r/C_f is as a function of r, using data from suitable systems, results in a linear binding isotherm with a gradient of K_i and an intercept of n.

This equation works for simple systems where the ligand binding to the protein has a specific and isolated binding site. This means that one ligand binding to the protein has no impact on other ligands which subsequently bind. When considering DNA and ligands binding to base pairs this assumption is not valid. DNA exists as a lattice of

binding sites, where binding to site on the lattice will make binding to the neighbouring site less favourable.[6] Effectively the binding sites are overlapping and the probability of binding is affected, both by the number of other ligands already bound, and their relative positions on the lattice. This ultimately results in a non-linear Scatchard plot, for which the Scatchard equation is not useful.

As the binding of most naturally occurring materials do not show linear isotherms, attempts were made to enhance the model, taking into account the more complicated binding situation.[7] One such model, developed by McGhee and von Hippel,[6] has become widely accepted when studying the binding of DNA and Ru(II)-polypyridyl complexes. The model takes into account the effects of a ligand occupying more than one site in the lattice. It also contains considerations for ligands that bind co-operatively or non-cooperatively. In the case of Ru(II)-polypyridyl complexes, that are assumed not to be attracted to one another, the non-cooperative equation is used:

$$\frac{r}{C_f} = K(1 - nr).\left[\frac{(1 - nr)}{1 - (n - 1)r}\right]^{n-1}$$

Equation 5.8

Where K is the binding constant and n is the number of lattice sites occupied.

The data collected from titration experiments are fitted to this equation using the graphical software, Sigma plot, to give an estimation of both the binding constant and binding site size. Only the data between $\chi = 0.3$ and 0.9 is used to avoid over-estimating the binding constant. This is because, at high levels of binding, an abnormally high concentration of ligand is needed to force saturation.

5.1.2 Viscosity measurements

Viscosity (η) is a measure of the internal friction of a fluid. Its measurement has become an established method for the characterisation of DNA interactions. Pioneered by Lerman when studying the DNA binding properties of acridines, an intercalative binding mode was proposed partly based on the fact that addition of acridine to a DNA solution resulted in an increase in viscosity.[8] The theory proposed that when a ligand, such as the planar aromatic structure of acridine in this case, intercalates into DNA it pushes the base pairs of the duplex apart. This in turn lengthens the DNA strand and

thus alters its hydrodynamic properties. The change results in an observable increase in viscosity of the bulk DNA solution.

The theory was developed into a model, considering the DNA as strands with a defined contour length. It is the increase in contour length that gives rise to the increased viscosity. The relationship between the two is described by the equation:

$$\frac{L}{L_0} = \left(\frac{[\eta]f(p)_0}{[\eta]_0 f(p)}\right)^{\frac{1}{3}}$$

Equation 5.9

Where L is the contour length, η is the relative viscosity and p is the axial ratio. This equation points to the key strength of viscosity measurements. Here, the relative viscosity, η is proportional to L^3 meaning that the viscosity of the solution is very sensitive to changes in the contour length, caused by intercalating ligands.

The method developed as a robust way to differentiate between two key types of DNA interaction associated with polypyridyl complexes, intercalation and groove-binding. This is achieved by comparing the viscosity results of studied molecules to those of two species that have well characterised binding interactions, ethidium bromide and Hoechst 33258.[9] Ethidium bromide is a known intercalator[10] and thus increases the viscosity of DNA solutions. Hoechst 33258 is a known groove binder, whereby it associates with the DNA groove without displacing the base pairs. This does not induce the increase in contour length, and thus viscosity, observed for intercalation. This interaction has been confirmed by other techniques, including x-ray crystallography[11] and NMR structural studies.[12] Using the relationship described in equation 5.9, this change in viscosity can be visualised using a plot of $(\eta/\eta_0)^{1/3}$ versus R^{-1}, where R is the ratio of bound complex to DNA. On the resultant graph a positive gradient will indicate intercalation, while a flat gradient will indicate groove binding. This is illustrated in figure 5.4.
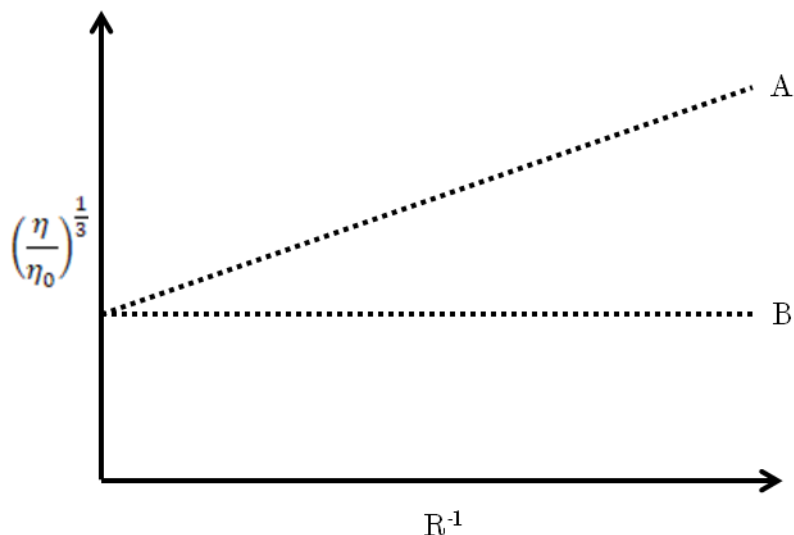
Figure 5.4 - Graphical representation of viscometry data, showing expected result for intercalation (A) and groove binding (B)

Practically, viscosity can be determined using a simple viscometer in the form of a capillary tube. As the viscosity of the solution in the tube increases it will take longer to fall through the tube, under the influence of gravity, known as the flow time. Relative viscosity can then be calculated by comparison of the flow time of the solvent alone and the flow time of the DNA solution as described by equation 5.10:

$$\eta = \frac{t - t_0}{t_0}$$

Equation 5.10

where t is the flow time of the DNA solution and t_0 is the flow time of the solvent alone.

The viscosity of the DNA solution relative to the viscosity of the buffer is set as initial viscosity, η_0. This is used alongside the relative viscosities of the solutions of DNA and increasing concentrations of complex to generate a plot similar to that shown in figure 5.4. The concentration of complex is kept low compared to DNA to avoid any confusion on saturating the DNA with complex where no further viscosity increase would be observed.

5.2 Experimantal Considerations

This section presents results from initial investigations into the DNA binding of the novel ruthenium complexes described in chapter 3. With the exeption of viscosity experiments, time constraints prevented the titration experiments from being repeated, resulting in large errors in the calculation of binding constants. The results presented in this section should be treated as initial estimates and further work is required to assess whether the binding constants, and features of the binding, are repeatable. This further work will result in more robust and reliable estimates of binding constant.

5.2.1 Sample preparation

All studies involving DNA were performed in an aqueous buffer, constituted of 5 mM Tris and 25 mM NaCl at pH 7.5. Calf thymus DNA (CT-DNA) was used for all binding studies. CT-DNA was prepared as a stock solution, dissolving strands of the DNA in the buffered solution. The solution was sonicated to form smaller DNA fragments and homogenise the size distribution. The sonication was performed as alternating on/off cycles and in ice to avoid damage to the DNA by heating.

Each of the complexes was converted to their respective chloride salt from the PF_6 form in which they were synthesised. This enabled their dissolution in the buffer.

5.3 UV-Visible Titrations of [Ru(tpyma)(NN)(py)]²⁺

5.3.1 Titration of [Ru(tpyma)(bpy)(py)]Cl₂

The UV-Visible absorbance traces for the titration of CT-DNA into a solution of [Ru(tpyma)(bpy)(py)]²⁺ are displayed in figure 5.5. The darkest trace indicates that no DNA has been added, while traces of lighter colour indicate the sequential addition of DNA, as per the inset legend of figure 5.5.
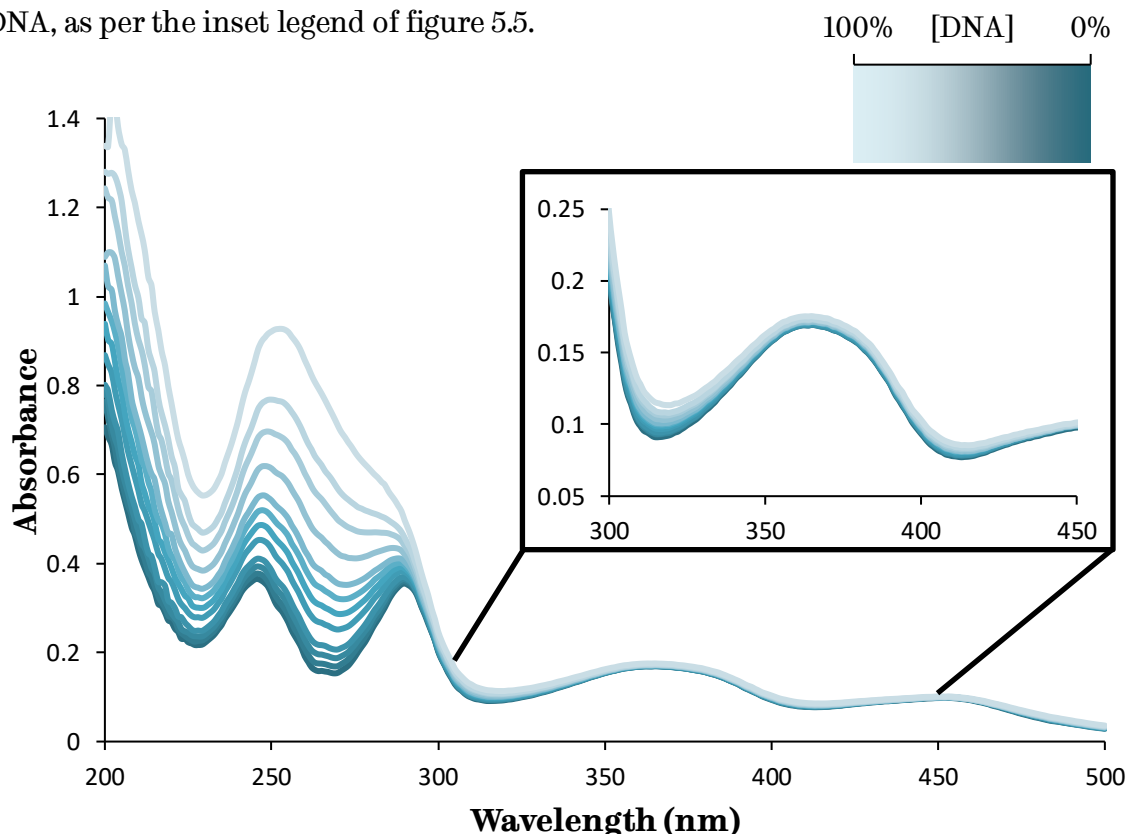
Figure 5.5 - UV-visible titration of 1.65 mM bp⁻¹ CT-DNA into 2.15 µM solution of [Ru(tpyma)(bpy)(py)]Cl₂ in buffer

As discussed in the introduction, the change in microenvironment of Ru(II)-polypyridyl complexes on binding to DNA normally results in hypochromicity of the absorption spectra. In the case of [Ru(tpyma)(bpy)(py)]²⁺ this is not observed. Rather there is hyperchromicity in the bands at 244 nm and 289 nm. This is assumed to be the influence of the absorbance of the CT-DNA added to the solution which absorbs maximally at 260 nm. The bands at 365 nm and 455 nm which have the most MLCT character are the most likely to be affected on binding to DNA, however no significant change is observed.

Due to the lack of hypochromicity in this case, it is not possible to construct a binding curve. Figure 5.6 tracks the maximum absorbance of the band at 365 nm showing that, rather than hypochromicity, a very slight hyperchromicity is observed. This could be due to slight background absorbance of the DNA. This very small change in the absorbance spectrum suggests that there is no significant change in the microenvironment of the complex when mixed with CT-DNA. It seems fair to assume that the complex does not bind to DNA. It is therefore a very useful compound to act as a control for future experiments. If this compound were to be bound to a surface, and then show some change in microenvironment, it would be known that some added binding event may be present in all the tested complexes. This would constitute a more complex binding picture than that which is observed in solution, thus requiring further study and understanding.

5.3.2 Titration of [Ru(tpyma)(phen)(py)]Cl₂

The UV-Visible absorbance traces for the titration of CT-DNA into a solution of [Ru(tpyma)(phen)(py)]$^{2+}$ are displayed in figure 5.7. The manner of displaying traces relating to higher concentrations of DNA as a lighter shade is the same as for the bpy complex.
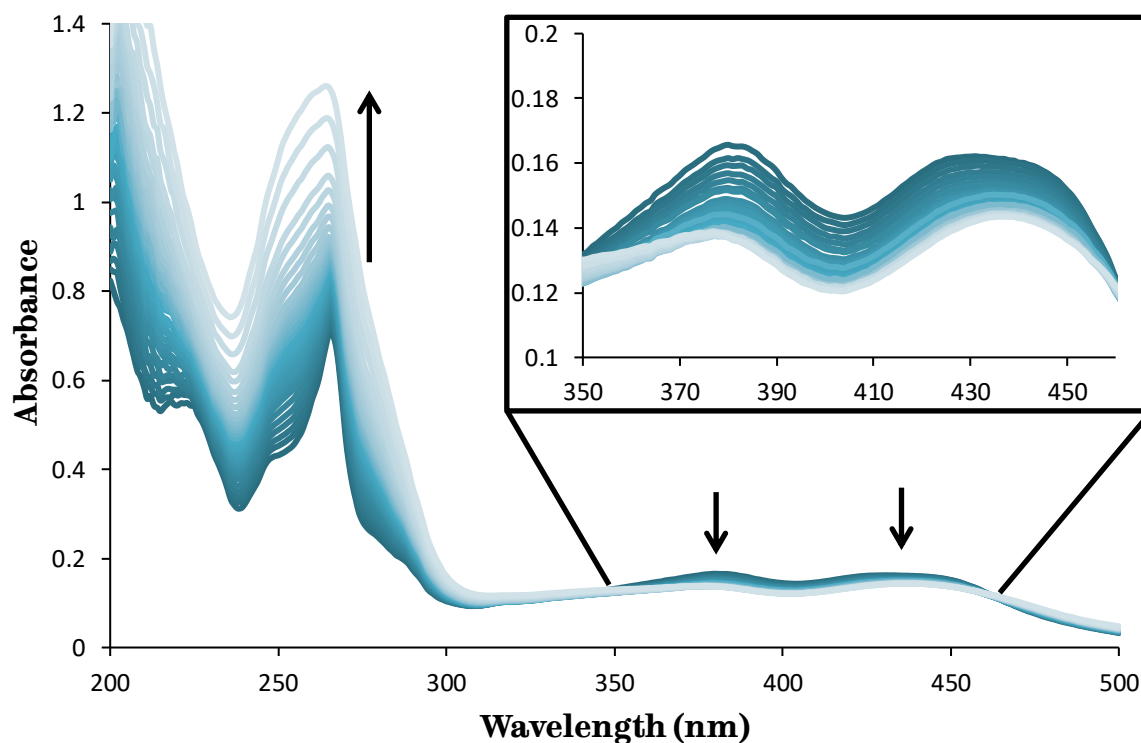
Figure 5.7 - UV-visible titration of 1.65 mM bp^{-1} CT-DNA into 2.15 μM solution of [Ru(tpyma)(phen)(py)]Cl₂ in buffer

Unlike the previous example, [Ru(tpyma)(phen)(py)]$^{2+}$ does show a hypochromic shift on the addition of DNA. Both the bands at 382 nm and 437 nm show this behaviour, indicating that in this case there is a change in microenvironment. The band around 264 nm is hyperchromic, though as with the bpy complex this is likely to be due to the added DNA having a maximal absorbance at 260 nm. Tracking the decreasing absorbance of the band at 382 nm enables the construction of a binding curve, shown in figure 5.8.
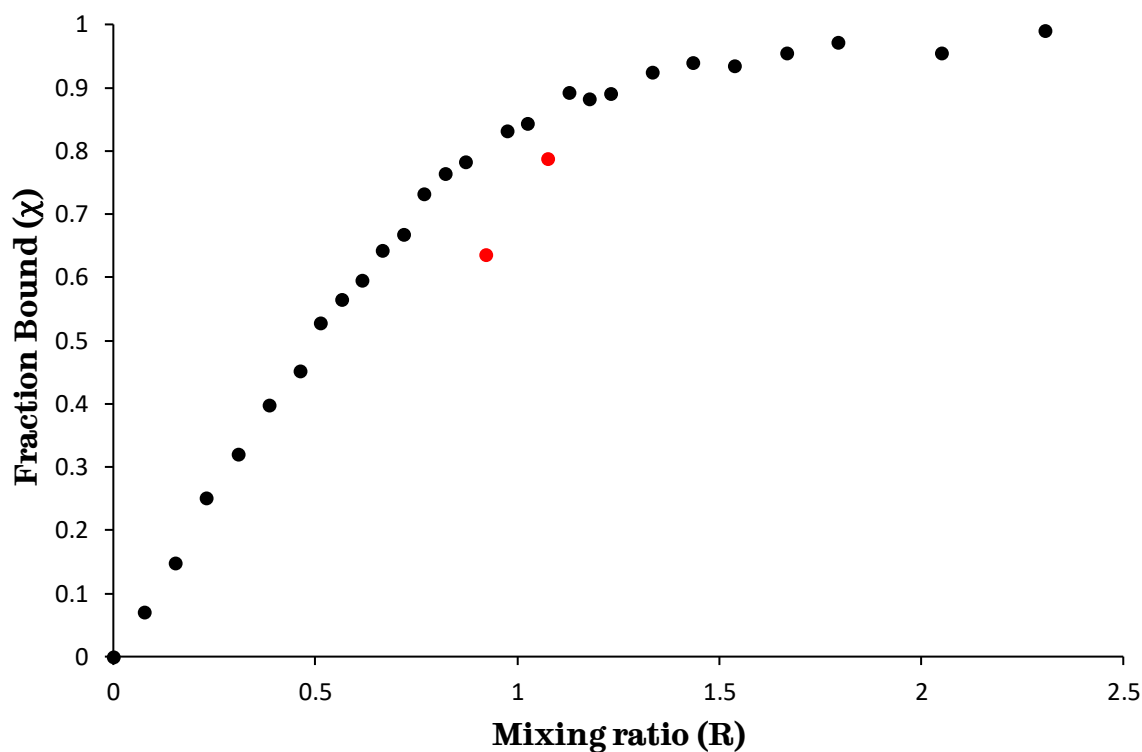
Figure 5.8 - Binding curve obtained for the titration of CT-DNA into a solution of [Ru(tpyma)(phen)(py)]Cl$_2$ in buffer. Points in red indicate anomalous results omitted from calculation of the binding constant

The binding curve for [Ru(tpyma)(phen)(py)]$^{2+}$ shows a definite interaction between the complex and CT-DNA, with the a plateau at a mixing ratio between 1.8 and 2.3. This indicates that, by building onto the bpy ligand and extending the aromatic system away from the complex centre, a binding interaction is induced. The points at R = 0.92 and 1.07 (displayed in red in figure 5.8) do not fit the surrounding data points and are omitted from further analysis. Using the remaining data points between χ = 0.3 and 0.9 it is possible to construct a Scatchard plot, shown in figure 5.9.

$K_b = 8.52 \pm 0.61 \times 10^5 \text{ M}^{-1}$

$n = 0.90 \pm 0.01 \text{ bp}$

$R^2 = 0.91$
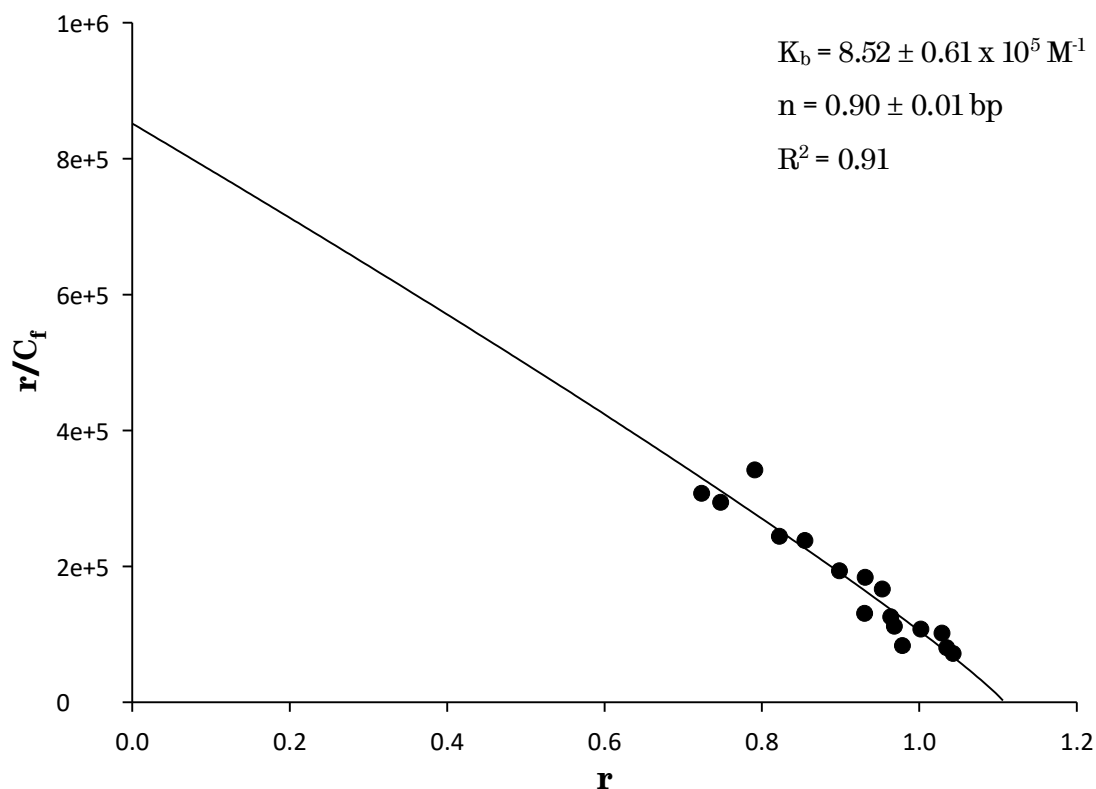
Figure 5.9 - Scatchard plot for the titration of CT-DNA into a into a solution of [Ru(tpyma)(phen)(py)]Cl$_2$. Line of fit calculated using the McGhee von Hippel non-cooperative binding model

Using the McGhee von Hippel model it was possible to fit the data and obtain an estimate of the binding constant and binding site size. The fitting displays a slight curve, as is expected for binding to CT-DNA with overlapping binding sites. The fit results in a value for binding constant, K, of $8.52 \times 10^5 \text{ M}^{-1}$ and a binding site size of 0.90 base pairs. This is significantly stronger binding that has been reported for [Ru(phen)$_3$]$^{+2}$ which displayed a binding constant of $6.2 \times 10^3 \text{ M}^{-1}$ ($\pm 2\%$).[13] This may be due to an added interaction between either the pendant pyridine or co-ordinated amine group of the tpyma, and the DNA backbone. Both of these parts possess the potential to form hydrogen bonding interactions which may grant a stronger binding interaction.

5.3.3 Titration of [Ru(tpyma)(dppz)(py)]Cl$_2$

The UV-Visible absorbance traces for the titration of CT-DNA into a solution of [Ru(tpyma)(dppz)(py)]$^{2+}$ are displayed in figure 5.10.
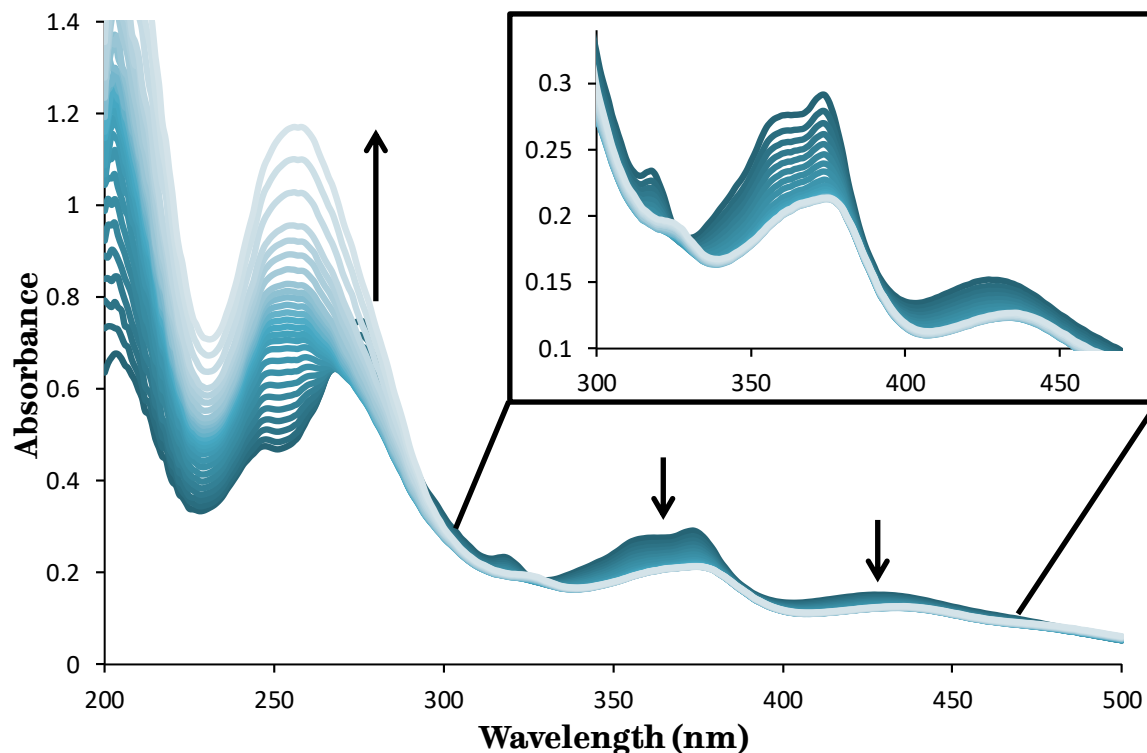
Figure 5.10 - UV-visible titration of 1.65 mM bp^{-1} CT-DNA into 1.54 μM solution of [Ru(tpyma)(dppz)(py)]Cl$_2$ in buffer

The UV-visible spectra for the titration of CT-DNA into [Ru(tpyma)(dppz)(py)]$^{2+}$ show a more significant hypochromicity than the spectra for the phen equivalent. This decrease in absorption is most prominent in the band around 373 nm but also seen in the band at 427 nm. As with both previous examples a hypochromicity is observed due to the addition of DNA and its maximal absorption at 260 nm. This growth in absorption also masks the hypochromicity of the band at 275 nm which initially decreases before merging with the growing band at 260 nm. In addition to the hypochromicity a bathochromic shift to longer wavelength is seen in both the MLCT bands, with the maxima of the 373 nm band shifting to 375 nm, and the maxima at 427 nm shifting to 436 nm. Trivially, the observation that there are much more significant changes in the UV-visible absorption of the dppz complex than the phen equivalent suggest a more significant change in microenvironment, and perhaps a stronger

binding interaction. Also the bathochromic shifts have been suggested as an indicator of intercalative binding of a single ligand,[14] which is expected for dppz complexes but not for phen.
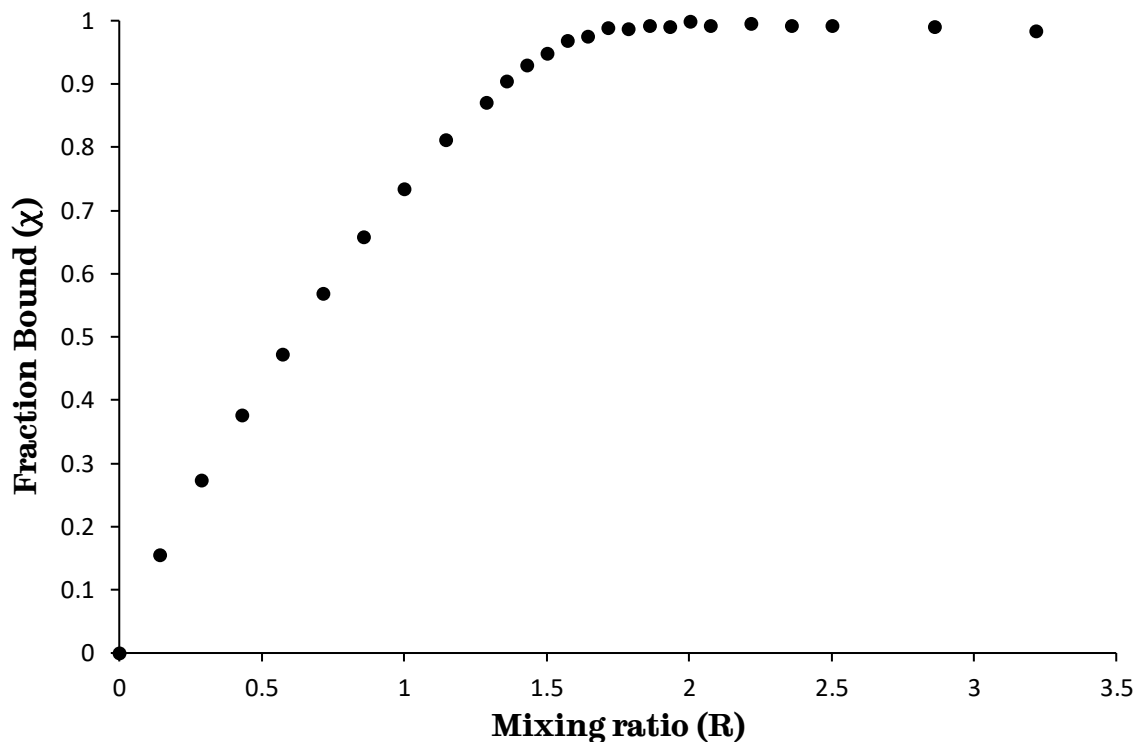
Figure 5.11 - Binding curve obtained for the titration of CT-DNA into a solution of [Ru(tpyma)(dppz)(py)]Cl$_2$ in buffer

The binding curve for [Ru(tpyma)(dppz)(py)]$^{+2}$ was calculated by tracking the hypochromicity of the band at 373 nm. As for the phen complex it shows a clear binding interaction, with a plateau beginning at R = 1.72. The plateau seems more defined than for the phen equivalent, with a sharper curve observed in the transition to the plateau. As with the phen complex, the data between χ = 0.3 and 0.9 was used to form a Scatchard plot shown in figure 5.12.

$K_b = 1.66 \pm 0.37 \times 10^6\,M^{-1}$

$n = 1.12 \pm 0.04\ \text{bp}$

$R^2 = 0.81$
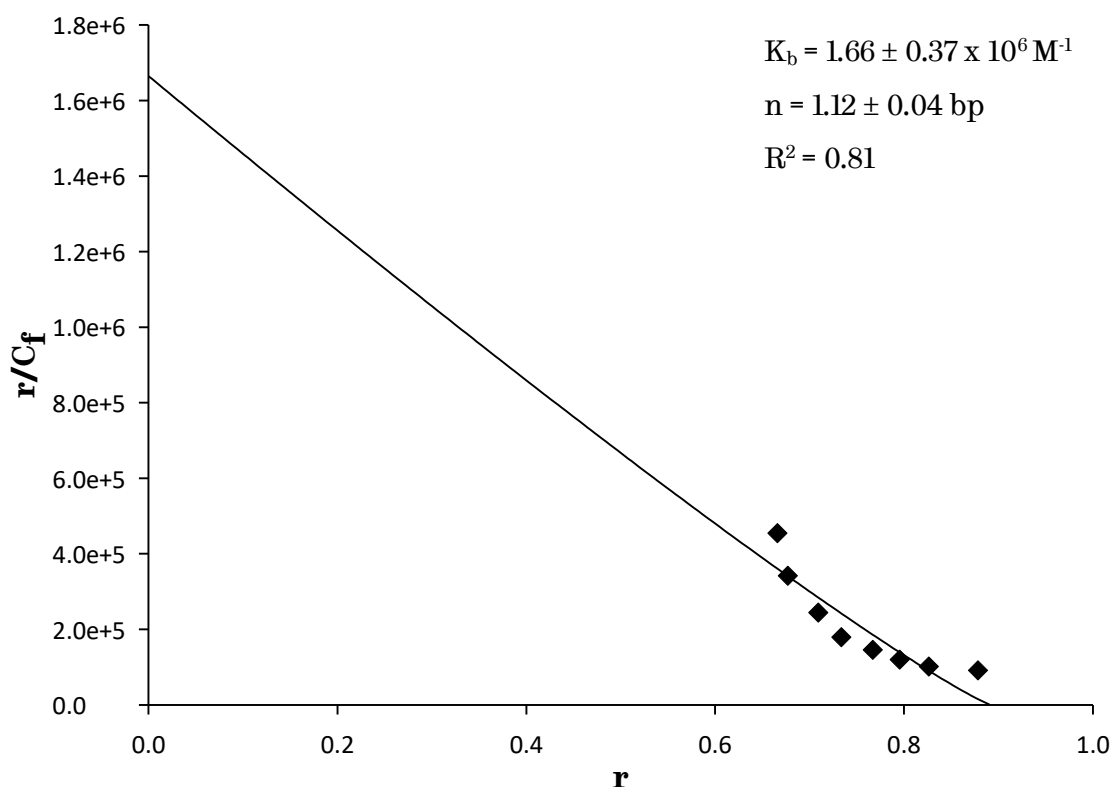
Figure 5.12 - Scatchard plot for the titration of CT-DNA into a into a solution of [Ru(tpyma)(dppz)(py)]Cl$_2$. Line of fit calculated using the McGhee von Hippel non-cooperative binding model

The Scatchard plot for [Ru(tpyma)(dppz)(py)]$^{2+}$ shows a more significant curvature than the phen complex. The fit results in a binding constant, K, of $1.66 \times 10^6\,M^{-1}$ and a site binding site of 1.12. The binding is significantly stronger than for the phen complex, as is expected due to the intercalation interaction that is common among complexes containing dppz as a ligand. Building upon the ligand, adding the phenazine unit to phen, grants more aromatic surface to interact with the DNA base pairs, resulting in stronger binding. This is comparable to the binding constants of similar dppz containing complexes. In particular it shows the same order of magnitude as the binding of another achiral complex, [Ru(tpm)(dppz)(py)]$^{2+}$, which is reported to have a binding constant of $5.2 \times 10^6\,M^{-1}$.[15] This suggests that the tpyma is not having a significant effect on the binding of the complex.

5.3.4 Titration of [Ru(tpyma)(dppn)(py)]Cl$_2$

The UV-Visible absorbance traces for the titration of CT-DNA into a solution of [Ru(tpyma)(dppn)(py)]$^{2+}$ are displayed in figure 5.13.
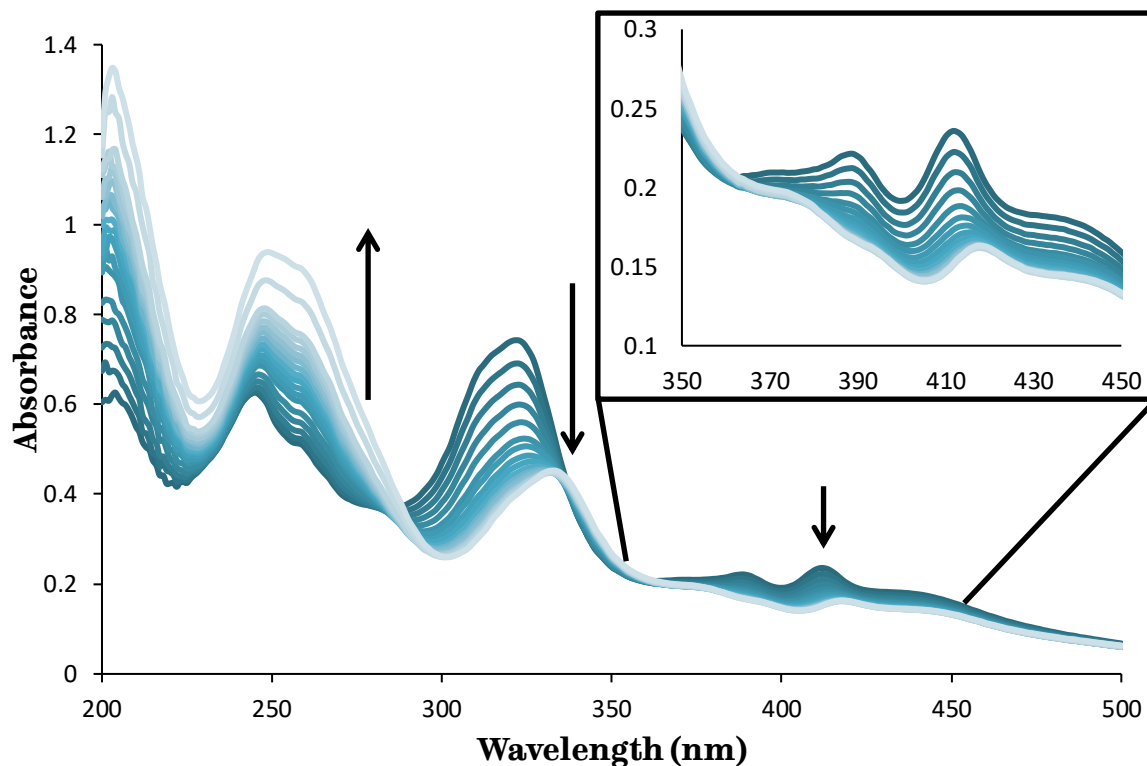
Figure 5.13 - UV-visible titration of 1.65 mM bp^{-1} CT-DNA into 1.59 µM solution of [Ru(tpyma)(dppn)(py)]Cl$_2$ in buffer

The changes in the UV-visible specra for the titration of CT-DNA into [Ru(tpyma)(dppn)(py)]$^{2+}$ are more significant than for the other ligands. The hypochromicity of the band at 322 nm is considerable and also experiences a large bathochromic shift. The maxima of the band shifts by 12 nm to 334 nm. There is also a hypochromic shift in the band at 412 nm, alongside a bathochromic shift of 6 nm, to a maxima at 418 nm. As with each of the previous titrations there is also the hyperchromic shift due to DNA absorption at 260 nm.
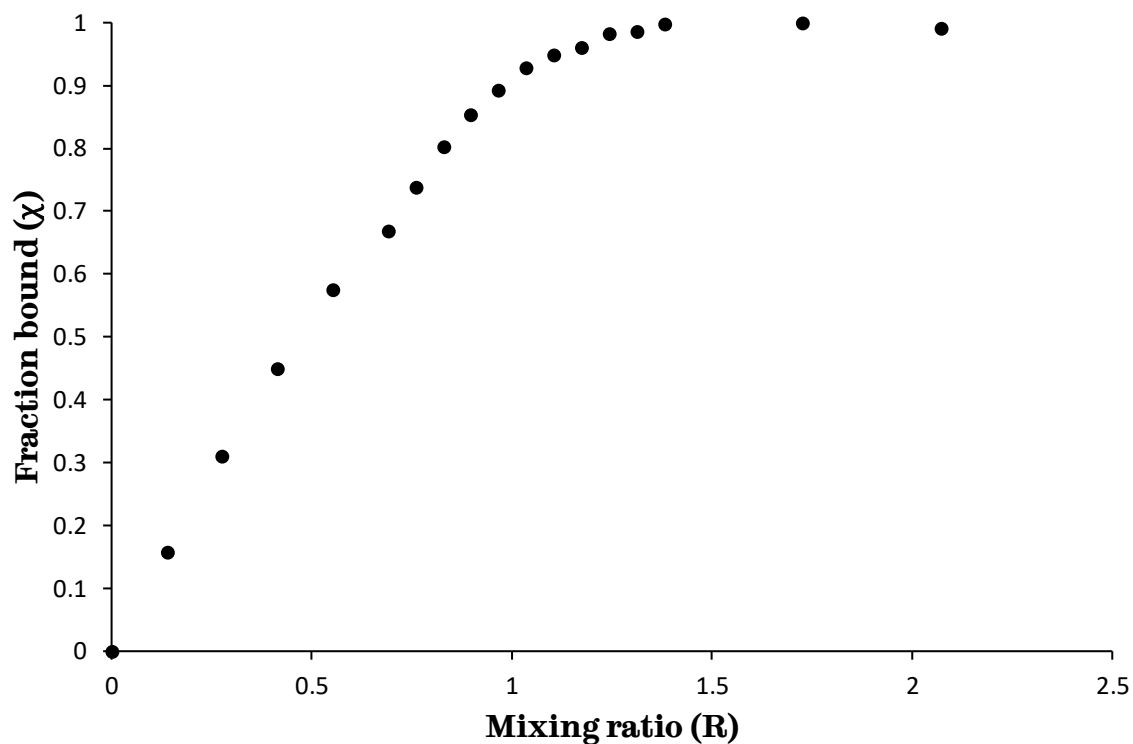
Figure 5.14 - Binding curve obtained for the titration of CT-DNA into a solution of [Ru(tpyma)(dppn)(py)]Cl$_2$ in buffer

The binding curve for [Ru(tpyma)(dppn)(py)]$^{+2}$ was calculated by tracking the hypochromicity of the band at 322 nm. The curve shows a very similar shape to that obtained for the dppz complex, with a plateau beginning slightly earlier, at R = 1.38. The data between χ = 0.3 and 0.9 was used to form a Scatchard plot shown in figure 5.15.

$K_b = 1.62 \pm 0.42 \times 10^6 \, M^{-1}$

$n = 0.87 \pm 0.03$ bp

$R^2 = 0.65$
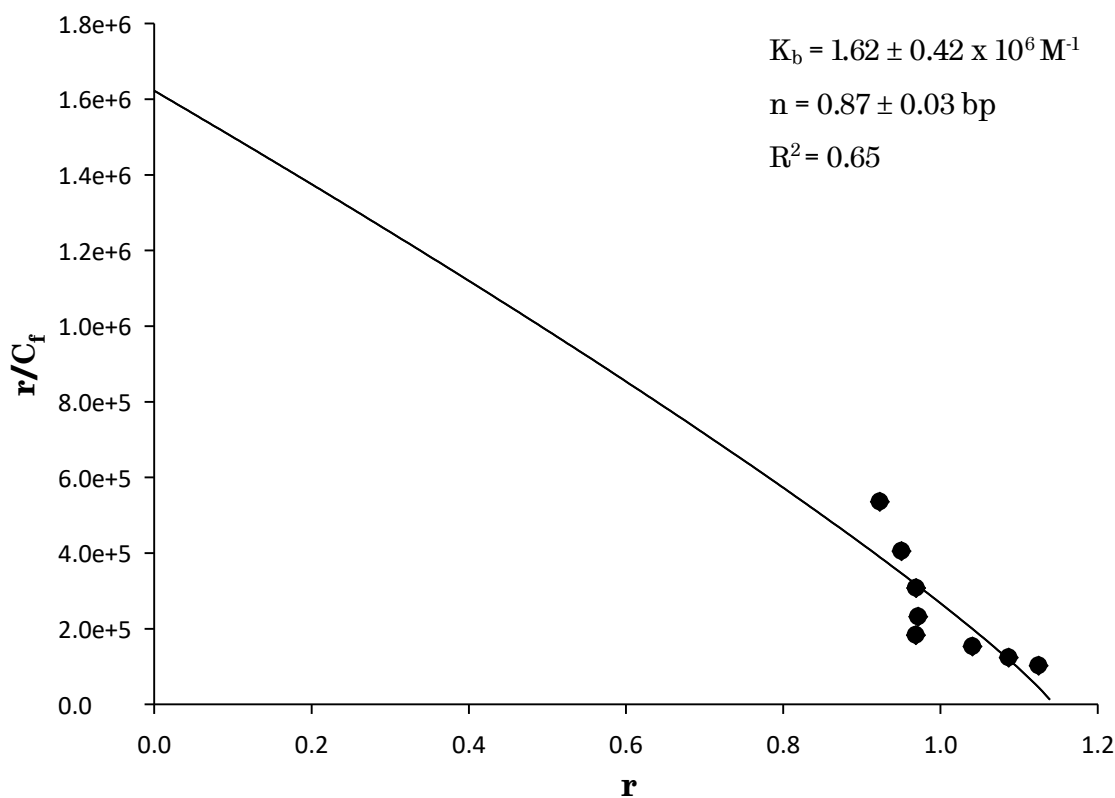
Figure 5.15 - Scatchard plot for the titration of CT-DNA into a into a solution of [Ru(tpyma)(dppn)(py)]Cl$_2$. Line of fit calculated using the McGhee von Hippel non-cooperative binding model

Fitting the Scatchard plot to the McGhee von Hippel model results in a binding constant, K, of $1.62 \times 10^6 \, M^{-1}$ and a site binding site of 0.87. This is very similar to that found for the dppz complex. However the fitting of the data to the model is poor with an R^2 value of only 0.65. The calculated binding constant may, therefore, not be a good estimation of the binding constant of the complex. The binding constant obtained is similar to the equivalent tpm compound, [Ru(tpm)(dppz)(py)]$^{2+}$, which is reported to have a binding constant of $1.9 \times 10^6 \, M^{-1}$.[15]

5.3.5 Summary

Figure 5.16 shows a graphical comparison of the calculated binding constants of the novel tpyma studied in this chapter. This includes the errors in the fitting model which form either side of the box. It is difficult to comment on any trend with only four reference points. It is however clear that building up the bidentate ligand of the complex leads to a stronger binding, with bpy displaying no binding up to dppz and dppn which have almost the same strength of interaction. It would be interesting to include the dpqx ligand in the series, which forms the intermediate between phen and dppz, but could not be synthesised.
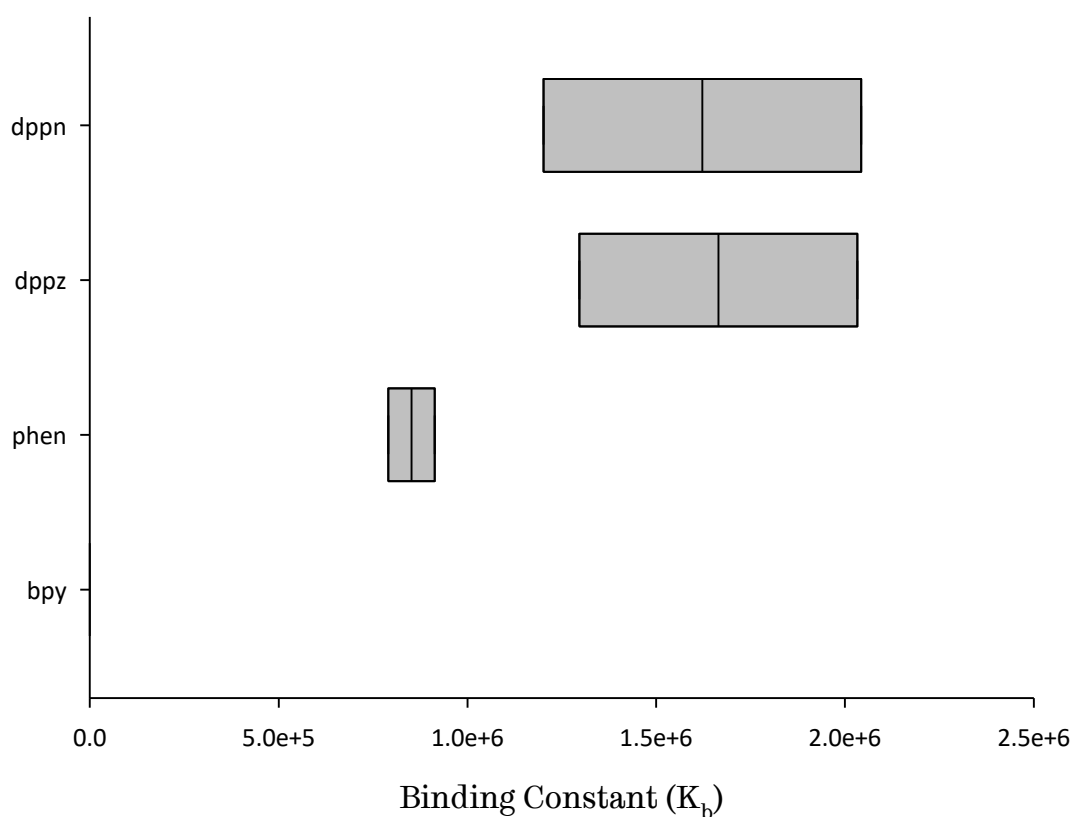
Figure 5.19 - Box plot comparing the binding constants calculated for [Ru(tpyma)(NN)(py)]Cl$_2$ complexes using UV-visible titration

5.4 Luminescence Titrations of [Ru(tpyma)(NN)(py)]$^{2+}$

5.4.1 Titration of [Ru(tpyma)(dppz)(py)]Cl$_2$

The emission spectra for the titration of CT-DNA into a solution of [Ru(tpyma)(dppz)(py)]$^{2+}$ are displayed in figure 5.17. As with the UV-Visible spectra the darkest trace indicates that no DNA has been added, while traces of lighter colour indicate the sequential addition of DNA. The solution was excited at a wavelength of 426 nm.
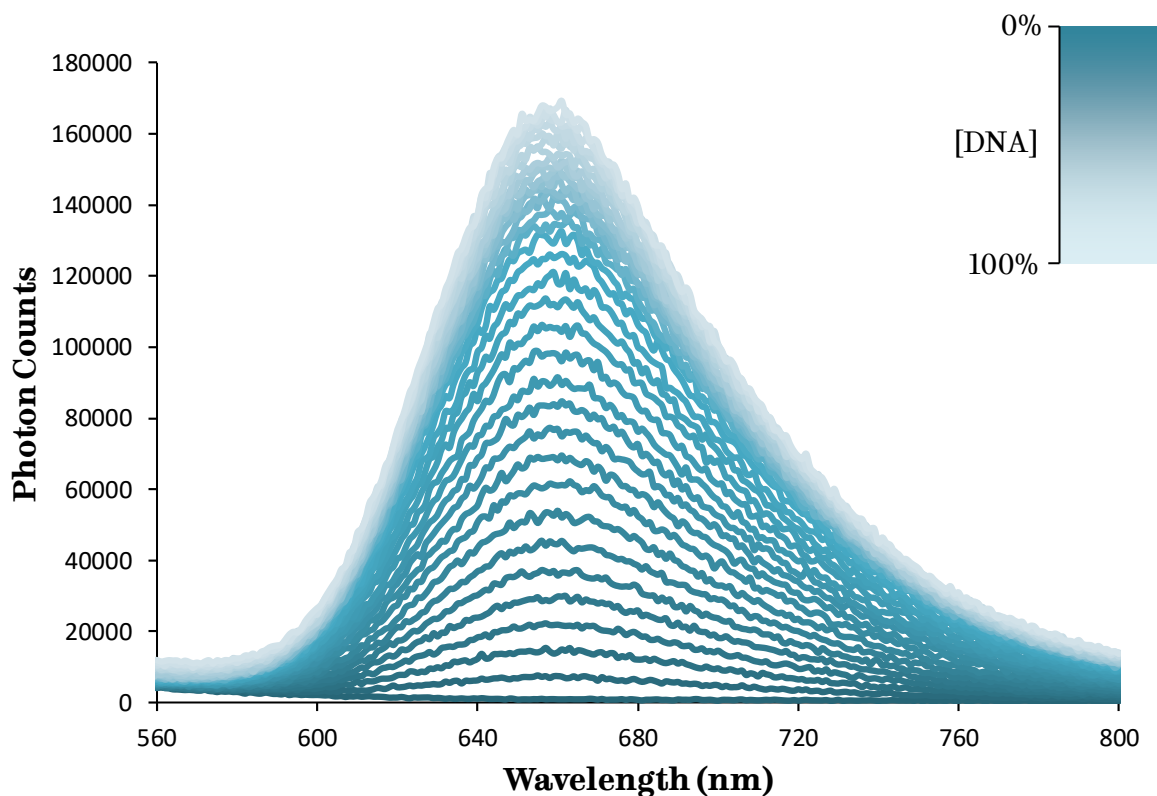
Figure 5.17 - Emission spectra of the titration of 1.65 mM bp^{-1} CT-DNA into 1.52 µM solution of [Ru(tpyma)(dppn)(py)]Cl$_2$ in buffer excited at 426 nm

As can be seen by the increased intensity of the band at 660 nm, [Ru(tpyma)(dppz)(py)]$^{2+}$ displays the classic light switch effect that has been observed for other Ru(II)-dppz complexes. The more DNA that is titrated into the solution, thus the more complex is bound, the greater the emission observed from the bulk solution. The saturation of the complex can also be seen by the convergence of the lighter coloured lines at the height of emission. A rising baseline is observed as DNA is added. This made the determination of the saturation point challenging as the emission continued to increase with the baseline. In order to normalise the data and remove this

effect the main band at 660 nm was initially integrated but the data still did not saturate. Instead the maxima of the raman scattering band was subtracted from the main band, allowing for the construction of the binding curve in figure 5.18.
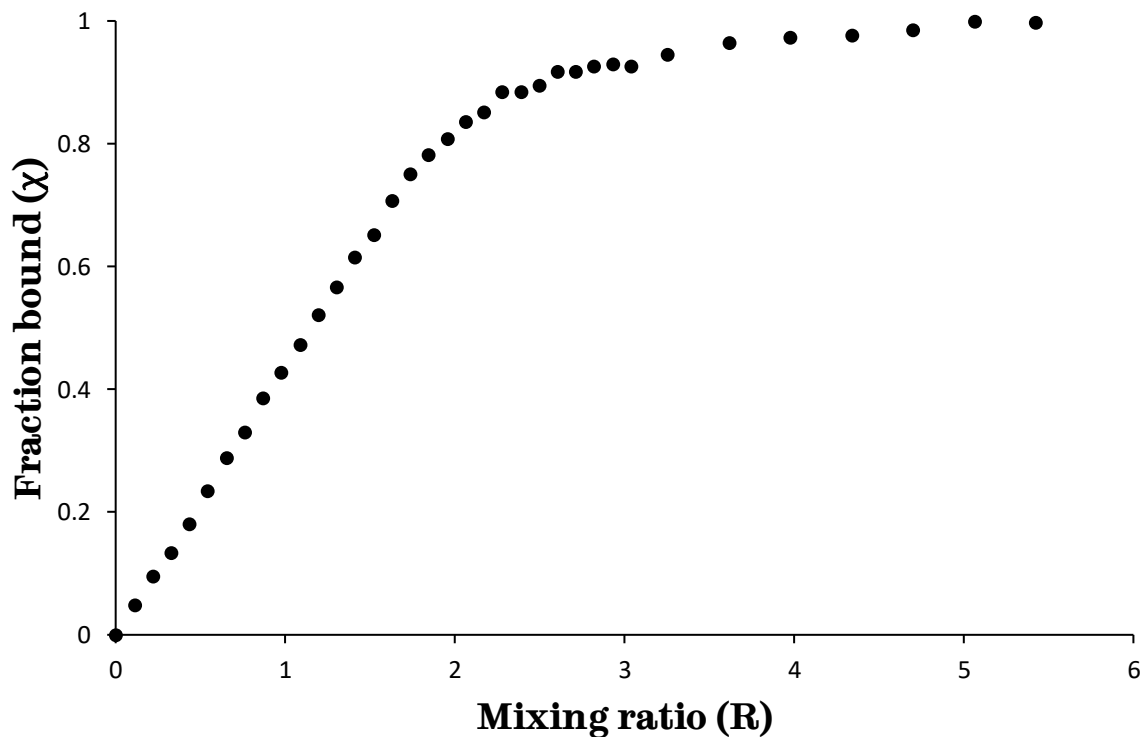
Figure 5.18 - Binding curve obtained for the luminescence titration of CT-DNA into a solution of [Ru(tpyma)(dppz)(py)]Cl$_2$ in buffer

The binding curve shows the expected shape, similar to that observed for the UV-visible titration. The plateau forms around R = 2.49. Having established the saturation point, the data from χ = 0.3 to 0.9 was used in the construction of the Scatchard plot shown in figure 5.19.
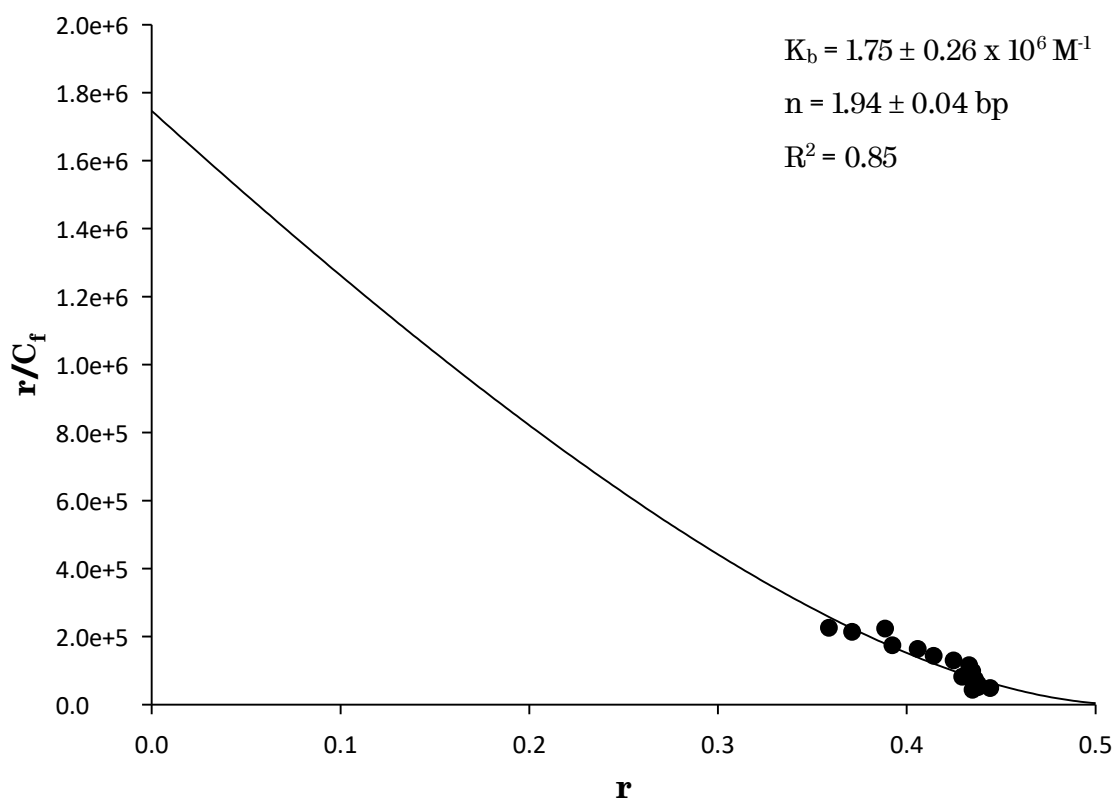
Figure 5.19 - Scatchard plot for the luminescence titration of CT-DNA into a into a solution of [Ru(tpyma)(dppz)(py)]Cl$_2$. Line of fit calculated using the McGhee von Hippel non-cooperative binding model

The binding constant calculated from the titration of luminescent emission is 1.73×10^6 M^{-1} with a binding site of 1.94 base pairs. The data fits the model slightly better than the UV-visible titration for the same complex, with $R^2 = 0.85$, but this correlation is still relatively low. The binding constant is within error of the value obtained from the UV-visible titration. Whilst the binding constant is in agreement, the binding site size is near double that calculated from the UV-visible data. The predicted binding site seems more sensible than some of the UV titrations which predicted a binding site of less than 1 base pair. Those titrations predicting binding sites of less than 1 base pair could be indicating surface binding to the DNA, in addition to intercalation, that is still altering the UV-visible spectrum.

5.5 Viscosity studies of [Ru(tpyma)(NN)(py)]$^{2+}$

Viscosity measurements were performed using a DNA-buffer solution, to which small amounts of highly concentrated complex-buffer solution were added. This prevents dilution effects being observed as changes in viscosity. The temperature was controlled by placing the viscometer in a water bath at 25 °C and allowing the solution to equilibrate between measurements. Figure 5.20 shows the results of the viscosity studies of the control compounds, ethidium bromide and Hoechst 33258, alongside the novel tpyma containing Ru(II) complexes for comparison.
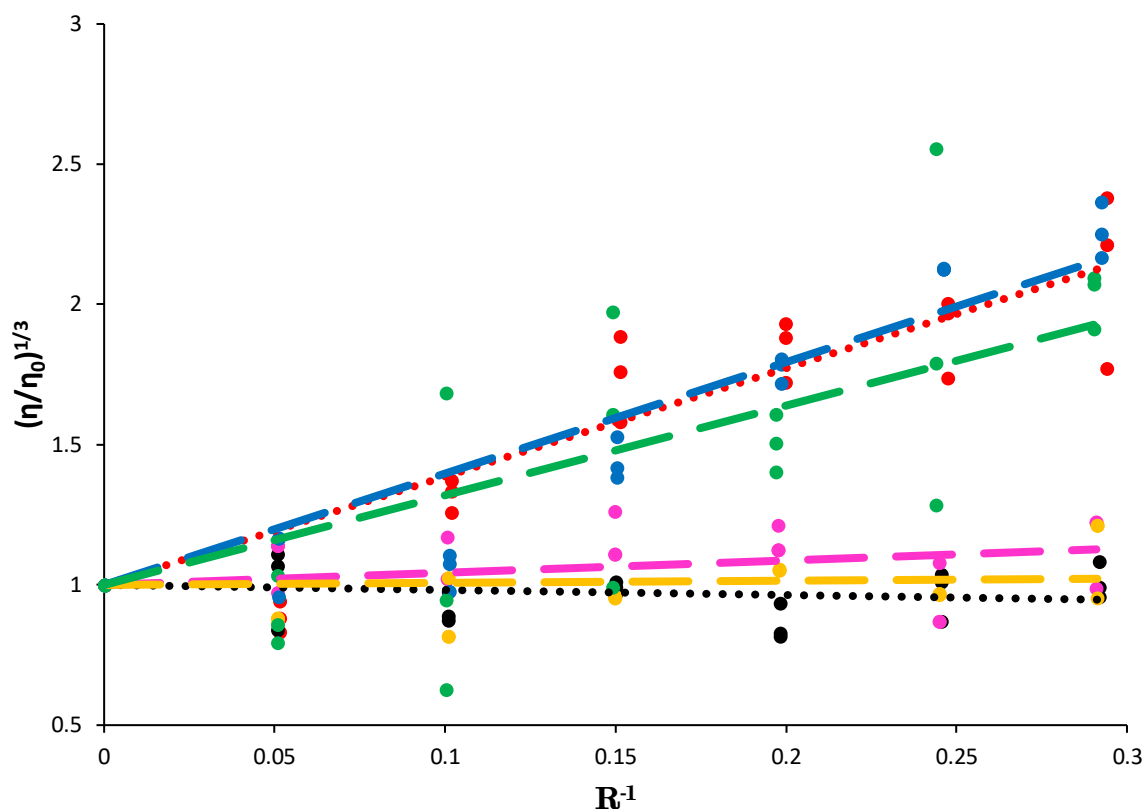
Figure 5.20 - The relative specific viscosity of calf thalamus DNA as a function of the binding ratio in the presence of ethidium bromide (●), Hoechst 33258 (●), [Ru(tpyma)(dppn)(py)]$^{2+}$ (●), [Ru(tpyma)(dppz)(py)]$^{2+}$ (●) [Ru(tpyma)(phen)(py)]$^{2+}$ (●) and [Ru(tpyma)(bpy)(py)]$^{2+}$ (●). Trendlines added to aid visualisation of change in viscosity

The control compounds show the expected behaviour, with ethidium bromide giving a marked increase in viscosity as its concentration increased, as is expected for an

intercalator. Hoechst 33258 does not show an increase as is expected due to its groove binding nature. These results allow for comparison to the studied Ru(II) complexes to assess whether they possess intercalating or groove binding behaviour.

The trendline for the data of complex [Ru(tpyma)(bpy)(py)]$^{2+}$ shows a very similar pattern to that for the groove binder Hoescht 33258, however it was shown not to exhibit a change in absorbance when subjected to DNA titration. Combination of these two experiments confirms that there is not any interaction between the bpy complex and DNA, rather than suggesting it is a groove binder. Extending the ligand to form [Ru(tpyma)(bpy)(py)]$^{2+}$ did show a change in absorbance and also mirrors the behaviour of Hoechst 33258. This suggests that the phen complex does act as a groove binder in a similar fashion to [Ru(phen)$_3$].[16] The combination of these experiments suggests that the tpyma ligand is not having a significant effect on the binding mode, neither preventing DNA interaction, nor encouraging intercalation.

The dppz and dppn ligands have a more extended aromatic system protruding from their respective Ru(II) complexes and as such are more likely to slip between the base pairs of DNA in an intercalative binding mode. In both cases, for [Ru(tpyma)(dppz)(py)]$^{2+}$ and [Ru(tpyma)(dppn)(py)]$^{2+}$ the trendlines of the data follow very closely to the ethidium bromide control. This confirms that their binding mode is intercalative. Again this suggests that the tpyma is not having a detrimental effect on DNA binding as it is not changing the binding mode. It could be conceived that the added steric bulk of tpyma could prevent the complex sliding between base pairs. This data suggests this is not the case.

5.6 Titrations of [Ru(dpyma)(dppz)(py)]$^{2+}$

5.6.1 UV-Visible titration of [Ru(dpyma)(dppz)(py)]Cl$_2$

The UV-Visible absorbance traces for the titration of CT-DNA into a solution of [Ru(dpyma)(dppz)(py)]$^{2+}$ are displayed in figure 5.21.
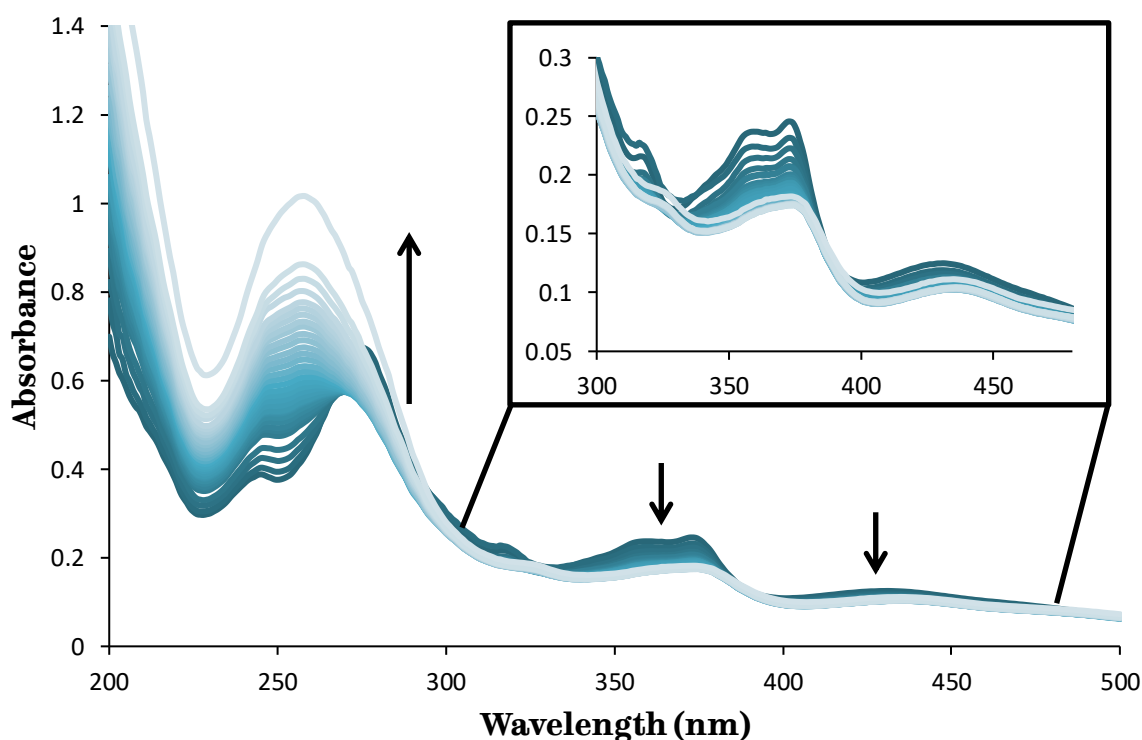
Figure 5.21 - UV-visible titration of 1.65 mM bp^{-1} CT-DNA into 1.52 μM solution of [Ru(dpyma)(dppz)(py)]Cl$_2$ in buffer

The absorption curve for [Ru(dpyma)(dppz)(py)]$^{2+}$ is very similar to that of [Ru(tpyma)(dppz)(py)] and the changes on introducing CT-DNA are much the same. This is to be expected as all the moieties bound to the ruthenium are the same, with the only change being the removal of the pendant pyridine. The band at 373 nm shares its maxima with the equivalent band for the tpyma complex while the band at 431 nm is 4 nm shifted from the tpyma complex. As with the tpyma complex both the bands are bathochromic, with the 373 nm band shifting 1 nm and the 431 nm band shifting by 8 nm. There is also a hypochromic shift in the band at 275 nm which is masked by the growing DNA absorbance at 260 nm. The maximal absorbance across the spectra also

appears lower than the equivalent for tpyma, indicating a lower extinction co-efficient. Calculating the co-efficient, to correct for the slight change in concentration, gives maxima of 44298 (275 nm), 16143 (373 nm) and 8211 mol^{-1} dm^3 cm^{-1} (431 nm) for dpyma versus 48655, 18944 and 9887 mol^{-1} dm^3 cm^{-1} for the equivalent tpyma peaks. This suggests the removal of the pyridine has diminished the ability of the complex to absorb light.
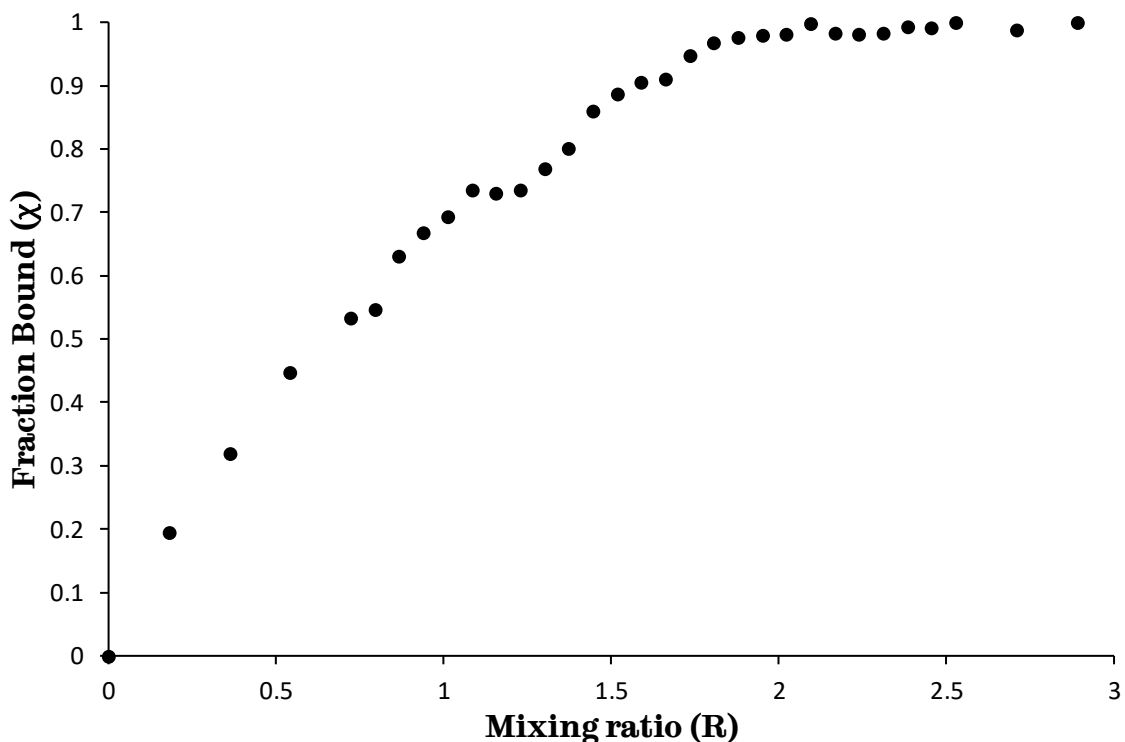
Figure 5.22 - Binding curve obtained for the UV-visible titration of CT-DNA into a solution of [Ru(dpyma)(dppz)(py)]Cl$_2$ in buffer

The binding curve derived from the UV-visible titration of CT-DNA into a solution of [Ru(dpyma)(dppz)(py)]$^{2+}$ is shown in figure 5.22. The data appears slightly more scattered than previous examples with a slight, unexpected plateau at R = 1.15. The main plateau of the data occurs after R = 1.88. Using the data from χ = 0.3 to 0.9, calculated using the saturation point, was used for the construction of the Scatchard plot in figure 5.23.
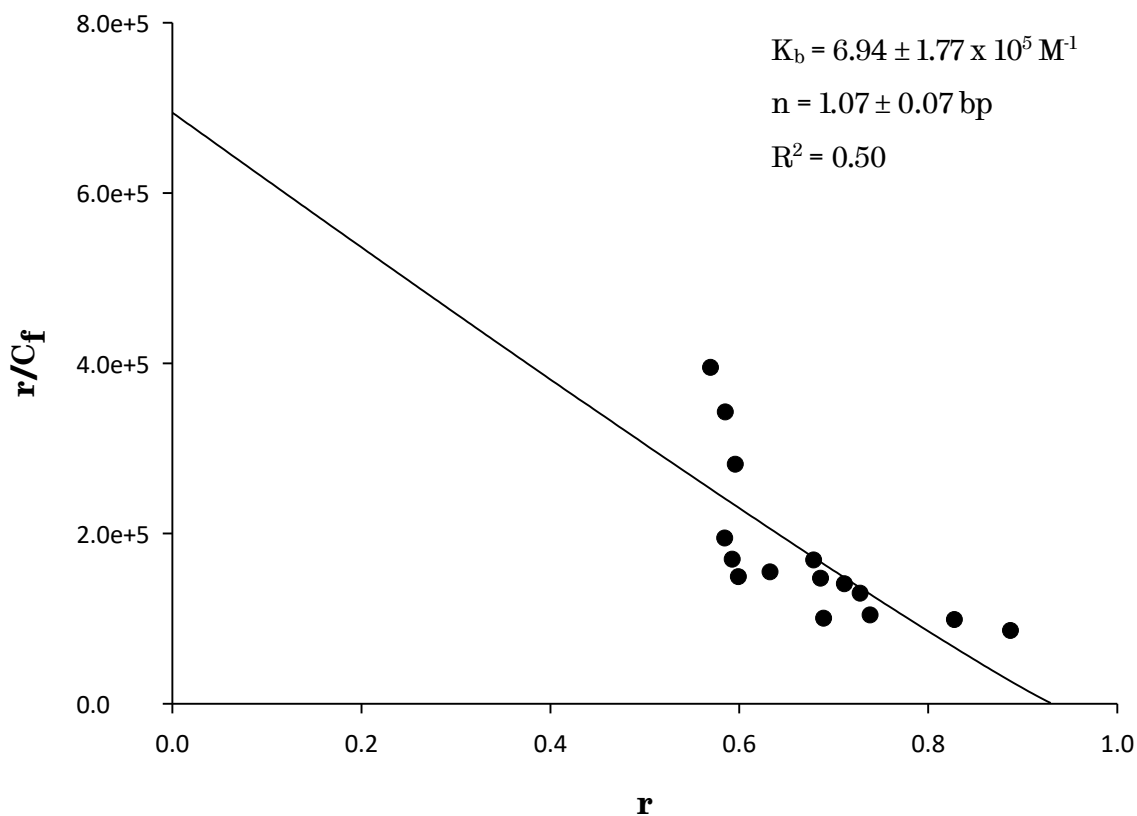
Figure 5.23 - Scatchard plot for the UV-visible titration of CT-DNA into a into a solution of [Ru(dpyma)(dppz)(py)]Cl$_2$. Line of fit calculated using the McGhee von Hippel non-cooperative binding model

The Scatchard plot shown in figure 5.23, shows very poor fitting to the model, with R^2 = 0.5. This is therefore not a reliable indication of the binding constant of the complex. The binding constant is estimated to be 6.94 x 10^5 M^{-1} with a binding site of 1.07 base pairs.

5.6.2 Luminescence Titration of [Ru(dpyma)(dppz)(py)]Cl$_2$

The emission spectra of the the titration of CT-DNA into a solution of [Ru(dpyma)(dppz)(py)]$^{2+}$ are displayed in figure 5.24.
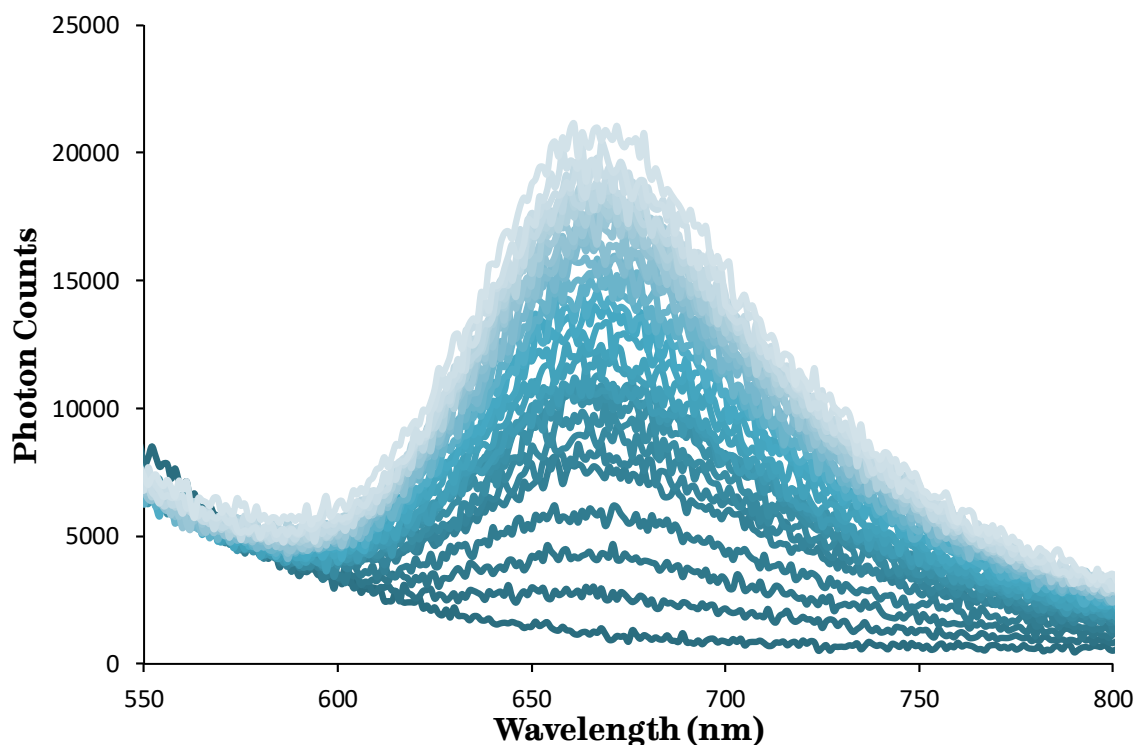
Figure 5.24 - Emission spectra of the titration of 1.65 mM bp^{-1} CT-DNA into 1.52 µM solution of [Ru(dpyma)(dppz)(py)]Cl$_2$ in buffer excited at 426 nm

The emission spectra of [Ru(dpyma)(dppz)(py)]$^{2+}$ show hyperchromicity on increasing DNA concentration, indicative of a light switch effect. The effect is however much less significant than the effect seen for tpyma. As can be seen in figure 5.24, the emission spectra for the dpyma complex are very noisy. This is possibly due to the fact that the photon count is very low and the observed emission is close to the minimum that the instrument can detect.

Figure 5.25 shows a comparison between the tpyma and dpyma complexes at their saturation point. The data has been altered so that the baselines of each of the spectra are at the same level for a meaningful comparison. It is surprising that a change as simple as removing the pyridine could have such a significant effect on the emission. As the light switch effect is thought to be dependent on hydrogen bonding, it could be

that the amine is more exposed to solvent when the pyridine is removed, and could be binding to solvent molecules. This could be quenching the excited state and thus reducing emission.
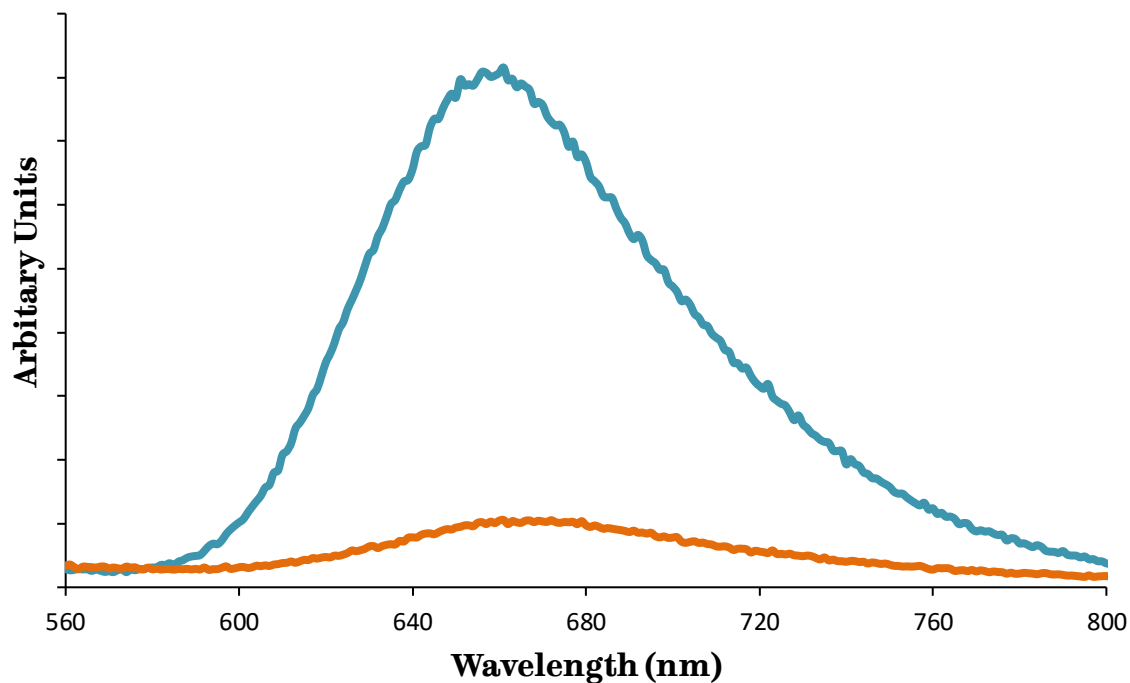
Figure 5.25 - Comparison of the emission of [Ru(tpyma)(dppz)(py)]Cl$_2$ (-) and [Ru(dpyma)(dppz)(py)]Cl$_2$ (-) on saturation with CT-DNA
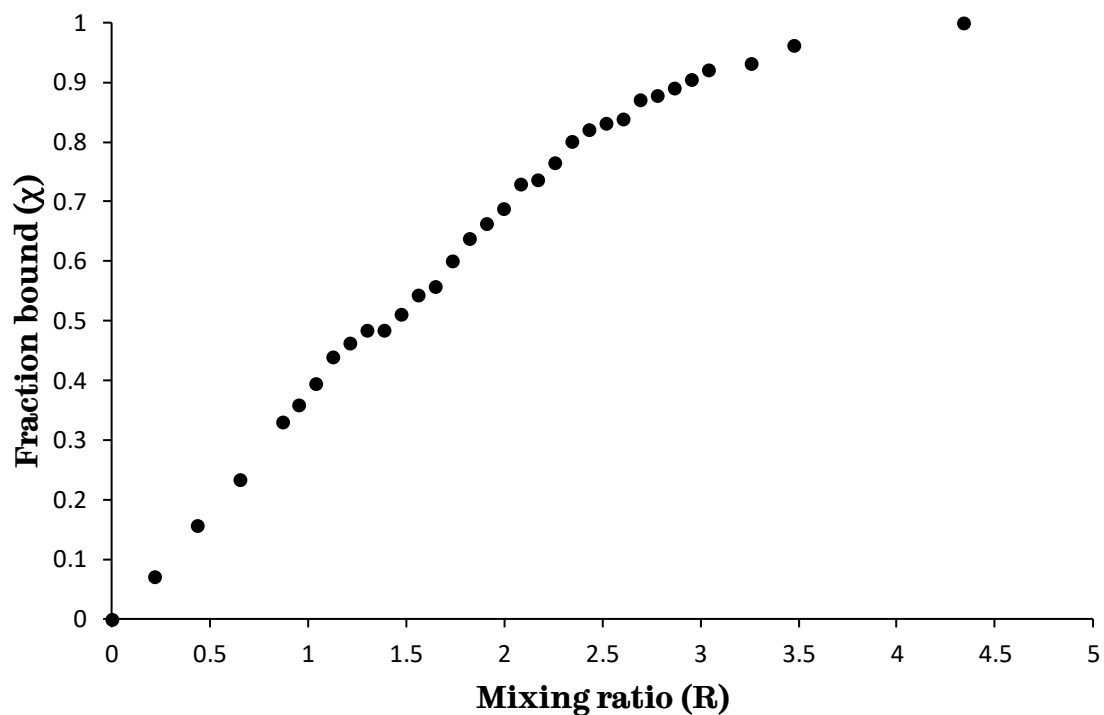
Figure 5.26 - Binding curve obtained for the luminescence titration of CT-DNA into a solution of [Ru(dpyma)(dppz)(py)]Cl$_2$ in buffer

Figure 5.26 shows the binding curve derived from the emission data for the dpyma complex. There was not as great a drift seen in the baseline as was the case for the tpyma complex. The data was therefore treated differently, with the maximum emission from 650 to 700 nm used to track the titration. The data appears less scattered than that present in the UV-visible titration. In this case the plateau is seen at a higher R = 3.47. The data from χ 0.3 to 0.9 was used to construct the Scatchard plot shown in figure 5.27.
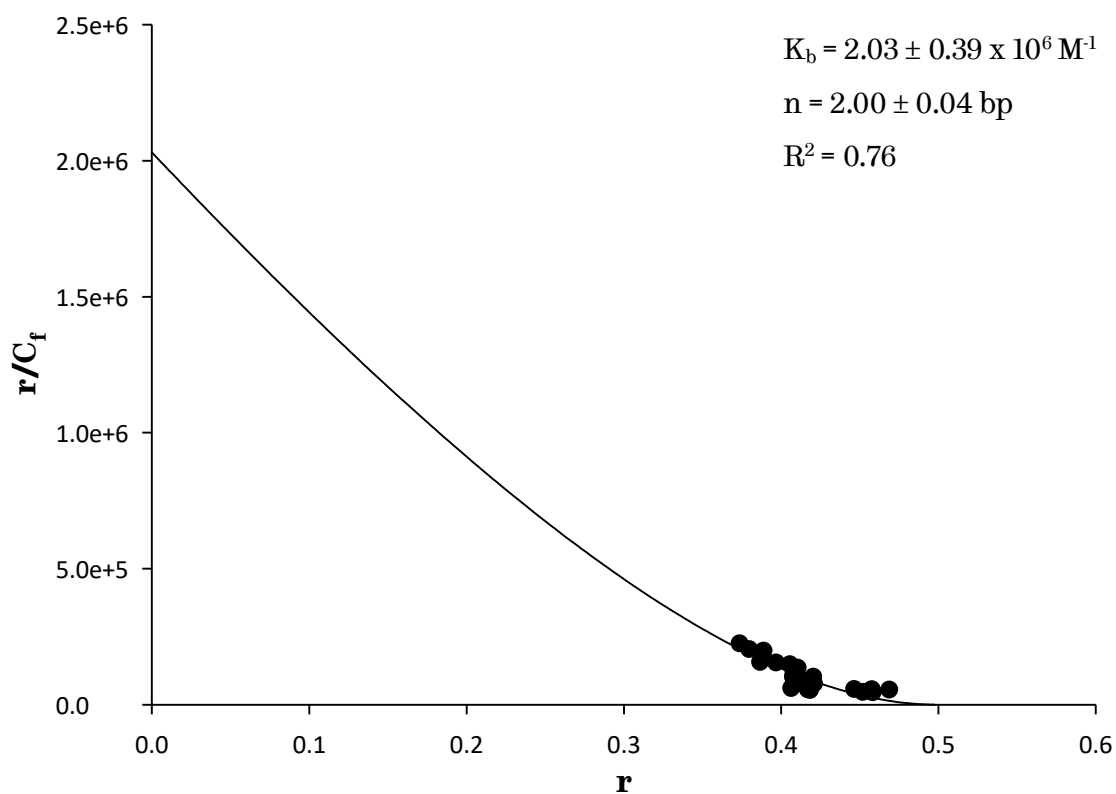
Figure 5.27 - Scatchard plot for the luminescence titration of CT-DNA into a into a solution of [Ru(dpyma)(dppz)(py)]Cl$_2$. Line of fit calculated using the McGhee von Hippel non-cooperative binding model

Statistically the fit for the luminescence measurements is more reliable than for the UV-visible measurements, with R^2 = 0.76. The estimated binding constant is significantly higher at 2.03×10^6 M^{-1} along with a binding site estimate of 2 base pairs, which is double the estimation from the UV-Visible data.

5.6.3 Summary

A comparative box plot of the binding constants of both [Ru(tpyma)(dppz)(py)]$^{2+}$ and [Ru(dpyma)(dppz)(py)]$^{2+}$ is shown in figure 5.28. This aids the comparison of the binding constants with a visualisation of the error calculated for the data as well.
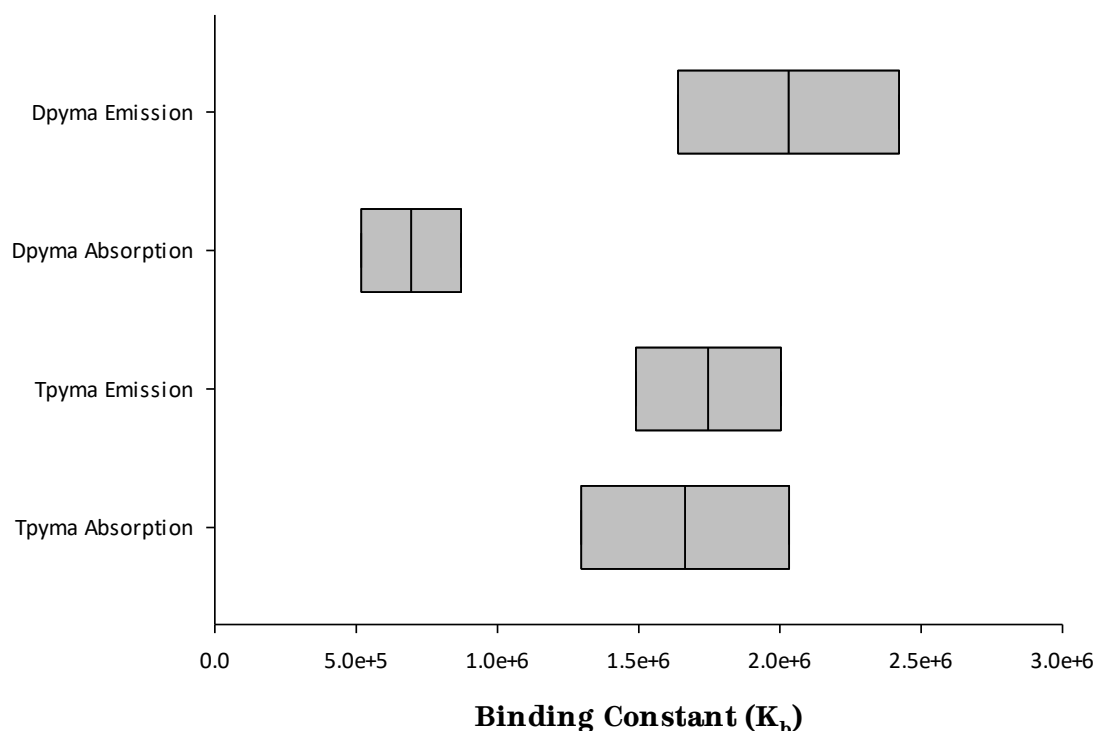
Figure 5.28 - Box plot of the calculated binding constants for [Ru(tpyma)(dppz)(py)]Cl$_2$ and [Ru(dpyma)(dppz)(py)]Cl$_2$ with CT-DNA

The box plot shows that the binding constants calculated for the tpyma complex are consistent across both the emission and absorption titrations, with the constant calculated from the UV-visible titration being fully within error of that calculated from the luminescence titration. It would be useful to compare these binding constants to that calculated for the dpyma complex, in order to assess the effect of removing the pyridine from the complex. Unfortunately this is difficult as the two techniques used to calculate the binding constant are not in agreement. The emission data suggests that the binding has not been affected, but the absorption data is closer to that of the phen complex, reported earlier, that is groove binding.

If binding were affected by changing the ancillary ligand this would inform further work in altering the dpyma ligand to add a surface binding attachment. If it were to restrict DNA binding, work to add surface binding capability may be futile, as it could result in a complex not suited to the aim of the project.

5.7 Conclusion

A series of novel ruthenium complexes, containing the tpyma ligand, of the form $[Ru(tpyma)(NN)(py)]^{2+}$, (where NN = bpy, phen, dppz or dppn) have been studied to assess their binding interactions with DNA. The key point of interest was to study if the tpyma ligand has any effect on the binding of the complex, in comparison with other ancillary ligands. To test this, the NN ligands used were selected as they have known interactions with DNA in other contexts. By comparing the behaviour of the tpyma containing complex to the expected behaviour of the NN ligand, it is possible to ascertain if the tpyma is playing a role in the binding.

The simplest of the NN ligands, bpy, does not protrude far from the centre of the complex and does not have a large planar aromatic surface to interact with the DNA through π-π stacking. It is therefore expected that it will have no significant binding interaction with DNA. Any binding would likely be due to the action of the tpyma ligand. The titration with CT-DNA displayed no hypochromicity, which would be indicative of a change in microenvironment of the complex, and thus a binding interaction. The complex also had no impact on the viscosity of a DNA solution, which is expected for intercalative binding. The studies suggest that $[Ru(tpyma)(bpy)(py)]^{2+}$ does not have a binding interaction with DNA as expected.

The phen ligand has an extra aromatic ring, compared to the bpy ligand, and some phen complexes are known to associate with the grooves of DNA. The titration in this case did demonstrate hypochromicity, which was tracked to estimate a binding constant for the complex. This was two orders of magnitude greater than reported for $[Ru(phen)_3]$ (10^5 vs 10^3) suggesting that the tpyma could be promoting binding to the DNA, possibly through hydrogen bonding interactions. The complex did not influence the viscosity of a DNA solution and displayed the same behaviour as the known groove binder Hoescht 33258. These findings confirm that, while there is an interaction with the DNA, unlike the bpy complex, $[Ru(tpyma)(phen)(py)]^{2+}$ acts as a groove binder.

The dppz and dppn ligands are further extensions of the phen ligand, with the introduction of phenazene or napthazene units. Both have extensive planar aromatic surface which protrudes far from the complex centre. This allows them to slip between base pairs and bind more strongly to DNA. The titration studies show that both have a strong interaction with DNA, of the order 10^6. The binding constants of each are very

similar to one another. The viscosity study also confirms their behaviour as intercalators, as they both increase the viscosity of a DNA solution in a similar manner to the known intercalator, ethidium bromide. The dppz also uniquely displays a strong light switch effect as is expected for such compounds. Both $[Ru(tpyma)(dppz)(py)]^{2+}$ and $[Ru(tpyma)(dppn)(py)]^{2+}$ act as intercalators as expected, with a binding strength similar to related compounds.

Overall this study has found that the tpyma ligand does not impede DNA binding or alter DNA binding mode for each NN ligand tested. It may enhance the binding of DNA, as is seen in the case of the phen complex.

The study was extended to include the dpyma ligand which lacks the pendant pyridine of the tpyma ligand. The purpose of this was to assess the role of the pyridine ligand and to test whether it could be replaced with another moiety to add surface binding function. The titration data was difficult to interpret due to poor fitting, but the emission titration suggested a similar binding strength to the tpyma complex. The light switch effect has been seriously diminished by the removal of the pyridine and would be worthy of further study to try and understand the mechanism by which the emission is lost.

To further understand the binding of each of the complexes described in this study, future work could include the collection of isothermal calorimetry titration data. This would give estimations of the enthalpy and entropy of the interactions of the complexes with the DNA which could allow for greater understanding of how they behave.

In order to achieve the overall goal of the project a stable molecule needs to be developed that can be connected to a surface. Repeat attempts could be made to synthesise the tiolated complex, $[Ru(tpm)(dppz)(py-SH)]^{2+}$ in order to obtain sufficient pure compound to test its suitability to both DNA binding and surface connection. Alternatively work could be continued to add the alkyne moiety to the dpyma ligand which would allow exploitation of the versatile alkyne-azide cycloaddition "click" chemistry. Once this molecule has been developed it can be attached to a gold surface and assessed using techniques such as X-ray photoelectron spectroscopy (XPS) which would allow for the characterisation of the surface. This technique should be able to detect if ruthenium had successfully bound to the surface.

Once a surface has been successfully functionalised with an intercalating complex it will be important to assess how the surface influences DNA binding. It could be that the steric factors introduced by holding the complex close to a surface hinders the binding of DNA. Some work is likely to be needed to optimise the length of the connection between the surface of the complex to minimise these issues. Work to study this binding could be conducted by photophysical studies alongside mechanical techniques such as atomic force microscopy (AFM), which could be used to both image the DNA and test its binding to the surface. The final step of this research would then be to investigate whether the surface does indeed enhance the emission from the bound complex. If this enhancement is present then attempts could be made to optimise its effect and ultimately adapt the technology to form a sensor device.

5.8 References

1   A. W. Adamson and J. N. Demas, *J. Am. Chem. Soc.*, 1971, **93**, 1800–1801.

2   G. L. Duveneck, C. V Kumar, N. J. Turro and J. K. Barton, *J. Phys. Chem.*, 1988, **92**, 2028–2032.

3   J. V. Caspar and T. J. Meyer, *J. Am. Chem. Soc.*, 1983, **105**, 5583–5590.

4   F. E. Poynton, J. P. Hall, P. M. Keane, C. Schwarz, I. V. Sazanovich, M. Towrie, T. Gunnlaugsson, C. J. Cardin, D. J. Cardin, S. J. Quinn, C. Long and J. M. Kelly, *Chem. Sci.*, 2016, **7**, 3075–3084.

5   G. Scatchard, *Ann. N. Y. Acad. Sci.*, 1949, **51**, 660–672.

6   J. D. McGhee and P. H. V Hippel, *J. Mol. Biol.*, 1974, **86**, 469–489.

7   D. M. Crothers, *Biopolymers*, 1968, **6**, 575–584.

8   L. S. Lerman, *J. Mol. Biol.*, 1961, **3**, IN13-IN14.

9   D. Suh and J. B. Chaires, *Bioorganic Med. Chem.*, 1995, **3**, 723–728.

10 P. V. Scaria and R. H. Shafer, *J. Biol. Chem.*, 1991, **266**, 5417–5423.

11 M. A. A. F. de C. T. Carrondo, M. Coll, J. Aymami, A. H. J. Wang, G. A. Van der Marel, J. H. Van Boom and A. Rich, *Biochemistry*, 1989, **28**, 7849–7859.

12 H. M. Sobell, C.-C. Tsai, S. C. Jain and S. G. Gilbert, *J. Mol. Biol.*, 1977, **114**, 333–365.

13 J. K. Barton, A. T. Danishefsky and J. M. Goldberg, *J. Am. Chem. Soc.*, 1984, **106**, 2172–2176.

14 G. Dougherty and J. R. Pilbrow, *Int. J. Biochem.*, 1984, **16**, 1179–1192.

15 S. P. Foxon, C. Metcalfe, H. Adams, M. Webb and J. A. Thomas, *Inorg. Chem.*, 2007, **46**, 409–416.

16 S. Satyanarayana, J. C. Dabrowiak and J. B. Chaires, *Biochemistry*, 1992, **31**, 9319–9324.

6.0 Experimental

6.1 Materials and equipment

6.1.1 Chemicals

The chemical and solvents detailed in this chapter were purchased from commercial sources and used as received unless otherwise stated.

6.1.2 Nuclear Magnetic Resonance (NMR)

Standard and COSY NMR experiments for both ^{1}H and ^{13}C specta were carried out on Bruker Avance III HD 400 spectrometer. The spectra produced are recorded at 400 MHz.

6.1.3 Mass Spectrometry

All mass spectra were produced by the University of Sheffield Centre of Chemical Instrumentation and Analytical services. Measurements were performed using an electrospray ionisation technique on a Waters LCT mass spectrometer.

6.1.4 Elemental Analysis

All elemental analyses were performed by the University of Sheffield Centre of Chemical Instrumentation and Analytical services. Measurements were conducted using a Vario MICRO cube CHN/S analyser.

6.1.5 UV-Visible Absorption Spectroscopy

UV-Visible spectra were recorded using a Varian – Cary 50 Probe spectrometer. Samples were contained in a quartz cuvette with a 1 cm path length. Samples were baseline corrected using a scan of pure solvent prior to sample addition. Samples were diluted to remain below and absorbance reading of 1.

6.1.6 Luminescence Spectroscopy

Luminescence spectra were recorded using a Horiba Jobin-Yvon FluoroMax-3 spectrometer with a Julabo F12 Refrigerated/Heated Circulator at 25 °C. Samples were contained in a quartz cuvette with a 1 cm path length. Excitation and emission slit widths were set at 5 nm.

6.1.7 Cyclic Voltammetry (CV)

CV measurements were made inside an EG&G Faraday cage, with electrodes connected to a Princeton Applied Research VersaSTAT 3 potentiostat. Potentials were measured against an Ag/AgCl reference electrode and platinum electrodes for the working and counter electrode. Samples were made up to approximately 2 mM concentration in a dry DMF solution containing 0.1 M Bu_4NPF_6. Prior to recording potentials the sample was degassed by bubbling N_2 through the solution.

6.1.8 X-ray Crystallography

Crystal structure data was obtained and analysed by the University of Sheffield Centre of Chemical Instrumentation and Analytical services. Crystals were analysed using a Bruker SMART 1000 or Bruker SMART Apex 2 area detector with low temperature facilities.

6.2 DNA Binding Studies

6.2.1 Buffer Preparation

Tris buffer was prepared using Millipore deionised water and Trizma HCl (Tris(hydroxymethyl)aminomethane) base at 5 mM concentration, and 25 mM NaCl. The solution was adjusted to pH 7.5 using dilute HCl and additional water added to achieve the correct volume. The solution were passed through 0.2 micron Millipore filter to sterilise. The solution was stored in a refrigerator at 4°C.

6.2.2 DNA Preparation

Calf thymus DNA (CT-DNA) was purchased from Sigma-Aldrich as a lyophilised sodium salt and used as received. Stock solutions were prepared by adding approximately 0.5 g solid DNA to 50 ml of tris buffer and left to dissolve in a refrigerator overnight. This solution was subjected to discontinuous sonication for 30 minutes using a Sonics Vibra Cell fitted with a 3 mm diameter probe. The sonication was conducted in on/off cycles of 30 seconds. The sample was kept in an ice bath during sonication. After sonication the sample was dialysed against buffer solution overnight in a refrigerator. The concentration (per base pair) of the resulting solution was determined by UV spectroscopy using ε_{260} = 13200 $M^{-1} cm^{-1}$. The stock solution was used for both titrations and viscometry.

6.2.3 Sample Preparation

The studied ruthenium complexes were converted to water soluble chloride salts using Dowex 1X8 chloride form. After conversion the solvent was removed *in vacuo* and the sample was dried in a vacuum oven. This solid was weighed and re-dissolved in tris buffer solution to form stock solutions for both titrations and viscosity measurements.

6.2.4 UV-Visible titrations

UV-Visible titrations were performed using a Varian – Cary 50 Probe spectrometer. A 3 ml volume quartz cuvette with a 1 cm path length was used in all titrations. The baseline of pure buffer was recorded before each titration to calibrate the setup. The complex stock solution was added to buffer to start the titrations with a concentration of ~1.5-2.2 mM. Spectra were recorded at medium scan rate from 200-800 nm. DNA stock solution of 1.65 mM bp^{-1} concentration was added by pipette in amounts ranging from

2-10 µL. After each addition the cuvette was agitated by inverting the cuvette for 1 minute and then left in the spectrometer for a further 4 minutes to equilibrate. The additions were continued until no further changes were observed in the spectrum, indicating saturation.

6.2.5 Luminescence titrations

Luminesence spectra were recorded using a Horiba Jobin-Yvon FluoroMax-3 spectrometer with a Julabo F12 Refrigerated/Heated Circulator at 25 °C. A 3 ml volume quartz cuvette with a 1 cm path length was used in all titrations. The complex stock solution was added to buffer to start the titrations with a concentration of ~1.5-2.2 mM. Samples were excited at a wavelength of 426 nm and emission recorded from ~ 480-830 nm. DNA stock solution of 1.65 mM bp^{-1} concentration was added by pipette in amounts ranging from 2-10 µL. After each addition the cuvette was agitated by inverting the cuvette for 1 minute and then left in the spectrometer for a further 4 minutes to equilibrate. The additions were continued until no further changes were observed in the spectrum, indicating saturation.

6.2.6 Viscometry

Viscosity experiments were performed on a Cannon Fenske viscometer (size 50) immersed in a temperature controlled water bath at 25 °C. The initial concentration of CT-DNA in the viscometer was ~ 50 µM bp^{-1}. Additions of the complex were made so that the values of 1/r (r = [DNA]/[ligand]) were between 0 and 0.3. After each addition of complex solution, air was bubbled through to mix the solution. The sample was left in the viscometer, submerged in the water bath, for 15 minutes to equilibrate before measurement of the flow time. The flow times were measured three times and averaged. After each experiment the viscometer was cleaned with diluted sulphuric acid, water and acetone. The water was drawn through the viscometer in reverse to remove any particulate matter that might block the flow.

6.3 Synthesis

6.3.1 Synthesis of tris(1-pyrazolyl)methane (tpm)
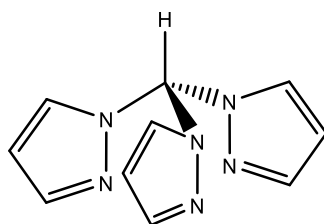
This compound was prepared using a previously reported procedure.[1] Pyrazole (29.88 g, 0.44 mol) and tetra-n-butylammonium bromide (4.93 g, 0.015 mol) were added to a three neck 1 L round bottom flask. De-ionised water (294 ml) and the mixture stirred using a mechanical stirrer. Sodium carbonate (191 g, 1.80 mol) was added slowly and the mixture was allowed to cool and the flask was then equipped with a condenser. Chloroform (147 ml, 1.82 mol) was added before the mixture was heated to reflux for 72 hours at 80 °C, forming a yellow solution. The solution was cooled and vacuum filtered to remove excess sodium carbonate. Water (150 ml) and Chloroform (150 ml) were added to the filtrate. The organic and aqueous phases were partitioned and the aqueous phase was extracted with dichloromethane (3 x 150 ml). The combined organic phase was then washed with brine (200 ml) and dried over magnesium sulphate. Solvent was removed *in vacuo* to give a brown viscous liquid which was placed in the freezer to form an orange solid. The solid was recrystallised from water to give pale cream coloured crystals. The crystals were dried in a vacuum dessicator to give tris(1-pyrazolyl)methane (14.86 g, 0.07 mol, 47.1%); Found: C, 56.0; H, 4.7; N,38.9 (Calc. for $C_{10}H_{10}N_6$: C, 56.0; H, 4.7; N, 39.2); ^{1}H NMR (400 MHz, CDCl$_3$) δ 8.46 (s, 1H), 7.70 (d, J = 1.6 Hz, 3H), 7.60 (d, J = 2.5 Hz, 3H), 6.39 (dd, J = 2.5, 2.0 Hz, 3H); ^{13}C NMR (101 MHz, CDCl$_3$) δ 141.9 (CH), 129.6 (CH), 107.4 (CH), 83.2 (CH); MS ES+, m/z (%): 237 (100) [MNa$^+$], 215 (7) [MH$^+$], 147 (83) [M-(py)]$^+$

6.3.2 Synthesis of [RuCl₃(tpm)]
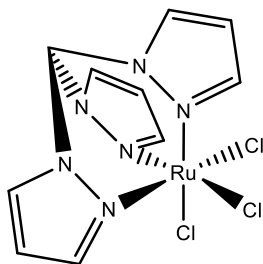
Tris(1-pyrazolyl)methane (0.41 g, 1.93 mmol) and ruthenium trichloride hydrate (0.50 g, 1.92 mmol) were added to a 250 ml round bottom flask with ethanol (175 ml) forming a deep red solution. The reaction was heated to reflux for 4 hours. The reaction was cooled to room temperature and the brown precipitate was collected in a sinter under vacuum filtration. The solid was washed with ethanol and acetone before air drying to give [RuCl₃(tpm)] (0.51 g, 1.22 mmol, 64 %) as a fine brown powder; Found: C, 28.9; H, 2.8; N, 18.2; Cl, 22.5 (Calc. for $C_{10}H_{10}N_6Cl_3Ru$: C, 28.5; H, 2.4; N, 19.9; Cl, 25.2); MS ES+, m/z (%): 417 (100), 387 (4) [M⁺-Cl]

6.3.3 Synthesis of 1,10-phenanthroline-5,6-dione (dpq)
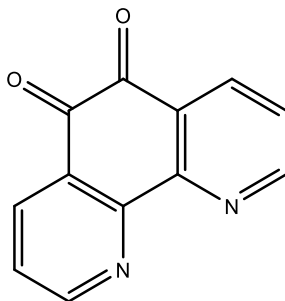
1,10-phenanthroline (10.23 g, 56.7 mmol) was added to a 250 ml round bottom flask containing 60% H_2SO_4 (70 ml). Solution was allowed to cool before addition of potassium bromate (38.71 g, 325 mmol) in small portions. Vigorous reaction after each addition was allowed to subside before subsequent addition. After completed addition the reaction was left to stir at room temperature for 2.5 hours. The yellow solution was poured over ice (200 g) in a beaker which was cooled in an ice bath. The reaction was neutralised with saturated NaOH, slowly added to keep the solution below 10 °C. The resulting aqueous solution was extracted with DCM (3 x 500 ml) and the combined extract was washed with water (500 ml) and brine solution (500 ml). The extract was dried over MgSO₄ and the solvent removed *in vacuo*. The resulting residue was recrystalised from ethanol and resulting crystals were collected in a sinter under

vacuum filtration. The solid was dried under vacuum at 40 °C to give 1,10-phenanthroline-5,6-dione (6.39 g, 30.4 mmol, 54 %) as a yellow solid; ^{1}H NMR (400 MHz, CDCl$_3$) δ 9.11 (dd, J = 4.5, 2.0 Hz, 2H), 8.50 (dd, J = 8.0, 2.0 Hz, 2H), 7.60 (dd, J = 8.0, 4.5 Hz, 2H); ^{13}C NMR (101 MHz, CDCl$_3$) δ 178.7 (CH), 156.4 (C), 152.9 (CH), 137.3 (C), 128.1 (CH), 125.7 (C), 50.8 (C); MS EI+, m/z (%): 210 (27) [M$^+$], 182 (100) [M$^+$-O$_2$].

6.3.4 Synthesis of dipyridoquinoxaline (dpqx)
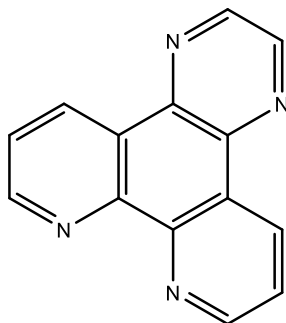
1,10-phenanthroline-5,6-dione (0.96 g, 4.57 mmol) and 1,2-ethylenediamine (0.34 ml, 5.09 mmol) were added to a 250 ml round bottom flask with ethanol (130 ml) forming a yellow solution. The reaction was heated to reflux and left overnight. The reaction was cooled to room temperature and the solvent was removed *in vacuo*. The residue was recrystalised from ethanol to give dipyridoqunioxaline (0.50 g, 2.14 mmol, 47 %) as a cream coloured solid; ^{1}H NMR (400 MHz, CDCl$_3$) δ 9.57 – 9.48 (m, 2H), 9.38 – 9.27 (m, 2H), 9.07 – 8.97 (m, 2H), 7.85 (dd, J = 8.2, 4.4 Hz, 2H); MS ES+, m/z (%): 233 (100) [MH$^+$].

6.3.5 Synthesis of dipyridophenazine (dppz)
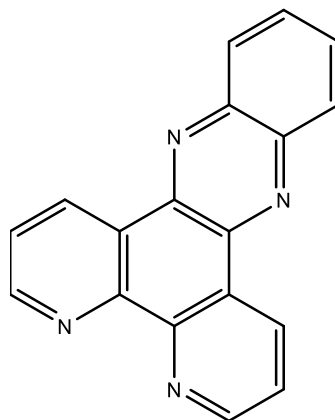
1,10-phenanthroline-5,6-dione (1.22 g, 5.79 mmol) and 1,2-phenylenediamine (0.62 g, 5.74 mmol) were added to a 250 ml round bottom flask with ethanol (100 ml) forming a black solution. The reaction was heated to reflux and the solution turned red. The reaction was left to reflux overnight. The reaction was cooled to room temperature and the solvent was removed *in vacuo*. The residue was recrystalised from ethanol to give dipyridophenazine (1.24 g, 4.40 mmol, 77 %) as a cream coloured solid. ^{1}H NMR (400 MHz, CDCl$_3$) δ 9.68 (dd, J = 8.0, 2.0 Hz, 2H), 9.31 (dd, J = 4.5, 2.0 Hz, 2H), 8.43 – 8.34 (m, 2H), 7.99 – 7.92 (m, 2H), 7.83 (dd, J = 8.0, 4.5 Hz, 2H); MS ES+, m/z (%): 282 (100) [M$^+$] 255 (26).

6.3.5 Synthesis of [RuCl(tpm)(dppz)]⁺PF₆⁻
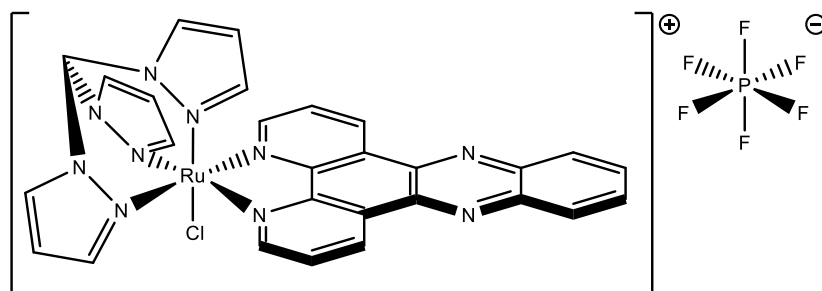
Dipyridophenazine (0.68 g 2.40 mmol) and [RuCl₃(tpm)] (1.01 g, 2.39 mmol) were added to a 250 ml two neck round bottom flask with a 3:1 ethanol: water solvent mix (100 ml) forming a deep red solution. The reaction was flushed with N_2 for 5 minutes before sealing and heating to reflux for 10 minutes before addition of triethylamine (0.1 ml). The reaction was stirred at reflux for a further hour. The reaction was cooled to room temperature and the solvent removed *in vacuo*. The residue was dissolved in 1:1 water:methanol (50 ml) and filtered to remove undissolved brown solid. The filtrate was treated with a saturated solution of KPF₆ and the resultant precipitate was collected in a sinter *via* vacuum filtration. The crude solid was subjected to column chromatography on alumina (neutral, Brockmann grade 1) using 1:1 acetonitrile:toluene as the eluent. The initial purple band was discarded and the subsequent brown band was collected. The solvent of the collected fraction was removed *in vacuo* and the residue was redissolved in a minimum amount of methanol. Saturated KPF₆ solution was added and the resultant precipitate collected in a sinter under vacuum filtration giving [RuCl(tpm)(dppz)]PF₆ (0.29 g, 0.38 mmol, 16 %) as a red solid; ¹H NMR (400 MHz, CD₃CN) δ 9.52 (d, J = 7.5 Hz, 2H), 9.18 (d, J = 4.5 Hz, 2H), 8.96 (s, 1H), 8.49 (d, J = 2.5 Hz, 2H), 8.45 (d, J = 2.0 Hz, 2H), 8.39 (dd, J = 6.5, 3.5 Hz, 2H), 8.33 (d, J = 3.0 Hz, 1H), 8.14 – 8.06 (m, 2H), 7.97 (dd, J = 8.0, 5.5 Hz, 2H), 6.78 (dd, J = 2.5, 2.5 Hz, 2H), 6.59 (d, J = 2.0 Hz, 1H), 6.25 – 6.19 (m, 1H); MS ES+, m/z (%): 633 (100) [M⁺].

6.3.7 Synthesis of tris-2,2,2-(1-pyrazolyl)ethanol (tpe)
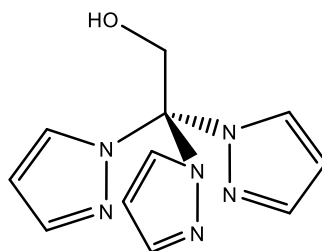
This compound was prepared using a previously reported procedure.[2] Tris(1-pyrazolyl)methane (6.42 g, 29.9 mmol) and potassium t-butoxide (10.14 g, 90.0 mmol) were added to an oven dried two neck 500 ml round bottom flask equipped with a magnetic flea. The flask was sealed and purged with nitrogen before the addition of dry tetrahydrofuran (300 ml) forming a yellow solution. Solution was stirred for 24 hours at room temperature. Water (300 ml) was added slowly and product was extracted with diethyl ether (3 x 150 ml). The organic phase was combined and dried over sodium sulphate. The solvent was removed *in vacuo* to give tris-2,2,2-(1-pyrazolyl)ethanol (5.78 g, 23.7 mmol, 79.0%) as an off white solid; Found: C, 54.1; H, 4.8; N,34.2 (Calc. for $C_{11}H_{13}N_6O$: C, 54.1; H, 5.0; N, 34.4); ^{1}H NMR (400 MHz, $CDCl_3$) δ 7.73 (d, J = 1.5 Hz, 3H), 7.16 – 7.08 (m, 3H), 6.39 (dd, J = 2.5, 2.0 Hz, 3H), 5.10 (d, J = 7.0 Hz, 2H), 4.91 (t, J = 7.0 Hz, 1H); ^{13}C NMR (101 MHz, $CDCl_3$) δ 141.7 (CH), 130.12 (CH), 106.9 (CH), 89.44 (C) 68.0 (CH_2); MS ES+, m/z (%): 245 (28) [MH^+], 177 (100) [M-(py)][+]

6.3.8 Synthesis of 1,1',1''-(2-(prop-2-yn-1-yloxy)ethane-1,1,1-triyl)tris(1H-pyrazole) (tppoe)
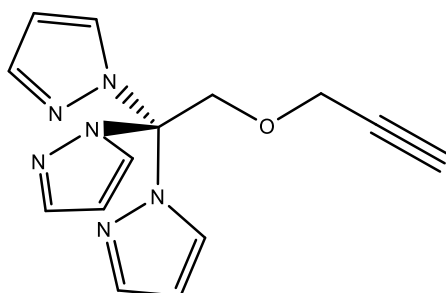
This compound was prepared using a previously reported procedure.[2] A three neck, 500 ml round bottom flask equipped with a dropping funnel and condenser were oven dried, sealed and purged with nitrogen. Sodium hydride, 60% dispersion in oil (0.83 g, 20.7 mmol) was handled and added under nitrogen followed by addition of Dry THF (50 ml). Tris-2,2,2-(1-pyrazolyl)ethanol (5.05 g, 20.6 mmol) was dissolved in dry THF (150 ml) under nitrogen and added to the sodium hydride dropwise, *via* the dropping funnel over 30 minutes. Mixture was heated to reflux at 85°C for 2.5 hours. Flask was covered with foil before addition of propargyl bromide (3.07 g, 20.7 mmol). Reaction mixture was allowed to reflux for a further 24 hours. Reaction was then allowed to cool before slow addition of water (100 ml) from the dropping funnel. The product was extracted with dichloromethane (3 x 100 ml) and the combined organic phase was washed with saturated sodium hydrogencarbonate solution (100 ml) followed by water (3 x 100 ml). The organic phase was dried over sodium sulphate and the solvent was removed *in vacuo* to give an orange/brown residue. After chromatography on silica gel with hexane: ethyl acetate (1 : 1) as eluent, 1,1',1''-(2-(prop-2-yn-1-yloxy)ethane-1,1,1-triyl)tris(1H-pyrazole) (3.60 g, 12.8 mmol, 61.9%) was obtained as yellow crystals; Found: C, 59.7; H, 4.8; N,29.4 (Calc. for $C_{14}H_{14}N_6O$: C, 59.6; H, 5.0; N, 29.8); ^{1}H NMR (400 MHz, CDCl$_3$) δ 7.69 (dd, J = 2.0, 0.5 Hz, 3H), 7.43 (dd, J = 2.5, 0.5 Hz, 3H), 6.36 (dd, J = 2.5, 2.0 Hz, 3H), 5.22 (s, 2H), 4.19 (d, J = 2.5 Hz, 2H), 2.53 (t, J = 2.5 Hz, 1H); ^{13}C NMR (101 MHz, CDCl$_3$) δ 141.4 (CH), 130.8 (CH), 106.6 (CH), 89.6 (C), 75.8 (C), 72.8 (CH$_2$), 59.2(CH$_2$); MS ES+, m/z (%): 283 (12) [MH$^+$], 215 (100) [M-(py)]$^+$

6.3.9 Synthesis of 3-azidopropan-1-thiol
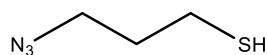
This compound was prepared using a previously reported procedure.[3] A water: ethanol mix (2:1, 10 ml) was added to a 100 ml round bottom flask equipped with a magnetic flea. 3-chloropropan-1-thiol (0.70 g, 6.36 mmol) was added whilst stirring, followed by sodium azide (0.81g, 12.45 mmol). Mixture was heated to reflux under nitrogen at 105 °C for 24 hours. The reaction was allowed to cool to room temperature before slow addition of water (50 ml). Product was extracted with diethyl ether (3 x 50 ml), then the combined organic phase was washed with water (150 ml) and dried over calcium chloride. The solvent was removed at ambient pressure to yield 3-azidopropan-1-thiol (0.27 g, 2.26 mmol, 35.6%) as a yellow oil; Found: C, 34.1; H, 5.2; N, 27.8; S, 30.3; (Calc. for $C_3H_6N_3SH$: C, 30.8; H, 6.0; N, 35.9; S, 27.4); v_{max}/cm^{-1} 2930 (CH), 2871 (CH) and 2089 (N_3); ^1H NMR (400 MHz, $CDCl_3$) δ 3.46 (t, J = 6.5 Hz, 2H), 2.77 (t, J = 7.0 Hz, 2H), 2.07 – 1.96 (m, 2H); ^{13}C NMR (101 MHz, $CDCl_3$) δ 49.7 (CH_2), 35.2 (CH_2), 28.2 (CH_2).

6.3.10 Synthesis of tris-2,2,2-(pyrazol-1-yl)ethoxy (1,2,3-triazole-1-(propan-3-thiol)-4-ethyl) ether
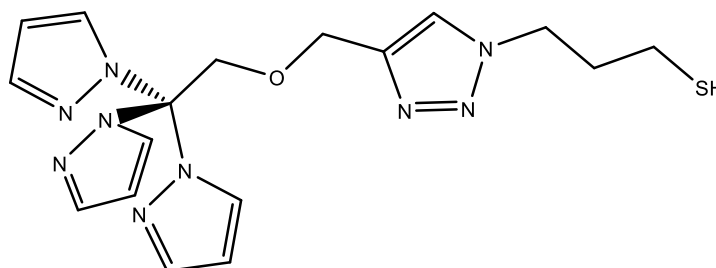
A water: ethanol mix (1:1, 15 ml) was added to a 25 ml round bottom flask equipped with a magnetic flea. To this, 3-azidopropan-1-thiol (0.11 g, 0.90 mmol), tris-2,2,2-(1-pyrazol-1-yl)ethoxypropargyl ether (0.24 g, 0.86 mmol), sodium ascorbate (0.016 g, 0.08 mmol, 10 mol%) and copper sulphate (0.001 g, 0.008 mmol, 1 mol%) were added. The yellow solution was left to stir for 48 hours. The product was extracted with diethyl ether (3 x 15 ml) and dried over magnesium sulphate. The solvent was removed at ambient pressure to give the product (0.25 g, 60 %); MS ES+, m/z (%): 797 (100) [M+M⁺], 399 (21) [M⁺].

6.3.11 Synthesis of 1,5 diazidopentane
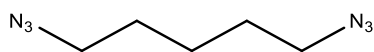
Dibromopentane (1.62 g, 7.11 mmol) and sodium azide (1.26 g, 19.31 mmol) were added to a 25 ml round bottom flask and dissolved in dimethylformamide (10 ml). Reaction was left to stir at room temperature for 20 hours. Water (5 ml) was added to the resulting turbid solution and the reaction was stirred for a further 20 hours. The product was extracted with diethyl ether. It was not possible to remove the ether from the product and so the solvated crude was used for subsequent reactions. ; MS EI+, m/z (%): 74.0 (100), 155.0 (5) [M+].

6.3.12 Synthesis of 1,5-bis(4-((2,2,2-tri(1H-pyrazol-1-yl)ethoxy)methyl)-1H-1,2,3-triazol-1-yl)pentane
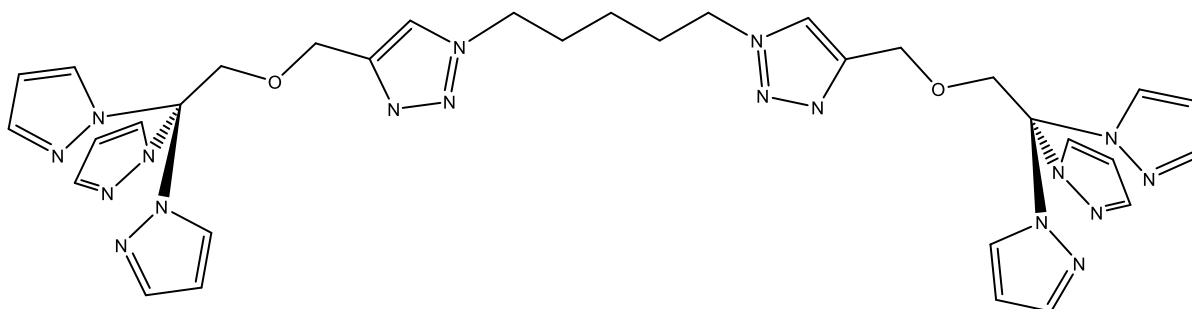
Diazidopentane (~0.135 g, ~0.88 mmol) in diethylether, 1,1',1''-(2-(prop-2-yn-1-yloxy)ethane-1,1,1-triyl)tris(1H-pyrazole) (0.51 g, 1.79 mmol), sodium ascorbate (0.01 g, 0.04 mmol) and anhydrous copper sulphate (0.05 g, 0.33 mmol) were added to a 100 ml round bottom flask. A 2:1 ethanol:water (50 ml) mix was added forming a pale yellow solution. Reaction was left stirring for 48 hours and solution became green. Product extracted with chloroform (100 ml) and water (50 ml). Solvent removed *in vacuo* giving an orange oil. The oil was purified by column chromatography on silica gel with DCM:MeOH (9:1) eluent. Yellow band collected and concentrated *in vacuo* to give 1,5-bis(4-((2,2,2-tri(1H-pyrazol-1-yl)ethoxy)methyl)-1H-1,2,3-triazol-1-yl)pentane (0.616 g, 0.86 mmol, 97.7%) as a yellow oil; ^{1}H NMR (400 MHz, CDCl$_3$) δ 7.67 (ddd, *J* = 2.2, 1.7, 0.9 Hz, 6H), 7.45 – 7.40 (m, 6H), 7.28 (s, 2H), 6.36 (ddd, *J* = 4.5, 2.5, 2.0 Hz, 6H), 5.15 (s, 4H), 4.67 (m, 4H), 4.31 (t, *J* = 7.0 Hz, 4H), 2.06 – 1.85 (m, 4H), 1.34 (ddt, *J* = 13, 10.0, 5.0 Hz, 2H); MS ES+, m/z (%): 757 (18) [MK+], 741 (100) [MNa+].

6.3.13 Synthesis of 2,2,2-tri(1H-pyrazol-1-yl)ethyl 4-iodobenzoate (tpeib)
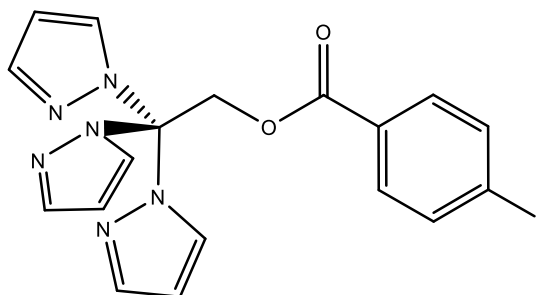
Sodium hydride (60% in oil) (0.33 g, 8.32 mmol) was added to a dry two neck 250 ml round bottom flask fitted with a condenser and flushed with nitrogen. Dry THF (20 ml) was added via syringe forming a slurry. Tris-2,2,2-(1-pyrazolyl)ethanol (tpe) (2.01 g, 8.22 mmol) was dissolved in dry THF (200 ml) and added to a dry dropping funnel *via* cannula. The tpe solution was added dropwise with stirring to the slurry forming a clear solution. The reaction was heated to reflux at 85 ºC for 2.5 hours. 4-iodobenzolyl chloride (2.19 g, 8.23 mmol) was added and the reaction was left to reflux overnight. Reaction was cooled to room temperature. Water (60 ml) was added dropwise. The solution was extracted with chloroform, dried and the solvent removed *in vacuo*. The resulting solid was subjected to column chromatography with ethyl acetate:pet ether (2:1) as eluent. The pure fractions were combined and solvent removed to give 2,2,2-tri(1H-pyrazol-1-yl)ethyl 4-iodobenzoate (2.79 g, 5.89 mmol, 71.7%) as a white solid; ^{1}H NMR (400 MHz, CDCl$_3$) δ 7.79 − 7.74 (m, 2H), 7.71 (d, *J* = 1.0 Hz, 3H), 7.54 − 7.48 (m, 2H), 7.29 (dd, *J* = 2.5, 0.5 Hz, 3H), 6.39 (dd, *J* = 2.5, 2.0 Hz, 3H), 5.92 (s, 2H); ^{13}C NMR (101 MHz, CDCl$_3$) δ 164.6, 142.0, 137.8, 131.2, 130.2, 128.7, 107.0, 101.4, 89.3, 67.2; MS ES+, m/z (%): 475 (64) [MH$^+$], 267 (100).

6.3.14 Synthesis of tris(pyrazolyl)bromomethylbenzeneoxyethane (tpbmb)
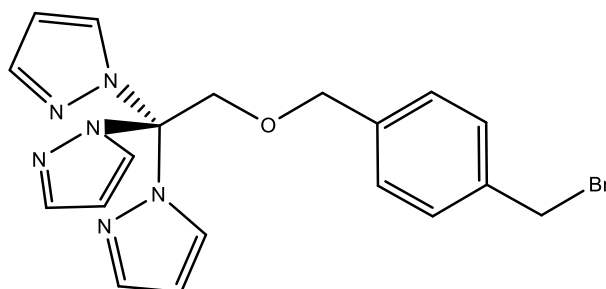
This compound was prepared using a previously reported procedure.[4] Sodium hydride (0.21 g, 60% in oil, 5.13 mmol) was added to a 100 ml oven dried round bottom flask and the flask was flushed with N_2. A slurry was formed on the addition of dry THF (15 ml). A solution of tris(pyrazolyl)ethanol (1.02 g, 4.17 mmol) in dry THF (15 ml) was added *via* syringe. The solution was left to stir at room temperature for 30 minutes. A separate solution of dibromoxylene (6.30 g, 23.85 mmol) and dry THF (15 ml) was prepared in a 100 ml round bottom flask and cooled to 0 °C in an ice bath. The orange solution of NaH and tpe in THF was transferred to the cold solution of dibromoxylene dropwise *via* syringe. The reaction was allowed to warm to room temperature and left stirring overnight. The solvent of the yellow solution was removed *in vacuo* and the residue was dissolved in DCM. The solution was subjected to purification by column chromatography with a silica gel stationary phase and DCM as the eluent. The product tris(pyrazolyl)bromomethylbenzeneoxyethane (1.48 g, 3.47 mmol, 83%) was obtained as a yellow oil. ^{1}H NMR (400 MHz, CDCl$_3$) δ 7.71 – 7.66 (m, 3H), 7.45 (dd, J = 2.5, 0.5 Hz, 3H), 7.36 (d, J = 8.0 Hz, 2H), 7.17 (d, J = 8.0 Hz, 2H), 6.37 (dd, J = 2.5, 2.0 Hz, 3H), 5.16 (s, 2H), 4.54 (s, 2H), 4.50 (s, 2H); ^{13}C NMR (101 MHz, CDCl$_3$) δ 141.4, 141.2, 137.5, 132.4, 130.9, 129.5, 129.2, 128.3, 128.2, 128.1, 106.7, 106.6, 73.7, 73.5, 33.2; MS ES+, m/z (%): 449 (4) [MNa$^+$], 291 (100).

6.3.15 Synthesis of tris(pyrazolyl)azidomethylbenzeneoxyethane (tpeazb)
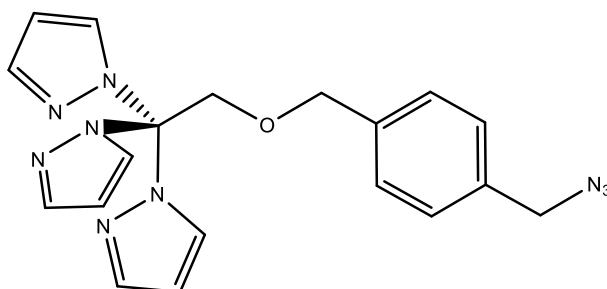
Tris(pyrazolyl)bromomethylbenzeneoxyethane (0.51 g, 1.19 mmol) was weighed into a 100 ml round bottom flask. A 1:1 ethanol:water (40 ml) solvent mix was added forming a yellow solution. Sodium azide (0.09 g, 1.34 mmol) was added and the reaction was heated to reflux overnight. The reaction was cooled to room temperature and water (30 ml) added. The aqueous solution was extracted with chloroform (3 x 50 ml). The combined yellow extract was dried over $MgSO_4$ and the solvent removed *in vacuo* to give tris(pyrazolyl)azidomethylbenzeneoxyethane (0.46 g, 1.18 mmol, 99%) as a yellow oil; v_{max}/cm^{-1} 2917 (CH), 2850 (CH) and 2095 (N_3); ^1H NMR (400 MHz, $CDCl_3$) δ 7.69 (d, *J* = 1.5 Hz, 3H), 7.46 (d, *J* = 2.5 Hz, 3H), 7.29 (d, *J* = 8.0 Hz, 2H), 7.22 (d, *J* = 8.0 Hz, 2H), 6.37 (dd, *J* = 2.5, 2.0 Hz, 3H), 5.17 (s, 2H), 4.55 (s, 2H), 4.34 (s, 2H); ^{13}C NMR (101 MHz, $CDCl_3$) δ 141.4, 137.3, 135.1, 130.9, 128.3, 128.2, 128.1, 127.9, 127.8, 127.1, 106.9, 106.6, 89.8, 74.0, 73.8, 73.5, 73.4, 72.4, 65.8, 64.9, 54.5.

6.3.16 Synthesis of tris(pyrazolyl)aminomethylbenzeneoxyethane (tpeamb)
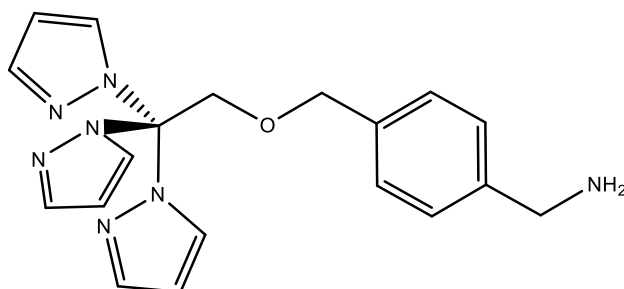
Triphenylphosphine (0.10 g, 0.35 mmol) was added to an oven dried 100 ml round bottom flask and flushed with N_2 for 5 minutes. Tris(pyrazolyl)azidomethylbenzeneoxyethane (0.10 g, 0.25 mmol) was dissolved in dry methanol (10 ml) and the yellow solution was transferred to the round bottom flask. The reaction was heated to reflux for 1 hour. The reaction was cooled to room temp and the solvent removed *in vacuo*. The residue was purified by column chromatography on silica gel and a 2% methanol in DCM solvent mix as eluent. The fractions were combined and solvent removed to give tris(pyrazolyl)aminomethylbenzeneoxyethane (0.04 g, 0.11 mmol, 44 %) as a yellow oil; ^{1}H NMR (400 MHz, CDCl$_3$) δ 7.68 (m, 3H), 7.45 (m, 3H), 7.36 – 7.23 (m, 2H), 7.22 – 7.08 (m, 2H), 6.36 (m, 3H), 5.13 (s, 2H), 4.52 (s, 2H), 3.89 (s, 2H).

6.3.17 Synthesis of [RuCl$_2$(dmso)$_4$]
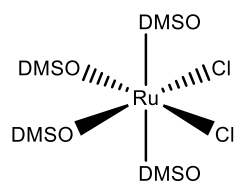
This compound was prepared using a previously reported procedure.[5] Dimethylsulphoxide (3 ml, 42.25 mmol) was added to a dry 50 ml round bottom flask which was sealed and flushed with nitrogen for 30 minutes. 2-propanol was added to a separate round bottom flask and also flushed with N$_2$ for 30 minutes. Ruthenium chloride hydrate (1.06 g, 4.05 mmol) was added against the N$_2$ flow. The previously degassed 2-propanol (10 ml) was added *via* syringe. The reaction was heated to 85 °C for 32 hours. The reaction was left to cool to room temperature, forming a yellow precipitate from the deep red solution. The reaction was left in the freezer overnight to maximise precipitation. The solid was collected *via* filtration and washed with excess acetone followed by excess toluene. The precipitate was air dried followed by drying in a vacuum desiccator to give [RuCl$_2$(dmso)$_4$] (1.80 g, 3.72 mmol, 92%) as a yellow solid. MS EI+, m/z (%): 421 (30) [MH$^+$], 375 (100)

6.3.18 Synthesis of [RuCl$_2$(dmso)$_2$(NN)]
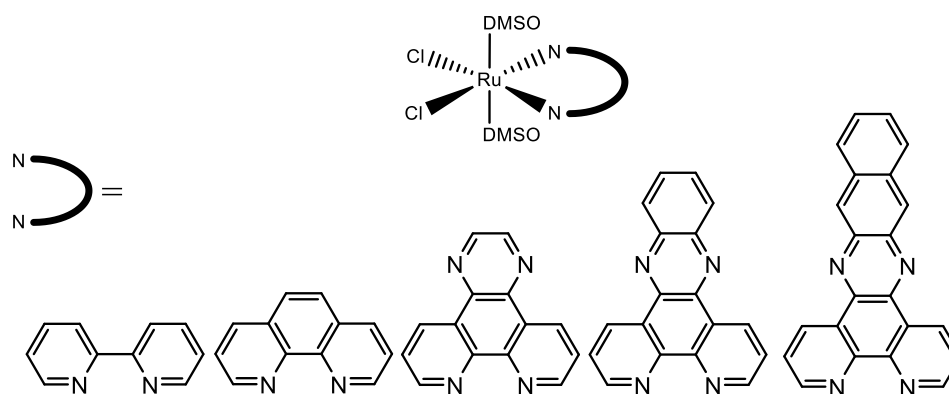
These compounds were prepared using an adapted literature procedure.[6] The NN ligand and [RuCl$_2$(dmso)$_4$] were added to a 100/250 ml two neck round bottom flask and flushed with N$_2$. Toluene was added to the flask. The reaction was fitted with condenser, sealed and covered in foil to exclude light. The suspension was heated to reflux overnight. After reflux, the reaction was cooled slightly and filtered hot through a sintered funnel. The solid brown precipitate was then washed with toluene and diethyl ether and dried in a vacuum oven to give the desired complex.

Bpy (0.45 g, 0.92 mmol) and [RuCl$_2$(dmso)$_4$] (0.15 g, 0.93 mmol) refluxed in toluene (60 ml) gave [RuCl$_2$(dmso)$_2$(bpy)] (0.43 g, 0.89 mmol, 96.7 %);

Phen (0.12 g, 0.64 mmol) and [RuCl$_2$(dmso)$_4$] (0.31 g, 0.64 mmol) refluxed in toluene (60 ml) gave [RuCl$_2$(dmso)$_2$(phen)] (0.27 g, 0.53 mmol, 83.6 %);

Dpqx (0.27 g, 1.18 mmol) and [RuCl$_2$(dmso)$_4$] (0.57 g, 1.17 mmol) refluxed in toluene (60 ml) gave [RuCl$_2$(dmso)$_2$(dpqx)] (0.60 g, 1.07 mmol, 91.8 %);

Dppz (1.30 g, 4.61 mmol) and [RuCl$_2$(dmso)$_4$] (2.24 g, 4.62 mmol) refluxed in toluene (140 ml) gave [RuCl$_2$(dmso)$_2$(dppz)] (2.72 g, 4.46 mmol, 96.7 %); MS ES+, m/z (%): 575 (100) [M$^+$-Cl], 497 (52) [M$^+$-Cl-dmso]

Dppn (0.15 g, 0.44 mmol) and [RuCl$_2$(dmso)$_4$] (0.21 g, 0.44 mmol) gave refluxed in toluene (60 ml) [RuCl$_2$(dmso)$_2$(dppn)] (0.25 g, 0.38 mmol, 85.3 %);

6.3.19 Alternative synthesis of [RuCl(tpm)(dppz)](PF$_6$)
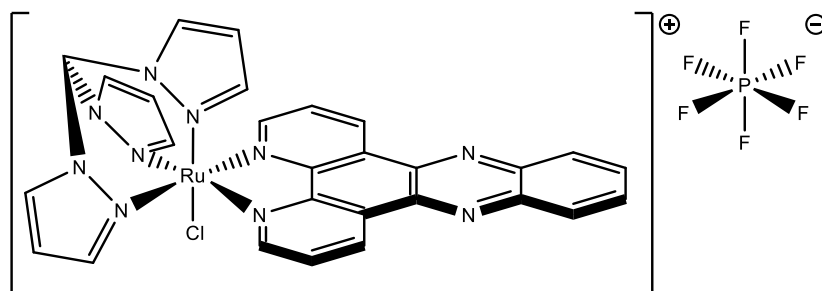
[RuCl$_2$(dppz)(dmso)$_2$] (0.29 g, 0.48 mmol) and tpm (0.11 g, 0.5 mmol) were added to a dry 100 ml RBF and flushed with N$_2$. Ethylene glycol (50 ml) was added forming a suspension. The flask was sealed with condenser fitted and covered in foil to exclude light. The reaction heated to 140 °C for 1 hour with stirring. The reaction became deep red and was cooled to room temp. A saturated solution of KPF$_6$ (100 ml) was added to precipitate the salt formed. The precipitate was collected and dried. The solid was subjected to column chromatography with 1:1 acetonitrile:toluene as eluent. The purple band was discarded and subsequent brown band collected. The solvent of the band was removed *in vacuo* and the salt was re-precipitated with sat. KPF$_6$ to yield [RuCl(tpm)(dppz)]PF$_6$ (0.19 g, 0.24 mmol, 49.5 %) as a red solid; ^{1}H NMR (400 MHz, CD$_3$CN) δ 9.49 (d, *J* = 8.0 Hz, 2H), 9.18 (d, *J* = 5.0 Hz, 2H), 8.95 (s, 1H), 8.56 – 8.41 (m, 4H), 8.41 – 8.22 (m, 2H), 8.09 (dd, *J* = 6.5, 3.0 Hz, 2H), 7.97 (dd, *J* = 8.0, 5.5 Hz, 2H), 6.79 (s, 2H), 6.59 (m, 1H), 6.23 (t, 1H); MS ES+, m/z (%): 633 (100) [M$^+$].

6.3.20 Synthesis of mercapto(pyridinylmethyl)undecanamide
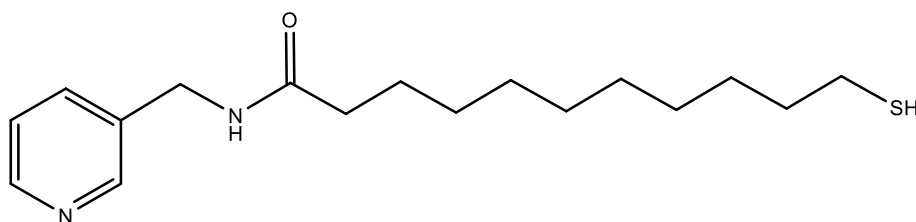
11-mercaptoundecanoic acid (0.31 g, 2.77 mmol), dicyclohexylcarbodiimide (DCC) (0.696 g, 3.73 mmol) and 1-hydroxybenzotriazole hydrate (HOBt) (0.47 g, 3.06 mmol) were added to a 100 ml round bottom flask and flushed with N_2. The flask was sealed and ice cooled dry DCM (40 ml) was added *via* syringe forming a cloudy suspension. The reaction flask was cooled in an ice bath and stirred for 1 hour. 3-picolylamine (0.34 ml, 3.34 mmol) was added *via* syringe. The ice bath was removed and the reaction was left to stir overnight. The reaction was partitioned with H_2O and extracted with DCM. The solvent of the extract was removed *in vacuo* yielding a white solid. The solid was subjected to silica gel column chromatography with DCM:MeOH (19:1). The fractions were visualised using a permanganate TLC dip. The pure fractions were combined and the solvent removed *in vacuo* to give mercapto(pyridinylmethyl)undecanamide (0.62 g, 2.02 mmol, 73.0 %) as a white solid; ^{1}H NMR (400 MHz, MeOD) δ 8.52 (d, *J* = 2.0 Hz, 1H), 8.47 (dd, *J* = 5.0, 1.5 Hz, 1H), 7.86 – 7.77 (m, 1H), 7.46 (ddd, *J* = 8.0, 5.0, 1.0 Hz, 1H), 4.42 (s, 2H), 2.60 (m, 2H), 2.26 (t, *J* = 7.5 Hz, 2H), 1.75 – 1.53 (m, 4H), 1.46 – 1.37 (m, 1H), 1.32 (s, 12H); MS ES+, m/z (%): 615 (11) [M-M$^+$], 308 (100) [M$^+$].

6.3.21 Synthesis of [Ru(tpm)(dppz)(py-SH)]²⁺(PF₆⁻)₂
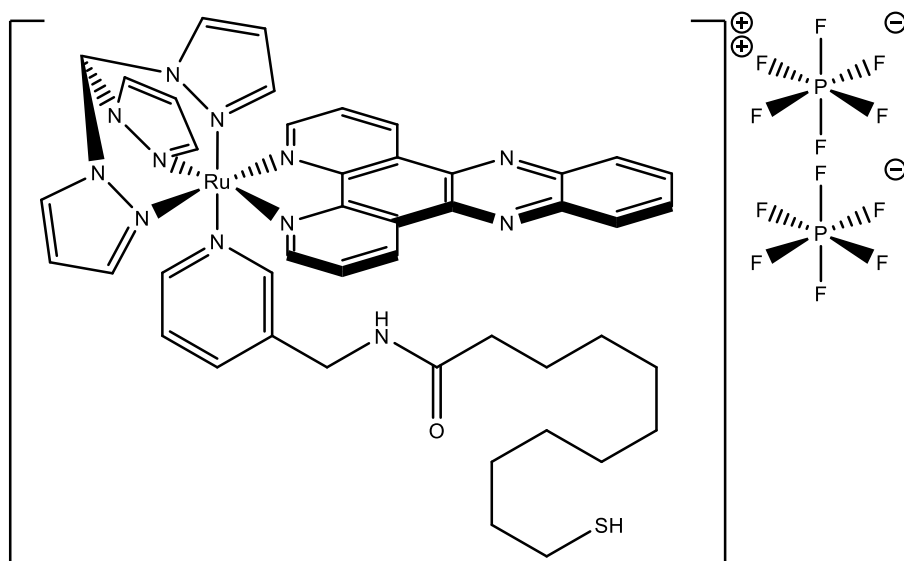
[RuCl(tpm)(dppz)]PF$_6$ (0.07 g, 0.08 mmol) was added to a 100 ml 2-neck round bottom flask and flushed with N$_2$. A 1:1 water:ethanol solvent mix (30 ml) was added to the flask forming a red solution. The flask was covered in foil to exclude light. AgOTf (0.05 g, 0.18 mmol) was added against the N$_2$ flow and the flask was sealed. The reaction was heated to reflux for 2 hrs. The reaction was cooled and filtered through celite filter cell, removing the precipitated AgCl. The reaction was returned to a round bottom flask. Mercapto(pyridinylmethyl)undecanamide (0.26 g, 0.84 mmol) was added under N$_2$ and the reaction was refluxed overnight. The reaction was cooled and solvent reduced *in vacuo*. Saturated KPF$_6$ solution was added to precipitate the salt. The precipitate was collected and purified by preparative HPLC, using a 5-95% MeOH in H$_2$O gradient over 15 minutes. Pure fractions were combined and solvent removed *in vacuo* to give [Ru(tpm)(dppz)(py-SH)](PF$_6$)$_2$ (0.01 g, 0.01 mmol, 12.5 %) as an orange solid; ^{1}H NMR (400 MHz, MeOD) δ 9.90 (ddd, *J* = 20.0, 8.0, 1.5 Hz, 2H), 9.23 – 9.10 (m, 2H), 8.73 (t, *J* = 3.0 Hz, 2H), 8.65 – 8.52 (m, 2H), 8.47 (t, *J* = 2.5 Hz, 1H), 8.26 (t, *J* = 2.5 Hz, 2H), 8.23 – 8.14 (m, 2H), 8.10 (td, *J* = 8.0, 5.5 Hz, 2H), 7.64 (d, *J* = 8.0 Hz, 1H), 7.49 – 7.42 (m, 2H), 7.15 (dd, *J* = 8.0, 6.0 Hz, 1H), 6.94 (dd, *J* = 5.5, 3.0 Hz, 2H), 6.72 (t, *J* = 1.5 Hz, 1H), 6.28 (dd, *J* = 5.0, 2.0 Hz, 1H), 3.93 (s, 2H), 2.74 – 2.50 (m, 2H), 1.61 (dd, *J* = 14.5, 7.0 Hz, 2H), 1.47 – 0.88 (m, 17H); MS ES+, m/z (%): 453 (11) [M²⁺], 308 (100).

6.3.22 Synthesis of tris(2-pyridyl)methylamine
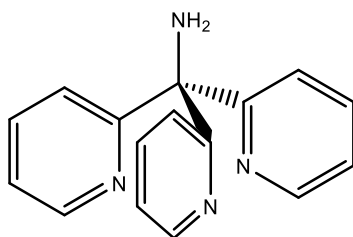
This compound was prepared using an adapted literature procedure.[7] 2-aminomethylpyridine (10.79 g, 100 mmol) was added to a two neck 250 ml oven dried round bottom flask. To the flask dry THF (100 ml) was added and the reaction was flushed with Ar. A dropping funnel was added to the side arm of the RBF and 2.5 M n-butyl lithium in hexane (40 ml) was added to the funnel. The reaction was cooled to -78 °C in a proponal/dry ice bath. n-BuLi was added to the stirred reaction solution dropwise forming a deep red colour. On completed addition of n-BuLi the solution was allowed to warm to room temperature and left stirring overnight. 2-bromopyridine (9.54 ml, 100 mmol) was added to the dropping funnel and added dropwise to the reaction. After addition the reaction was stirred overnight. Water (30 ml) was added to quench the reaction and stirred for 30 mins. The solution was extracted with DCM (3 x 200 ml). The extract was combined and dried over $MgSO_4$ and the solvent removed *in vacuo*. Tris(2-pyridyl)methylamine (4.45 g, 16.96 mmol, 17 %) was obtained as a brown oil. ^{1}H NMR (400 MHz, Acetone) δ 8.51 (ddd, J = 5.0, 2.0, 1.0 Hz, 3H), 7.74 − 7.66 (m, 3H), 7.40 (dt, J = 8.0, 1.0 Hz, 3H), 7.24 (ddd, J = 7.5, 5.0, 1.0 Hz, 3H); ^{13}C NMR (101 MHz, Acetone) δ 205.3 (C), 165.5 (C), 148.2 (CH), 135.8 (CH), 123.2 (CH), 121.7 (CH); MS ES+, m/z (%): 263 (100) [MH$^+$].

6.3.23 Synthesis of tris(2-pyridyl)carbinol
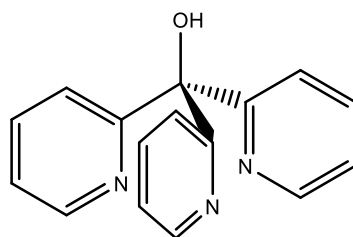
This compound was prepared using a previously reported procedure.[8] 2-bromopyrdine (2.5ml, 26.21 mmol) was added to a two neck 250 ml oven dried round bottom flask. To the flask dry THF (40 ml) was added and the reaction was flushed with Ar. A dropping funnel was added to the side arm of the RBF and 2.5 M n-butyl lithium in hexane (11 ml) was added to the funnel. The reaction was cooled to -78 °C in a proponal/dry ice bath. n-BuLi was added to the stirred reaction solution dropwise forming a deep red colour. On completed addition of n-BuLi a solution of di(2-pyridyl)ketone (4.53 g, 24.60 mmol) in dry THF (35 ml) was added to the dropping funnel. The solution was then added dropwise to the reaction forming a purple colour. After addition the reaction was stirred for 1 hour. Methanol (60 ml) was added to the reaction and warmed to room temperature. Water (50 ml) and a 10% HCl solution (50 ml) were added to quench the reaction. The solution was extracted with DCM (3 x 100 ml) giving a yellow extract. The extract was combined and dried over $MgSO_4$ and the solvent removed *in vacuo*. The yellow solid was recrystalised from acetone to give tris(2-pyridyl)carbinol (2.01 g, 7.63 mmol, 31 %) as pale yellow crystals; ^{1}H NMR (400 MHz, CDCl$_3$) δ 8.57 (ddd, *J* = 5.0, 2.0, 1.0Hz, 3H), 7.76 (dt, *J* = 8.0, 1.0 Hz, 3H), 7.70 (td, *J* = 7.5, 2.0 Hz, 3H), 7.21 (ddd, *J* = 7.5, 5.0, 1.5 Hz, 3H); 13C NMR (101 MHz, CDCl3) δ 162.8 (C), 147.8 (CH), 136.5 (CH), 123.0 (CH), 122.4 (CH), 81.2 (C); MS ES+, m/z (%): 264 (100) [MH$^+$].

6.3.24 Synthesis of mercapto(tris(2-pyridyl)methyl)undecanamide
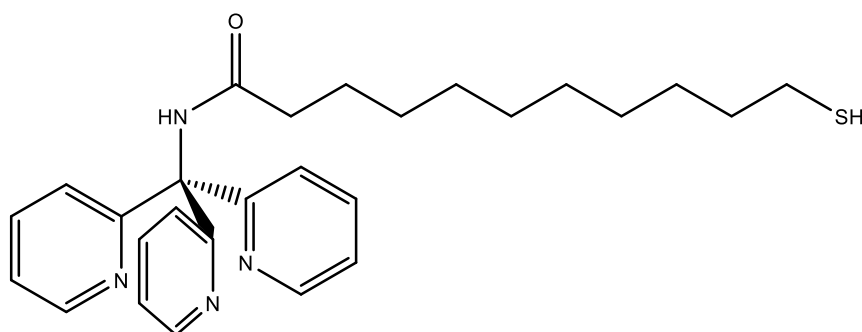
11-mercaptoundecanoic acid (0.61 g, 2.78 mmol), dicyclohexylcarbodiimide (DCC) (0.69 g, 3.34 mmol) and 1-hydroxybenzotriazole hydrate (HOBt) (0.47 g, 3.05 mmol) were added to a 100 ml round bottom flask and flushed with N_2. The flask was sealed and ice cooled dry DCM (40 ml) was added *via* syringe forming a cloudy suspension. The reaction flask was cooled in an ice bath and stirred for 1 hour. Tris(pyridyl)methylamine (0.72 g, 2.73 mmol) was added under N_2, forming orange suspension. The ice bath was removed and the reaction was left to stir overnight. The reaction was partitioned with H_2O and extracted with DCM. The solvent of the extract was removed *in vacuo* yielding a brown oil. The solid was subjected to silica gel column chromatography with DCM:MeOH (19:1). The pure fractions were combined and the solvent removed *in vacuo* to give mercapto(tris(pyridyl)methyl)undecanamide (0.32 g, 2.02 mmol, 25 %) as a pale yellow oil; ^{1}H NMR (400 MHz, Acetone) δ 9.30 (s, 1H), 8.49 (dd, *J* = 5.0, 1.0 Hz, 3H), 7.74 – 7.65 (m, 3H), 7.58 (d, *J* = 8.0 Hz, 3H), 7.24 (ddd, *J* = 7.5, 5.0, 1.0 Hz, 3H), 2.80 (dt, Hz, 2H), 2.60 – 2.47 (m, 2H), 2.38 (t, *J* = 7.5 Hz, 2H), 1.72 – 1.52 (m, 2H), 1.47 – 1.37 (m, 1H), 1.30 (s, 10H); ^{13}C NMR (101 MHz, Acetone) δ 205.3, 170.4, 161.5, 147.2, 135.8, 124.6, 122.0, 43.6, 38.5, 36.5, 34.0, 33.7, 25.5, 23.9; MS ES+, m/z (%): 463 (100) [MH$^+$], 285 (16).

6.3.25 Synthesis of tris(2-pyridyl)methylazide
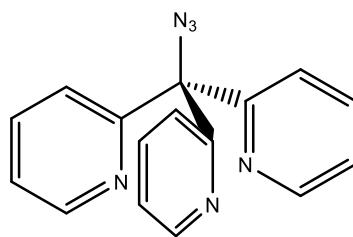
Sodium azide (0.43 g, 6.65 mmol) was added to an oven dried 25 ml RBF and flushed with Ar. The flask was sealed and dry MeCN (10 ml) added *via* syringe. The reaction was cooled in an ice bath. Triflic anhydride (1 ml, 5.94 mmol) was added *via* syringe and the solution was stirred for 2 hours. Solution became yellow with some white precipitate. Tris(2-pyridyl)methylamine (1.45 g, 5.53 mmol), copper sulphate (0.05 g, 0.20 mmol) and triethylamine (1.5 ml, 10.76 mmol) were added to a separate oven dried 50 ml RBF and flushed with Ar. The flask was sealed, dry MeCN (10 ml) added, and cooled in an ice bath. The initial solution of azide and anhydride was transferred to the 50 ml RBF via syringe. The solution turned from a red solution to a darker, almost black solution. The solution was left to stir overnight. Water was added (20 ml) and the solution was extracted with DCM (3 x 30 ml). The combined extract was dried and solvent removed *in vacuo*. The black residue was subjected to silica gel column chromatography with DCM:MeOH (9:1) as eluent. The pure fractions were combined and solvent removed *in vacuo* to give tris(2-pyridyl)methylazide (0.31 g, 1.06 mmol, 19%) as a black solid. MS ES+, m/z (%): 289 (100) [MH$^+$], 261 (12) [MH$^+$-N$_2$].

6.3.26 Synthesis of [RuCl(tpyma)(NN)]PF$_6$
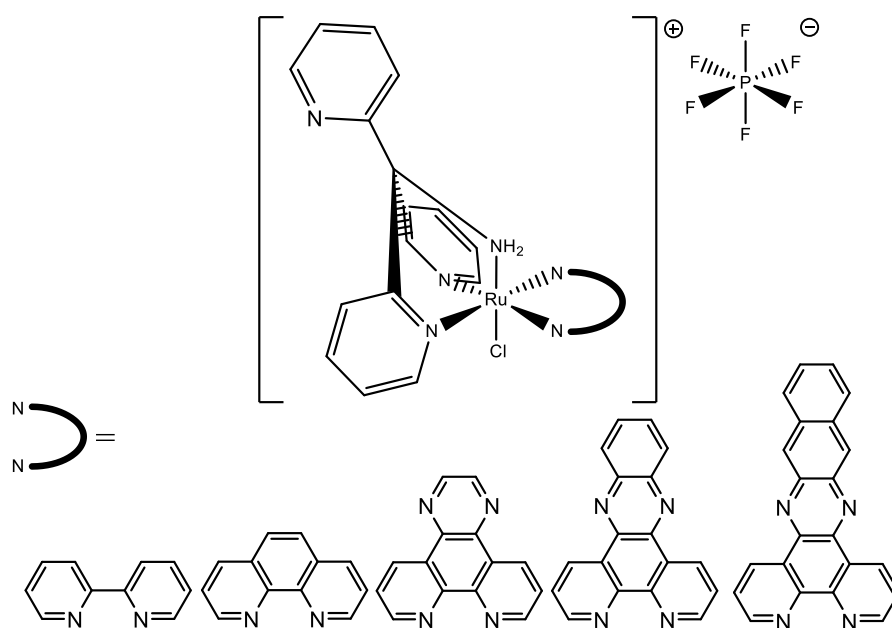
[RuCl$_2$(NN)(dmso)$_2$] and tpyma were added to a dry 100 ml RBF and flushed with N$_2$. Ethylene glycol was added forming a suspension. The flask was sealed with condenser fitted and covered in foil to exclude light. The reaction heated to 140 °C for 1 hour with stirring. The reaction became deep red and was cooled to room temp. A saturated solution of KPF$_6$ (50 ml) was added to precipitate the salt formed. The precipitate was collected and dried. The solid was subjected to column chromatography with 1:1 acetonitrile:toluene as eluent. The orange band was collected. The solvent of the band was removed *in vacuo* and the salt was re-precipitated with sat. KPF$_6$ to yield [RuCl(tpyma)(NN)]PF$_6$ as a red solid.

[RuCl$_2$(bpy)(dmso)$_2$] (0.30 g, 0.61 mmol) and tpyma (0.16 g, 0.61 mmol) heated in ethylene glycol (35 ml) gave [RuCl(tpyma)(bpy)]PF$_6$ (0.04 g, 0.06 mmol, 9.8 %); MS ES+, m/z (%): 555 (100) [M$^+$].

[RuCl$_2$(phen)(dmso)$_2$] (0.28 g, 0.54 mmol) and tpyma (0.14 g, 0.55 mmol) heated in ethylene glycol (35 ml) gave [RuCl(tpyma)(phen)]PF$_6$ (0.09 g, 0.12 mmol, 22.2 %); MS ES+, m/z (%): 579 (100) [M$^+$].

[RuCl$_2$(dpqx)(dmso)$_2$] (0.31 g, 0.54 mmol) and tpyma (0.14 g, 0.55 mmol) heated in ethylene glycol (35 ml) gave [RuCl(tpyma)(dpqx)]PF$_6$ (0.06 g, 0.07 mmol, 13.0 %); MS ES+, m/z (%): 631 (100) [M$^+$].

[RuCl$_2$(dppz)(dmso)$_2$] (0.19 g, 0.32 mmol) and tpyma (0.08 g, 0.32 mmol) heated in ethylene glycol (25 ml) gave [RuCl(tpyma)(dppz)]PF$_6$ (0.11 g, 0.13 mmol, 41.6 %); MS ES+, m/z (%): 681 (100) [M$^+$].

[RuCl$_2$(dppn)(dmso)$_2$] (0.23 g, 0.34 mmol) and tpyma (0.09 g, 0.34 mmol) heated in ethylene glycol (30 ml) gave [RuCl(tpyma)(dppn)]PF$_6$ (0.13 g, 0.15 mmol, 44.1 %); MS ES+, m/z (%): 731 (100) [M$^+$].

6.3.27 Synthesis of [Ru(tpyma)(py)(NN)](PF$_6$)$_2$
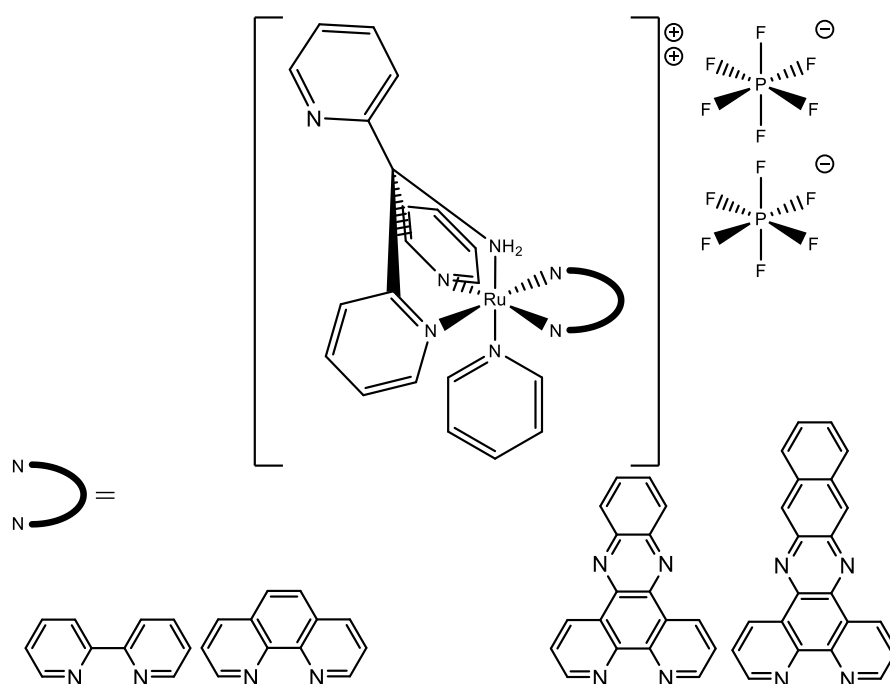
[RuCl(tpyma)(NN)]PF$_6$ was added to a 100 ml 2-neck round bottom flask and flushed with N$_2$. A 1:1 water:ethanol solvent mix was added to the flask forming a red solution. The flask was covered in foil to exclude light. AgOTf was added against the N$_2$ flow and the flask was sealed. The reaction was heated to reflux for 1 hr. The reaction was cooled and filtered through celite filter cell, removing the precipitated AgCl. The reaction was returned to a round bottom flask. Pyridine was added *via* syringe and the reaction was refluxed for a further 3 hours. The reaction was cooled and solvent reduced *in vacuo*. Saturated KPF$_6$ solution was added to precipitate the salt. The precipitate was collected and dried in a vacuum oven to give [Ru(tpyma)(py)(NN)](PF$_6$)$_2$ as an orange solid.

[RuCl(tpyma)(bpy)]PF$_6$ (0.04 g, 0.06 mmol), AgOTf (0.04 g, 0.22 mmol) and pyridine (1 ml, 12.4 mmol) heated in ethanol:water (40 ml) gave [Ru(tpyma)(py)(bpy)](PF$_6$)$_2$ (0.03 g, 0.03 mmol, 52.5 %); ^{1}H NMR (400 MHz, Acetone) δ 9.04 – 8.98 (m, 1H), 8.95 (d, J = 5.0 Hz, 2H), 8.94 – 8.87 (m, 4H), 8.34 (d, J = 8.0 Hz, 2H), 8.28 – 8.20 (m, 2H), 8.16 (td, J = 8.0, 1.5 Hz, 2H), 8.12 – 8.04 (m, 1H), 8.01 (d, J = 8.0 Hz, 1H), 7.98 – 7.92 (m, 1H), 7.86 (dd, J = 6.5, 1.5 Hz, 2H), 7.79 – 7.70 (m, 2H), 7.70 – 7.62 (m, 3H), 7.39 (dd, J = 7.5, 6.5 Hz, 2H), 5.79 (s, 2H).

[RuCl(tpyma)(phen)]PF$_6$ (0.09 g, 0.12 mmol), AgOTf (0.06 g, 0.36 mmol) and pyridine (1 ml, 12.4 mmol) heated in ethanol:water (35 ml) gave [Ru(tpyma)(py)(phen)](PF$_6$)$_2$ (0.03 g, 0.04 mmol, 30.1 %); ^{1}H NMR (400 MHz, Acetone) δ 9.31 (d, J = 5.5 Hz, 2H), 9.10 (d, J = 5.5 Hz, 2H), 9.00 (dd, J = 4.5, 1.0 Hz, 1H), 8.85 (dd, J = 8.0, 1.0 Hz, 2H), 8.47 (s, 2H), 8.38 (d, J = 8.0 Hz, 2H), 8.19 (td, J = 8.0, 1.5 Hz, 2H), 8.04 (dd, J = 8.0, 5.5 Hz, 3H), 7.90 (ddd, J = 9.0, 7.5, 5.0 Hz, 2H), 7.83 – 7.76 (m, 2H), 7.73 (d, J = 5.0 Hz, 2H), 7.65 (dd, J = 7.5, 5.0 Hz, 1H), 7.32 – 7.24 (m, 2H), 5.69 (s, 2H).

[RuCl(tpyma)(dppz)]PF$_6$ (0.49 g, 0.59 mmol), AgOTf (0.21 g, 0.82 mmol) and pyridine (5 ml, 61.82 mmol) heated in ethanol:water (60 ml) gave [Ru(tpyma)(py)(dppz)](PF$_6$)$_2$ (0.22 g, 0.21 mmol, 35.6 %); ^{1}H NMR (400 MHz, Acetone) δ 9.83 (d, J = 8.0 Hz, 2H), 9.40 (d, J = 5.5 Hz, 2H), 9.14 (d, J = 5.0 Hz, 2H), 9.01 (d, J = 5.0 Hz, 1H), 8.57 (dd, J = 6.5, 3.5 Hz, 2H), 8.40 (d, J = 8.0 Hz, 2H), 8.23 (ddd, J = 13.0, 7.5, 4.5 Hz, 6H), 8.06 (t, J = 8.0 Hz, 1H), 7.94 (dt, J = 15.5, 9.5 Hz, 4H), 7.86 – 7.77 (m, 2H), 7.71 – 7.60 (m, 1H), 7.29 (t, J = 7.0 Hz, 2H), 5.86 (s, 2H).

[RuCl(tpyma)(dppn)]PF$_6$ (0.33 g, 0.37 mmol), AgOTf (0.22 g, 0.86 mmol) and pyridine (3 ml, 37.09 mmol) heated in ethanol:water (50 ml) gave [Ru(tpyma)(py)(dppz)](PF$_6$)$_2$ (0.10 g, 0.09 mmol, 24.3 %); ^{1}H NMR (400 MHz, Acetone) δ 9.82 (dd, J = 8.0, 1.5 Hz, 2H), 9.38 (dd, J = 5.5, 1.0 Hz, 2H), 9.25 (s, 2H), 9.14 (d, J = 5.0 Hz, 2H), 9.01 (ddd, J = 5.0, 2.0, 1.0 Hz, 1H), 8.47 (dd, J = 6.5, 3.0 Hz, 2H), 8.40 (d, J = 8.0 Hz, 2H), 8.28 – 8.16 (m, 4H), 8.11 – 8.03 (m, 1H), 8.03 – 7.96 (m, 2H), 7.96 – 7.86 (m, 1H), 7.83 (ddd, J = 5.5, 4.0, 2.0 Hz, 3H), 7.66 (dd, J = 7.5, 4. Hz, 1H), 7.34 – 7.27 (m, 2H), 5.88 (s, 2H).

6.3.28 Synthesis of [RuCl(tpyc)(dppz)]PF$_6$
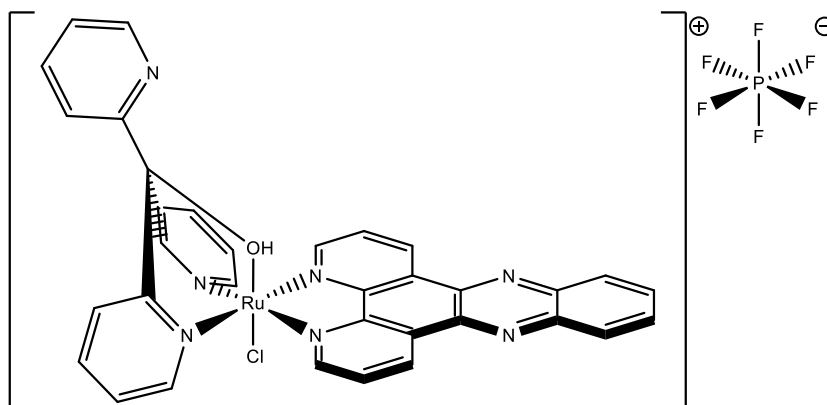
[RuCl$_2$(dppz)(dmso)$_2$] (0.47, 0.76 mmol) and typc (0.20, 0.77 mmol) were added to a dry 100 ml RBF and flushed with N$_2$. Ethylene glycol (30 ml) was added forming a suspension. The flask was sealed with condenser fitted and covered in foil to exclude light. The reaction heated to 140 °C for 1 hour with stirring. The reaction became deep red and was cooled to room temp. A saturated solution of KPF$_6$ (30 ml) was added to precipitate the salt formed. The precipitate was collected and dried. The solid was subjected to column chromatography with 1:1 acetonitrile:toluene as eluent. The dark brown band was collected. The solvent of the band was removed *in vacuo* and the salt was re-precipitated with sat. KPF$_6$ to yield [RuCl(tpyc)(dppz)]PF$_6$ (0.11, 0.13 mmol, 17.2%) as a black solid. MS ES+, m/z (%): 682 (100) [M$^+$], 355 (15).

6.3.29 Synthesis of [Ru(tpyc)(dppz)(py)](PF₆)₂
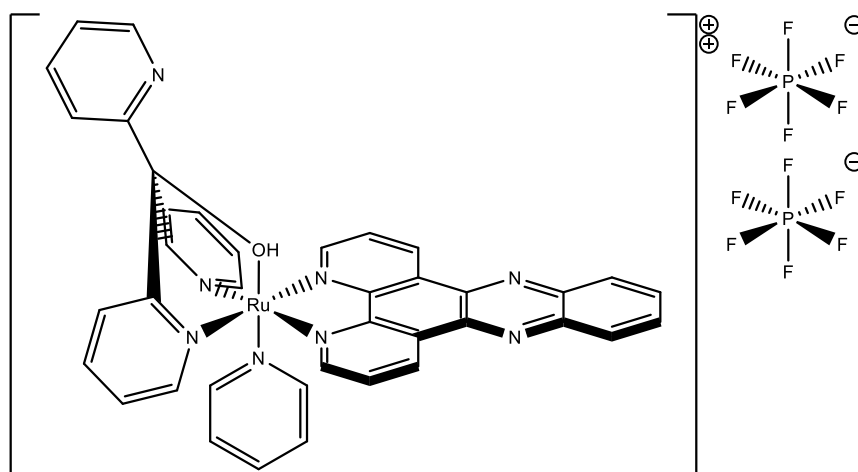
[RuCl(tpyc)(dppz)]PF$_6$ (0.11 g, 0.13 mmol) was added to a 100 ml 2-neck round bottom flask and flushed with N$_2$. A 1:1 water:ethanol solvent mix was added to the flask forming a red solution. The flask was covered in foil to exclude light. AgOTf (0.07 g, 0.26 mmol) was added against the N$_2$ flow and the flask was sealed. The reaction was heated to reflux for 1 hr. The reaction was cooled and filtered through celite filter cell, removing the precipitated AgCl. The reaction was returned to a round bottom flask. Pyridine (3 ml, 37.2 mmol) was added *via* syringe and the reaction was refluxed for a further 3 hours. The reaction was cooled and solvent reduced *in vacuo*. Saturated KPF$_6$ solution was added to precipitate the salt. The precipitate was collected and dried in a vacuum oven to give [Ru(tpyc)(py)(dppz)](PF$_6$)$_2$ (0.12 g, 0.12 mmol, 92.3 %) as an black solid. MS ES+, m/z (%): 725 (31) [M$^+$], 363 (100) [M^{2+}].

6.3.30 Synthesis of di(2-pyridyl)oxime
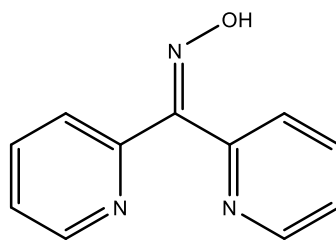
This compound was prepared using a previously reported procedure.[9] Potassium acetate (4.38 g, 43.65 mmol) was added to a two neck 100 ml round bottom flask. Water (40 ml) was added to the flask followed by hydroxylamine hydrochloride (3.04 g, 43.70 mmol). The flask was flushed with N_2 for five minutes, then sealed with a suba seal. The solution was heated to 60 °C for 1 hour. Di-pyridyl ketone (4.05 g, 22 mmol) was weighed into a sample tube and dissolved in methanol (8 ml) forming an orange solution. This solution was transferred to the reaction flask *via* syringe. The reaction remained stirring at 60 °C overnight. The reaction was cooled to room temperature and a white precipitate formed. Water (50 ml) was added to the slurry and the solid was collected by vacuum filtration. The solid was washed in the filter with water and methanol. The solid was recrystalised from water and acetone (1:1). The resultant precipitates was collected by vacuum filtration and dried under vacuum at 40 °C to give di(2-pyridyl)ketone (3.62 g, 18.17 mmol, 83%) as a white solid; ^{1}H NMR (400 MHz, CDCl$_3$) δ 8.70 – 8.60 (m, 2H), 7.94 – 7.78 (m, 3H), 7.68 (d, *J* = 8.0 Hz, 1H), 7.47 (ddd, *J* = 7.5, 5.0, 1.0 Hz, 1H), 7.37 (ddd, *J* = 7.0, 5.0, 2.0 Hz, 1H); MS ES+, m/z (%): 200 (100) [MH$^+$].

6.3.31 Synthesis of di(2-pyridyl)methylamine
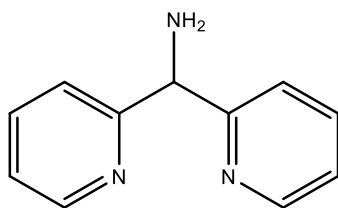
This compound was prepared using a previously reported procedure.[9] Ammonium acetate (1.07 g, 13.88 mmol) and di(2-pyridyl)oxime (2.59 g, 13.00 mmol) were added to a 100 ml 2 neck round bottom flask. Ethanol (15 ml) and 25% ammonia solution were added forming a white suspension. The reaction was flushed with N_2 for five minutes, then the flask was sealed with a suba seal. Zinc powder (3.17 g) was weighed under N_2 and added to the flask against N_2 flow in small portions over 30 minutes. On completing additions the solution became green. The reaction was heated to reflux for 2.5 hours. The reaction was cooled to room temperature and left stirring overnight. A light blue suspension was formed. The zinc powder was removed by filtration through celite and washed with ethanol (10 ml). The pale yellow filtrate was transferred to a round bottom flask and the solvent removed *in vacuo* to yield a waxy yellow solid. The solid was dissolved in 2 M NaOH (30 ml) and extracted with DCM (3 x 30 ml). The combined extract was washed with brine (100 ml) and dried over $NaSO_4$. The solvent was removed *in vacuo* to give a yellow oil. The oil was dissolved in a minimum amount of acetone and cooled in a freezer overnight. Yellow crystals were precipitated and collected by vacuum filtration. The crystals were dried under vacuum at 40 °C to give di(2-pyridyl)methylamine (0.33 g, 1.77 mmol, 13.6 %) as a black solid; ^{1}H NMR (400 MHz, CDCl$_3$) δ 8.56 (dddd, J = 6.5, 5.0, 2.0, 1.0 Hz, 2H), 7.64 (tdd, J = 7.5, 3.5, 2.0 Hz, 2H), 7.51 (d, J = 8.0 Hz, 2H), 7.14 (tdd, J = 7.5, 5.0, 1.0 Hz, 2H); MS ES+, m/z (%): 186 (100) [MH$^+$], 169 (9).

6.3.32 Synthesis of di(2-pyridyl)-1-amino-3-butyne
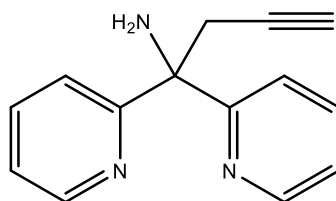
Di(2-pyridyl)methylamine (0.21 g, 1.14 mmol) was added to an oven dried 100 ml RBF and flushed with N_2. Dry THF (10 ml) was added forming a dark brown solution and the solution was cooled to -78 °C in a propanol/dry ice bath. Butyl lithium (2.5M in hexanes) (0.52 ml, 1.30 mmol) was added dropwise from a syringe and the solution became deep purple. Left the solution to stir for 30 minutes after which the solution had turned deep red. Added propargyl bromide (0.1 ml, 1.32 mmol) and left stirring overnight while dry ice slowly evaporated to bring the solution to room temperature. Solution was extracted with diethyl ether (3 x 10 ml) and combined giving a brown solution. The extract was washed with brine and dried over $MgSO_4$. Solvent was removed *in vacuo* to give di(2-pyridyl)-1-amino-3-butyne (0.22 g, 0.97 mmol, 85.3 %) as a brown oil. MS ES+, m/z (%): 224 (100) [MH+].

6.3.33 Synthesis of [RuCl(dpyma)(dppz)]PF$_6$
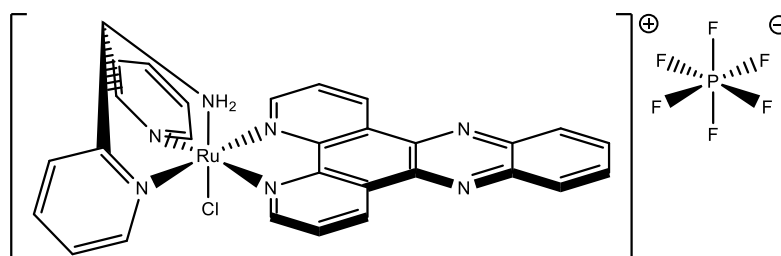
[RuCl$_2$(dppz)(dmso)$_2$] (0.14, 0.22 mmol) and dpyma (0.04 g, 0.23 mmol) were added to a dry 100 ml RBF and flushed with N_2. Ethylene glycol (50 ml) was added forming a suspension. The flask was sealed with condenser fitted and covered in foil to exclude light. The reaction heated to 140 °C for 1 hour with stirring. The reaction became deep red and was cooled to room temp. A saturated solution of KPF$_6$ (50 ml) was added to precipitate the salt formed. The precipitate was collected and dried. The solid was subjected to column chromatography with 1:1 acetonitrile:toluene as eluent. The orange band was collected. The solvent of the band was removed *in vacuo* and the salt was re-precipitated with sat. KPF$_6$ to yield [RuCl(dpyma)(dppz)]PF$_6$ (0.06 g, 0.07 mmol, 33.4 %) as a red solid; MS ES+, m/z (%): 682 (38), 604 (100) [M+].

6.3.34 Synthesis of [Ru(dpyma)(dppz)(py)](PF₆)₂
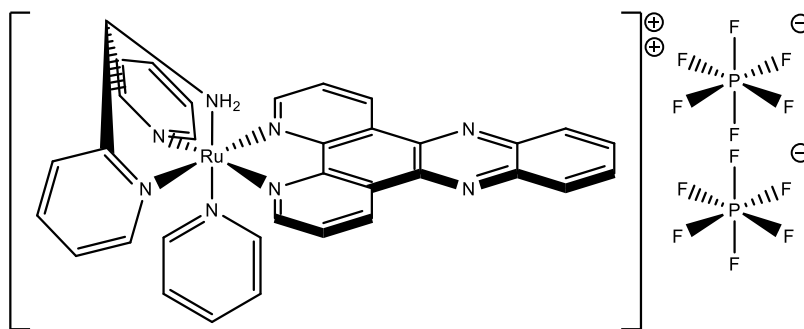
[RuCl(dpyma)(dppz)]PF$_6$ (0.06 g, 0.07 mmol) was added to a 100 ml 2-neck round bottom flask and flushed with N$_2$. A 3:1 ethanol:water solvent mix (40 ml) was added to the flask forming a red solution. The flask was covered in foil to exclude light. AgOTf (0.04, 0.16 mmol) was added against the N$_2$ flow and the flask was sealed. The reaction was heated to reflux for 1 hr. The reaction was cooled and filtered through celite filter cell, removing the precipitated AgCl. The reaction was returned to a round bottom flask. Pyridine (2 ml, 24.8 mmol) was added *via* syringe and the reaction was refluxed for a further 3 hours. The reaction was cooled and solvent reduced *in vacuo*. Saturated KPF$_6$ solution (40 ml) was added to precipitate the salt. The precipitate was collected and dried in a vacuum oven to give [Ru(dpyma)(py)(dppz)](PF$_6$)$_2$ (0.03 g, 0.03 mmol, 47 %) as an orange solid; ^{1}H NMR (400 MHz, Acetone) δ 9.80 (dd, *J* = 8.0, 1.0 Hz, 2H), 9.38 (dd, *J* = 5.5, 1.0 Hz, 2H), 9.08 (d, *J* = 5.5 Hz, 2H), 8.56 (dd, *J* = 6.5, 3.5 Hz, 2H), 8.32 – 8.15 (m, 8H), 7.91 – 7.85 (m, 3H), 7.82 (ddd, *J* = 7.5, 5.5, 2.0 Hz, 2H), 7.25 (dd, *J* = 8.0, 6.0 Hz, 2H), 6.48 (s, 1H), 5.00 (s, 2H); MS ES+, m/z (%): 647 (11) [M$^+$], 324 (100) [M^{2+}].

6.3.35 Synthesis of [Ru(dppz)(py)₄](PF₆)₂
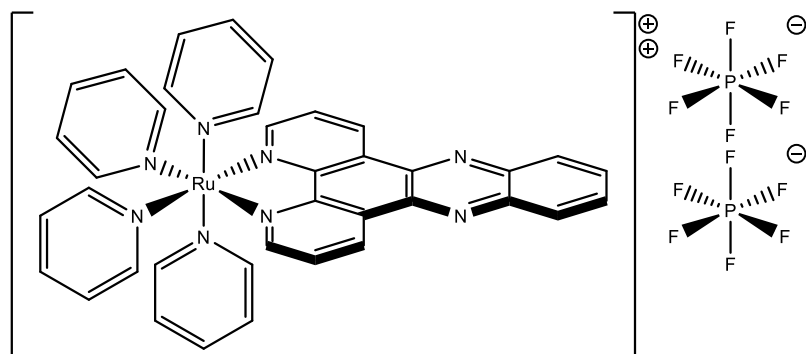
[RuCl$_2$(dppz)(dmso)$_2$] (0.03 g, 0.05 mmol) was added to a 100 ml 2-neck round bottom flask and flushed with N$_2$. A 1:1 water:ethanol solvent mix (20 ml) was added to the flask forming a suspension. The flask was covered in foil to exclude light. AgOTf (0.03 g, 0.10 mmol) was added against the N$_2$ flow and the flask was sealed. The reaction was heated to reflux for 1 hr. The reaction was cooled and filtered through celite filter cell, removing the precipitated AgCl. The reaction was returned to a round bottom flask. Pyridine (1 ml, 12.4 mmol) was added *via* syringe and the reaction was refluxed for a further 3 hours. The reaction was cooled and solvent reduced *in vacuo*. Saturated KPF$_6$ solution was added to precipitate the salt. The precipitate was collected and dried in a vacuum oven to give [Ru(dppz)(py)$_4$](PF$_6$)$_2$ (0.01 g, 0.01 mmol, 45.0 %) as an orange solid. ^{1}H NMR (400 MHz, Acetone) δ 9.84 (d, *J* = 8.0 Hz, 2H), 9.42 (d, *J* = 5.5 Hz, 2H), 8.86 (d, *J* = 5.0 Hz, 4H), 8.56 – 8.45 (m, 2H), 8.41 – 8.10 (m, 10H), 7.87 (t, *J* = 7.0 Hz, 2H), 7.82 – 7.70 (m, 4H), 7.26 (t, *J* = 6.5 Hz, 4H); MS ES+, m/z (%): 350 (27) [M^{2+}], 310 (100) [M^{2+}-py].

6.3.36 Synthesis of [Ru(dppz)(MeCN)$_3$(dmso)](PF$_6$)$_2$
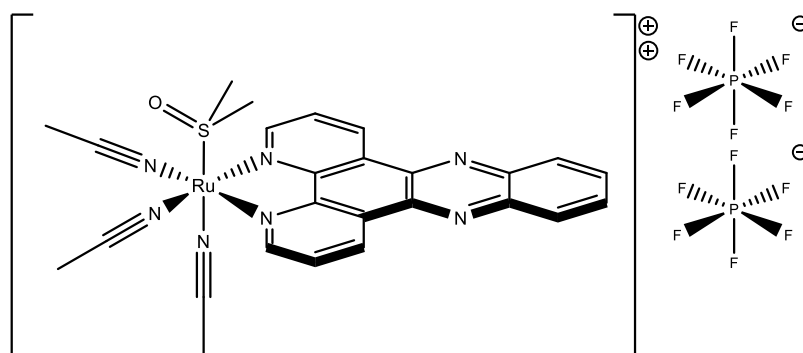
[RuCl$_2$(dppz)(dmso)$_2$] (0.10, 0.17 mmol) was added to a 100 ml 2-neck round bottom flask and flushed with N$_2$. Acetonitrile (40 ml) was added to the flask forming a suspension. The flask was covered in foil to exclude light. AgOTf (0.17, 0.68 mmol) was added against the N$_2$ flow and the flask was sealed. The reaction was heated to reflux for 3 hrs. The reaction was cooled and filtered through celite filter cell, removing the precipitated AgCl. The solvent was reduced *in vacuo*. Saturated KPF$_6$ solution was added to precipitate the salt. The precipitate was collected and dried in a vacuum oven to give [Ru(dppz)(MeCN)$_3$(dmso)](PF$_6$)$_2$ (0.13 g, 0.14 mmol, 84.7 %) as a yellow solid; ^{1}H NMR (400 MHz, Acetone) δ 9.88 (ddd, J = 8.0, 4.5, 1.0 Hz, 2H), 9.76 (ddd, J = 26.5, 5.5, 1.0 Hz, 2H), 8.50 (dd, J = 6.5, 3.5 Hz, 2H), 8.35 (ddd, J = 8.5, 5.5, 4.0 Hz, 2H), 8.21 (dd, J = 6.5, 3.5 Hz, 2H), 6.69 – 6.16 (m, 2H), 3.24 (s, 9H), 3.21 (s, 6H); MS ES+, m/z (%): 293 (46) [M^{2+}], 272 (100) [M^{2+}-MeCN], 252 (80) [M^{2+}-2MeCN], 231 (15) [M^{2+}-3MeCN].

6.3.37 Synthesis of [Ru(tpya)(dppz)](PF$_6$)$_2$
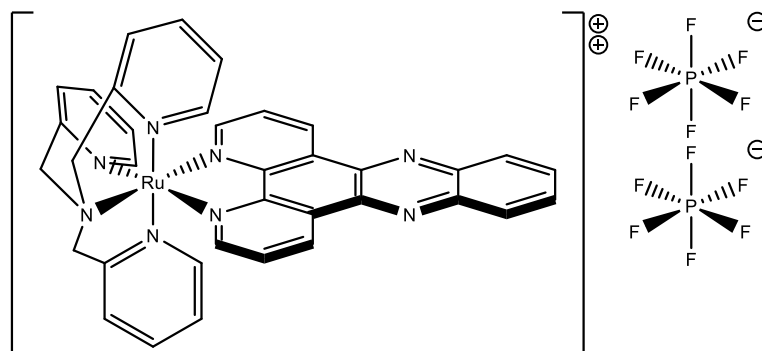
[RuCl$_2$(dppz)(dmso)$_2$] (0.10 g, 0.17 mmol) and typa (0.05 g, 0.17 mmol) were added to a dry 100 ml RBF and flushed with N$_2$. Ethylene glycol (30 ml) was added forming a suspension. The flask was sealed with condenser fitted and covered in foil to exclude light. The reaction heated to 140 °C for 1 hour with stirring. The reaction became deep red and was cooled to room temp. A saturated solution of KPF$_6$ (30 ml) was added to precipitate the salt formed. The precipitate was collected and dried. The solid was subjected to column chromatography with 1:1 acetonitrile:toluene as eluent. The second orange band was collected. The solvent of the band was removed *in vacuo* and the salt was re-precipitated with sat. KPF$_6$ to yield [Ru(tpya)(dppz)]PF$_6$ (0.06 g, 0.06 mmol, 35.3 %) as an orange solid. ^{1}H NMR (400 MHz, Acetone) δ 10.49 (d, J = 5.5 Hz, 1H), 10.04 (dd, J = 5.5, 1.0 Hz, 1H), 9.98 (dd, J = 8.0, 1.0 Hz, 1H), 9.69 (dd, J = 8.0, 1.0 Hz, 1H), 9.64 (d, J = 5.5 Hz, 1H), 8.64 (dd, J = 8.0, 5.5 Hz, 1H), 8.59 – 8.55 (m, 1H), 8.52 – 8.47 (m, 1H), 8.26 – 8.17 (m, 2H), 8.14 (dd, J = 8.0, 5.5 Hz, 1H), 8.08 (d, J = 5.5 Hz, 2H), 7.88 (td, J = 7.5, 1.5 Hz, 1H), 7.75 (td, J = 8.0, 1.5 Hz, 2H), 7.63 (d, J = 8.0 Hz, 3H), 7.58 – 7.43 (m, 1H), 7.07 (t, J = 6.0 Hz, 2H), 6.12 (d, J = 17.0 Hz, 2H), 5.60 (d, J = 17.0 Hz, 2H), 5.18 (s, 2H); MS ES+, m/z (%): 673 (6) [M$^+$], 337 (100) [M^{2+}].

6.4 References

1   D. L. Reger, T. C. Grattan, K. J. Brown, C. A. Little, J. J. S. Lamba, A. L. Rheingold and R. D. Sommer, *J. Organomet. Chem.*, 2000, **607**, 120–128.

2   D. L. Reger, J. R. Gardinier, R. F. Semeniuc, U. H. F. Bunz and M. D. Smith, *New J. Chem.*, 2005, **29**, 1035–1043.

3   M. N. Tahir, N. Lämmerhardt and P. Mischnick, *Carbohydr. Polym.*, 2012, **88**, 154–164.

4   K. Mitsumoto, H. Nishikawa, G. N. Newton and H. Oshio, *Dalton Trans.*, 2012, **41**, 13601.

5   E. Iengo, E. Zangrando, E. Baiutti, F. Munini and E. Alessio, *Eur. J. Inorg. Chem.*, 2005, 1019–1031.

6   C. M. Shade, R. D. Kennedy, J. L. Rouge, M. S. Rosen, M. X. Wang, S. E. Seo, D. J. Clingerman and C. A. Mirkin, *Chem. - Eur. J.*, 2015, **21**, 10983–10987.

7   P. J. Arnold, S. C. Davies, J. R. Dilworth, M. C. Durrant, D. V Griffiths, D. L. Hughes, R. L. Richards and P. C. Sharpe, *J. Chem. Soc. Trans.*, 2001, 736–746.

8   R. T. Jonas and T. D. P. Stack, *Inorg. Chem.*, 1998, **37**, 6615–6629.

9   S. Rana, A. Dey and D. Maiti, *Chem. Commun.*, 2015, **51**, 14469–14472.